# Ultracold Atoms in Artificial Gauge Fields

by Tobias Graß

PhD Thesis

Thesis Advisor: Dr. Maciej Lewenstein

Thesis Co-Advisor: Dr. Bruno Juliá-Díaz

Submitted in October 2012

at

Institut de Ciències Fotòniques

and

Universitat Politècnica de Catalunya

*"Die Vernunft muß mit ihren Prinzipien, nach denen allein übereinkommende Erscheinungen für Gesetze gelten können, in einer Hand, und mit dem Experiment, das sie nach jenen ausdachte, in der anderen, an die Natur gehen, zwar um von ihr belehrt zu werden, aber nicht in der Qualität eines Schülers, der sich alles vorsagen läßt, was der Lehrer will, sondern eines bestallten Richters, der die Zeugen nötigt, auf die Fragen zu antworten, die er ihnen vorlegt."*

*(Reason must approach nature with the view, indeed, of receiving information from it, not, however, in the character of a pupil, who listens to all that his master chooses to tell him, but in that of a judge, who compels the witnesses to reply to those questions which he himself thinks fit to propose.)*

Immanuel Kant [1]

[1] Kritik der reinen Vernunft, Vorrede zur zweiten Auflage, 1787. Übersetzung ins Englische von J. M. D. Meiklejohn.

# Abstract

The present thesis studies a variety of cold atomic systems in artificial gauge fields. In the first part we focus on fractional quantum Hall effects, asking whether interesting topological states can be realized with cold atoms. We start by making a close connection to solid-state systems and first consider fermionic atoms with dipolar interactions. Assuming the system to be in the Laughlin state, we evaluate the energy gap in the thermodynamic limit as a measure for the robustness of the state. We show that it can be increased by additionally applying a non-Abelian gauge field squeezing the Landau levels. We then switch to bosonic systems with repulsive contact interactions. Artificial magnetic fields for cold bosons have extensively been discussed before in the context of rotating Bose gases. We follow a different approach where the gauge field is due to an atom-laser coupling. Thus, transitions between different dressed states have to be taken into account. They are shown to break the cylindrical symmetry of the system. Modifying the Laughlin state and the Moore-Read state accordingly, we determine the parameter regimes where these states represent well the ground state of the system obtained via exact diagonalization. One of the most interesting features of fractional quantum Hall states is the anyonic behavior of their excitations. We therefore also study quasiholes in the Laughlin state and the modified Laughlin state. They are shown to posses anyonic properties, which become manifest even in small systems. Moreover, the dynamics of a single quasihole causes visible traces in the density of the system which allow to clearly distinguish the Laughlin regime from less correlated phases. In the latter, a sequence of collapses and revivals of the quasihole can be observed, which is absent in the Laughlin regime. Extending our study to bosonic systems with a pesudospin-$\frac{1}{2}$ degree of freedom, we discuss the formation of strongly correlated spin singlets. Strikingly, at filling $\nu = \frac{4}{3}$, the system is described by a state with non-Abelian excitations, which is constructed as the zero-energy ground state of repulsive three-body contact interactions. Systems with internal degrees of freedom also allow for implementing artificial spin-orbit coupling. This gives rise to a variety of incompressible states. In the second part of the thesis, we concentrate on condensed systems. Bose-Einstein condensates with spin-orbit coupling are shown to have a degeneracy on the mean-field level, which is lifted by quantum and thermal fluctuations. The system becomes experimentally feasible in three dimensions, where the condensate depletion remains finite. It may thus allow for an experimental observation of this order-by-disorder mechanism. Finally, we study the influence of Abelian and non-Abelian gauge fields on the quantum phase transitions of bosons in a square

optical lattice. Re-entrant superfluid phases and superfluids at finite momenta are interesting properties featured by such systems.

# Contents


**1 "Ultracold" and "artificial" - do we still study nature? 1**
Bose-Einstein condensates as quantum simulators. . 2
Example: Bose-Hubbard model. . . . . 2
Artificial gauge fields. . . . . 4
Quantum simulation = quantum realization. . . . . 5
Realization of anyons. . . . . 6
Outline of the thesis. . . . . 7

**2 Synthesizing gauge fields 11**
2.1 Rotation of the system . . . . . 11
2.2 Gauge fields due to a geometric phase . . . . . 13
2.3 Non-Abelian gauge fields . . . . . 18
2.3.1 Definition of non-Abelian gauge fields . . . . . 18
2.3.2 Synthesizing non-Abelian gauge fields . . . . . 21
2.4 Artificial gauge fields in optical lattices . . . . . 22

**I Fractional Quantum Hall Systems 25**

**3 Quantum Hall effects - from electrons to atoms 27**
3.1 Introduction to quantum Hall effects . . . . . 27
3.1.1 Integer quantum Hall effect . . . . . 28
3.1.2 Fractional quantum Hall effect . . . . . 31
3.1.2.1 Laughlin state . . . . . 32
3.1.2.2 Moore-Read state and Read-Rezayi series . . . . . 34
3.1.2.3 Spinful FQH states and NASS series . . . . . 36
3.2 Laughlin states of dipolar atoms . . . . . 38
3.2.1 Quasihole excitation gap . . . . . 39
3.2.1.1 Different types of quasiholes . . . . . 41
3.2.1.2 Evaluation of the gap . . . . . 43
3.2.2 Laughlin state and quasihole gap in non-Abelian gauge fields 45
3.2.2.1 Hamiltonian structure . . . . . 45
3.2.2.2 Squeezing transformation . . . . . 47

3.2.2.3 Gap above squeezed Laughlin state . . . . . 47

**4 Fractional quantum Hall states of laser-dressed bosons 51**
4.1 Effective Hamiltonian . . . . . 53
4.2 Exact diagonalization method . . . . . 55
4.3 Results: From condensates to strongly correlated phases . . . . . 59
4.3.1 Adiabatic case: $\Omega_0 \to \infty$ . . . . . 59
4.3.2 Non-adiabatic case: finite $\Omega_0$. . . . . 63
4.3.2.1 Properties of the system . . . . . 63
4.3.2.2 Generalized wave functions . . . . . 65
4.3.2.3 Overlaps . . . . . 67
4.3.3 Experimental feasibility . . . . . 70

**5 Testing the system with quasiholes 73**
5.1 Anyonic behavior of excitations . . . . . 75
5.1.1 Quasiholes in the adiabatic case . . . . . 75
5.1.1.1 Fractional charge . . . . . 76
5.1.1.2 Fractional statistics . . . . . 78
5.1.2 Non-adiabatic effects on the properties of quasiholes . . . . 80
5.2 Dynamics of quasiholes . . . . . 83
5.2.1 Quasiholes in the Laughlin state . . . . . 83
5.2.2 Quasiholes in the $L = 0$ condensate . . . . . 85
5.2.3 Quasiholes in the Laughlin quasiparticle state . . . . . 93
5.2.4 Applications . . . . . 96

**6 Fractional quantum Hall states of pseudospin-1/2 bosons 97**
6.1 Landau levels on the torus . . . . . 99
6.2 Translational symmetries on the torus . . . . . 103
6.3 Spin singlet states . . . . . 106
6.4 Incompressible phases and NASS states . . . . . 108
6.5 Effects of spin-orbit coupling . . . . . 113
6.5.1 Laughlin-like states . . . . . 117
6.5.1.1 At filling $\nu = 1/2$. . . . . 117
6.5.1.2 At filling $\nu < 1/2$. . . . . 120
6.5.2 Incompressible phases at the degeneracy point . . . . . 122

**II Condensed Systems 127**

**7 Bose-Einstein condensates with spin-orbit coupling 129**
7.1 Mean-Field Solution . . . . . 131
7.2 Quantum Fluctuations . . . . . 135
7.2.1 Order-by-disorder mechanism . . . . . 135
7.2.2 Collective Excitations . . . . . 135

7.2.3 Free energy . . . 141
7.2.4 Condensate Depletion . . . 144

**8 Mott transition in synthetic gauge fields 149**
8.1 The Model . . . 152
8.2 Mott insulating phase . . . 154
8.2.1 Hopping expansion . . . 154
8.2.2 Independent species . . . 155
8.2.2.1 Constant gauge potential without magnetic flux ($\Phi = 0$) . . . 156
8.2.2.2 Gauge potential with magnetic flux ($\Phi = 1/2$) . . . 158
8.2.3 XY configuration . . . 161
8.3 Superfluid phase . . . 165

**9 Gauge fields for cold atoms - Where, when, and why? 169**
9.1 Summary of Part I . . . 170
9.2 Summary of Part II . . . 172
9.3 A brief perspective . . . 173

**A Strongdeco: Expansion of analytical, strongly correlated quantum states into a many-body basis 177**
Applications . . . 184

**Bibliography 185**

**List of Figures 195**

**Acknowledgements 199**

# Chapter 1

# "Ultracold" and "artificial" - do we still study nature?

The subject of physics, stemming from the Greek word *phýsis* "nature", undoubtedly is supposed to be nature. The present thesis, studying "ultracold" atoms in "artificial" gauge fields, however, might seem not to cope with this definition: "Ultracold", this means colder than anything in the universe - except for those atoms which by excessive cooling have been made "ultracold" in the laboratory. "Artificial" gauge fields, this refers to sophisticated techniques which make the atoms feel the effect of, for instance, a magnetic field, as if they were charged particles, while in nature an atom, being electroneutral, is not sensitive to true magnetic fields. Due to these discrepancies between "natural" atoms and the "manipulated" atoms considered here, it appears to be indicated to first point out which insight to nature we may expect from the subject of this thesis.

Let us therefore briefly recall a revolutionary idea which accompanied the invention of modern age physics more than 300 years ago: In order to study the bright and colorful nature of light, I. Newton decided to move back into a dark chamber, where the only light entered through tiny slits. In this way, he obtained beams of light which he was able to direct through lenses or prisms. These simple experiments, described in Newton's *Opticks*, defined a ground-breaking concept of physics: the use of completely artificial setups in order to gain empirical insight to nature. Methodically, indeed, the situation in Newton's dark chamber is similar to the one in modern ultracold laboratories. Just as restricting white light to a

narrow beam had allowed for decomposing it into its spectrum colors by using a prism, cooling down atomic ensembles revealed the quantum-statistical nature of atoms which at any temperature occurring naturally is hidden beyond thermal fluctuations. Both setups are artificial, but they allow to study fundamental properties of nature.

**Bose-Einstein condensates as quantum simulators.** Certainly the most spectacular success achieved by cooling atoms, awarded the 2001 Nobel Prize, dates back to 1995 when bosonic atoms have been condensed into a state of matter described by a macroscopic wave function [1, 2]. Although atoms outside the laboratory are not in this phase of matter, its experimental realization increased our understanding of nature, as it confirmed a phase which was predicted seven decades earlier by A. Einstein and S. Bose, and which thus has been named Bose-Einstein condensate (BEC). However, as the exploding amount of research dedicated to ultracold atomic systems since 1995 clearly shows (cf. [3, 4]), the realization of BECs has not been the final stroke to a long search for this exotic phase of matter. Contrarily, it opened a new field of physics, where much, if not most, of the research is not primarily motivated by the interest in the behavior of cold atoms on their own. But often, studying these objects might teach us something about the behavior of other particles - under less artificial circumstances.

**Example: Bose-Hubbard model.** To illustrate this, let us consider a seminal experiment which was thought of in 1998 by D. Jaksch *et al.* [5] and which was accomplished successfully in 2002 by M. Greiner *et al.* [6]. This experiment studies ultracold atoms in periodic potentials which are built up by a set of counter-propagating laser beams and are therefore called optical lattices. The analogy to a crystal where electrons or, taking into account the bosonic nature of the atoms, Cooper pairs move in the potential of periodically ordered ions is obvious. But while in any real crystal impurities and perturbations impede the deduction from the observed behavior to the basic laws governing it, the ultracold setup is free from defects. It allows to study an *ideal model*. Furthermore, parameters which might hardly be controllable in a crystal can be modified in the system of ultracold atoms by changing the design of the setup or just tuning experimental parameters.

Conceptually, this goes beyond the before-mentioned strategy, where the nature of a physical system (e.g. white light) is revealed by deducing it from the behavior of the same system within an abstract setup (e.g. a single light beam). But it seems to be a natural generalization of this old concept, if we now try to understand the behavior of a physical system by deducing it from the behavior of an *analog* system. This concept of studying difficult and relevant quantum many-body systems by realizing analog problems artificially in clean and highly controllable environments is called *quantum simulation* [7].

The pioneering 2002 experiment realized the Bose-Hubbard model [8], in which bosonic particles hop between neighboring sites of a hypercubic lattice, and interact locally on each site. The model describes a competition between these two processes, whose energies are quantified by the hopping amplitude $J$ and the interaction strength $U$. In the limit $J = 0$, each atom sits on a lattice site and is described by a completely local wave function with a random phase. As demanded by the Heisenberg uncertainty relation, the atoms have no well-defined momentum. The system is said to be in a Mott insulating phase. In the opposite limit $U = 0$, the system shows a superfluid behavior: every atom extends throughout the whole lattice, and therefore must have a sharp momentum. In the ground state, all atoms have the same momentum defined by the minimum of the lattice dispersion. This implies a phase correlation between the particles, which means that the phase-rotational symmetry of the Mott phase must be broken. Clearly, the ratio of the two model parameters $J$ and $U$ controls, whether the system is superfluid or Mott insulating. Ultrapassing a critical value $(J/U)_{\mathrm{crit}}$, the atoms undergo a quantum phase transition. If we think of a solid, it will certainly be very difficult or even impossible to modify this ratio. In the experiment with cold atoms, however, $J/U$ can be tuned just by changing the depth of the lattice potential, i.e. by tuning the intensity of the lasers. In this way, it became possible to realize this paradigm of a quantum phase transition [9] and to clearly detect it. The latter was achieved by releasing the trapping potential of the atoms which makes them expand freely in space, according to their initial momentum. Photographs of the atomic cloud after a short expansion time, the so-called time-of-flight absorption pictures, therefore reproduce the initial momentum distribution, integrated in one spatial direction. As we argued above, this distribution characterizes the superfluid phase through its peaked structure.

As in the case of the experimental realization of Bose-Einstein condensates, the observation of the Mott-superfluid transition strikingly confirmed a theoretical

prediction of a fundamental physical phenomenon. The importance of this experiment goes far beyond this: Providing experimental access to the phase boundary of the Bose-Hubbard model, the quantum gas might be seen to solve this model. One may argue that this is not quite a groundbreaking achievement, in view of different theoretical techniques which allow for a precise calculation of the phase diagram for bosons in a lattice: The scaling arguments from Ref. [8] give a qualitatively correct picture. Perturbation theory on the mean-field levels yields quantitatively good results [9, 10]. Further improvements achieved by going beyond mean-field make theoretical results quantitatively exact [11–13]. Most accurate calculations have been done using the Monte-Carlo method [14]. From this point of view, no new insight is gained from experimentally realizing the model with cold atoms. However, having the theoretical predictions at hand, the realization of the Bose-Hubbard model must be seen as a ground-breaking proof-of-principle experiment. We shall stress at this point the huge versatility of ultracold lattice gases, which allows to explore much more complicated models. To give just a few examples: one can, nearly at will, modify the geometry of the lattice, given by the lasers. This also includes the dimensionality of the system. It is possible to tune the interaction of the particles, whose strength is subject to Feshbach resonances and even whose range can be modified, e.g. by using dipolar atoms and suppressing s-wave scattering. And, although cooling techniques for fermions are less efficient, it is also possible to fill an optical lattice with Bose-Fermi mixtures or fermions [15, 16]. In contrast to the Bose-Hubbard model, the phase diagram of the Fermi-Hubbard model is strictly speaking unknown. Especially, despite decades of research, there is still debate, whether or not this microscopic model is able to describe the physics of high-$T_c$ superconductors. It is a promising idea to answer these questions by realizing the model with cold atoms.

**Artificial gauge fields.** If we wish to simulate systems of elementary particles using cold atoms, sooner or later a substantial drawback will show up: atoms are neutral with respect to the fundamental gauge fields, while it is no exaggeration to say that gauge fields are the central elements of modern physics. All fundamental interactions can be derived from postulating gauge symmetries in the theories for the free particles: Electromagnetic forces, mediated by photons, follow from a U(1) gauge invariance in the Dirac equation. Weak and strong interactions, mediated by three weak bosons and eight gluons, are the consequence of an SU(2) and an SU(3) invariance, respectively. They are thus fundamental examples of non-Abelian gauge theories. In order to access the broad range of physics related

to gauge fields, it is a prerequisite to synthesize these gauge fields for atoms. Certainly, the effective implementation of *dynamical* gauge fields, as the sources of interaction between elementary particles, in systems of cold atoms is one of the most challenging prospects for quantum simulations. Unfortunately, they seem to be still a long way off.

However, active research work, and this thesis is supposed to be a piece of it, is dedicated to investigating *static* or *external* gauge fields in cold atomic systems. Examples for static gauge fields occurring in nature and the fascinating physics due to them are manifold. There is, for instance, the Aharanov-Bohm effect [17], where a charged particle moving in the fieldfree region around a magnetic flux feels a U(1) Berry phase due to the non-zero electromagnetic potential. In two-dimensional systems subjected to a strong magnetic field we may encounter the vast field of quantum Hall physics [18], which we will discuss in more detail at a later stage of this thesis. Non-Abelian gauge fields show up when, for instance, the particle spin is coupled to the orbital motion. Predicting the behavior of such systems is often quite difficult due to their strongly correlated nature, especially when interactions come into play. Therefore, such systems are very interesting candidates for doing quantum simulations. Such simulations, involving cold atoms in artificial gauge fields, could increase our understanding of relevant problems in condensed matter physics like topological insulators [19] or fractional quantum Hall effect. On the latter, we will focus in the first part of the thesis.

**Quantum simulation = quantum realization.** Discovered in the 1980s on layers between semiconducting materials [20], the fractional quantum Hall effect originally is a solid state phenomenon. Thus, realizing it with cold atoms could be considered a quantum simulation of a solid. This might help to answer pending questions like, for instance, the nature of the fractional quantum Hall state at filling factor $\nu = 5/2$, for which a Hall plateau has already been observed [21], but which cannot be understood in the spirit of Laughlin's argument valid for odd-denominator filling factors [22].

Certainly, the implementation of a fractional quantum Hall Hamiltonian in cold atomic systems can be motivated by the quest for solutions to open problems like that. However, at this point it seems to be important to stress that a quantum simulation is not a "virtual" process, where the simulated particles exists only in the memory of some computing machine. Contrarily, the simulators themselves, i.e. the atoms, are real particles. This implies that the *simulation* of a relevant

many-body problem with cold atoms is, at the same time, its *realization*. We can thus use the versatility of cold atomic systems not only to mimic nature, but moreover to confront nature with exotic conditions. Such conditions might not even exist outside the cold atomic framework. Bose-Einstein condensation itself is an exotic phase of matter for which the universe is just too hot, but experiments have shown that nature is created such that it really supports this phase if we cool it. There are many other exotic situations which we can think of. And at least some of them may be realized in experiments, thereby realizing intriguing properties of nature which emerge from these exotic conditions.

**Realization of anyons.** From this point of view, the study of fractional quantum Hall physics is motivated on quite a fundamental level, as it considers nature in the very exotic situation of being confined to two spatial dimensions, while our universe appears to be locally a $(3+1)$-dimensional Minkowski space. Whether such a setup is realized in solid materials as done since the 1980s, or with cold atoms, as expected to be achieved in the near future, actually plays no role. The versatility of cold atoms, though, is a huge advantage for fully exploring this exotic regime.

The main motivation to realize fractional quantum Hall systems is a drastic consequence for (quasi)particles which emerge from a two-dimensional many-body system: They may not behave like bosons or fermions, as any particle or quasiparticle in three or higher dimensions does [23, 24]. To understand this, we must realize that interchanging a pair of particles (or quasiparticles) twice must be equivalent to wrapping one particle around the other. In three dimensions, the trajectory of this particle can be smoothly deformed into one where none of the particles moves at all. Thus, the wave function describing the particles is not allowed to change. Consequently, interchanging particles only yields a $\pm$ sign, restricting the particles' statistics to the bosonic or fermionic one. In two dimensions, however, the above argument does not hold. Trying to deform the trajectory of the particle which moves around the other, we will at some point hit the other particle. Thus, statistical phases different from $\pm 1$ become possible. Such particles have been named *anyons* [25]. It has then also been pointed out that, given an $N$-fold degenerate ground state of a system in two dimensions, the statistical phase does not necessarily belong to U(1), but can also be element of SU($N$). Such particles have been named *non-Abelions* or *non-Abelian anyons* [23, 24].

The realization of such (quasi)particles in two-dimensional cold atomic systems with artificial gauge fields should be possible. Though being an emergent phenomenon, within the cold atomic world these quasiparticles are *real* particles. Provocatively, one might say that they are as real as, for instance, the paradigm of an elementary particle, the "free" electron, which is nothing else than the quasiparticle excitation of the Dirac sea [26]. Whether or not one agrees with this opinion, what we, once more, want to stress is that such quasiparticles are not only simulated, but cold atoms can really provide them.

This distinction is especially relevant in so far as a main driving force for studying the fractional quantum Hall effect is a future technological utilization of non-Abelian anyons in quantum-logical gates [27]. Due to the topological origin of these quasiparticles, gates operating with anyons give the hope that they will allow for constructing fault-tolerant quantum computers. The future will show whether solid-state systems are the most feasible ones to provide such anyons, having the great advantage of needing less cooling, or the ones emerging from the more versatile cold atom systems, or even others (e.g. out of photons, cf. [28]). In all cases, cold atoms in artificial gauge fields seem to be useful: either as a versatile quantum simulator of a solid (or anything else), or as a real physical system with its own very interesting and very real properties.

**Outline of the thesis.** With this motivation for studying ultracold atoms in artificial gauge fields, we can now give a detailed outline of the contents of this thesis.

In Chapter 2 we will present different proposals how to synthesize gauge fields for atoms. The simplest idea, considered in Section 2.1, is a rotation of the system. In more details we will investigate a proposal to implement artificial magnetic fields by an atom-laser coupling in Section 2.2. In Section 2.3, we will sketch a generalization of this proposal to non-Abelian gauge field. While most physicists have an understanding about what is a magnetic field, non-Abelian gauge fields are less common, so we will also give a brief introduction into this mathematical construction. Finally, in Section 2.4 proposals to implement gauge fields in optical lattices are shortly discussed.

The following Chapters 3–6 form the first original part of the thesis, which is dedicated to quantum Hall physics. The first section of chapter 3 gives a brief introduction, and presents a variety of relevant fractional quantum Hall states.

As we seek to make a close connection between the electronic quantum Hall effects and the atomic counterpart, we start by investigating a system of fermionic atoms with dipolar interaction in Section 3.2. Here, we will assume that their behavior is described by the Laughlin wave function, and investigate the energy gap in the thermodynamic limit. We will start with an artificial magnetic field, which we then generalize to a non-Abelian gauge field. Thereby we are able to squeeze the relevant single-particle states, which is shown to increase the energy gap, making the system more robust against perturbations.

Chapter 4 is closely linked to the proposal of Section 2.2. By means of exact diagonalization, which is briefly introduced in Section 4.2, we investigate the bosonic fractional quantum Hall states which can be produced within this setup. Our focus is on the "undesired" terms in the Hamiltonian, which inevitably are carried along, if we use laser-dressing of atoms to generate an artificial magnetic field. This study reveals the conditions under which fractional quantum Hall physics should become observable in the laboratory. While Chapter 4 considers the ground states of the system, Chapter 5 is dedicated to probably the most fascinating feature of fractional quantum Hall effect, the quasiparticle excitations. In this chapter, we calculate the fractional "charge" and the fractional statistics of excitations above the Laughlin state. Again, we contrast the "pure" effect without undesired terms, and the "real" effect taking into account imperfections stemming from the concrete proposal. We also discuss the dynamics of quasiholes in the Laughlin state, and contrast it to holes in less correlated systems. In the latter, collapse-and-revival effects are found to take place, which may allow for spectroscopy in the lowest Landau level. They also distinguish the Laughlin state from other regimes, which could facilitate its experimental detection.

While Chapters 4 and 5 exclusively consider one-component Bose gases, an additional spin degree of freedom may change the nature of the states. In Chapter 6, we consider a pseudospin-$\frac{1}{2}$ Bose gas in an artificial magnetic field. We show that a series of non-Abelian spin singlet states describe the ground states at different filling factors. Here, *non-Abelian* refers to the nature of their excitations. This finding is striking, as these states are constructed as eigenstates of a $k$-body contact interaction (with $k$ in general larger than 2), while we consider the realistic setup of a two-body contact potential. Thus, our results provide evidence that these interesting many-body quantum states, so far just a theoretical construction, could become real in experiments with ultracold atoms. Furthermore, the pseudospin degree of freedom allows to couple the external motion to

the internal dynamics. The influence of such a spin-orbit coupling, described by a non-Abelian gauge field, on the strongly correlated phases of the system is investigated in Section 6.5.

Chapters 7 and 8 form the second original part of the thesis, which focuses on condensation phenomena in bosonic systems exposed to artificial gauge fields. Chapter 7 considers BECs with a spin-orbit coupling. While on the non-interacting level, this coupling causes a huge degeneracy, the mean-field ground state is shown to possess only a two-fold degeneracy. Calculating the collective excitations, we are able to show that quantum and/or thermal fluctuations select a unique ground state. Differently to the fractional quantum Hall part of the thesis, here we consider systems not only in two but also in three dimension. In fact, our calculations show that the condensate is stable against thermal fluctuations only in three dimensions.

The only chapter dedicated to systems in optical lattices is Chapter 8. We investigate a Bose-Hubbard model in two dimensions, where the atoms are exposed to Abelian and non-Abelian gauge fields. Above we have already outlined the spectacular success of realizing quantum phase transitions of cold atoms in optical lattices. In this thesis, we analyze the effect of the gauge fields on this Mott transition. We also calculate the excitation spectra in the Mott phase and at the phase boundary. Our analysis shows that they have an intriguing discontinuity upon tuning the gauge field strength. We find re-entrant superfluid phases, and condensates of finite momenta.

Most of the work presented in this thesis has been published previously in the following articles:

(I) T. Graß, M. A. Baranov, M. Lewenstein. *Robustness of Fractional Quantum Hall States with Dipolar Atoms in Artificial Gauge Fields.* Phys. Rev. A **84** 043605 (2011)

(II) T. Graß, K. Saha, K. Sengupta, M. Lewenstein. *Quantum Phase Transition of Ultracold Bosons in the Presence of a Non-Abelian Synthetic Gauge Field.* Phys. Rev. A **84** 053632 (2011)

(III) B. Juliá-Díaz, D. Dagnino, K. J. Günter, T. Graß, N. Barberán, M. Lewenstein, J. Dalibard. *Strongly Correlated States of a Small Cold Atomic Cloud from Geometric Gauge Fields.* Phys. Rev. A **84** 053605 (2011)

(IV) R. Barnett, S. Powell, T. Graß, M. Lewenstein, S. Das Sarma. *Order by Disorder in Spin-Orbit Coupled Bose-Einstein Condensates.* Phys. Rev. A **85** 023615 (2012)

(V) B. Juliá-Díaz, T. Graß, N. Barberán, M. Lewenstein. *Fractional Quantum Hall States of Few Bosonic Atoms in Geometric Gauge Fields.* New J. Phys. **14** 055003 (2012)

(VI) B. Juliá-Díaz, T. Graß. *Strongdeco: Expansion of Analytical, Strongly Correlated Quantum States into a Many-Body Basis.* Com. Phys. Comm. **183** 737 (2012)

(VII) T. Graß, B. Juliá-Díaz, N. Barberán, M. Lewenstein. *Non-Abelian Spin Singlet States of Two-Component Bose Gases in Artificial Gauge Fields.* Phys. Rev. A **86** 021603(R) (2012)

(VIII) T. Graß, B. Juliá-Díaz, M. Lewenstein. *Quasihole dynamics as a detection tool for quantum Hall phases.* Phys. Rev. A **86** 053629 (2012)

(IX) T. Graß, B. Juliá-Díaz, M. Burrello, M. Lewenstein. *Fractional quantum Hall states of a Bose gas with spin-orbit coupling.* arXiv:1210.8035

Note that the articles (VIII) and (IX) have been prepared after submission of this thesis.

These publications overlap with this thesis at the following places: Section 2.2 presents the proposal also discussed in (III) and (V). The whole Chapter 4, and Section 5.1 are based on material from these two publications. Directly related to them is publication (VI), which is further described in the appendix. Section 5.2 overlaps with (VIII). Section 3.2 is based on (I). Chapter 6 is based on (VII), Chapter 7 is related to (IV) and (IX), and Chapter 8 is based on (II).

# Chapter 2

# Synthesizing gauge fields

In this chapter we will review different proposals how to make atoms behave as if there was a gauge field acting on them.

## 2.1 Rotation of the system

Conceptually certainly the simplest way to synthesize a magnetic field is the rotation of the system. The effect of a constant magnetic field $\boldsymbol{B}$ on a charged particle is the Lorentz force $\boldsymbol{F}_{\mathrm{L}} \sim \boldsymbol{v} \times \boldsymbol{B}$ perpendicular to the velocity $\boldsymbol{v}$ of the particle. Recalling coordinate transformation laws from classical mechanics, we see that rotating the system mimics this force: When going from an inertial reference frame into a rotating one, fictitious forces have to be included in Newton's laws of motion in order to keep their validity. To describe a particle rotating with constant angular velocity $\boldsymbol{\Omega}_{\mathrm{rot}}$, a centrifugal force is needed to keep the rotation. If the particle moves with a velocity $\boldsymbol{v}$ within the rotating frame, it will additionally feel the Coriolis force $\boldsymbol{F}_{\mathrm{C}} \sim \boldsymbol{v} \times \boldsymbol{\Omega}_{\mathrm{rot}}$. Apart from the proportionality constant, this force will thus exactly mimic the Lorentz force, given that $\boldsymbol{\Omega}_{\mathrm{rot}}$ is parallel to $\boldsymbol{B}$.

To put this on a more formal level, we write down the Hamiltonian of a gas in an axial-symmetric harmonic trap with frequencies $\omega_\perp$ in the $xy$-plane and $\omega_\parallel$ along

the $z$-axis [29]:

$$H = \sum_{i=1}^{N} \left[ \frac{\boldsymbol{p}_i^2}{2M} + \frac{1}{2} M\omega_\perp^2 (x_i^2 + y_i^2) + \frac{1}{2} M\omega_\parallel^2 z_i^2 \right] + \frac{1}{2} \sum_{ij} V(\boldsymbol{r}_i, \boldsymbol{r}_j). \tag{2.1}$$

For completeness, we have included some, at this point unimportant, two-body potential $V$. In a frame rotating around the $z$-axis with constant angular velocity $\boldsymbol{\Omega}_{\mathrm{rot}} = \Omega_{\mathrm{rot}} \boldsymbol{e}_z$, the Hamiltonian transforms as $H_{\mathrm{rot}} = H - \boldsymbol{\Omega}_{\mathrm{rot}} \cdot \boldsymbol{L}$, with $\boldsymbol{L} = \sum_i \boldsymbol{r}_i \times \boldsymbol{p}_i$, and can thus be re-written as

$$\begin{aligned} H_{\mathrm{rot}} = & \sum_{i=1}^{N} \left[ \frac{(\boldsymbol{p}_i - M\boldsymbol{\Omega}_{\mathrm{rot}} \times \boldsymbol{r_i})^2}{2M} + \frac{1}{2} M(\omega_\perp^2 - \Omega_{\mathrm{rot}}^2)(x_i^2 + y_i^2) + \frac{1}{2} M\omega_\parallel^2 z_i^2 \right] \\ & + \frac{1}{2} \sum_{ij} V(\boldsymbol{r}_i, \boldsymbol{r}_j), \end{aligned} \tag{2.2}$$

which is equivalent to the Hamiltonian of $N$ particles with charge $q$ in a magnetic field $\boldsymbol{B} = (0, 0, B)$, if we choose $qB = 2M\Omega_{\mathrm{rot}}$. We note that the vector potential $\boldsymbol{A}$ for the magnetic field is fixed to the symmetric gauge: $\boldsymbol{A} = \frac{B}{2}(y, -x, 0)$. The effect of the centrifugal force, appearing in the second term of Eq. (2.2), is to reduce the effective $xy$ trapping frequency.

The latter implies that the system becomes unstable, when $\Omega_{\mathrm{rot}}$ approaches $\omega_\perp$. This is a serious drawback, since interesting strongly correlated phases occur in this limit (cf. Section 4.3.1). At this stage, let us only qualitatively discuss the physical situation. First we note that by choosing $\omega_\parallel$ very large, the third term in $H_{\mathrm{rot}}$ can be completely neglected, as it just confines the system to effectively two dimensions [29]. Then, the first term in $H_{\mathrm{rot}}$ introduces a Landau level (LL) structure, that is, harmonic oscillator levels with an infinite angular momentum degeneracy in every level. The energy levels are separated from each other by a gap $2\Omega_{\mathrm{rot}}$. Assuming weak enough interactions, all particles will remain within the lowest LL (LLL). In this regime, strongly correlated states occur at high total angular momentum $L$, where many different single-particle states are available. The second term in Eq. (2.2) takes care of the finite size of the system, and introduces a Fock-Darwin spectrum. It removes the LL degeneracy, but for the effective trapping frequency $\omega_{\mathrm{eff}} = \sqrt{\omega_\perp^2 - \Omega_{\mathrm{rot}}^2}$ small compared to the LL gap, the LLs remain quasi-degenerate. The effective trapping enhances population of single-particle states with smaller angular momentum. Therefore, highly correlated states become accessible only for small $\omega_{\mathrm{eff}}$, i.e. near the instability.

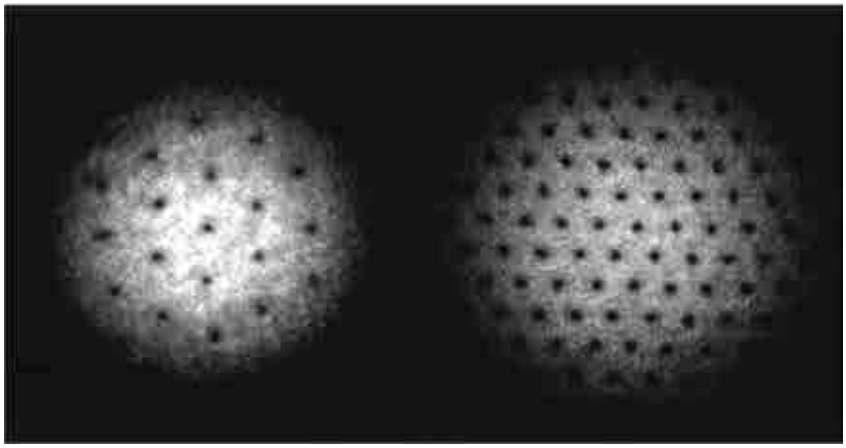

FIGURE 2.1: Vortex lattices observed in Ref. [30]. The lattice on the left is formed in a slowly-rotating trap, while the right side shows a vortex lattice due to a rapidly rotating trap.

This complication has so far hindered the experimental realization of strongly correlated states with cold Bose gases by rotating the trap. Nevertheless, regimes of smaller $L$ have already been accessed (see Ref. [31] for a review). As in the case of Helium II, a BEC can carry angular momentum only in form of quantized vortices, which are visible in experimental pictures of the density. In the strongly correlated regime, the number of vortices has to be of the same order as the number of particles. As shown in Fig. 2.1, by increasing the rotation frequency, the number of vortices (and thus $L$) is increased, but it has so far not been achieved to go beyond the regime where vortices form a lattice, i.e. with many more atoms than vortices.

## 2.2 Gauge fields due to a geometric phase

Due to the limitations of the method described in the previous section, a different approach might turn out to be more feasible. In this section we describe a scheme for synthesizing a magnetic field which is based on the coupling of internal atomic levels to laser beams. As reviewed in Ref. [32], there exists a variety of proposals falling into this category. We focus on the simplest one, which involves only two atomic levels and a single laser beam. It not only illustrates in the clearest way the mechanism of generating gauge fields due to geometric phases, but might indeed allow for realizing the desired strongly correlated states. Properties of

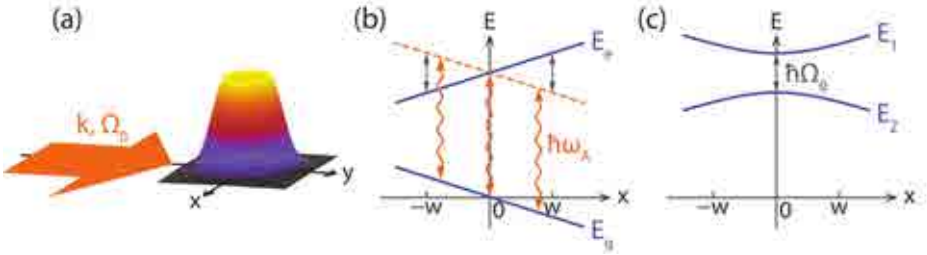


FIGURE 2.2: Scheme for achieving a geometric phase by coupling atoms to a laser beam: (a) Atoms are trapped in the $x$–$y$ plane and illuminated with a plane wave propagating along the $y$ direction. (b) The energy difference between the two internal states that are coupled by the laser field varies linearly along the $x$ direction. (c) Energy eigenvalues of the atom–laser coupling in the rotating wave approximation. From: [34]

these states and their dependence on the experimental parameters are studied in Chapters 3 and 4. In this section, however, we restrict ourselves to describing the proposal, closely following our presentation of Refs. [33, 34].

The idea at the bottom of all proposals involving dressed atoms is the mathematical equivalence of gauge potentials and Berry curvatures, giving rise to geometric phases [35]. A Berry phase, $\mathrm{e}^{i\gamma(C)}$, is obtained by a particle on a trajectory $C$ due to the topology of the space, in which it evolves. It has to be distinguished from the dynamical phase, $\mathrm{e}^{iEt}$, which is due to the time-evolution of the particle. It is obvious that magnetic fields implement Berry phases, as the wave function of a particle with charge $q$ subjected to a magnetic vector potential $\boldsymbol{A}(\boldsymbol{r})$ acquires a phase $\mathrm{e}^{iq\int_C \boldsymbol{A}(\boldsymbol{r})\cdot\mathrm{d}\boldsymbol{r}}$ when the particle moves along $C$. In order to mimic gauge fields acting on neutral particles, we thus must think of a mechanism which affects the phase of the particle's wave function in the same way as the magnetic vector potential would do, if the particle was charged. We will now show how this is possible due to a coupling between atoms and photons.

Again we assume an atomic cloud with harmonic confinement, which in the $z$-direction is so strong that the system effectively is two-dimensional. Onto this cloud we shine a single laser beam with wave number $k$ and frequency $\omega_\mathrm{L}$, which propagates in the $y$-direction and is close to the resonance with a transition between two internal atomic states, $|\mathrm{g}\rangle$ and $|\mathrm{e}\rangle$, $\omega_\mathrm{L} = \omega_\mathrm{A}$, see also Fig. 2.2a. The interaction between the electric field of the laser and the induced electric dipole is modeled by the atom-laser Hamiltonian, which in the rotating-wave

approximation and in the rotating frame is given by [36, 37]

$$H_{\mathrm{AL}} = E_{\mathrm{g}} \left|\mathrm{g}\right\rangle \left\langle \mathrm{g}\right| + \left(E_{\mathrm{e}} - \hbar\omega_{\mathrm{L}}\right) \left|\mathrm{e}\right\rangle \left\langle \mathrm{e}\right| + \frac{\hbar\Omega_0}{2} \mathrm{e}^{iky} \left|\mathrm{e}\right\rangle \left\langle \mathrm{g}\right| + \frac{\hbar\Omega_0}{2} \mathrm{e}^{-iky} \left|\mathrm{g}\right\rangle \left\langle \mathrm{e}\right| \quad (2.3)$$

where $E_{\mathrm{g}}$ and $E_{\mathrm{e}}$ are the energies of the bare atomic ground and excited state, and $\Omega_0$ is the Rabi frequency, which is proportional to the laser intensity.

Instead of describing the external dynamics of the system in terms of the bare atoms, the coupling suggests to consider objects which are in a superposition of both atomic levels, being the eigenstates of the atom-laser coupling, also called dressed states. Since these new "internal" states depend on the position of the atom, the center-of-mass movement is accompanied by a well-defined evolution of the internal state. This is the clue which allows to get the geometric phases mimicking a magnetic field.

But still, for the gauge potential to be non-trivial, we have to introduce a dependence on $x$ in the coupling. This can be achieved with a real magnetic field, which via the Zeeman effect makes the internal energy levels vary linearly in $x$, see Fig. 2.2b. Introducing a parameter $w$, setting the length scale of this shift, we have,

$$E_{\mathrm{g}} = -\frac{\hbar\Omega_0}{2}\frac{x}{w}\,, \qquad E_{\mathrm{e}} = \hbar\omega_{\mathrm{A}} + \frac{\hbar\Omega_0}{2}\frac{x}{w}\,. \quad (2.4)$$

Then, the single particle Hamiltonian is given by

$$H_{\mathrm{sp}} = \frac{\boldsymbol{p}^2}{2M} + \frac{1}{2}M(\omega_x^2 x^2 + \omega_y^2 y^2) + \frac{\hbar\Omega}{2}\begin{pmatrix} \cos\theta & \mathrm{e}^{i\phi}\sin\theta \\ \mathrm{e}^{-i\phi}\sin\theta & -\cos\theta \end{pmatrix}, \quad (2.5)$$

where the third term is the atom-laser Hamiltonian represented in the $\{\left|\mathrm{e}\right\rangle, \left|\mathrm{g}\right\rangle\}$ basis. Here, $M$ is the atomic mass, $\Omega = \Omega_0\sqrt{1 + x^2/w^2}$, $\sin\theta = w/\sqrt{w^2 + x^2}$, $\cos\theta = x/\sqrt{w^2 + x^2}$, and $\phi = ky$. Below, we will fix the trapping frequencies $\omega_x$ and $\omega_y$ in a convenient way.

At this point, we switch from the representation in terms of pure atomic states to the dressed state picture. The energy levels of the dressed states are shown in Fig. 2.2c. There is a freedom in choosing the dressed states, which is the counterpart of the gauge freedom one has for choosing gauge potentials to a given field. As we will see below, the following choice will yield a description in the symmetric

gauge:

$$|\Psi_1\rangle = \mathrm{e}^{-iG}\begin{pmatrix} C\ \mathrm{e}^{i\phi/2} \\ S\ \mathrm{e}^{-i\phi/2}\end{pmatrix}, \qquad |\Psi_2\rangle = \mathrm{e}^{iG}\begin{pmatrix} -S\ \mathrm{e}^{i\phi/2} \\ C\ \mathrm{e}^{-i\phi/2}\end{pmatrix}, \tag{2.6}$$

in the $\{|\mathrm{e}\rangle, |\mathrm{g}\rangle\}$ basis, where $C = \cos\theta/2$, $S = \sin\theta/2$, and $G = \frac{kxy}{4w}$. Then, the atomic state can be expressed as,

$$\chi(\boldsymbol{r}) = a_1(\boldsymbol{r}) \otimes |\Psi_1\rangle + a_2(\boldsymbol{r}) \otimes |\Psi_2\rangle \tag{2.7}$$

where $a_i$ captures the external dynamics and $|\Psi_i\rangle$ represents the "internal" degree of freedom. The single-particle Hamiltonian, expressed in the $\{|\Psi_1\rangle, |\Psi_2\rangle\}$ basis, reads

$$H_{\mathrm{sp}} = \begin{pmatrix} H_{11} & H_{12} \\ H_{21} & H_{22}\end{pmatrix}, \tag{2.8}$$

where the diagonal elements can conveniently be written down, if we define a vector potential $\boldsymbol{A}$,

$$\boldsymbol{A}(\boldsymbol{r}) = \hbar k \left(\frac{y}{4w}, \frac{x}{4w} - \frac{x}{2\sqrt{x^2+w^2}}\right), \tag{2.9}$$

and a scalar potential $U$,

$$U(\boldsymbol{r}) = \frac{\hbar^2 w^2}{8M\left(x^2+w^2\right)}\left(k^2 + \frac{1}{x^2+w^2}\right). \tag{2.10}$$

With this, we get

$$H_{11} = \frac{\left[\boldsymbol{p} - \boldsymbol{A}(\boldsymbol{r})\right]^2}{2M} + U(\boldsymbol{r}) + V(\boldsymbol{r}) + \frac{\hbar\Omega(\boldsymbol{r})}{2}, \tag{2.11}$$

and

$$H_{22} = \frac{\left[\boldsymbol{p} + \boldsymbol{A}(\boldsymbol{r})\right]^2}{2M} + U(\boldsymbol{r}) + V(\boldsymbol{r}) - \frac{\hbar\Omega(\boldsymbol{r})}{2}, \tag{2.12}$$

which are the Hamiltonians driving the external dynamics of atoms being in the internal state $|\Psi_1\rangle$ and $|\Psi_2\rangle$, respectively. By expanding the $H_{ij}$ terms up to second order in $x$ and $y$, which is justified by choosing $w$ to be larger than the extension of the cloud, we find that the energy distance between these two manifolds is given by $\hbar\Omega_0$. For convenience, we make the Hamiltonian element

for the low energy manifold, $H_{22}$, independent of $\Omega_0$ by adding the constant term $\frac{\hbar\Omega_0}{2}$ to the diagonal of $\hat{H}_{\rm sp}$. Further we note that with the explicit selection of Eq. (2.6) and for $x, y \ll w$, $\boldsymbol{A}$ is in the symmetric gauge: $\boldsymbol{A} \approx \frac{\hbar k}{4w}(y, -x)$. This allows for making $H_{22}$ fully symmetric by a proper choice of the trapping frequencies:

$$\frac{1}{2}M\omega_\perp^2(x^2+y^2) = U(\boldsymbol{r}) - \frac{\hbar\Omega(\boldsymbol{r})}{2} + \frac{\boldsymbol{A}^2(\boldsymbol{r}}{2M} + \frac{1}{2}M(\omega_x^2 x^2 + \omega_y^2 y^2). \tag{2.13}$$

Eq. (2.12) then takes the form

$$\begin{aligned} H_{22} &= \frac{\boldsymbol{p}^2}{2M} + \frac{\boldsymbol{p}\cdot\boldsymbol{A}}{M} + \frac{M}{2}\omega_\perp^2(x^2+y^2) \\ &= \frac{(\boldsymbol{p}+\boldsymbol{A})^2}{2M} + \frac{M}{2}(\omega_\perp^2 - \omega_{\rm c}^2/4)(x^2+y^2), \end{aligned} \tag{2.14}$$

with $\omega_{\rm c} = \hbar k/(2Mw)$ the cyclotron frequency. This final expression is formally equal to the single-particle part of Eq. (2.2), if we choose $\omega_{\rm c} = 2\Omega_{\rm rot}$, or to the Hamiltonian of a charged particle in two dimensions under the influence of a magnetic field $\boldsymbol{B} = (0, 0, B)$ described in the symmetric gauge. The field strength $B$ is given by $B = \hbar k/(2w)$.

This equivalence holds only for $H_{22}$, but does not for $H_{11}$. Due to the off-diagonal terms in $H_{\rm sp}$, these two manifolds are coupled. Typical expected values of $H_{12}$ and $H_{21}$ are of the order of the recoil energy $E_{\rm R} = \frac{\hbar^2 k^2}{2M}$ which gives the scale for the kinetic energy of the atomic center-of-mass motion when it absorbs or emits a single photon. If we consider $\hbar\Omega_0 \gg E_{\rm R}$, this coupling is small, and we can restrict ourselves to the low energy manifold. This limit is called adiabatic approximation, as the internal dynamics is assumed to be fast enough to follow the center of mass motion adiabatically. It means that, once prepared in the lower state $|\Psi_2\rangle$, the atoms will never be in the excited internal state $|\Psi_1\rangle$.

However, the accessible range of $\Omega_0$ is limited if one wants to avoid undesired excitations of atoms in the sample to higher levels and/or an unwanted laser assisted modification of the atom-atom interaction. This seems to be a drawback of all the proposals making use of a coupling of different atomic states. It it thus important to check the validity regime for the adiabatic approximation. In Chapter 4, we will study the influence of finite Rabi frequencies on the system's behavior by considering the high-energy manifold as a small perturbation. At this point, however, we just assume that we can neglect it.

There is a second weak point deserving discussion. Namely, in Eq. (2.3) we did not consider the spontaneous emission of photons from the excited state, which would lead to a decoherence of the photons. Certainly, this assumption is only justified as long as the lifetime of the excited state is longer than the typical duration of an experiment. This can, for instance, be achieved with Ytterbium or some alkaline earth metals having atomic states with lifetimes of several seconds.

Other setups circumvent this problem without depending on long-lived atomic states. Here we only mention a scheme where the geometric phase is inscribed by a two-photon Raman coupling of three hyperfine states whose energies are linearly shifted in one spatial direction by a Zeeman effect. With the frequencies of the Raman lasers being far from a resonance with excited levels, no spontaneous emission may occur. This scheme has already been implemented with $^{87}$Rb [38, 39], and has allowed for observing a few vortices.

## 2.3 Non-Abelian gauge fields

In order to motivate the idea of synthesizing magnetic fields by rotation, we have been able to argue with the equivalence between Lorentz and Coriolis force. With respect to the scheme based on atom-laser coupling, our arguments became more abstract, as we had to resort to the Berry phase. As in this section we will turn our attention to more general gauge fields, it seems to be indicated to go into a bit more details.

### 2.3.1 Definition of non-Abelian gauge fields

From a mathematical point of view, a magnetic field is a U(1) gauge field, which means that the gauge potential couples to a U(1) degree of freedom, i.e. the phase of the particle: Assume the Schrödinger equation

$$H\Psi(\boldsymbol{r}) = \frac{1}{2M}\left(\boldsymbol{p} + \boldsymbol{A}\right)^2 \Psi(\boldsymbol{r}) = E\Psi(\boldsymbol{r}), \tag{2.15}$$

which is solved by some complex function $\Psi : \mathbb{R}^D \mapsto \mathbb{C}$. The Schrödinger equation remains invariant under gauge transformations

$$\boldsymbol{A} \rightarrow \boldsymbol{A} + \nabla\Lambda(\boldsymbol{r}), \tag{2.16}$$

$$\Psi(\boldsymbol{r}) \rightarrow \exp[-\frac{i}{\hbar}\Lambda(\boldsymbol{r})]\Psi(\boldsymbol{r}), \tag{2.17}$$

which locally change the phase of the wave function $\Psi$. Here, the gauge function $\Lambda$ and all elements of the gauge potential $\boldsymbol{A}$ are functions mapping the real space $\mathbb{R}^D$ onto $\mathbb{R}$.

Clearly, for more complex Hilbert spaces, we can think of more complex transformations of this kind. For instance, let us consider the state $|\Psi\rangle$ as an $n$-spinor $\boldsymbol{\Psi}(\boldsymbol{r}) = (\Psi^1(\boldsymbol{r}), \cdots, \Psi^n(\boldsymbol{r}))^T$ with each component $\Psi^i$ mapping from $\mathbb{R}^D$ to $\mathbb{C}$. Apart from phase rotations, we then can also perform spin rotations described by SU($n$) matrices $R$, $\boldsymbol{\Psi} \rightarrow R\boldsymbol{\Psi}$. For simplicity, let us assume that $R$ is a constant matrix. It then passes through the derivatives, $\boldsymbol{p} = -i\hbar\nabla$, in the Hamiltonian (2.15). But now also the elements of $\boldsymbol{A}$ can generally be Hermitian $n \times n$ matrices, which not necessarily commute with $R$. However, we get an invariance of (2.15) under the gauge transformations

$$A_i \rightarrow RA_iR^{-1}, \tag{2.18}$$

$$\boldsymbol{\Psi} \rightarrow R\boldsymbol{\Psi}. \tag{2.19}$$

Such gauge potentials $A_i$ which stem from gauge transformations described by elements of a non-commutative group like SU($n$) with $n > 1$, are called *non-Abelian* gauge potentials. One then usually has

$$[A_i, A_j] = A_iA_j - A_jA_i \neq 0, \tag{2.20}$$

which is a more restrictive definition, since by demanding that the $A_i$ belong to a non-commutative group we do not assure that they do not commute.

We note that the global gauge transformation defined in Eqs. (2.18) and (2.19) becomes trivial if $R$ and all $A_i$ commute, as Eq. (2.18) reduces to $A_i \rightarrow A_i$. This is equivalent to the fact that no Berry phase $\gamma = \frac{1}{\hbar}\oint \boldsymbol{A} \cdot \mathrm{d}\boldsymbol{r}$ is accumulated if a particle moves on a closed contour within a constant Abelian gauge potential. Or simpler: The gauge field $\boldsymbol{B}$ derived from a constant Abelian gauge potential $\boldsymbol{A}$ is zero. From electrodynamics we are familiar with the relation $\boldsymbol{B} = \nabla \times \boldsymbol{A}$, which reflects these observations.

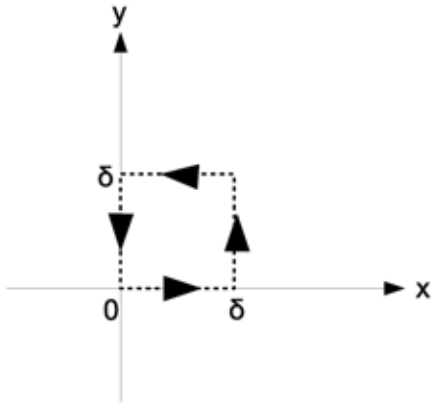


FIGURE 2.3: Closed loop along a square contour.

It is clear that we have to modify this relation for non-Abelian gauge fields. The effect of a constant non-Abelian gauge potential is to rotate the spinor while the particle moves on a trajectory in real space. The rotation axis depends on the direction of the trajectory. To see that the non-commutativity of the gauge potential yields a non-zero Berry "phase", we assume a particle moving on an infinitesimal square contour $C$. For instance, the particle might first make a small step of length $\delta$ in positive $x$-direction, then a $\delta$-step in positive $y$-direction, and go back along $x$ and $y$, cf. Fig. 2.3. Since $\delta$ is assumed to be small, we may expand the effect of each step, e.g.

$$\exp(i\delta A_x)\mathbf{\Psi}(\boldsymbol{r}) = [1 + i\delta A_x - \frac{1}{2}\delta^2 A_x^2 + \mathcal{O}(\delta^3)]\mathbf{\Psi}(\boldsymbol{r}), \tag{2.21}$$

for a step along the positive $x$-axis, and the analogous expression with $A_y$ for steps along the $y$-axis. For backward steps, we have to take the complex conjugate. For the closed contour $C$, we then find in the lowest non-vanishing order:

$$\exp(i \oint \boldsymbol{A} \cdot \mathrm{d}\boldsymbol{r})\mathbf{\Psi}(\boldsymbol{r}) = [1 + \delta^2[A_x, A_y] + \mathcal{O}(\delta^3)]\mathbf{\Psi}(\boldsymbol{r}). \tag{2.22}$$

If we define a gauge field $\boldsymbol{B} = (0, 0, i[A_x, A_y])$ and calculate the surface integral of the contour $C$, $\exp[i \int_{S(C)} \boldsymbol{B} \cdot \mathrm{d}\boldsymbol{S}]$, we obtain, to lowest order, exactly the same result. This motivates the general relation, according to which the gauge fields are derived from a non-Abelian gauge potential:

$$\boldsymbol{B} = \nabla \times \boldsymbol{A} + i \sum_{ijk} \epsilon_{ijk} A_i A_j \boldsymbol{e}_k, \tag{2.23}$$

with $\epsilon_{ijk}$ the totally antisymmetric tensor. For Abelian $\boldsymbol{A}$, the second term vanishes, and Eq. (2.23) reduces to the formula known from electrodynamics. On the other hand, the first term vanishes for constant gauge potentials.

Although the non-Abelian part of the gauge potentials which we will consider in this thesis are always constant, we give, for completeness, the generalization of the Eqs. (2.18) and (2.19) to space-dependent gauge potentials:

$$A_i \quad \rightarrow \quad RA_iR^{-1} - \frac{1}{g}(\partial_i R)R^{-1}, \tag{2.24}$$

$$\boldsymbol{\Psi}(\boldsymbol{r}) \quad \rightarrow \quad R\boldsymbol{\Psi}(\boldsymbol{r}). \tag{2.25}$$

The gauge transformation reduces to the Abelian one of Eq. (2.16), if we set $R = \mathrm{e}^{-\frac{i}{\hbar}\Lambda(\boldsymbol{r})}$ and the coupling constant $g = i\hbar$.

The non-Abelian potentials in the focus of this thesis belong to the SU(2) group, which is the most relevant non-Abelian gauge group in physics, as it describes rotations of spin-1/2. Of course, for composite particles with larger spin, or for the elementary quarks with a threefold color degeneracy, SU($n$) gauge fields with $n > 2$ also become relevant.

### 2.3.2 Synthesizing non-Abelian gauge fields

In the previous sections we have discussed two schemes for synthesizing magnetic fields. The first was based on a rotation of the system, while the second one mimicked the magnetic field by implementing a Berry phase due to an atom-laser coupling. The latter scheme stands out due to its huge versatility. Especially, it allows for synthesizing SU($n$) gauge fields if there is an $n$-fold degenerate manifold of dressed states.

We can achieve this within a so-called multipod scheme which couples $n + 1$ degenerate atomic ground states $|\mathrm{g}_i\rangle$ to an excited state $|\mathrm{e}\rangle$ via laser fields with complex Rabi frequencies $\kappa_i(\boldsymbol{r})$. The energy spectrum of the dressed states $|\chi_i(\boldsymbol{r})\rangle$ then has $n$ states with energies $E = 0$, while the remaining two states have a finite energy $\pm E$ with $E = \sum_i |\kappa_i(\boldsymbol{r})|^2$ [32]. Within an adiabatic approximation, the states at finite energy can be neglected. Then, the dynamics of the degenerate manifold can, in full analogy to the Abelian case, be described in terms of a scalar potential $U$ and a vector potential $\boldsymbol{A}$. However, now the potentials $U$ and $A_i$ are $n \times n$ matrices. With $V_{\mathrm{trap}}(\boldsymbol{r})$ being the external trapping potential, the gauge

potentials are given by [40]:

$$U_{ij} = \langle \chi_i | \, V_{\mathrm{trap}}(\boldsymbol{r}) \, | \nabla \chi_j \rangle \,, \tag{2.26}$$

$$\boldsymbol{A}_{ij} = i \, \langle \chi_i | \, \nabla \chi_j \rangle \,, \tag{2.27}$$

where in the latter we recognize the Berry connection due to the space-dependence of the dressed states. With the proper choice of these spatial dependencies, which are controlled by the laser fields, we can obtain a large variety of SU($n$) potentials.

Considering a tripod scheme, explicit formulas relating the Rabi frequencies to the resulting SU(2) gauge potentials have been derived in Ref. [40], where the focus has been put on synthesizing magnetic monopoles. In this thesis we only consider simple non-Abelian fields of the form $\boldsymbol{A} = (\boldsymbol{\alpha} \cdot \boldsymbol{\sigma} + f(\boldsymbol{r})\mathbb{1}, \;\; \boldsymbol{\beta} \cdot \boldsymbol{\sigma} + g(\boldsymbol{r})\mathbb{1}, \;\; 0)$, with $f$ and $g$ linear in $\boldsymbol{r}$, and $\boldsymbol{\sigma} = (\sigma_x, \sigma_y, \sigma_z)$ the Pauli matrices. As shown in Ref. [41], it is possible to achieve such gauge potentials within the scope of a tripod scheme.

We note that a first experimental realization of an SU(2) gauge field has been achieved recently within the group of I. Spielman [42], but there $\boldsymbol{A} \sim (\sigma_y, 0, 0)$, and thus the gauge potential is Abelian in the strict sense of Eq. (2.20).

## 2.4 Artificial gauge fields in optical lattices

For completeness we conclude this chapter by outlining a scheme to synthesize gauge fields in optical lattices. The first proposal was made in Ref. [43] for Abelian gauge fields in effectively two-dimensional optical lattices. Atoms in two hyperfine states $|\mathrm{g}\rangle$ and $|\mathrm{e}\rangle$ are trapped in an optical lattice, in which along one spatial direction, say $x$, the potential maxima for $|\mathrm{g}\rangle$ coincide with the potential minima for $|\mathrm{e}\rangle$. This is possible by the proper choice of the laser polarization. Then the internal state of the atoms alternates from site to site when going along the $x$-direction. By choosing the trapping in $x$-direction strong enough, tunneling in this direction is fully suppressed, but can be stimulated by two Raman lasers in resonance with transitions between $|\mathrm{g}\rangle \leftrightarrow |\mathrm{e}\rangle$. Tilting the lattice either by accelerating it or by applying a real electric field induces an energy offset between neighboring sites. From this follows that each laser is either in resonance with a hopping in forward or backward direction. If the laser fields are plane waves running in $y$-direction, the laser-induced hopping processes are associated with

a phase factor $e^{\pm iqy}$ with $q$ the wave number of the laser. This space-dependent phase makes the atoms accumulate a Berry phase when moving through the lattice, and effectively mimics a constant magnetic field perpendicular to the lattice.

In Ref. [44], this scheme has been generalized to non-Abelian gauge potentials. The basic ingredient for an SU($n$) gauge field are $n$ different Zeeman sublevels $|g_i\rangle$ and $|e_i\rangle$ with $i = 1 \dots n$. They represent the different internal states on which the non-Abelian field may act. Since the resonance frequencies of transitions from $|g_i\rangle$ and $|e_i\rangle$ will be different for each $i$, different phase factors $e^{\pm iq_i y}$ are acquired. However, this still does not lead to a non-Abelian gauge potential. We also need a mechanism which transfers atoms from one into another internal state. Ref. [44] proposes to do this by making also the hopping in $y$-direction laser-assisted, such that it drives transitions $|g_i\rangle \leftrightarrow |g_j\rangle$ and $|e_i\rangle \leftrightarrow |e_j\rangle$.

For completeness, let us also mention some alternative routes to artificial gauge fields in optical lattices: Instead of superposing "standard" optical lattice with additional lasers modifying the tunneling process, it is also possible to implement the artificial gauge field directly within the optical potential of the lattices. These so-called optical flux lattices use laser configurations which apart from generating a periodic scalar potential also couple different internal states, effectively yielding a magnetic flux [45, 46]. Another scheme which has recently been implemented in one dimension is the so-called "Zeeman" lattice, which arises from a combination of Raman and radio-frequency coupling of Zeeman-split spin states [47]. While all these methods involve the dressing of different internal states, driven optical lattices have recently been proven feasible for realizing artificial gauge fields for cold atoms without relying on any internal structure [48].

# Part I

# Fractional Quantum Hall Systems

# Chapter 3

# Quantum Hall effects - from electrons to atoms

The integer quantum Hall effect (IQHE) discovered in 1980 by K. v. Klitzing, G. Dorda, and M. Pepper [49] and the fractional quantum Hall effect (FQHE) discovered two years later by D.C. Tsui, H.L. Stormer, and A.C. Gossard [20] have become two of the most studied phenomena in solid state physics (cf. [18, 50]). After 30 years, they still attract great deal of attention, as nowadays quantum Hall physics is also explored in the field of quantum gases. In this chapter we try to summarize the most basic facts about quantum Hall effects, with a focus on the FQHE. For introducing these effects it seems to be most pedagogical to refer to the electronic case. We afterwards dedicate a separate section to relate the electronic FQHE to an atomic counterpart with dipolar interactions.

## 3.1 Introduction to quantum Hall effects

Originally, Hall effects are charge transport phenomena, and are thus best introduced by considering electrons in a metal. The main ingredients of any kind of Hall effect are a strong confinement of the electrons to a thin piece of metal of thickness $d$, and a magnetic field $B$ perpendicular to this plane. It is then a well-known phenomenon that by applying an electric potential in $x$-direction, the Hall voltage $V_{\mathrm{H}}$ will be induced in $y$-direction. It is due to the Lorentz force which

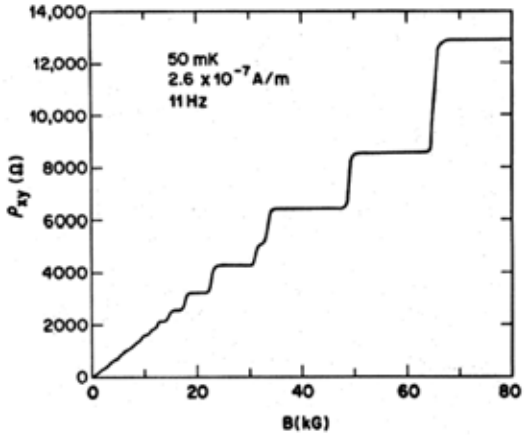


FIGURE 3.1: Hall resistance $\rho_{xy}$ in $x, y$-direction for an electric field in $x$-direction as a function of a perpendicular $B$-field. Measured in [51].

makes the electrons moving along $x$ to drift along $y$. Just by considering a balance between the Lorentz force and a Coulomb force which results from the induced voltage, one finds the classical relation $V_{\mathrm{H}} = -IB/(ned)$ with $e$ the electron's charge, $I$ the current, and $n$ the charge carrier density. This effect thus allows to determine the number of charge carriers of a material, but for us the essential part of this formula is the proportionality between $V_{\mathrm{H}}$ and $B$, or better $\rho_{xy} \sim B$, where $\rho_{xy} = E_y/j_x$ is the Hall resistivity measuring the ratio between the induced electric field $E_y$ and the current density $j_x$ due to the applied potential.

By using, for instance, heterojunctions with a conducting layer confined between two semiconductors, it is possible to get effectively two-dimensional electronic systems. For sufficiently pure materials and at low enough temperature, there is a regime of strong magnetic fields, where $\rho_{xy}$ is no longer linear in $B$, but shows its quantized nature, as it abruptly jumps between plateaus. This effect, shown in Fig. 3.1, is called *quantum Hall effect*.

### 3.1.1 Integer quantum Hall effect

The values of the Hall resistivity on the plateaus is given by $\rho_{xy} = \frac{1}{\nu}\frac{h}{e^2}$, where $\nu$ can either be an integer or a fractional number $p/q$ with $p, q$ integer. This criterion distinguishes phenomenologically between the integer and the fractional quantum Hall effect, but it hides the fact that the two effects are based on quite different mechanisms. Their remarkable common property, however, is the independence

of $\rho_{xy}$ from the specific material and its amount of impurities, which is a strong hint for the topological nature of both effects.

For understanding the IQHE, we have to consider a gas of *non-interacting* electrons. Within the given setup of a two-dimensional confinement and a perpendicular magnetic field, the single-particle wave functions are harmonic oscillator levels, which we can easily derive for a Hamiltonian given by Eq. (2.14). Here we note that on the single-particle level, the only difference between the atomic and the electronic case is the existence of an effective harmonic trap in Eq. (2.14). We include this trap in our derivation, but we note that it can be switched off at any point in the calculation just by choosing $\omega \equiv \sqrt{\omega_\perp^2 - \omega_c^2/4} = 0$. For convenience, our derivation is in the symmetric gauge, but with slight re-definitions all steps can equally be carried out in other gauges.

It is useful to introduce complex coordinates $z = x - iy$, which we will keep throughout the thesis. With this, the Hamiltonian reads, after setting $\hbar \equiv 1$ and $M \equiv 1/2$:

$$H = -4\partial_z\partial_{\bar{z}} + (B^2 + \omega^2)/4z\bar{z} + B(z\partial_z - \bar{z}\partial_{\bar{z}}), \tag{3.1}$$

with $\bar{z}$ the complex conjugate of $z$. Now we define bosonic ladder operators [52]

$$\hat{\mathrm{a}} = \sqrt{\Omega B/8}\left(z + \tfrac{4}{B\Omega}\partial_{\bar{z}}\right), \tag{3.2}$$

$$\hat{\mathrm{b}} = \sqrt{\Omega B/8}\left(\bar{z} + \tfrac{4}{B\Omega}\partial_{z}\right). \tag{3.3}$$

with $\Omega = \sqrt{1 + \omega^2/B^2}$, and accordingly their Hermitian conjugates $\hat{\mathrm{a}}^\dagger$ and $\hat{\mathrm{b}}^\dagger$. With this, the Hamiltonian takes the form $H = \Omega_+\hat{\mathrm{a}}^\dagger\hat{\mathrm{a}} + \Omega_-\hat{\mathrm{b}}^\dagger\hat{\mathrm{b}} + \text{const}$. There are two types of excitations, with energies given by $\Omega_\pm = B(\Omega \pm 1)$. In general, we have $\Omega_- \ll \Omega_+$, or even $\Omega_- = 0$ in the absence of a trap. Thus, the excitations characterized by $m = \langle\hat{\mathrm{b}}^\dagger\hat{\mathrm{b}}\rangle$ do not contribute much to the energy of a state, which is basically given by the energy quantum number $n = \langle\hat{\mathrm{a}}^\dagger\hat{\mathrm{a}}\rangle$. For a state $|n, m\rangle$, the excitation energy is by

$$E_{n,m} = n\Omega_+ + m\Omega_-. \tag{3.4}$$

The quasidegenerate levels characterized by $n$ are called Landau levels (LLs). For an interpretation of the quantum number $m$, we derive the eigenfunctions by applying the raising operators $\hat{\mathrm{a}}^\dagger$ and $\hat{\mathrm{b}}^\dagger$ to the vacuum, i.e. the state which is destroyed by $\hat{\mathrm{a}}$ and $\hat{\mathrm{b}}$. This state $|0, 0\rangle$ is given by a Gaussian $\exp[-z\bar{z}/(4\lambda^2)]$

where $\lambda^{-2} = B\Omega$. We will in the following use $\lambda$ as a unit for length, and consider $z$ a dimensionless quantity. The states of the lowest LL (LLL), obtained by applying $m$ times the operator $\hat{\mathrm{b}}^\dagger$ to the vacuum, have the form

$$\phi^{\mathrm{FD}}_{0,m}(z) \sim z^m \exp(-z\bar{z}/4). \tag{3.5}$$

We shall refer to these functions $\phi^{\mathrm{FD}}_{n,m}$ as the Fock-Darwin functions. Within the LLL, $n = 0$, the quantum number $m$ represents angular momentum, as shown by Eq. (3.5). For arbitrary LLs, the angular momentum is given by $m - n$.

First let us consider a system of electrons in a solid, i.e. without harmonic trap. Then each LL has, in principle, an infinite degeneracy. However, one has to take into account the finite size of the system. Obviously, this will truncate the maximum angular momentum, so the degeneracy becomes finite [18]. The levels are separated by an energy gap $2B$, which usually is large enough to make a completely filled LL inert. A completely filled LL then behaves as an insulator.

However, a contribution of an inert LL to the system's conductivity may come from the edge of the system. Indeed, the behavior there turns out to be significant, as it is determined by topology and thus robust against impurities of the material. To understand what this means, let us apply the following semi-classical picture: Depending on the direction of the magnetic field, the motion of an electron may either be right- or left-handed. This chirality is a constant of the motion, and thus electrons at the edge of the sample can only be reflected in a forward direction. Therefore, just like in a superconductor, there is no backscattering at impurities, making the contribution of every filled LL to the total conductivity independent from material properties. Thus, this conductivity quantum of each LL is found to be given only in terms of fundamental constants, $h/e^2$. We note that these "superconducting" edges and the insulating bulk make quantum Hall samples effectively behave in the same way as topological insulators [53–55], but in the latter this behavior is caused by an intrinsic mechanism, the spin-orbit coupling, while in quantum Hall samples the external magnetic field breaks time-reversal symmetry and thereby imposes the chirality of the electrons.

To fully understand Fig. 3.1, we still have to note that increasing $B$ amounts to decreasing the Fermi energy. As long as the Fermi energy lies within the gap between two LLs, the number of filled LLs remains the same, and thus the transport behavior does not change. This is reflected in the plateaus of $\rho_{xy}$. A

broadening of the density of states of each LL around the corresponding energy is responsible for the shape of $\rho_{xy}$ between the plateaus.

### 3.1.2 Fractional quantum Hall effect

The reasoning of the previous subsection cannot be carried over to Hall plateaus at resistivities $\rho_{xy} = \frac{1}{\nu}\frac{h}{e^2}$ characterized by rational values of $\nu$. Indeed, the existence of such plateaus would rather be contradicted by the given arguments. But they were based on the assumption of non-interacting electrons. Certainly, the screening of the electrons by the positively charged background ions effectively weakens the interactions, and in case of completely filled LLs, the gap between the (non-interacting) ground state is much larger than typical interaction energies. Interactions then will not essentially modify the ground state. Thus, in the integer case, the previous reasoning indeed holds. The situation is different, though, for partly filled LLs, where the non-interacting system has a huge degeneracy, and interactions therefore cannot be considered in a perturbative way. However, it happens at certain filling factors, which coincide with the fractional number $\nu$ so far used to quantify the Hall resistivity, that the interacting ground state has an excitation gap in the thermodynamic limit. From this follows an insulating behavior of the electrons in the bulk of the system, and only at the edges where the Fermi energy crosses the confining potential we have gapless states contributing to the conductivity. The mechanism for fractional quantum Hall (FQH) physics is therefore based on the existence of a strongly correlated, gapped ground state at certain filling factors.

Still, the question is how to find the spectrum of the interacting system. As we will describe in more detail in the next chapter, a common method to achieve this is exact diagonalization. Very often, the states obtained by this numerical method are compared with "guessed" candidates for the ground state and its low-lying excitations. During the last three decades, an immense variety of different approaches for guessing FQH states has emerged, including composite-particle constructions where magnetic fluxes are attached to the charge carriers [56, 57], Cherns-Simons-Ginzburg-Landau theories which formalize this flux attachment in a field-theoretic manner [58], or conformal field theory [24, 59] deriving FQH states from correlators of a conformal field theory.

In the remainder of this section, we will give an overview of important FQH states.

#### 3.1.2.1 Laughlin state

The first and most famous FQH state was discovered in 1982 by R. Laughlin from a simple variational ansatz [22]. This ansatz reads

$$\Psi_{\mathrm{L}} = \mathcal{N}_{\mathrm{L}} \prod_{i<j} (z_i - z_j)^q \mathrm{e}^{-\sum_i |z_j|^2/4}, \tag{3.6}$$

where $q$ is, a priori, the variational parameter, and $\mathcal{N}_{\mathrm{L}}$ is a normalization factor. The exponential is common to all single-particle states and just fixes the center of mass. The interesting part is the polynomial. As it contains only $z$ and not $\bar{z}$, the wave function lives exclusively within the LLL. The degree of the polynomial, depending on $q$, determines the total angular momentum $L$ (always in this thesis in units of $\hbar$):

$$L = \frac{q}{2} N(N-1). \tag{3.7}$$

On the other hand, angular momentum is related to the filling factor $\nu$, specifying the number of magnetic fluxes (or vortices) per particle. To determine the filling factor of the Laughlin state, we note that due to the structure of the wave function any particle feels the other particles as $q$ vortices, such that $\nu = N/q(N-1) \to 1/q$ in the thermodynamic limit [60]. Thus, the filling factor fixes the variational parameter $q$ before performing the minimization of energy. What might seem to be a deficit, just demonstrates the power of the Laughlin wave function. Indeed, for most repulsive interactions it turns out that the form of Eq. (3.6) is already a very effective choice for making the particles avoiding each other. For contact interactions (thinking of bosons), it can be seen directly, that Eq. (3.6) is an exact zero-energy eigenstate (not taking into account kinetic energy).

It is easy to see that the Laughlin wave function is (anti-)symmetric for even (odd) values of $q$, which on the one hand allows for bosonic and fermionic realizations of the Laughlin state. On the other hand, it also restricts the wave function to the corresponding filling factors $\nu = 1/q$. Luckily, the most pronounced plateau which has been observed for electrons is found filling $\nu = 1/3$, and thus can be well described by the Laughlin wave function. We note, however, that for Coulomb interactions, the Laughlin wave function is not the exact ground state, but very large overlaps have been found between it and the exact ground state obtained by numerical diagonalization of small systems [22, 61].

This fact appears more natural if one is aware of the analogy to plasma physics [22]. Let us therefore assume that the electrons form a classical one-component plasma embedded in two dimensions. Since the positively charged ions are too heavy to move, we consider them as a homogeneous background potential. Neglecting the kinetic energy, the free energy $\mathcal{F}$ contains a part stemming from the repulsive interactions of the electrons, $\mathcal{F} \sim -\sum_{i<j} \log|z_i - z_j|$. The logarithmic form is due to the dimensionality of the system, as it solves Poisson equation in two dimensions. Interactions with the background contribute a term $\sim \sum_i r_i^2$. The partition function, $\mathcal{Z} \sim \exp(-\beta\mathcal{F})$ with $\beta = 1/q$, then is seen to have exactly the same form as the quantum probability distribution of the electrons in the Laughlin state, $|\Psi_{\mathrm{L}}|^2 \sim \exp\left[\frac{2}{q}\sum_{i<j}\log|z_i - z_j| + \sum_i r_i^2/2\right]$.

This relation between the quantum state and a classical partition function is particularly helpful in order to understand the physics of the system, especially in order to guess the excitations of the system. They can be interpreted as quasiholes pierced into the plasma, or alternatively as quasiparticles in form of a local increase of the density. This quasiparticle character of the excitations makes it natural for them to have an energy gap. Especially intriguing is their fractional behavior: They have fractional charges, the $q$th part of the unit charge, and also their quantum statistics does not fall in the usual categories of bosons or fermions, where interchanging two particles yields a phase $\exp(in\pi)$, with $n$ an integer. In the case of quasiholes or quasiparticles above the Laughlin state, $n$ acquires the value $1/q$. Such an anyonic quantum statistics is only possible in two spatial dimensions. While these properties have been derived in the thermodynamic limit [25, 62], we will later analyze in detail the behavior of quasiholes above a bosonic Laughlin state of only a few particles (see Chapter 5).

The analytic wave function for the state where one quasihole is pierced into the Laughlin state reads [22]

$$\Psi_{\mathrm{qh}} = \mathcal{N}_{\mathrm{qh}} \prod_i (z_i - \xi)\Psi_{\mathrm{L}}, \tag{3.8}$$

with $\mathcal{N}_{\mathrm{qh}}$ a normalization factor and $\xi$ the position of the quasihole. Similarly, a quasiparticle state can be defined, if we replace in Eq. (3.8) the coordinates $z_i$ by the derivatives $\partial_{z_i}$. In order to remain within the LLL, these derivatives shall only act on the polynomial part of the wave function, i.e.

$$\Psi_{\mathrm{qp}} = \mathcal{N}_{\mathrm{qp}} \mathrm{e}^{-\sum_i |z_j|^2/4} \prod_i (\partial_i - \xi) \prod_{i<j} (z_i - z_j)^q. \tag{3.9}$$

It is straightforward to generalize these expression to states with more than one excitations. For two quasiholes we have

$$\Psi_{2\mathrm{qh}} = \mathcal{N}_{2\mathrm{qh}} \prod_i (z_i - \xi_1) \prod_j (z_j - \xi_2) \Psi_{\mathrm{L}}. \tag{3.10}$$

#### 3.1.2.2 Moore-Read state and Read-Rezayi series

The Laughlin states can describe systems at filling $1/q$ with $q$ odd if the system is fermionic, or $q$ even for bosonic systems. A very prominent FQH plateau, however, is found in electronic systems at filling $\nu = 5/2$, and thus cannot be described with Laughlin's variational wave functions.

It has then been noted by G. Moore and N. Read [24] that the fermionic Laughlin wave functions can be interpreted as a Bose-condensation of composite particles built up by the original fermionic particle and magnetic fluxes attached to it. For this composite particle to be a boson, the number of fluxes has to be odd, which restricts the filling factor to odd denominators. However, also pairs of composite fermions should be able to condense, which motivated the so-called Moore-Read (or Pfaffian) wave function

$$\Psi_{\mathrm{MR}} = \mathcal{N}_{\mathrm{MR}} \ \mathrm{Pf}\left(\frac{1}{z_i - z_j}\right) \prod_{i<j} (z_i - z_j)^q \mathrm{e}^{-\sum_i |z_j|^2/4}, \tag{3.11}$$

where Pf denotes the Pfaffian determinant of a skew-symmetric $N \times N$ matrix. It is given by

$$\mathrm{Pf}\,(M_{ij}) = \frac{1}{2^{N/2}(N/2)!} \sum_{\sigma \in S_N} \mathrm{sgn}\sigma \prod_{k=1}^{N/2} M_{\sigma(2k-1),\sigma(2k)}. \tag{3.12}$$

Here, $\sigma$ denotes the elements of the permutation group $S_N$ of $N$ objects. In Eq. (3.11), the Pfaffian acts as a pairing function, while the rest of the wave function describes a Laughlin state with exponent $q$. In each term of the sum over $\sigma$ the $N$ particles are divided in $N/2$ pairs, and for every pair, one zero of the form $z_i - z_j$ is taken out from the Laughlin part by multiplication with the Pfaffian. The total angular momentum is thus given by

$$L = \frac{q}{2} N(N-1) - \frac{N}{2} = \frac{q}{2} \left[ N(N - 1 - \frac{1}{q}) \right]. \tag{3.13}$$

Since the Pfaffian yields a fully antisymmetric factor, the Laughlin part has to be (anti)symmetric for fermions (bosons), i.e. $q$ has to be odd for bosons, while even for fermions. As for the Laughlin state, the filling factor is given by $\nu = 1/q$, but for fermions it may also describe a half filled LL on top of completely filled LLs, e.g. $\nu = 5/2$.

Let us put some attention to the simplest bosonic case with $q = 1$. The Laughlin part of Eq. (3.11) has one first-order zero on every pair, but each term in the pairing function takes out one zero for every of the $N/2$ pairs. This means that in every term of the wave function each particle shares a zero with all other particles, except for exactly one particle with which it is paired. Thus, oppositely to the bosonic Laughlin wave function, the bosonic Moore-Read function is not a zero-energy eigenstate of two-body contact interaction, but the wave function must vanish whenever three particles come together. It is an exact zero-energy eigenstate of three-body contact interaction.

Generalizing this idea of pairing composite particles, N. Read and E. Rezayi [59] proposed a series of states which are exact zero-energy eigenstates of $(k+1)$-body contact interaction by clustering the particles into groups of $k$ particles. For $k = 1$, this is just the Laughlin state. Clusters of $k = 2$ particles yield the Moore-Read state. For general $k$, one gets so-called parafermionic states which have filling factors $\nu = k/2$. The corresponding wave functions are symmetric. Subsequently, these states can be generalized to filling factors $\nu = k/(Mk+2)$, with $k \in \mathbb{N}$ and $M \in \mathbb{N}_0$. The wave functions are symmetric for $M$ even, and antisymmetric for $M$ odd.

Although for bosons the most relevant situation is $M = 0$, which is nicely illustrated by the property of vanishing interaction energy in $(k+1)$-body contact potentials, we should briefly mention the more general derivation based on a formal framework [24, 59]: Namely, the particles are expressed by vertex operators $\exp[iq\phi(z)]$ of a conformal field theory. The $\phi(z)$ are free scalar fields in two dimensions, characterized by the correlator $\langle\phi(z)\phi(z')\rangle = -\log|z-z'|$. While the correlator $\langle{:}\exp[iq\phi(z_1)]:\ldots:\exp[iq\phi(z_N)]{:}\rangle$, with $:\,:$ denoting a normal ordering, is then found to reproduce the Laughlin state, an additional clustering field is needed in the Read-Rezayi case. This additional field, $\Psi$, obeys a $\mathbb{Z}_k$ algebra, i.e. it is a parafermionic field. For $k = 2$, this field describes massless Majorana fermions, which are characterized by $\langle\Psi(z)\Psi(z')\rangle = (z-z')^{-1}$. Then, the correlator $\langle\Psi(z_1):\exp[iq\phi(z_1)]:\ldots\Psi(z_N):\exp[iq\phi(z_N)]{:}\rangle$ yields the Moore-Read wave function, Eq. (3.11). The algebra of the conformal field theory determines

the statistics of the quasiparticles, and it can be shown, that all states of this Read-Rezayi series which have the parafermionic field (i.e. with $k > 1$) support excitations with a non-Abelian quantum-statistics.

The mechanism for the non-Abelian character of quasiholes is pairing (in the Moore-Read case) or clustering (in the Read-Rezayi case) of particles. Without applying the formal machinery involved in the CFT derivation, we can follow the argument of Ref. [24], which demands that a quasihole in the Moore-Read state is single-valued only when it encircles *a pair* of composite particles. This allows for excitations carrying half-flux. As we can add only full quanta of flux, at least two quasiholes must be created. Different from Eq. (3.10) for Laughlin quasiholes, each Moore-Read quasihole thus demands a prefactor which introduces relative angular momentum only with respect to half of the particles. This suggests the following wave function [24, 63, 64]:

$$\Psi_{2\text{qhMR}} \sim \text{Pf}\left(\frac{(z_i-\xi_1)(z_j-\xi_2)+i\leftrightarrow j}{z_i-z_j}\right)\prod_{i<j}(z_i-z_j)^q \mathrm{e}^{-\sum_i |z_j|^2/4}. \qquad (3.14)$$

Generalizing this formula to four quasiholes, it is seen to be no longer unique: Within the Pfaffian, we could pair the quasiholes 1 and 2 with particle $i$, while quasiholes 3 and 4 are paired with particle $j$, but also 1 and 3 (or 1 and 4) could form pairs with $i$, and correspondingly 2 and 4 (or 2 and 3) would have to be paired with $j$. It has been shown that from this three choices, only two are linearly independent, which results in a two-fold degeneracy of the Moore-Read state with four quasiholes. It is the existence of this degenerate manifold which allows for a non-Abelian structure when particles are braided, i.e. interchanged [24, 63].

#### 3.1.2.3 Spinful FQH states and NASS series

The Laughlin state and all other states of the Read-Rezayi series describe spinless particles, or particles in a spin-polarized configuration. In the "real" quantum Hall effect, i.e. where the particles are charged and feel a true electromagnetic field, the latter will indeed tend to polarize the particles' spin, as a consequence of the Zeeman splitting $g\mu_\text{B}B$, with $\mu_\text{B}$ the Bohr magneton. Taking the $g$-factor of free electrons and the free electron mass, this splitting is as large as the LL gap. However, $g$ is typically much smaller than 2 for electrons in a solid, and the

effective mass might be heavily increased. Both effects together yield a gyromagnetic ratio as small as 0.02 in GaAs [65]. This has, since the early days of FQHE, motivated to formulate also spin-unpolarized wave functions. For the FQHE with cold atoms, where spin is a pseudospin, represented by different internal atomic states, the occurrence of spinful FQH states is natural.

A generalization of the Laughlin wave function to systems with spin was given by B. I. Halperin [66]:

$$\Psi_{\mathrm{H}} = \mathcal{N}_{\mathrm{H}} \prod_{i<j}^{N_\uparrow} (z_{i\uparrow} - z_{j\uparrow})^m \prod_{k<l}^{N_\downarrow} (z_{k\downarrow} - z_{l\downarrow})^{m'} \prod_{i,k} (z_{i\uparrow} - z_{k\downarrow})^n \mathrm{e}^{-\sum_i |z_i|^2/4}. \quad (3.15)$$

States described by a wave function of this form are usually called $(m, m', n)$ Halperin states. It is easy to see that the orbital part of this wave function reduces to the Laughlin wave function with $\nu = 1/m$, if we choose $m = m' = n$.

It is obvious that, if $m$, $m'$, and $n$ are larger than zero, the $(m, m', n)$ Halperin states are states with zero interaction energy in a two-body contact potential. To be bosonic, symmetry demands $m$ and $m'$ to be even, while no restriction exists for $n$, as it is the exponent of coordinate differences $(z_{i\uparrow} - z_{k\downarrow})$ belonging to particles which are distinguishable due to their spin. Thus, the $(2, 2, 1)$ Halperin state, having $\nu = 2/3$, corresponds to the $\nu = 1/2$ Laughlin state in the sense that it is the bosonic state of lowest angular momentum being a zero-energy eigenstate of two-body contact interactions. It is the unique ground state, if the interaction is repulsive between all particles, and for $N_\uparrow = N_\downarrow$. This directly implies that the $z$-component of spin is zero, $S_z = N_\uparrow - N_\downarrow = 0$. Due to the uniqueness of the ground state, this requires also the total spin to vanish, $\boldsymbol{S}^2 = 0$, i.e. the system forms a spin singlet.

It is then possible to repeat the procedure of the previous subsection, but instead of considering spin-polarized configurations, demand the states to be spin singlets. This had led to a generalization of the whole Read-Rezayi series, known as the non-Abelian spin singlet (NASS) series [67, 68], characterized by the filling $\nu = \frac{2k}{2kM+3}$ with $k \in \mathbb{N}$ and $M \in \mathbb{N}_0$. The term "non-Abelian" refers to the nature of the excitations. Just like in the Read-Rezayi series, the excitations are still Abelian for $k = 1$, i.e. in the Halperin state, but for any $k \geq 2$, non-Abelian excitations are supported.

As for the Read-Rezayi series, all states of this series with $M = 0$ are unique zero-energy eigenstates of repulsive $(k + 1)$-body contact interactions. We will

further study these states in Chapter 7 on a torus geometry. Due to the non-trivial topology of this surface, so-called topological degeneracies arise, which, together with the filling factor, allow to characterize the NASS phases.

In the following, we come back to the simplest FQH state, the Laughlin state. We are interested in the "smoothest" connection between the electronic FQHE and atomic realizations. Therefore we will now consider a setup of fermionic atoms with dipolar interactions.

## 3.2 Laughlin states of dipolar atoms

Using fermionic atoms with polarized spin, the Pauli principle prohibits two atoms to be at the same position, so there will not be contact interactions except for the quantum-statistical ones. Instead, however, we might assume that the atoms have an electric dipole moment, which causes interactions. In two dimensions, the dipole interaction becomes formally similar to the Coulomb interaction if we align the dipoles perpendicular to the plane. Then there are no anisotropy effects, and the dipoles just repel each other according to the dipole-dipole potential

$$V_{\mathrm{dd}} = \sum_{i<j} \frac{d^2}{|z_i - z_j|^3}, \tag{3.16}$$

with $d$ the dipole moment. The only difference to the Coulombic case $\sim 1/r$ is the cubic decay with distance. We may thus assume that the correlations induced by the dipolar interaction are similar to the ones due to Coulomb interaction, which are well described by the Laughlin wave function. Especially, since the dipolar interaction has a shorter range, the Laughlin wave function can be expected to even better agree with the exact ground state of a dipolar system than it does in the case of electrons.

An essential difference, however, distinguishing the Coulombic case from the dipolar one, is the absence of a background potential in the latter. In the solid, to have electroneutrality, every electronic charge is compensated by a positively-charged ion. Due to the low mobility of the ions, one usually thinks of this potential as a homogeneous background potential. It is easy to see that a Coulombic system requires such a potential. Namely, we can think of the Laughlin state as a homogeneous liquid and assume that particles sufficiently far from each do not have any correlations. Then, the large-distance contribution to the potential energy

per particle, $U$, has the following asymptotic behavior

$$U \propto \int_{R_0}^{\infty} V(r) r \mathrm{d}r, \tag{3.17}$$

with some lower bound $R_0 > 0$. For a Coulombic $1/r$ potential this integral diverges, so a screening background is necessary to stabilize the system. For the dipolar $1/r^3$ potential, no contributions stem from the upper limit of the integral, i.e. there are no interactions on large distances.

### 3.2.1 Quasihole excitation gap

Having the analytic expressions for the ground state and excited states, Eqs. (3.6) and (3.8), we can evaluate the excitation gap. For instance, one can perform classical Monte Carlo and just sample over different configurations of the coordinates $z_1, \ldots, z_N$. Hereby, one starts with a random configuration and calculates its energy, $U = \sum_{i<j} V(z_i, z_j)$. An algorithm, e.g. the Metropolis algorithm [69], generates new configurations and, depending on their probability given by the corresponding wave function amplitude, accepts them or not. This procedure allows for evaluating expectation values for a given wave function. The so-obtained energy can be crosschecked with the one obtained by exact diagonalization studies [70].

An elegant way to approximate the gap has been developed by S. Girvin [60, 71], using analytic expressions for the density-density correlation functions of the Laughlin state, $g_0(z_1, z_2)$, and the quasihole state, $g_{\mathrm{qh}}(z_1, z_2)$. The standard definition of these quantities reads

$$g(z_1, z_2) = \sum_{ijkl} \phi_i^*(z_1)\phi_j^*(z_2)\phi_k(z_1)\phi_l(z_2) \left\langle \Psi \right| \hat{\mathrm{c}}_i^\dagger \hat{\mathrm{c}}_j^\dagger \hat{\mathrm{c}}_k \hat{\mathrm{c}}_l \left| \Psi \right\rangle, \tag{3.18}$$

for an arbitrary $N$-body state $|\Psi\rangle$, with $\phi_i$ a single-particle basis, and $\hat{\mathrm{c}}_i$ ($\hat{\mathrm{c}}_i^\dagger$) the corresponding annihilation (creation) operators. Such a correlation function quantifies, for a given state $|\Psi\rangle$, the probability of finding a pair of particles at positions $z_1$ and $z_2$. Thus, the two-body interaction energy can be evaluated as $U = \frac{1}{2} \int\int \mathrm{d}z_1 \mathrm{d}z_2 \; g(z_1, z_2) V(z_1, z_2)$. The energy difference between the quasihole and the Laughlin state in a dipolar potential is thus obtained by evaluating the

following integral

$$\Delta = \frac{1}{2}\int \mathrm{d}^2 z_1 \int \mathrm{d}^2 z_2 \; V_{\mathrm{dd}}(z_1, z_2)\left[g_{\mathrm{qh}}(z_1, z_2) - g_0(z_1, z_2)\right]. \tag{3.19}$$

The problem hereby is that, despite the knowledge of analytic expressions for the states, closed analytic expressions for $g_0$ and $g_{\mathrm{qh}}$ are unknown. This is where the key idea of Ref. [71] comes into play: It relates the correlation function of the Laughlin state with the one of a homogeneous one-component plasma, which allows for finding an approximation for $g_0(z_1, z_2)$. The assumed homogeneity implies the thermodynamic limit, i.e. $N \to \infty$ particles. Explicitly, the plasma analogy then yields the expression [71]

$$g_0(z_1, z_2) = \frac{\nu^2}{(2\pi)^2}\Big(1 - \mathrm{e}^{-\frac{|z_1 - z_2|^2}{2}} - 2\sum_j^{\mathrm{odd}} \frac{C_j}{4^j j!}\,|z_1 - z_2|^{2j}\,\mathrm{e}^{-\frac{|z_1 - z_2|^2}{4}}\Big). \tag{3.20}$$

From this expression for the Laughlin state, also the correlation function, $g_{\mathrm{qh}}$ of the quasihole system has been derived [60]. Therefore one has to push a particle from the center to the "edge" of the infinite system, i.e. remove the particle. One explicitly obtains [60]

$$\begin{aligned} g_{\mathrm{qh}}(z_1, z_2) = \frac{\nu^2}{(2\pi)^2}\Bigg[\prod_{j=1}^{2}\left(1 - \mathrm{e}^{-\frac{|z_j|^2}{2}}\right) - \mathrm{e}^{-\frac{|z_1|^2 + |z_2|^2}{2}}\Bigg(\left|\mathrm{e}^{\frac{z_1 \bar{z}_2}{2}} - 1\right|^2 \\ + 2\sum_j^{\mathrm{odd}} \frac{C_j}{4^j j!}\sum_{k=0}^{\infty}\frac{|F_{j,k}(z_1,\, z_2)|^2}{4^k k!}\Bigg)\Bigg], \end{aligned} \tag{3.21}$$

$$F_{j,k}(z_1, z_2) = \frac{z_1 z_2}{2}\sum_{r=0}^{j}\sum_{s=0}^{k}\binom{j}{r}\binom{k}{s}\frac{(-1)^r z_1^{r+s} z_2^{j+k-(r+s)}}{\sqrt{(r+s+1)(j+k+1-(r+s))}}. \tag{3.22}$$

Using these expressions, the gap of a dipolar system according to Eq. (3.19) has first been calculated in Ref. [72]. There, a huge gap has been claimed. Redoing the calculation, however, we find a much smaller number, published in Ref. [73]. Furthermore, the absence of a background potential in the dipolar system turns out to be a delicate issue. For obtaining a positive gap at all, the thermodynamic quasihole state has to be properly defined. Before continuing with the evaluation of Eq. (3.19), we discuss this subject in the following subsection.

#### 3.2.1.1 Different types of quasiholes

In a finite system, we can think of creating a quasihole in three different ways [60, 70]:

(i) by increasing the area of the system at constant particle number,

(ii) by reducing the particle number,

(iii) by changing the magnetic field at constant particle number and constant area.

We will have to specify which kind of quasihole should be considered in order to define the quasihole excitation gap. Since the first two possibilities either lower the number of particles or their density, we should expect also a lowered interaction energy within the quasihole state. In an electronic system, the positively charged background (partly) compensates these losses, resulting in a positive energy gap for any of the three definitions [60, 70]. Contrarily, in the dipolar case, energy "gaps" defined according to (i) or (ii) will turn out to have a negative sign. The only meaningful definition for the energy gap then is according to (iii). The energy of a quasihole should be compared with the ground-state energy while the system remains with the same number of particles occupying the same area, similarly to the definition of the quasihole excitation energy in a normal Fermi system.

If $\lambda$ is kept constant, the correlation function given by Eq. (3.21) describes a quasihole according to (ii). This is seen by noticing that sufficiently far from the edges the density of the quasihole state has the form $n_{\mathrm{qh}}(z) = n_{\mathrm{L}}[1 - \exp(-|z|^2/2\lambda^2)]$, while the Laughlin state has the uniform density $n_{\mathrm{L}} = \nu/2\pi\lambda^2$, see Ref. [60]. From this we find that the difference in the number of particles for the states (3.6) and (3.8) in a finite area around the origin with the size much larger than $\lambda$ is simply $\nu$. In the finite-size expressions, Eqs. (3.6) and (3.8), these particles are pushed to the edge of the system, resulting in a quasihole according to (i). The expressions from Eqs. (3.20) and (3.21) consider the thermodynamic limit. In infinite systems, pushing particles to the edge is equivalent to removing them from the system. Thus, the calculation in the following subsection, based on these thermodynamic expressions, will yield a "gap" according to the definition (ii), i.e. $\Delta = E_{\mathrm{qh}}^{(N-\nu)} - E_0^{(N)}$. This gap compares the energy of $N - \nu$ particles in a quasihole state with the energy of $N$ particles in the Laughlin state.

Fortunately, we are able to easily relate this quantity to the gaps according to (i) and (iii). We therefore write $E_0 = N\epsilon_0$, where $\epsilon_0$ is the energy of one particle in the Laughlin state. This quantity can readily be evaluated by substituting $z_- \equiv z_1 - z_2$ in $V_{\mathrm{dd}}(z_1, z_2) = V(z_-)$ and in $g_0(z_1, z_2) = g_0(z_-)$. The energy is then obtained by the integral:

$$\epsilon_0 = \frac{(2\pi)^2}{2\nu} \int_{-\infty}^{\infty} \mathrm{d}z_- \; g_0(z_-) V_{\mathrm{dd}}(z_-). \tag{3.23}$$

Demanding a constant particle number, we may re-define the gap as

$$\Delta_N \equiv E_{\mathrm{qh}}^{(N-\nu)} - E_0^{(N-\nu)} = \Delta + \nu\epsilon_0. \tag{3.24}$$

This definition describes a quasihole created according to (ii). However, as argued before, apart from a fixed particle number, we should also demand a fixed volume. Therefore we notice that each Landau state occupies an area $\propto \lambda^2$. For the Laughlin state with $N$ particles to occupy the same area as the quasihole state with $N$ particles and one quasihole, we thus have to modify the length scale $\lambda'$ of the excited state according to:

$$\frac{\lambda'^2}{\lambda^2} = \frac{N}{N+\nu}. \tag{3.25}$$

Now we have to note that the energies in the dipolar system scale with $\lambda^{-3}$. Since we wish to compare states at different magnetic fields, we define the gap at constant particle number and constant volume as:

$$\frac{\Delta_V}{\lambda^3} = \frac{E_{\mathrm{qh}}^{(N)}}{\lambda'^3} - \frac{E_0^{(N)}}{\lambda^3}. \tag{3.26}$$

By noticing that

$$\frac{E_{\mathrm{qh}}^{(N)}}{\lambda'^3} = \left( \Delta \frac{\lambda^3}{\lambda'^3} + N\epsilon_0 \frac{\lambda^3}{\lambda'^3} \right) \frac{N}{N-\nu}, \tag{3.27}$$

and approximating $N/(N-\nu) \approx (N+\nu)/N$ for large $N$, we find with Eq. (3.25):

$$\Delta_V = \Delta + \frac{5}{2}\nu\epsilon_0. \tag{3.28}$$

According to our reasoning above, this quantity is the relevant gap for a quasihole of type (iii).

#### 3.2.1.2 Evaluation of the gap

Now we evaluate the integral in Eq. (3.19), making use of the expressions given by Eqs. (3.20) and (3.21). First, we shall specify the coefficients $C_j$ in Eqs. (3.20) and (3.21). It is shown in Ref. [71] that by setting all $C_j = 0$, a system with a completely filled Landau level is described, $\nu = 1$. For this choice of $C_j$, the resulting correlation functions are denoted by $g_0^{(1)}$ and $g_{\rm qh}^{(1)}$. In order to have a FQHE, we need a fractional filling, $\nu = 1/q$, which requires the coefficients $C_j$ with $j \leq q$ to be non-zero. For fermions, the most robust effect is expected for $\nu = 1/3$, where the choice $C_1 = 1$ and $C_3 = -1/2$ is best suited. We call the corresponding correlation functions $g_0^{(3)}$ and $g_{\rm qh}^{(3)}$, and also define for convenience the differences $\Sigma_0 \equiv g_0^{(3)} - g_0^{(1)}$ and $\Sigma_{\rm qh} \equiv g_{\rm qh}^{(3)} - g_{\rm qh}^{(1)}$.

Turning now to the integral in Eq. (3.19) with $\nu = 1/3$, we note that in the Abelian limit it reduces to the one considered in Ref. [72]. As our numerical result, however, drastically differs from Ref. [72], a careful analysis is of order. Therefore we split the integral Eq. (3.19) into two parts, $P_1 \equiv \int \mathrm{d}z_1 \int \mathrm{d}z_2\, V_{\rm dd}(g_{\rm qh}^{(1)} - g_0^{(1)})$, which is analytically solvable, and $P_2 \equiv \int \mathrm{d}z_1 \int \mathrm{d}z_2\, V_{\rm dd}$ $(\Sigma_{\rm qh} - \Sigma_0)$, which we treat numerically.

For the analytic part we find $P_1 = -\sqrt{2\pi}/\nu^2 \frac{d^2}{\lambda^3}$. Note that for $\nu = 1$, this negative number would be the full, completely analytic result for the energy difference $\Delta$ defined in Eq. (3.19). This clearly shows what we have anticipated in the beginning of this section, namely that this definition is not the appropriate one for the energy gap in a dipolar system.

Before we evaluate $P_2$ numerically, we examine the asymptotic behavior of the integrand. As the divergence in the interaction term for $z_1 \to z_2$ is compensated by the vanishing of the correlations, this limit can easily be handled by a regularization of the integral. The limit of $z_+ \equiv z_1 + z_2 \to \infty$, however, turns out to be problematic: For finite particle distance, $|z_1 - z_2| < \infty$, this contribution is not suppressed by the interaction, and the convergence of the integral Eq. (3.19) requires that $\Sigma_0$ and $\Sigma_{\rm qh}$ have the same asymptotic behavior. However, the completely different structure of both functions obscure the latter. Contrariwise, we should note that if we truncate the infinite sum in $\Sigma_{\rm qh}$, stemming from the $s$-sum in Eq. (3.22), this expression gets exponentially damped for large center-of-mass coordinates, while $\Sigma_0$ depends only on the relative coordinates, yielding $\Sigma_0 - \Sigma_{\rm qh} \neq 0$ for $|z_+| \to \infty$.

To circumvent this problem, we bring $\Sigma_0$ to a form similar as $\Sigma_{\rm qh}$, which is possible by factoring out a damping $\exp[-(|z_1|^2+|z_2|^2)/2]$ and Taylor expanding the remaining exponential $\exp[|z_+|^2]$. We are then able to write

$$\Sigma_0(z_1,z_2) = \mathrm{e}^{-\frac{|z_1|^2+|z_2|^2}{2}} \sum_j \frac{-2C_j}{4^j j!} \sum_{k=0}^{\infty} \frac{|F^{(0)}_{j,k}(z_1,z_2)|^2}{4^k k!}, \tag{3.29}$$

$$F^{(0)}_{j,k}(z_1,z_2) = \sum_{r=0}^{k}\sum_{s=0}^{k} \binom{j}{r}\binom{k}{s}(-1)^{j-r} z_1^{r+s} z_2^{j+k-(r+s)}. \tag{3.30}$$

As now each term in both $\Sigma_0$ and $\Sigma_{\rm qh}$ is damped by a factor $\exp[-(|z_1|^2+|z_2|^2)/2]$, they all vanish in the limit $|z_+| \to \infty$, and we may truncate the infinite sums at a sufficiently large value of $k$. Note that due to the different orders in $z_1$ and $z_2$ of $F_{j,k}$ in Eq. (3.22) and $F^{(0)}_{j,k}$ in Eq. (3.29), the sum in $\Sigma_0$ should contain two more terms than the sum in $\Sigma_{\rm qh}$ for a quick convergence.

Now we are able to perform the numerical integration. The error due to the truncation still is 5% for 10 terms, but can be minimized by a finite-size analysis of our results taking into account up to 25 terms. We then find $P_2 = (0.1875 \pm 0.0010)\frac{d^2}{\lambda^3}$. With this, we find $\Delta = 0.5(P_1+P_2) = -(0.0455 \pm 0.0010)\frac{d^2}{\lambda^3}$. As we have already argued before, this negative value is due to the reduced density of the system.

We continue with calculating the gap as defined in Eq. (3.24). Therefore we have to evaluate the integral Eq. (3.23). We obtain $\epsilon_0 = \frac{\sqrt{\pi}}{2\nu}\left(\frac{\sqrt{2}}{2} - \frac{15}{32}\right)\frac{d^2}{\lambda^3}$. Plugged into Eq. (3.24), we find that also $\Delta_N < 0$. The negative value for $\Delta_N$ can be understood by noticing that the particle taken away at the origin now has been added at the edge of the system. Accordingly, the volume of the system has increased, so $\Delta_N$ corresponds to the energy of a quasihole according to (ii). As long as such a process is possible, the system is unstable as it tries to reduce its density by diluting.

Finally, we turn to definition Eq. (3.28). Only in this case, we obtain a positive gap, $\Delta_V = (0.0132 \pm 0.0020)\frac{d^2}{\lambda^3}$, which however is much smaller than the number found in Ref. [72], $(0.9271 \pm 0.019)\frac{d^2}{\lambda^3}$, but compares well with the gap obtained via exact diagonalization of a small dipolar system in Ref. [74], where the discrepancy to Ref. [72] has been attributed to the different system size. The deviation of our result from the one obtained in Ref. [72] is due to the different handling of the infinite sum in Eq. (3.22). By the method described here, based on the expansion of Eq. (3.20) into Eq. (3.29), the correct asymptotic behavior of

$g_0 - g_{\mathrm{qh}}$ is guaranteed for arbitrarily large variables $z_1$ and $z_2$ even after truncating the sum. The opposite is true if one just truncates the sum in Eq. (3.22) and leaves $g_0$ as defined in Eq. (3.20). As argued above, the latter always produces wrong results for large center-of-mass coordinates, such that the validity of the integrand in Eq. (3.19) is restricted to a finite regime around the hole. It turns out that a very large number of terms would have to be taken into account, in order to capture the whole regime which substantially contributes to the integral.

### 3.2.2 Laughlin state and quasihole gap in non-Abelian gauge fields

As mentioned in Chapter 2, with cold atoms we can do more than just mimicking magnetic fields. It is also possible to design gauge fields, which, apart from multiplying a local U(1) phase to the wave function, rotate the state if it has some internal structure. We will now consider atoms with two internal states, described by a two-component spinor. Additionally to the Abelian gauge potential, which we leave as before, we consider also a non-Abelian gauge potential, which we assume to be constant in space and which can be expressed in terms of the Pauli matrices $\sigma_x$ and $\sigma_y$:

$$\boldsymbol{A}^{\mathrm{nA}} = (\alpha\sigma_x + \beta\sigma_y, \gamma\sigma_x + \delta\sigma_y). \tag{3.31}$$

We may interpret such a gauge potential as a coupling of the (pseudo)spin to the orbital movement of the atoms, if we properly choose the parameters $\alpha$, $\beta$, $\gamma$, and $\delta$. Choosing $\beta = -\gamma$ and $\alpha = \delta = 0$, the gauge potential describes a Rashba coupling [75]. For $\alpha = -\delta$ and $\beta = -\gamma = 0$, we have a Dresselhaus coupling [76], see also Chapter 7. We will first derive, for this general gauge field, the Hamiltonian in terms of the previously defined ladder operators $\hat{\mathrm{a}}$, $\hat{\mathrm{a}}^\dagger$, $\hat{\mathrm{b}}$, and $\hat{\mathrm{b}}^\dagger$. We will then make a particular choice, in which we obtain squeezed LLs, and thus a squeezed Laughlin state. Then we repeat the above calculation in this new scenario, which will demonstrate that such a squeezing increases the gap above the Laughlin state, and thus stabilizes this state.

#### 3.2.2.1 Hamiltonian structure

Up to an irrelevant constant, the presence of a non-Abelian gauge potential will not modify the Abelian part of the Hamiltonian, $H$, given by Eq. (3.1). Including

the non-Abelian part, we get

$$\begin{aligned} H^{\mathrm{nA}} &= H\mathbb{1} + \sigma_x \left[2\alpha p_x + 2\gamma p_y - \alpha B y + \gamma B x\right] \\ &\quad + \sigma_y \left[2\beta p_x + 2\delta p_y - \beta B y + \delta B x\right]. \end{aligned} \tag{3.32}$$

If $\alpha, \beta, \gamma, \delta \in \mathbb{R}$, the Hamiltonian is Hermitean. We then define

$$H^{\mathrm{nA}} \equiv \begin{pmatrix} H & H_{\uparrow\downarrow} \\ H_{\uparrow\downarrow}^{\dagger} & H \end{pmatrix}, \tag{3.33}$$

with

$$\begin{aligned} H_{\uparrow\downarrow} =& \partial_x(-2i\alpha - 2\beta) + \partial_y(-2i\gamma - 2\delta) + y(-\alpha B + i\beta B) + x(\gamma B - i\delta B) \\ =& \sqrt{\frac{B}{2\Omega}} \Big\{ (-i\alpha + \beta + \gamma + i\delta) \left[\hat{\mathrm{a}}(1+\Omega) + \hat{\mathrm{b}}^{\dagger}(1-\Omega)\right] \\ &+ (i\alpha - \beta + \gamma + i\delta) \left[\hat{\mathrm{a}}^{\dagger}(1+\Omega) + \hat{\mathrm{b}}(1-\Omega)\right] \Big\}. \end{aligned} \tag{3.34}$$

In the second line we have used the definitions from Eqs. (3.2) and (3.3). Oppositely to the diagonal elements, which are quadratic, i.e. given in terms of $\hat{\mathrm{a}}^{\dagger}\hat{\mathrm{a}}$ and $\hat{\mathrm{b}}^{\dagger}\hat{\mathrm{b}}$, the off-diagonal terms in the Hamiltonian are linear in the operators and will thus mix different levels. In the trapped system, with $1 - \Omega_{-} \neq 0$, we have no solution for this Hamiltonian, but without trap the situation becomes analytically treatable, as the Hamiltonian will not any longer depend on the operators $\hat{\mathrm{b}}, \hat{\mathrm{b}}^{\dagger}$.

The situation becomes particularly easy if we choose an isotropic configuration with either $-i\alpha + \beta + \gamma + i\delta = 0$ or $i\alpha - \beta + \gamma + i\delta = 0$. Then each off-diagonal element depends either on $\hat{\mathrm{a}}$ or on $\hat{\mathrm{a}}^{\dagger}$, but not on both. With this, the Hamiltonian is a Jaynes-Cummings-type Hamiltonian, and the solutions are easily found. They are given in Ref. [41], and are just spinors of the form $(c_{\uparrow} |n, m\rangle, c_{\downarrow} |n-1, m\rangle)^T$, with $c_{\uparrow,\downarrow}$ some coefficients which have to be properly chosen. This will be done in Chapter 6, where we consider two-component Bose gases. In this chapter, we will focus on an unpaired solution of the form $(0, |0, m\rangle)^T$. Note that this solution has higher energy than the lowest paired level with $n = 1$, but as we deal with fermions, we can choose the Fermi energy in such a way that the unpaired level becomes the lowest, not completely filled energy level. With that choice for the LLL, the non-Abelian system becomes, up to a constant shift in the energy, equivalent to the spinless case discussed in Section 3.2.1.

#### 3.2.2.2 Squeezing transformation

This equivalence between the Abelian and the non-Abelian problem holds only in the isotropic case. Now we wish to focus on anisotropic configurations in the non-Abelian gauge field. To make the off-diagonal elements $H_{\uparrow\downarrow}$ real, we may choose $\alpha = \delta = 0$. Anisotropic configurations are then defined by $\beta + \gamma \neq 0$ and $\beta - \gamma \neq 0$. With this, $H_{\uparrow\downarrow}$ depends on $\hat{a}$ and $\hat{a}^\dagger$.

For the low-energy physics in such a configuration, Ref. [77] has pointed out that the isotropic case is related to the anisotropic one through a squeezing transformation:

$$\hat{S}(\xi) = \exp[\frac{\xi}{2}(\hat{a}^2 - \hat{a}^{\dagger\ 2})], \tag{3.35}$$

$$\xi = -\tanh^{-1}\left(\frac{\gamma - \beta}{\gamma + \beta}\right), \tag{3.36}$$

The eigenstates of the anisotropic Hamiltonian can then be obtained from the isotropic solutions by applying $\hat{S}$. Accordingly, the solutions have the same form as before, but now the spinors explicitly read $(c_\uparrow \hat{S}^\dagger |n, m\rangle, c_\downarrow \hat{S}^\dagger |n-1, m\rangle)^T$ for the paired solutions. We will focus on the unpaired solution, which is given by

$$\left(0,\ \hat{S}(\xi)^\dagger |0, m\rangle\right)^{\mathrm{T}} = \left(0,\ \hat{S}(\xi)^\dagger [z^m \exp(-|z|^2/4)]\right)^{\mathrm{T}}. \tag{3.37}$$

Choosing the Fermi energy such that this level is the LLL, the only modification with respect to the Abelian case enters through the squeezing transformation. Note that this squeezing transformation is effectively given by just replacing the original variables $z$ by squeezed ones $\tilde{z}$:

$$\left[z \equiv x - iy\right] \to \left[\tilde{z}(\xi) \equiv \cosh\xi\ z - \sinh\xi\ \bar{z}\right]. \tag{3.38}$$

#### 3.2.2.3 Gap above squeezed Laughlin state

The many-body states are obtained by filling the LLL, so they are equally affected by the squeezing. Thus, we can easily adapt the Laughlin wave function and the quasihole wave function, Eqs. (3.6) and (3.8), to the anisotropic scenario by making the replacement Eq. (3.38). Accordingly, also the correlation functions Eqs. (3.20–3.22) hold, if we make the same substitution. The gap, as defined in Eq. (3.19), becomes a function of the squeezing parameter $\xi$. It is explicitly

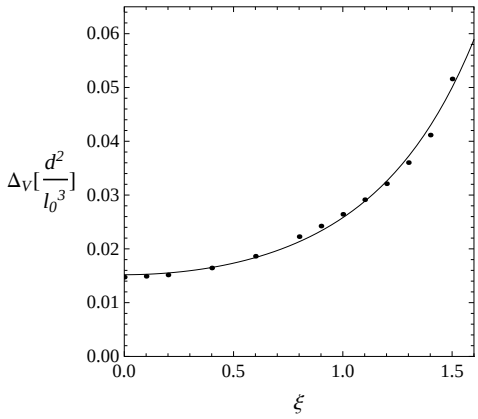


FIGURE 3.2: The gap $\Delta_V$ at constant volume and constant particle number as a function of the squeezing parameter $\xi$: The dots are obtained by a numerical evaluation of Eq. (3.19) for different $\xi$, a fit of this data yields the solid line. From: [73].

given by the integral

$$\Delta(\xi) = \frac{1}{2} \int \mathrm{d}^2 z_1 \int \mathrm{d}^2 z_2 \; V_{\mathrm{dd}}(z_1, z_2) \left[ g_{\mathrm{qh}}(\tilde{z}_1(\xi), \tilde{z}_2(\xi)) - g_0(\tilde{z}_1(\xi), \tilde{z}_2(\xi)) \right] . \quad (3.39)$$

In the same way, we generalize the ground-state energy defined in Eq. (3.23) to be a function $\epsilon_0(\xi)$ of the squeezing parameter. Following the derivation of Section 3.2.1.2, we finally arrive at the equation $\Delta_V(\xi) = \Delta(\xi) + \frac{5}{2}\nu\epsilon_0(\xi)$.

The calculation of Section 3.2.1.2 applied to a system with finite squeezing $\xi$ is similar as before, but now the whole integral has to be solved numerically. Again we find negative values for $\Delta(\xi)$ and $\Delta_N(\xi)$, which even decrease with larger $\xi$. However, as also the ground-state energy $\epsilon_0(\xi)$ increases with $\xi$, the gap $\Delta_V(\xi)$ at constant particle number and constant volume finally has a positive balance for all $\xi$. As shown in Fig. 3.2, it increases with $\xi$, and a convenient fit to the numerical data is found to be:

$$\Delta_V(\xi) = \Delta_V(0) \exp\left(\alpha \; \xi^2\right) . \quad (3.40)$$

We obtain $\alpha = 0.529$ and $\Delta_V(0) = 0.0152 \; d^2/\lambda^3$.

To understand this behavior, we note that the squeezing allows the particles to get closer in one direction, while the particle distance is increased in the other direction. Due to $1/r^3$ behavior of the dipole-dipole interaction, the interaction energy is much more sensitive to changes of the density distribution at short

distances rather than at large ones. Thus, compressing in one direction and stretching in another one increases the interaction energy. As a consequence of Eq. (3.28), this gives rise to a bigger energy gap.

We thus conclude that non-Abelian gauge fields may allow for achieving a more robust Laughlin state, if they are used to introduce an anisotropy squeezing the states.

# Chapter 4

# Fractional quantum Hall states of laser-dressed bosons

In the previous chapter the FQHE was introduced as a strongly correlated phase of matter which can be described by analytic wave functions like the Laughlin wave function, Eq. (3.6), or the Moore-Read wave function, Eq. (3.11). We assumed that, due to the similarity between dipolar and Coulomb interaction, fermionic atoms in an artificial gauge field exhibit a FQHE just like electrons in a magnetic field. We thus described such a system by the Laughlin wave function, which allowed us to evaluate its energy gap in the thermodynamic limit, as a benchmark of experimental feasibility.

We have not checked up to which degree and under which circumstances atoms in artificial gauge fields can indeed be described by the Laughlin wave function. In this chapter, we shall be more concrete. To that aim, we focus on an explicit proposal for generating an artificial magnetic field in the lab. Namely, we will consider the setup described in Section 2.2, where the gauge field is due to a coupling of the atoms to a laser field. The single-particle Hamiltonian $H_{\mathrm{sp}}$ is given by Eq. (2.8). An important energy scale in this problem is the Rabi frequency $\hbar\Omega_0$ which fixes the splitting between the low energy manifold $H_{22}$ and the high energy manifold $H_{11}$. An ideal situation is the limit $\Omega_0 \to \infty$, as we

can then restrict ourselves to $H_{22}$ from Eq. (2.14). In this chapter we wish to compare this ideal limit with realistic choices for $\Omega_0$.

Another important quantity on the single-particle level is the gauge field strength $B$, which fixes the LL spacing $\hbar B/M$, the cyclotron frequency $\omega_\mathrm{c} = B/M$, and thus also the effective trapping frequency $\omega \equiv \sqrt{\omega_\perp^2 - \omega_\mathrm{c}^2/4}$. Experimentally, $B$ is controlled by the wave number of the laser field $k$, and the length scale $w$ of the Zeeman splitting: $B = \frac{\hbar k}{2w}$. It is convenient to define also the experimentally free parameter

$$\eta = \frac{\omega_\mathrm{c}}{2\omega_\perp} = \frac{\hbar}{2M\omega_\perp}\frac{k}{w}. \tag{4.1}$$

Then the energy of a single-particle state in the LLL with angular momentum $\ell$ simply reads

$$E_\ell = \hbar\omega_\perp \ell(1-\eta). \tag{4.2}$$

To derive this, we can follow the steps described below Eq. (3.1), adapting the units accordingly.

On the many-body level, we will now consider bosons, as they are experimentally the more feasible choice. We assume them to interact via a two-body contact potential, characterized by the dimensionless parameter $g$:

$$V = \frac{g\hbar^2}{M}\sum_{i<j}\delta(z_i - z_j). \tag{4.3}$$

We will keep $gN = 6$ in the numerical study, but a discussion how varying $g$ would influence the behavior is given in Section 4.3.3.

The goal of this chapter is to study which strongly correlated states we can expect in this setup. Such states are based on having a relatively high angular momentum, which allows to introduce many zeros of the form $z_i - z_j$ into the wave function. While these zeros are favorable for reducing the interaction energy, they cost kinetic energy. It will thus depend critically on the parameter $\eta$ whether such states are realized. Note that this parameter is the analog of rotation frequency in a system where the gauge field is due to a rotation of the system. No analog exists for the second parameter, $\Omega_0$. We will use a perturbative expansion to derive an effective Hamiltonian, which will then allow to treat the influence of $\Omega_0$

numerically by applying the exact diagonalization method. This restricts us to small-sized systems.

For convenience, we will in this and the next chapter use units of length which are given by $\lambda_\perp = \sqrt{\hbar/M\omega_\perp}$. They are related to the unit of length $\lambda$ from the previous chapter by a factor $\sqrt{2}$. This change affects only normalization factors and the Gaussian part of all wave functions. In the latter we now have to write $\exp(-|z|^2/2)$ instead of $\exp(-|z|^2/4)$.

## 4.1 Effective Hamiltonian

On the single-particle level, we can simplify the problem if the Hamiltonian of Eq. (2.8) divides into two well-separated energy manifolds, each of them described by $H_{11}$ and $H_{22}$, respectively. In fact, the two components are separated by an energy of the order $\hbar\Omega_0$. We assume that this can be made much larger than the typical expected values of $H_{22}$. The latter are of the order of the recoil energy $E_\mathrm{R} = \hbar^2k^2/(2M)$. We know that the Fock-Darwin functions $\phi^\mathrm{FD}_{0,i}$ from Eq. (3.5) solve the Hamiltonian $H_{22}$.

Let us first assume that the coupling between both manifolds were zero, i.e. $H_{12} = H_{21} = 0$. The low-energy physics would then be fully described by spinors of the form $|(0,i)\rangle \equiv (0, \phi^\mathrm{FD}_{0,i})^T$, with eigenenergies $E_i$ being identical to the eigenenergies of $\phi^\mathrm{FD}_{0,i}$ with respect to $H_{22}$. We see that we could just replace the Hamiltonian matrix $H_\mathrm{sp}$ by $H_{22}$, and instead of spinors, we would just have single-component states $|i\rangle$.

In our case, though, the off-diagonal elements are non-zero, but due to the huge energy difference between the manifolds, we can expect transitions into the higher manifold to be sufficiently short-lived. We thus restrict ourselves on a low-energy Hilbert space, given by the lower manifold, and consider virtual transitions into higher states perturbatively. Therefore we expand the Hamiltonian matrix to second order in the off-diagonal part, which we denote by $H^\mathrm{off}$. This expansion

reads

$$\begin{aligned}\langle (0,i)|\, H_{\rm sp}\, |(0,j)\rangle =& E_i\delta_{ij} + \langle (0,i)|\, H^{\rm off}\, |(0,j)\rangle \\ &+ \frac{1}{2}\sum_k \langle (0,i)|\, H^{\rm off}\, |(k,0)\rangle \langle (k,0)|\, H^{\rm off}\, |(0,j)\rangle \\ &\times \left(\frac{1}{E_i - E_{k,0}} + \frac{1}{E_j - E_{k,0}}\right) + \ldots, \end{aligned} \tag{4.4}$$

where $|(k,0)\rangle$ denotes a spinor of the form $(f_k, 0)^T$, i.e. with zero weight in the lower component, and $f_k$ is some eigenfunction of $H_{11}$ with corresponding eigenenergy $E_{k,0}$. We do not need to know neither the functions nor the eigenenergy. It is enough to know that the energy difference $E_i - E_{k,0}$ is large, and can be approximated by $E_i - E_{k,0} \approx \hbar\Omega_0$.

With this Eq. (4.4) becomes

$$\langle (0,i)|\, H_{\rm sp}\, |(0,j)\rangle = \langle i|\, H_{22} - \frac{H_{21}H_{12}}{\hbar\Omega_0}\, |j\rangle + \ldots, \tag{4.5}$$

so we have reduced the problem to a one-component problem, described by the effective Hamiltonian

$$H_{\rm eff} = H_{22} - \frac{H_{21}H_{12}}{\hbar\Omega_0}. \tag{4.6}$$

Truncating the perturbation term $H_{21}H_{12}$ in second order in $x$, $y$, $\partial_x$, and $\partial_y$, it explicitly reads

$$\begin{aligned} H_{21}H_{12} = \frac{\hbar^2}{M^2}\Bigg[ &\frac{1}{4w^4} - \frac{2x^2}{w^6} + \frac{k^2x^2}{16w^4} + \frac{k^4x^2}{64w^2} + \frac{ikxy}{4w^5} + \frac{k^2y^2}{64w^4} \\ &+ \left(-\frac{ikx}{4w^3} - \frac{ik^3x}{8w}\right)\partial_y + \left(\frac{x}{w^4} - \frac{iky}{8w^3}\right)\partial_x \\ &+ \left(-\frac{k^2}{4} + \frac{k^2x^2}{4w^2}\right)\partial_y^2 + \left(-\frac{1}{4w^2} + \frac{x^2}{2w^4}\right)\partial_x^2\Bigg]. \end{aligned} \tag{4.7}$$

One can show that this operator does not conserve $L$, as it connects $L'$-subspaces with $L' = L + \Delta$ where $\Delta = 0, \pm 2, \pm 4$. We will solve $H^{\rm eff}$ numerically by exact diagonalization together with the interaction term.

## 4.2 Exact diagonalization method

Now we are prepared to achieve our actual goal, namely to find the ground state and low-lying excitations of the system. Therefore, we have to numerically solve the Hamiltonian

$$H = \sum_{i=1}^{N} H_i^{\text{eff}} + V, \tag{4.8}$$

where $H_i^{\text{eff}}$ is the single-particle Hamiltonian $H_{\text{eff}}$ acting on particle $i$, as given by Eq. (4.6), and the interaction $V$ has been defined in Eq. (4.3).

To solve the Hamiltonian, we express it as a matrix $H_{ij} = \langle i| H |j\rangle$, with $|i\rangle$ a basis spanning the whole Hilbert space, and then numerically diagonalize this matrix using standard routines. We thereby obtain results which are numerically exact with respect to the considered Hamiltonian, but the method requires a finite dimensional Hilbert space. In our problem, the Hilbert space has in principle infinitely many dimensions, but we already have enough insight into the problem to identify several truncations we can safely make.

First of all, we do not expect the LL structure of well separated energy levels, Eq. (3.4), to be destroyed by neither the interaction nor the perturbation due to the atom-laser coupling. The latter is assured by $\hbar\Omega_0 \gg E_{\text{R}}$, while for the interactions the validity of this assumption will depend on the interaction energy which is tuned by $g$. It should be smaller than the level spacing $\hbar B/M$. We now could *a priori* derive a limiting value for $g$ by demanding that the mean-field interaction energy per particle $gN\hbar\omega_\perp/2$ is smaller than the level spacing $2\eta\hbar\omega_\perp$. In the strongly correlated regime, however, interactions are expected to be significantly reduced, so this condition seems to be too restrictive [78]. More conveniently, we check the consistency of our results with the LLL assumption *a posteriori*. With this in mind, we can safely truncate the single-particle basis by restricting ourselves to the states spanning the LLL. As a basis for this space we can conveniently take the exact solutions of $H_{22}$, i.e. the Fock-Darwin functions $\phi_{0,\ell}^{\text{FD}}(z)$ given by Eq. (3.5).

But still, these function span an infinitely large Hilbert space, as $\ell$ can run from 0 to $\infty$. However, the trapping potential causes an energy cost for increasing angular momentum. This assures that we can also truncate with respect to single-particle angular momentum. *A priori*, we do not know at which $\ell$ we can

safely make this truncation, so we will have to make convergency checks to find this out.

For the time being, we assume some maximum $\ell_{\max}$, which then allows to construct a finite many-body basis for $N$ particles by just giving the occupation numbers $n_\ell$ of each single-particle state $\ell$. These so-called Fock states read

$$|n_0, n_1, \cdots, n_{\ell_{\max}}\rangle = \\ \mathcal{S}\left[\phi^{\mathrm{FD}}_{0,0}(z_1)\cdots\phi^{\mathrm{FD}}_{0,0}(z_{n_0})\phi^{\mathrm{FD}}_{0,1}(z_{n_0+1})\cdots\phi^{\mathrm{FD}}_{0,1}(z_{n_0+n_1})\ldots\phi^{\mathrm{FD}}_{0,\ell_{\max}}(z_N)\right]. \tag{4.9}$$

Here $\mathcal{S}$ symmetrizes with respect to all permutations of $\{z_1, \ldots, z_N\}$ in order to make the state bosonic. We also define operators $\hat{\mathrm{c}}_i^\dagger$ and $\hat{\mathrm{c}}_i$ creating or annihilating particles in Fock-Darwin states $\phi^{\mathrm{FD}}_{0,i}$ from a vacuum $|\mathbf{0}\rangle$. The Fock states can then be written as

$$|n_0, n_1, \ldots, n_{\ell_{\max}}\rangle = \frac{1}{\sqrt{n_0!\ldots n_{\ell_{\max}}!}}\left(\hat{\mathrm{c}}_0\right)^{n_0}\cdots\left(\hat{\mathrm{c}}_{\ell_{\max}}\right)^{n_{\ell_{\max}}}|\mathbf{0}\rangle. \tag{4.10}$$

The action of these operators on a Fock states is as usual: $\hat{\mathrm{c}}_i\,|\ldots, n_i, \ldots\rangle = \sqrt{n_i}\,|\ldots, n_i - 1, \ldots\rangle$ and $\hat{\mathrm{c}}_i^\dagger\,|\ldots, n_i, \ldots\rangle = \sqrt{n_i + 1}\,|\ldots, n_i + 1, \ldots\rangle$, and the usual bosonic commutation relations apply. The Hamiltonian $H$ reads in this second quantized notation:

$$H = \sum_{i,j=0}^{\ell_{\max}} e_{ij}\hat{\mathrm{c}}_i^\dagger\hat{\mathrm{c}}_j + \sum_{ijkl} V_{ijkl}\hat{\mathrm{c}}_i^\dagger\hat{\mathrm{c}}_j^\dagger\hat{\mathrm{c}}_k\hat{\mathrm{c}}_l, \tag{4.11}$$

with

$$e_{ij} = \langle i|\, H^{\mathrm{eff}}_{22}\,|j\rangle = \int \mathrm{d}^2 z\ \bar{\phi}^{\mathrm{FD}}_{0,i}(z) H^{\mathrm{eff}}\phi^{\mathrm{FD}}_{0,j}(z), \tag{4.12}$$

and

$$V_{ijkl} = \langle i|\otimes\langle j|\, V\,|k\rangle\otimes|l\rangle = g\int \mathrm{d}^2 z\ \bar{\phi}^{\mathrm{FD}}_{0,i}(z)\bar{\phi}^{\mathrm{FD}}_{0,j}(z)\phi^{\mathrm{FD}}_{0,k}(z)\phi^{\mathrm{FD}}_{0,l}(z), \tag{4.13}$$

where lengths are measured in units of $\lambda_\perp$, and energies in units of $\hbar\omega_\perp$. Solving the integrals in Eqs. (4.13) and especially (4.12) is a lengthy but straightforward task, which is achieved by Mathematica. As mentioned before, due to the perturbative term in $H_{\mathrm{eff}}$, the elements $e_{ij}$ are not diagonal. However we find that $e_{ij} = 0$ if $|i - j| > 4$. For the interaction part, it can directly be seen that $V_{ijkl} \sim \delta_{i+j-k-l}$, i.e. it conserves angular momentum.

Since the feasibility of the numerical diagonalization crucially depends on the size of the matrix, let us now analyze the Hilbert space dimension. The total particle number of a Fock state in Eq.(4.9) is $N = \sum_{i=0}^{\ell_{\max}} n_i$. Thus, the number of different many-body states within the basis can be calculated from an urn problem of $\ell_{\max}+1$ different balls, which are drawn $N$ times and placed back after each drawing. Since the sequence of drawing does not matter, there are $D = \binom{n+\ell_{\max}}{n}$ combinations, defining the dimension $D$ of the Hilbert space. Since we can expect that $\ell_{\max}$ must be increased when $N$ is increased, we find an exponential growth of $D$ for large $N$. In the Laughlin wave function of Eq. (3.6), for instance, $\ell_{\max} = qN$, and from Stirling's formula we then would get $D \sim (q+1)^{(q+1)N}/\sqrt{\pi N}$ for $N \to \infty$. In reality, we can further restrict our basis: Since the average $\langle \ell \rangle = \langle L \rangle / N \ll \ell_{\max}$ in any relevant many-body state, we can choose the maximum value $L_{\max}$ of total angular momentum much smaller than $N\ell_{\max}$. Then the dimension of the Hilbert space can no longer be obtained by means of a simple combinatorial model. Instead we construct the basis explicitly on a computer. We find that $D$ is still rapidly growing with $N$: We chose to truncate the total angular momentum $L$ at a value which is 16 units above the Laughlin angular momentum, $L_{\text{Laughlin}} = N(N-1)$ for $q = 2$. With this the many-body basis of $N = 4$ particles contains $2 \cdot 10^3$ states, while for $N = 8$ we already get $D \sim 3 \cdot 10^6$. We note that the chosen truncation at $L = L_{\text{Laughlin}} + 16$ turned out to be valid for all relevant states with $N = 4$ *a posteriori*, while we have not tried to reach $N = 8$, and therefore cannot judge its validity here. It rather seems to be optimistic to believe that the same truncation holds, when $\langle L \rangle$ is much larger.

An important issue which often significantly increases the accessible system sizes are symmetries in the Hamiltonian. Each symmetry is related to a conserved quantity $O$ being eigenvalue of some operator $\hat{\mathrm{O}}$. Then $[H, \hat{\mathrm{O}}] = 0$, from which it is easy to show that $\langle O_1 | H | O_2 \rangle = 0$, where $|O_i\rangle$ shall denote eigenstates of $\hat{\mathrm{O}}$ belonging to different eigenvalues. Thus, in an eigenbasis of $\hat{\mathrm{O}}$, the Hamiltonian matrix has a block structure, and each block of dimension $d_i < D$ can be diagonalized separately. In our concrete Hamiltonian, with the complicated perturbation on the single-particle level in Eq. (4.6), there seems to be no such symmetry which we could exploit. Obviously, if we neglect the perturbation, i.e. if we consider the limit $\Omega_0 \to \infty$, the Hamiltonian $H$ shows a rotational symmetry in the $xy$-plane, which results in conservation of total angular momentum $L$, measured by the operator $\hat{\mathrm{L}} = \sum_{i=1}^{N} x_i \partial_{y_i} - y_i \partial_{x_i}$. The Fock basis is already eigenbasis of $\hat{\mathrm{L}}$, so the Hilbert space is easily divided in blocks with definite $L$.

Then the many-body basis for $N = 6$ particles at $L = L_{\text{Laughlin}}$ contains $1 \cdot 10^3$ states, while $3 \cdot 10^6$ states are needed to treat $N = 10$ particles. Let us note that, without perturbation, the system is equivalent to a system of rotating bosons, which has been numerically studied before [79].

Obviously treating matrices of this size, is a numerical challenge. The number of matrix elements is $D^2$, and, assuming 32 bit floating point numbers, the memory needed to store the full matrix is $8D^2$ byte. This means that matrices up to $D = 5 \cdot 10^4$ fit into a typical RAM of 16GB. To treat bigger matrices, one can make use of the sparseness of the matrix. Since any term in the Hamiltonian of Eq. (4.11) acting on a state of the Fock basis will at most change four occupation numbers, most of the Hamiltonian matrix elements are zero. We need not waste memory for storing these zeros, especially since there exist diagonalization algorithms which are based on operations which only multiply the matrix with a vector $\mathbf{v}$: $\mathbf{v}^{(i+1)} = H\mathbf{v}^{(i)}$. If $H$ is a positive definite matrix, and if the initial state $\mathbf{v}^{(0)}$ has non-zero overlap with the ground state, this procedure will converge to the ground state after typically $i \approx 50$ iterations. A more sophisticated variation of this so-called power method are different Lanczos methods [80]. They do not rely on positive-definiteness of the matrix, and are not restricted to the ground state. We find them implemented in standard routines. Even using Lanczos, RAM still sets a boundary to the system size, as reasonably quick computations require that all non-zero matrix elements can be stored. Also, as one sees by considering the simple power method, each iteration step contains at least $kD$ floating point operations. Thus, computation time increases faster than system size, which makes the treatment of large systems very costly.

Since our intention in this chapter is to vary, over wide ranges, the experimental parameters $\Omega_0$ and $\eta$, we do not try to reach the largest possible sizes. Instead, we will mostly be restricted to $N = 4$, without any need to apply Lanczos methods. The situation will be different in Chapter 6, where we assume, for a different system, an idealized Hamiltonian. There, we will also find it convenient to study the bulk phenomena by considering a finite systems without edges, e.g. on a sphere or on a torus.

Another quite technical issue which we should mention at this place concerns the evaluation of the results obtained by exact diagonalization. We will get the eigenstates of the system expressed as a $D$-component vector, where every coefficient gives the contribution of the corresponding Fock state. We will be interested in the overlaps of these state with the trial states presented in Chapter

3. However, we know these states only in a first-quantized notation. Of course it would be a straightforward task to also write down the Fock states in a first-quantized notation, but for calculating then the overlap we would need to evaluate an integral over all coordinates, i.e. in a $2N$-dimensional space. It is clear that this task becomes very difficult and costly as $N$ increases.

We therefore choose the opposite way, in which we first express the trial states in the Fock basis. Once this has been achieved, the overlap is simply the scalar product of two vectors. Here, the difficulty is the decomposition of the first-quantized states. For the particle numbers we are able to reach with our numerical diagonalization, this job is done by a Mathematica code which we developped for this goal, and which we have published in Ref. [81]. Due to its technical nature, we provide this material in the appendix of this thesis.

## 4.3 Results: From condensates to strongly correlated phases

We now present the results which have been published in Refs. [33, 34]. We will encounter different regimes, from condensed phases in relatively weak gauge fields up to the strongly correlated Laughlin state close to the instability at $\eta \to 1$. To get a "clean" overview, we first analyze the adiabatic case, where the perturbation $H_{21}H_{12}/(\hbar\Omega_0)$ is not included.

### 4.3.1 Adiabatic case: $\Omega_0 \to \infty$

The adiabatic case of an infinitely large Rabi frequency is formally equivalent to a rotating Bose gas. Its behavior, including the formation of vortices and their melting into highly correlated states, has extensively been studied (cf. Ref. [29] for a review). Accordingly, the findings of this section agree fully with previous results on rotating Bose gases, notably the ones published in Refs. [79, 82, 83]. The main goal of the present section is to prepare the presentation of results for the non-adiabatic regime in Section 4.3.2.

To classify the different ground states (GSs), we have evaluated several quantities: 1) their interaction energy $E_{\mathrm{int}}$, 2) their angular momentum $L$, 3) their entropy

$S$. The latter quantity is defined as

$$S = -\mathrm{Tr}\left[\rho^{(1)} \ln \rho^{(1)}\right], \tag{4.14}$$

with $\rho^{(1)}$ the one-body density matrix associated to the GS wave function. It is given by

$$\rho^{(1)}(\boldsymbol{r}, \boldsymbol{r'}) = \langle \mathrm{GS}|\hat{\Psi}^\dagger(\boldsymbol{r})\hat{\Psi}(\boldsymbol{r'})|\mathrm{GS}\rangle \tag{4.15}$$

where $\hat{\Psi}(\boldsymbol{r})$ is the field operator, $\hat{\Psi}(\boldsymbol{r}) = \sum_\ell \phi_{0,\ell}^{\mathrm{FD}} \hat{\mathrm{c}}_\ell$. With the density matrix we are also able to define the natural orbitals, $\phi_i(\boldsymbol{r})$, and their corresponding occupations, $n_i$, by the eigenvalue problem,

$$\int d\boldsymbol{r} \rho^{(1)}(\boldsymbol{r}, \boldsymbol{r'})\phi_i(\boldsymbol{r}) = n_i \phi_i(\boldsymbol{r'}). \tag{4.16}$$

Then the entropy can be directly evaluated as $S = -\sum_i n_i \ln n_i$. It is a measure of the amount of correlations in the system and provides information of the entanglement between one particle and the rest of the system.

The results for $N = 4$ are shown in Fig. 4.1 within the range $0.7 \leq \eta < 1$. Lower values of $\eta$ would lie beyond our lowest Landau level approximation. Four clearly distinct regions are detected, characterized by constant values of $E_{\mathrm{int}}$, $L$, and $S$. Sharp jumps between these plateaus mark the boundary of each region. As plotted in Fig. 4.2, the energy gap closes at these boundaries, which thus can be understood as level crossings. As expected, interaction energy and angular momentum are found to behave complementary. While the latter increases with $\eta$, interaction energy gets reduced. At the same time, the number of correlations, measured by $S$, increases. As the lower panel of Fig. 4.1 shows, this allows to reach the strongly correlated states discussed in Chapter 3.

In the following, we summarize our observations in order to classify each of the four regions:

- The first region corresponds to a fully condensed system with zero angular momentum and vanishing one-body entanglement entropy, see Fig. 4.1. Accordingly, the ground state is given by the wave function $\Phi_0 = \mathcal{N}_{\mathrm{c}} e^{-\sum_i z_i^2/2}$, with $\mathcal{N}_{\mathrm{c}}$ a normalization constant.

- At the critical value $\eta_1 = 1 - gN/(8\pi) \approx 0.76$, $(gN = 6)$, a degeneracy between states with $L = 0$, 2, 3, and 4 occurs, see Fig. 4.2. A state with broken symmetry, combination of several $L$-eigenstates, is precursor of the

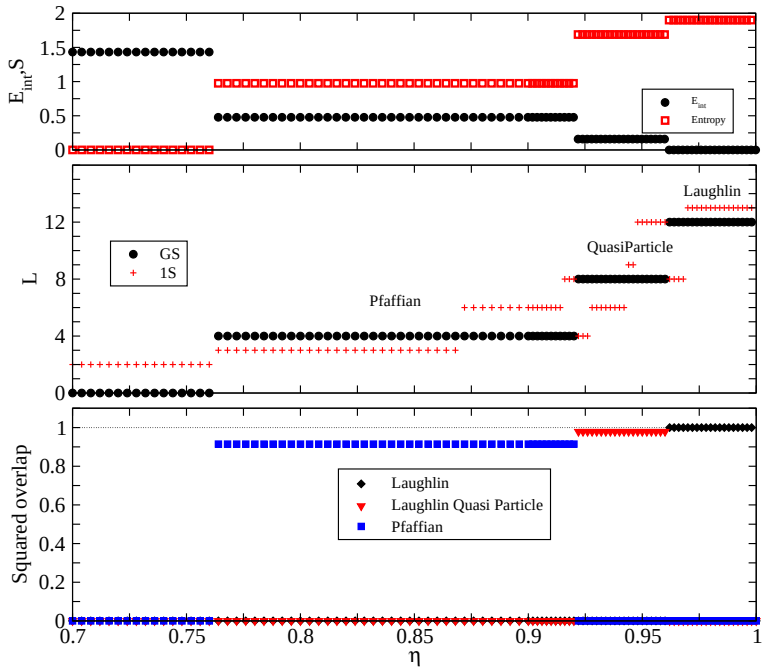


FIGURE 4.1: (upper panel) Interaction energy in units of $\hbar\omega_\perp$ (black circles) and one-body entanglement entropy (red squares) of the ground state as a function of $\eta$. (middle panel) Angular momentum in units of $\hbar$ of the ground state and of the first excited state as a function of $\eta$. (lower panel) Squared overlap between the ground state of the system and the exact Laughlin, Pfaffian and Laughlin-quasiparticle states. The plots corresponds to the adiabatic case $\Omega_0 \to \infty$. From: [33].

nucleation of the first vortex state [84]. Increasing $\eta$ the ground state recovers the cylindrical symmetry and the GS angular momentum is uniquely $L = 4$. All this phenomenology can be inferred from the Yrast line displayed in Fig. 4.3. The Yrast line is constructed by plotting the interaction energy contribution of the lowest energy state for each $L$. From this line, the addition of the kinetic energy, which reads (up to a term independent of $L$ and $\eta$) $E_{\rm kin} = (1-\eta)L\hbar\omega_\perp$, produces the total energy with its minimum at the angular momentum of the ground state, $L_{GS}$. This is exemplified for $\eta = 0.85$ and 0.94 in Fig. 4.3.

The ground state with $L = N$ is known to be exactly given by [85, 86]

$$\Psi_{L=N} = \mathcal{N}_{L=N} \prod_{i=1}^{N} (z_i - Z) e^{-\sum_i z_i^2/2} \tag{4.17}$$

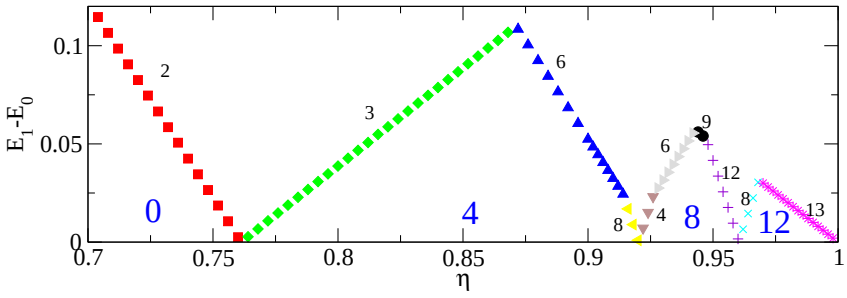


FIGURE 4.2: Energy difference, in units of $\hbar\omega_\perp$, between the ground state and its first excitation as a function of $\eta$. The large blue numbers correspond to the value of $L$ for the ground state. The small numbers quote the value of $L$ of the first excited state. $\Omega_0 \to \infty$. From: [33].

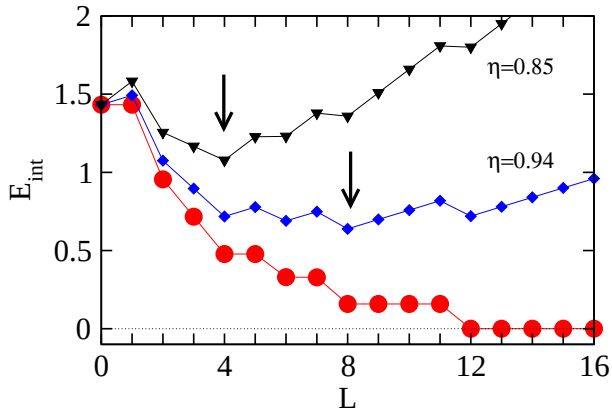


FIGURE 4.3: Yrast line for $N = 4$, solid red circles, which corresponds to the interaction energy contribution of the lowest eigenstates for each value of $L$. The triangles and diamonds depict the sum of the interaction energy and the kinetic contribution for $\eta = 0.85$ and $\eta = 0.94$, respectively. The arrows mark the value of $L$ which corresponds to the GS in each case. The energies are given in units of $\hbar\omega_\perp$. From: [33].

with $Z = (1/N)\sum_{i=1}^{N} z_i$. This wave function describes a state with one vortex in the center-of-mass. As the sizeable entanglement entropy indicates (see Fig. 4.1), this state is not fully condensed. We shall note, however, that in the limit $N \to \infty$, the center-of-mass is pinned to the origin [29], and the state becomes fully condensed (cf. Fig. 4 of Ref. [87]).

Assuming a single vortex in the center of our finite system, turns out to poorly represent the true GS. The squared overlap between the one-vortex

state, given by

$$\Psi_{1\mathrm{vx}} = \mathcal{N}_{1\mathrm{vx}} \prod_{i=1}^{N} z_i e^{-\sum_i z_i^2/2}, \tag{4.18}$$

and the GS, Eq. (4.17), is analytically found to be $15/32 \approx 0.47$ for $N = 4$.

A much higher squared overlap of $32/35 \approx 0.91$ is found between the exact ground state and the Moore-Read state, which has $L = N$ in the case of $N = 4$. We note that, except for $N = 4$, the Moore-Read state has $L > N$. It then defines a distinct plateau in the evolution of the system with $\eta$ [82, 83].

We find three different kinds of excitations, $L = 3$, 6 and 8, as can be seen in Fig. 4.2. The latter is found to have a large overlap with the Laughlin-quasiparticle state.

- For $0.92 \leq \eta \leq 0.96$, the ground state has $L = 8$, a higher entanglement entropy, and a smaller interaction energy. The ground state has a large overlap with the Laughlin-quasiparticle state, as shown in Fig. 4.1. This quasiparticle region has four different excitations, $L = 4, 6, 9$ and 12. The $L = 9$ corresponds to a center of mass excitation of the system as dictated by Kohn's theorem [88, 89].

- Finally, for $\eta \gtrsim 0.96$, the ground state wave function is the Laughlin wave function, with zero interaction energy. Its excitations are the Laughlin-quasiparticle ($L = 8$), and a center of mass excitation ($L = 13$). Its analytical form is $\Psi = \mathcal{N}(z_1 + z_2 + z_3 + z_4)\Psi_{\mathcal{L}}$. In this region, $2N - 1$ single-particle states are approximately equally populated, and the entropy is $S \approx \ln(2N - 1)$.

### 4.3.2 Non-adiabatic case: finite $\Omega_0$.

We repeat the analysis from the previous section, but now we take into account a finite Rabi frequency $\Omega_0$ within the realistic range from $10E_{\mathrm{R}}$ to $100E_{\mathrm{R}}$.

#### 4.3.2.1 Properties of the system

Interaction energy, angular momentum, and entropy are analyzed as a function of $\eta$ and $\hbar\Omega_0/E_{\mathrm{R}}$ in Fig. 4.4. We note that angular momentum is now only given

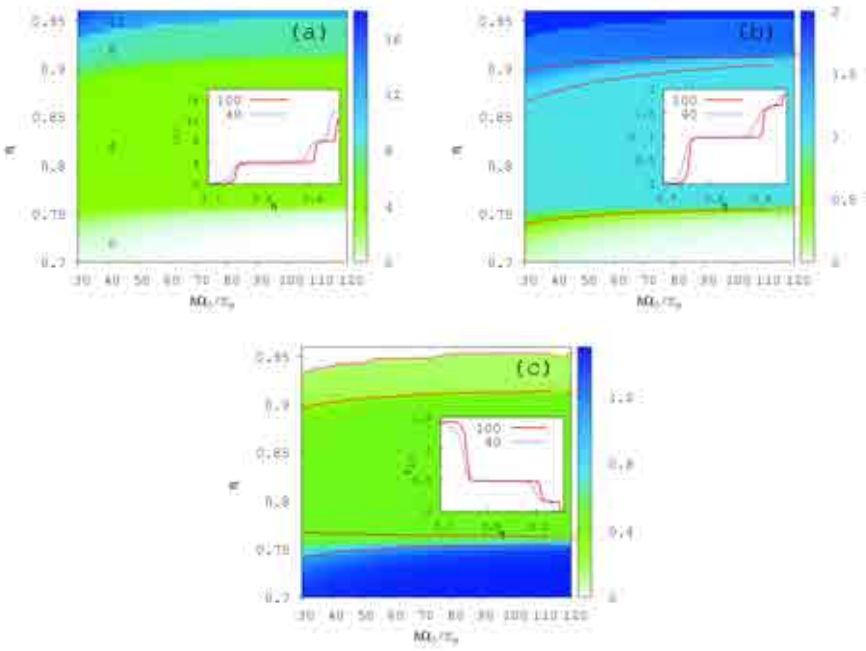


FIGURE 4.4: *(a):* GS average of the total angular momentum, in units of $\hbar$, for $N = 4$, as a function of $\eta$ and $\hbar\Omega_0/E_R$. The insets concentrate on two different values of $\hbar\Omega_0/E_R = 40$, and 100, respectively. *(b):* Entropy. *(c):* Interaction energy. From: [34].

as an expected value, and not anymore as a quantum number of the states. For large $\Omega_0$ we recover the step-like structure from the adiabatic case. Decreasing the values of $\Omega_0$, the transitions between the plateaus become broader and are displaced towards smaller values of $\eta$. However, the characteristic values on each plateau are not modified by the finite Rabi frequency. An exception hereof is the expected value of the total angular momentum in the strongly correlated regime: The Laughlin plateau with $L = N(N-1)$ is replaced by a region which is characterized by $\langle \mathrm{GS}|\hat{L}|\mathrm{GS}\rangle \geq N(N-1)$. Apart from this increased angular momentum, the strongly correlated region ($\eta \gtrsim 0.93$) still shows the Laughlin-like behavior: The entropy again reaches the value $\ln(2N-1)$, and also the average interaction energy vanishes.

Other observable quantities which we can use to characterize the state are the density and the pair-correlation function. The density can be obtained from Eq. (4.15) by choosing $\boldsymbol{r} = \boldsymbol{r}'$. It is depicted in panels (a,b) of Fig. 4.5. The pair-correlation function $g(\boldsymbol{r}, \boldsymbol{r}_0)$, defined in Eq. (3.18), is plotted in the panels (c,d)

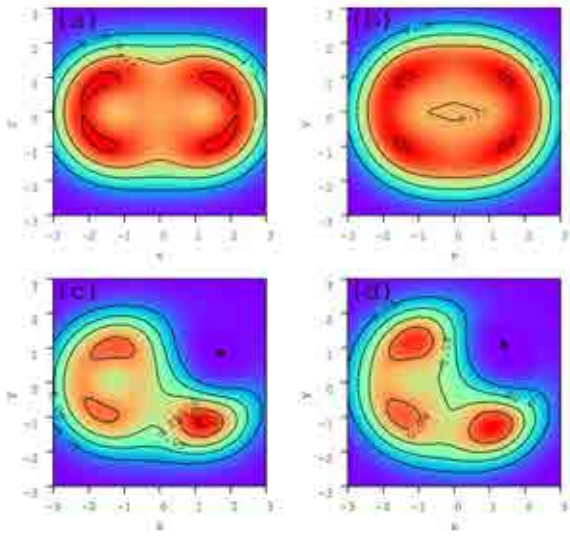

FIGURE 4.5: Density of atoms, panels (a) and (b), and pair correlation, panels (c) and (d), of the ground state for $\hbar\Omega_0/E_{\mathrm{R}} = 40$ (a,c) and 100 (b,d), respectively. The values of $\eta$ are 0.942 and 0.955 for $\hbar\Omega_0/E_{\mathrm{R}} = 40$ and 100, respectively. The solid circle marks the position of $\boldsymbol{r}_0$. From: [34].

of Fig. 4.5. We have fixed $\boldsymbol{r}_0$ at the position with the highest density. Contrarily to the Laughlin state, for finite $\hbar\Omega_0/E_{\mathrm{R}}$ the atomic cloud is anisotropic as a consequence of broken rotational symmetry of the Hamiltonian. Nevertheless, the pair-correlation functions still share an important common feature. Detecting one particle in $\boldsymbol{r}_0$, the other three particles appear localized at the remaining three vertices of a rectangle. This shows that particles tend to maximally avoid each other, in the same way as they do in the exact Laughlin wave function. This is possible, as the perturbation increases the angular momentum. On the other hand, for ground states with $L < N(N-1)$, it would be impossible to have correlations like this.

#### 4.3.2.2 Generalized wave functions

In view of the observable properties shown above, the highly correlated regime for finite $\Omega_0$ resembles a Laughlin state with deformed density and increased angular momentum. It is obvious that these deformations will reduce the overlap between the GS and the Laughlin wave function, as $\Omega_0$ increases.

Therefore we propose a new trial wave function, which is based on the Laughlin wave function, but without being restricted to a subspace with fixed angular momentum. Instead we include terms with $L = N(N-1)+2$ which are obtained by multiplying the Laughlin wave function with additional Jastrow factors. This form guarantees that the test states have zero interaction energy. Our ansatz for this "generalized Laughlin state" (GL) reads

$$\Psi_{\mathcal{GL}} = \alpha\Psi_{\mathcal{L}} + \beta\Psi_{\mathcal{L}1} + \gamma\Psi_{\mathcal{L}2}. \tag{4.19}$$

with $\Psi_{\mathcal{L}1} = \mathcal{N}_1\,\Psi_{\mathcal{L}} \cdot \sum_{i=1}^{N} z_i^2$, $\Psi_{\mathcal{L}2} = \mathcal{N}_2\left(\tilde{\Psi}_{\mathcal{L}2} - \langle\Psi_{\mathcal{L}1}|\tilde{\Psi}_{\mathcal{L}2}\rangle\Psi_{\mathcal{L}1}\right)$, and $\tilde{\Psi}_{\mathcal{L}2} = \tilde{\mathcal{N}}_2\,\Psi_{\mathcal{L}} \cdot \sum_{i<j}^{N} z_i z_j$, such that we ensure $\langle\Psi_{\mathcal{L}}|\Psi_{\mathcal{L}i}\rangle = 0$ and $\langle\Psi_{\mathcal{L}i}|\Psi_{\mathcal{L}j}\rangle = \delta_{ij}$.

The values of $\alpha$, $\beta$ and $\gamma$ are computed as $\alpha = \langle\Psi_{\mathcal{L}}|\mathrm{GS}\rangle/\sqrt{\mathcal{N}}$, $\beta = \langle\Psi_{\mathcal{L}1}|\mathrm{GS}\rangle/\sqrt{\mathcal{N}}$, and $\gamma = \langle\Psi_{\mathcal{L}2}|\mathrm{GS}\rangle/\sqrt{\mathcal{N}}$, with

$$\mathcal{N} = |\langle\Psi_{\mathcal{L}}|\mathrm{GS}\rangle|^2 + |\langle\Psi_{\mathcal{L}1}|\mathrm{GS}\rangle|^2 + |\langle\Psi_{\mathcal{L}2}|\mathrm{GS}\rangle|^2.$$

This definition maximizes the overlap between the numerical GS and the expression from Eq. (4.19).

Quasihole excitations to such a ground state are obtained by multiplying with a wave function zero at the quasihole position $\xi$,

$$\Psi_{\mathcal{GL}\mathrm{qh}} = \prod_{i=1}^{N}(z_i - \xi)\Psi_{\mathcal{GL}}, \tag{4.20}$$

or with two zeros for two excitations

$$\Psi_{\mathcal{GL}2\mathrm{qh}} = \prod_{i=1}^{N}(z_i - \xi_1)\prod_{j=1}^{N}(z_j - \xi_2)\Psi_{\mathcal{GL}}. \tag{4.21}$$

Similarly, we also define a generalized Pfaffian (GPf) state as

$$\Psi_{\mathcal{GP}} = \alpha\Psi_{\mathcal{P}} + \beta\Psi_{\mathcal{P}1} + \gamma\Psi_{\mathcal{P}2}\,, \tag{4.22}$$

with $\Psi_{\mathcal{P}1} = \mathcal{N}_{\mathcal{P}1}\,\Psi_{\mathcal{P}} \cdot \sum_{i=1}^{N} z_i^2$, $\Psi_{\mathcal{P}2} = \mathcal{N}_{\mathcal{P}2}\left(\tilde{\Psi}_{\mathcal{P}2} - \langle\Psi_{\mathcal{P}1}|\tilde{\Psi}_{\mathcal{P}2}\rangle\Psi_{\mathcal{P}1}\right)$, and $\tilde{\Psi}_{\mathcal{P}2} = \tilde{\mathcal{N}}_{\mathcal{P}2}\,\Psi_{\mathcal{P}} \cdot \sum_{i<j}^{N} z_i z_j$. Again, the parameters $\alpha$, $\beta$, and $\gamma$ are fixed to maximize the overlap of the numerical ground state with $\Psi_{\mathcal{GP}}$.

Also for the Laughlin-quasiparticle state we define a generalized version (GLQP), built up from the same Jastrow factors used in Eq. (4.19), i.e.

$$\Psi_{\mathcal{GL}_{\mathrm{qp}}} = \alpha\Psi_{\mathcal{L}_{\mathrm{qp}}} + \beta\Psi_{\mathcal{L}_{\mathrm{qp1}}} + \gamma\Psi_{\mathcal{L}_{\mathrm{qp2}}}\,, \tag{4.23}$$

with

$$\begin{aligned}
\Psi_{\mathcal{L}_{\mathrm{qp1}}} &= \mathcal{N}_{\mathcal{L}_{\mathrm{qp1}}}\,\Psi_{\mathcal{L}_{\mathrm{qp}}} \cdot \sum_{i=1}^{N} z_i^2,\\
\Psi_{\mathcal{L}_{\mathrm{qp2}}} &= \mathcal{N}_{\mathcal{L}_{\mathrm{qp2}}}\left(\tilde{\Psi}_{\mathcal{L}_{\mathrm{qp2}}} - \langle\Psi_{\mathcal{L}_{\mathrm{qp1}}}|\tilde{\Psi}_{\mathcal{L}_{\mathrm{qp2}}}\rangle\Psi_{\mathcal{L}_{\mathrm{qp1}}}\right),\\
\tilde{\Psi}_{\mathcal{L}_{\mathrm{qp2}}} &= \tilde{\mathcal{N}}_{\mathcal{L}_{\mathrm{qp2}}}\,\Psi_{\mathcal{L}_{\mathrm{qp}}} \cdot \sum_{i<j}^{N} z_i z_j.
\end{aligned}$$

#### 4.3.2.3 Overlaps

In Fig. 4.6 we show the squared overlap between the numerical ground state and the three original correlated states (left panel) and their generalized versions (right panel) from Eqs. (4.19), (4.22), and (4.23). It turns out that in all three cases the state which is proportional to $\gamma$ is much less populated than the states proportional to $\alpha$ and $\beta$. We can thus safely neglect the contribution of this term. As shown in Fig. 4.6, overviewing all three regimes, the largest improvement by using the generalized versions occurs in the Laughlin region. Here, the total angular momentum increases continously with $\eta$, leading to substantial occupation of the state proportional to $\beta$.

Detailed information about the effect of the perturbation is shown in Figs. 4.7, 4.8, and 4.9 for each of the three regions separately. First, in Fig. 4.7 we consider the overlap with the Pfaffian (Pf) and GPf, exploring fairly low values of $\hbar\Omega_0/E_{\mathrm{R}}$. Lower values of $\hbar\Omega_0/E_{\mathrm{R}}$ would require the consideration of higher order terms in the expansion of $H_{\mathrm{sp}}$, Eq. (4.4).

As one could have expected from the observables shown before, by decreasing the value of $\hbar\Omega_0$, the maximum overlap is shifted towards smaller $\eta$: In the symmetric case, the region of sizable squared overlap between the Pfaffian state and the exact ground state was $0.75 \lesssim \eta \lesssim 0.92$, for $\hbar\Omega_0/E_{\mathrm{R}} = 20$ it is displaced to $0.73 \lesssim \eta \lesssim 0.89$. At the same time, the squared overlap with the Pfaffian is reduced, from around 0.9 in the symmetric case, to 0.7 for $\hbar\Omega_0/E_{\mathrm{R}} = 10$.

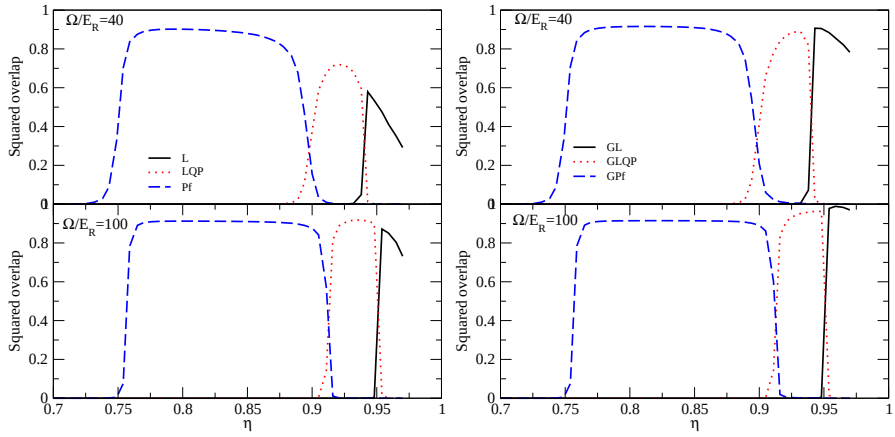


FIGURE 4.6: (left panel) Squared overlap between the ground state and the original strongly correlated states considered, namely, the Pfaffian, Laughlin and Laughlin-quasiparticle states as a function of $\eta$ for $\hbar\Omega_0/E_{\rm R} = 40$ and 100. (right panel) Squared overlap between the GS and the generalized correlated states considered, GPf, GL and GLQP as a function of $\eta$ for $\hbar\Omega_0/E_{\rm R} = 40$ and 100. From: [33]

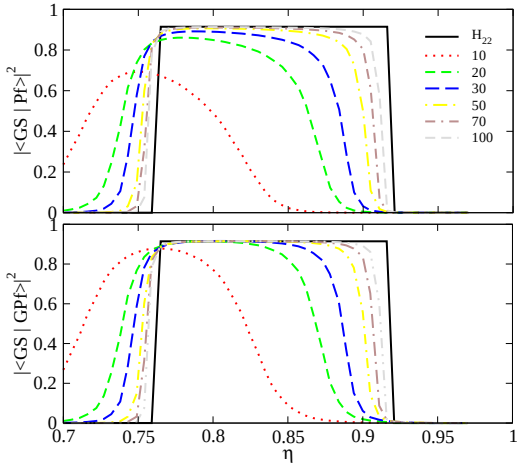


FIGURE 4.7: Squared overlap between the ground state and the Pfaffian and generalized Pfaffian states defined in the text, upper and lower panels, respectively, as a function of $\eta$. The different lines correspond to different values of $\hbar\Omega_0/E_{\rm R}$. The solid line is obtained in the adiabatic case, i.e. $H^{\rm eff} = H_{22}$. From [33].

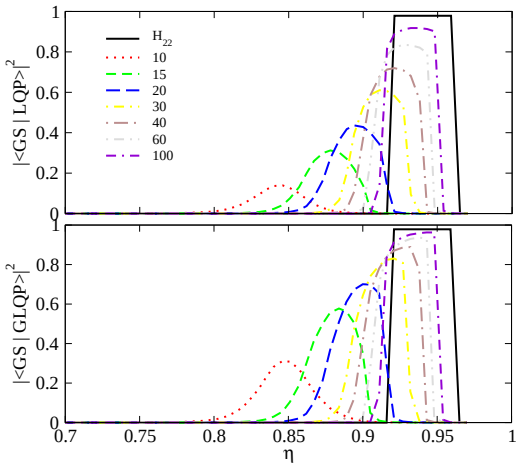


FIGURE 4.8: Squared overlap between the exact ground state and the Laughlin-quasiparticle (LQP) and generalized Laughlin-quasiparticle (GLQP) states defined in the text, upper and lower panels, respectively, as a function of $\eta$. The different lines correspond to different values of $\hbar\Omega_0/E_{\rm R}$. The solid line is obtained in the adiabatic case. From [33].

The overlap increases by using the generalized wave function GPf as trial wave functions. This shows that a main effect of the perturbation is to populate states with additional Jastrow factors. Strikingly, we find large values of the squared overlap with the GPf state ($> 0.8$) even for relatively strong perturbations $\hbar\Omega_0/E_{\rm R} \approx 20$. This could be relevant from an experimental point of view as it increases the window of observability.

A similar behavior is found when studying the squared overlap of the Laughlin-quasiparticle (LQP) state with the exact ground state of the system. As shown in Fig. 4.8, the region of sizeable overlap with the Laughlin-quasiparticle state gets shifted towards lower values of $\eta$ as we decrease $\Omega_0$. As before in the Pf regime, the generalized wave function (GLQP) turns out to be a better trial state than the normal LQP state. Using the GLQP wave function, large values of the squared overla ($> 0.8$) can be found for values of $\hbar\Omega_0/E_{\rm R} > 30$.

In Fig. 4.9 we finally present the overlaps with the Laughlin state and the generalized Laughlin state. Again, we note the shift towards lower values of $\eta$ as we decrease the value of $\hbar\Omega_0/E_{\rm R}$. Squared overlaps larger than 0.8 are only obtained only for $\hbar\Omega_0/E_{\rm R} > 40$, using the generalized expression.

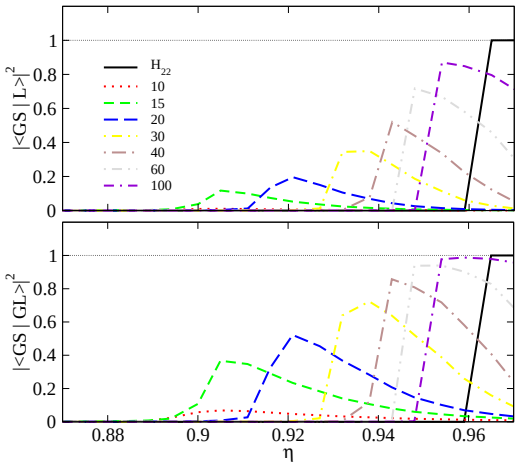


FIGURE 4.9: Squared overlap between the exact ground state and the Laughlin (L) and generalized Laughlin (GL) states defined in the text, upper and lower panels, respectively, as a function of $\eta$. The different lines correspond to different values of $\hbar\Omega_0/E_\mathrm{R}$. The solid line is obtained in the adiabatic case. From: [33].

### 4.3.3 Experimental feasibility

As we have shown in the previous subsection, within the experimentally realistic range of $10 \leq \hbar\Omega_0/E_\mathrm{R} \leq 100$, the discussed proposal is in principal able to bring cold atoms into a Laughlin-like ground state. Whether a cooling into this state can successfully be achieved, however, will strongly depend on its energy gap, which must be large enough to protect the state.

It is hereby important to distinguish between the bulk gap and possibly gapless edge excitation. As shown in Fig. 4.3, the system can increase its angular momentum without changing its interaction energy. In the limit $\eta \to 1$, this yields zero-energy excitation. Such excitations, however, can be ignored, as they will modify the system only at the edge. For an estimate of the bulk gap, we should extend the linear left branch in the Laughlin region in Fig. 4.2 up to $\eta = 1$. The energy which we thereby find coincides with the energy difference between the Laughlin state and the first excitation with the same angular momentum. This shows that the bulk gap can be obtained by diagonalizing the interaction in a Hilbert space with fixed angular momentum, $L = N(N-1)$. We denote this quantity by $\Delta$.

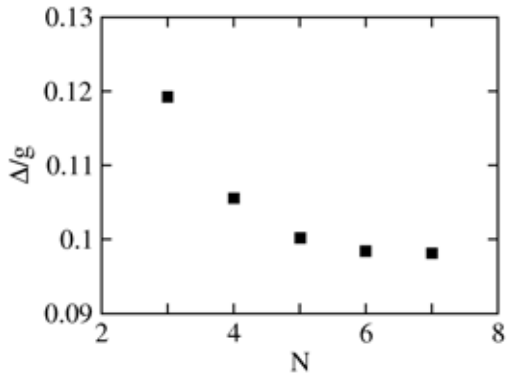


FIGURE 4.10: $\Delta/g$, in units of $\hbar\omega_\perp$, of the Laughlin state as a function of $N$ in the adiabatic case. From: [33]

In Fig. 4.10(a) we show the evolution of $\Delta/g$ with $N$ for a constant value of $g$. Alternatively, we could have set $gN =$ constant, which yields exactly the same figure, as a consequence of the fact that $\Delta$ is proportional to $g$ and independent of $N$ for large values of $N$. This result is in agreement with the calculations reported in Ref. [78]. The tendency up to $N = 7$ is to asymptotically recover the value of 0.1 previously obtained by Regnault *et al.* [90] assuming a spherical geometry and later reproduced by Roncaglia *et al.* [91].

Keeping $gN$ constant when increasing $N$ has the advantage that also the mean-field interaction energy per particle remains constant. This guarantees the validity of the LLL approximation [78]. However, it also results in a vanishing gap, $\Delta \sim 1/N$ in the thermodynamic limit.

Apart from interactions, also the degeneracy lifting of the LLs for $\eta < 1$ can give rise to LL mixing. In the Laughlin state at filling $\nu = 1/2$, the highest occupied single-particle angular momentum is $\ell = 2(N-1)$, and thus has a kinetic energy of $2\hbar\omega_\perp(N-1)(1-\eta)$. This energy has to be compared to the LL gap which is $2\eta\hbar\omega_\perp$, and thus independent from $N$. Increasing $N$ thus requires to approach the instability limit $\eta \to 1$, in order to keep the LLL approximation valid. As our study in the previous section has shown, in this limit the effect of non-adiabatic transitions tends to increase the angular momentum, making the ground state strongly deviate from the Laughlin state.

These considerations suggest that the particle number has to be kept low, if one wishes to realize the Laughlin state following the studied proposal. Oppositely, we might try to waive the LLL approximation. Of course, for being in the Laughlin

state the system has to be in the LLL, but the question is whether this is really a restriction on $g$. Certainly, with strong interaction particles could easily scatter into higher LLs, and very different, new states would have to be expected in the spectrum. On the other hand, due to a peculiarity of contact interactions, the ground state at $L = N(N-1)$ should not be affected. In the contact potential, the Laughlin state already has zero interaction energy, so it is impossible to reduce the energy by occupying higher LLs. In fact, apart from the additional kinetic energy, explicit calculations in the first and second excited LL have shown that, oppositely, the interaction energy even increases in higher LLs. This means that by increasing $g$ via Feshbach resonances, we could be able to reach a situation where the energy of the lowest excitation is given by the LL gap, i.e. $\Delta \approx 2\eta\hbar\omega_\perp$.

An even stronger reason for increasing $g$ is the instability at $\eta = 1$, which must be approached when we wish to realize the Laughlin state for large $N$ at a fixed $g$. The critical value for $\eta$ arises from a competition between the kinetic energy proportional to $1 - \eta$, and the interaction energy proportional to $g$. This means that larger $g$ would favor the Laughlin state already at smaller $\eta$, and thus further away from the trapping instability. The fact that, in principle, smaller $\eta$ would more easily cause a LL mixing due to the stronger degeneracy lifting, does not play a role here for the reasons mentioned before.

It therefore seems to be interesting to study this approach in a more quantitative analysis, taking into account at least two LLs from the beginning. Especially, from our general arguments it is not clear what happens before reaching the Laughlin regime, i.e. for strongly correlated states at smaller $L$, e.g. in the Pfaffian region. Since in this regime ground states have finite interaction energy even in the LLL, they might be strongly affected by scattering into higher LLs. This also poses the question whether and how it can be achieved to cool down the system from these states into the Laughlin state.

# Chapter 5

# Testing the system with quasiholes

In the previous chapter, we have studied the ground states of a two-dimensional Bose gas exposed to an artificial gauge field. Especially, we have seen that, for a fixed contact interaction strength, the parameter $\eta$ allows to tune the system from condensed states at $L = 0$ or $L = N$ through different strongly correlated states into the regime, where a Laughlin-like state is the ground state of the system. In this chapter we will study excitations above these ground states. Hereby, we will focus on quasihole excitations. They can be achieved in a controlled way by shining a laser beam onto the atomic cloud. Theoretically, this is described by adding the following potential to the single-particle Hamiltonian of Eq. (4.6) [92]:

$$V_L(\xi) \propto I \sum_i \delta(\xi - z_i), \tag{5.1}$$

where $I$ is the laser intensity, and $\xi$ is the position onto which the beam is focused. As such a potential energetically penalizes particles being at position $\xi$, it will, for sufficiently strong $I$, transfer states described by some wave function $\Psi$ into states described by $\prod_i (z_i - \xi)\Psi$, resulting in a hole at position $\xi$. States with more than one quasihole can be achieved by several such potentials. Below, we will explicitly test this mechanism by an exact diagonalization study.

Once the system is brought into a quasihole state, we can move the quasiholes by adiabatically moving the laser focus $\xi$. If we then measure the phase shift due

to this displacement, e.g. via a Ramsey-type interference measurement [92], we can extract the effective "charge" of the quasiholes, and their quantum-statistical behavior. For quasiholes in the Laughlin state, the fractional charge and anyonic quantum statistics are intriguing features [25]. They are well known for thermodynamically large systems where they can be derived from Laughlin's plasma analogy [62]. In Section 5.1, we directly analyze the wave function for a small cloud of atoms ($N \lesssim 6$) in the Laughlin state with one or two quasiholes. Thereby we are able to show that this system size is sufficient for observing excitations with a robust anyonic character. Moreover we show that also generalized Laughlin states as discussed in the previous chapter support this kind of exotic excitations.

In Section 5.2, we study the dynamics of a quasihole after abruptly switching off the potential from Eq. (5.1). Here we compare the behavior in the Laughlin regime with the one in denser regimes where the ground states possess lower angular momentum $L_{\mathrm{GS}}$. In general, a quasihole state is a coherent superposition of states with angular momentum $L_{\mathrm{GS}} \leq L \leq L_{\mathrm{GS}} + N$. While in the Laughlin regime the coherence between these different contributions is found to be preserved during the time evolution, it is lost in other regimes. This "collapse" is clearly visible in the density as a smearing out of the quasihole. It is followed by periodic "revivals", where the coherence is restored and a quasihole forms again. We show that this dynamics describes the free evolution of a condensed system into a correlated state, followed by the reverse process.

This dynamics is reminiscent of the collapse and revival of a coherent light field which resonantly interacts with a two-level atom. This effect has been studied theoretically in the framework of the Jaynes-Cummings model since the early 1980s [93, 94], and has experimentally been observed in systems of Rydberg atoms [95–97], or trapped ions [98]. With the realization of a Bose-Einstein condensate (BEC) in 1995, also interacting many-body systems have become candidates for studying such collapse-and-revival effects: In Ref. [99] it has been argued that quantum fluctuations cause a phase diffusion which leads to a collapse of the macroscopic wave function. As a consequence of the discrete nature of the spectrum, periodic revivals of the macroscopic wave function have been predicted in Refs. [100, 101]. It has been proposed to produce macroscopic entangled states by time-evolving a condensed state [102, 103]. An interesting scenario has been discussed in Refs. [104, 105], studying collapse and revival of the relative phase between two spatially separate BECs. Measuring phase correlations between many BECs which are distributed on an optical lattice has allowed for observing the

collapse and revival of matter waves [106]. Recently, the observation of quantum state revivals has been proven to provide relevant information about the nature of multi-body interactions in a Bose condensed atomic cloud [107].

Also the collapse and revival which we discuss in Section 5.2 allow to extract useful information: The effect itself not only clearly distinguishes the Laughlin regime from denser ones. Measurement of revival times and positions also allows to determine kinetic and interaction contribution to the energy of the system.

## 5.1 Anyonic behavior of excitations

In the following, we will first study Laughlin quasiholes in the adiabatic regime, i.e. for $\Omega_0 \to \infty$. While the standard literature (e.g. Ref. [18, 62]) usually considers the thermodynamic limit, applying the plasma analogy, we will focus on small systems. We will see how the fractional behavior of the excitations becomes a robust property as particle number increases.

Afterwards we will also consider slightly non-adiabatic situations, where quasiholes are pierced into the generalized Laughlin state, as defined by Eq. (4.20). We compare the quasiholes in both the Laughlin and the generalized Laughlin state with respect to their fractional character.

### 5.1.1 Quasiholes in the adiabatic case

As already discussed in Chapter 4, for $\hbar\Omega_0 \gg E_R$, the GS squared overlap with the Laughlin state is effectively 1, above a critical value of $\eta$. Now we consider the system with the additional term (5.1) and find that there is also a region of $\eta$ where the overlap of the ground state of the system with the analytical quasihole state is effectively 1, see Fig. 5.1. This shows that the potential of Eq. (5.1) is able to produce quasiholes described by Eq. (3.8). Similarly, adding two such lasers we also find a region of $\eta$ where the overlap between the exact ground state and the analytical state with two holes, Eq. (3.10), approaches 1. However, we notice that the values of $\eta$ at which the overlap for one or two quasiholes reaches 1 differ from each other, and both are found for values larger $\eta$ than the onset of the Laughlin state, see Fig. 5.1. These features are essentially independent of the laser strength $I$, for sufficiently large $I$. On the other hand, since the Laughlin

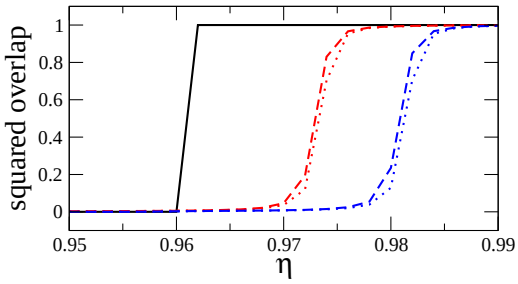


FIGURE 5.1: Squared overlap between the exact ground state of the system where none (solid, black), one (red) or two (blue) quasiholes have been pierced as described in the text and the corresponding analytical wave functions given in Eqs. (3.6), (3.8) and (3.10). The quasiholes are created by a laser with intensity $I = 10\frac{\hbar\omega_\perp}{\lambda_\perp^2}$ (dotted lines) and $I = 30\frac{\hbar\omega_\perp}{\lambda_\perp^2}$ (dashed lines), see Eq. (5.1).

state is protected against quasihole excitations by a bulk gap (cf. Section 4.3.3), a weak laser potential will not be able to induce any new states.

#### 5.1.1.1 Fractional charge

The most interesting property of these excitations is their fractionality, that is, fractional charge and statistics. To study the fractional charge of the quasiholes, we first note that in our electro-neutral system subjected to an artificial magnetic field, there exists the analog of an electric charge which can be defined via the behavior of a particle or quasiparticle moving within the gauge field. To this end, we consider the phase a quasihole picks up while being adiabatically displaced following a closed trajectory. The general expression for the Berry phase on a closed loop $C$ is given by [35]

$$\gamma_{\mathrm{C}} = i \oint_{\mathrm{C}} \langle \Psi(\boldsymbol{R}) | \nabla_{\boldsymbol{R}} | \Psi(\boldsymbol{R}) \rangle \cdot \mathrm{d}\boldsymbol{R}, \tag{5.2}$$

with $|\Psi(\boldsymbol{R})\rangle$ the state of the system, characterized by a parameter $\boldsymbol{R}$, which in our case is the position of the quasihole. For simplicity, we now assume that the quasihole is fixed at a radial position $|\xi| = R\lambda_\perp$, but is moved along a circle centered at the origin, see Fig. 5.2. Its position is then parametrized by the angle $\phi$. The movement on such a simple contour is sufficient to test the fractional behavior.

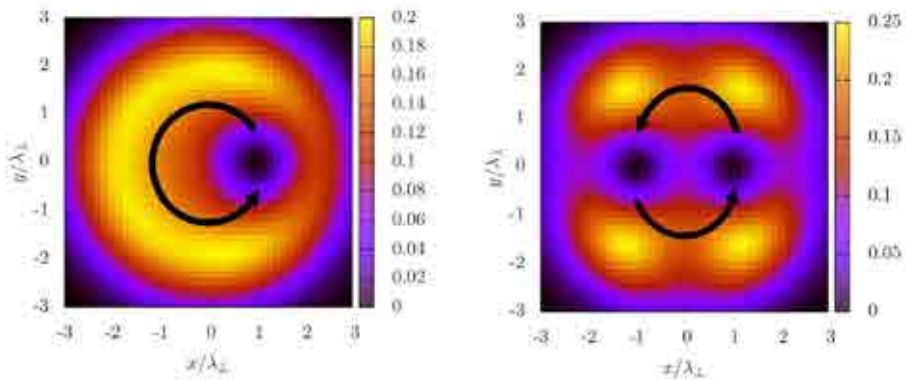


FIGURE 5.2: Moving one or two quasiholes at fixed radial positions on circles around the origin allows for determining the effective charge and the statistical phase angle. The quasiholes are always fixed at a radial position $R = 1$ (in units of $\lambda_\perp$).

For general contours, one can extract the acquired phases from the normalization factor of the quasihole state, as described in [62]. For our circularly symmetric contour, however, the situation is simpler, as we can re-write Eq. (5.2) as

$$\gamma_{\mathrm{C}} = i \int_0^{2\pi} \langle \Psi_{\mathcal{L}\mathrm{qh}}(\phi) | \partial_\phi | \Psi_{\mathcal{L}\mathrm{qh}}(\phi) \rangle \mathrm{d}\phi \equiv \int_0^{2\pi} f(R) \mathrm{d}\phi \,. \tag{5.3}$$

Here we note that, due to the circular symmetry of the Laughlin state, the integrand does not depend on the angular position of the quasihole. The function $f(R)$ can be calculated by decomposing the Laughlin quasihole state into the Fock-Darwin basis, which we have done analytically for particle numbers up to $N = 6$.

This decomposition, though being quite straightforward, for increasing $N$ and $L$ soon becomes very involved, as the polynomial wave function contains a lot of terms. We have developed a Mathematica code which achieves this decomposition. It is published in Ref. [81], and described in the appendix.

Since expressions become very large, we explicitly give here only the result for $N = 4$:

$$\gamma_{\mathrm{C}} = 2\pi f(R) = 2\pi \frac{4\left(10128R^2 + 5313R^4 + 1659R^6 + 553R^8\right)}{85572 + 40512R^2 + 10626R^4 + 2212R^6 + 553R^8} \,. \tag{5.4}$$

If we assume that the quasihole is moved sufficiently close to the center, i.e. $R \lesssim 1$, we can expand this expression in $R$ and find, $\gamma_C = 2\pi(0.473426R^2 + 0.0242202R^4 + \mathcal{O}(R^6)) \approx \pi R^2$. Thus, the acquired phase is approximately given by the enclosed area in units of $\lambda_\perp^2$.

To obtain the effective charge of the quasihole, we must compare this result with the geometric phase which a particle acquires due to the gauge field when it moves along the same contour. In the Laughlin regime, where $\eta \approx 1$, we find with Eq. (4.1) $B \approx 2\frac{\hbar}{\lambda_\perp^2}$, thus the acquired phase $\varphi$ is two times the enclosed area in units of $\lambda_\perp^2$, i.e. $\varphi = \frac{1}{\hbar}B_0(R\lambda_\perp)^2\pi \approx 2R^2\pi$. From this follows the effective charge of the quasihole to be $q_{\text{eff}} = \frac{\gamma_C}{\varphi} \sim 0.47$, close to the expected value for the Laughlin state, which at half filling should be $1/2$ in the thermodynamic limit [22, 25]. We have performed a similar study for $N = 5$ and $N = 6$, finding that for $N = 5$, the effective charge is about 0.48, and for $N = 6$ it is found to be 0.49, i.e. by increasing the particle number the value $1/2$ is approached.

#### 5.1.1.2 Fractional statistics

To prove the fractional statistics of the quasihole excitations we now consider the system with two quasiholes at $\xi_1 = |\xi_1|e^{i\phi_1}$ and $\xi_2 = |\xi_2|e^{i\phi_2}$, which we assume to sit on opposite radial positions, i.e. $|\xi_1| = |\xi_2| = R\lambda_\perp$ and $\phi_2 - \phi_1 = \pi$. We now consider the simultaneous adiabatic movement of the two quasiholes on two half circles, in such a way that, at the end, the quasiholes interchange position (see Fig. 5.2). This differs from a more common setup to test the statistical angle, where one quasihole is fixed in the center, while the other is encircling it. Our setup has the advantage that it allows for larger distance between the two quasiholes. Note that in Fig. 5.2, the radial position is chosen at $R = 1$, i.e. the distance between the center of the quasiholes is $2\lambda_\perp$, which seems to be the minimum distance needed for not having a significant overlap ($< 10\%$) between the two quasiholes, see Fig. 5.3 (a). On the other hand, in this small system of just four particles, larger radial positions lead to quasiholes overlapping with the system's edge.

The total phase picked up during the described movement should be the sum of the phase picked up by one quasihole moved along a circle plus a phase factor due to the interchange of the two quasiholes. Again the phase gradient turns out to be independent from the angular position, but is described by a different

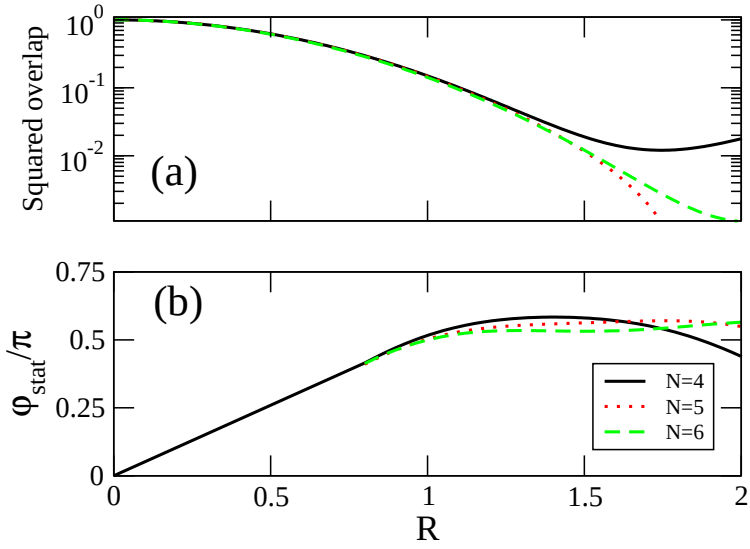


FIGURE 5.3: (a) Squared overlap between the quasihole wave functions, $|\langle\Psi_{\mathcal{L}\mathrm{qh}}(\xi_1)|\Psi_{\mathcal{L}\mathrm{qh}}(\xi_2)\rangle|^2$ at opposite angular positions, $\phi_1 - \phi_2 = \pi$, as a function of their distance to the center, $|\xi_1| = |\xi_2| = R\lambda_\perp$. (b) Statistical angle of two quasiholes at opposite angular positions and radial position $R\lambda_\perp$. In both panels we present results for $N = 4$ (black solid), $N = 5$ (red dotted), and $N = 6$ (green dashed).

function $\tilde{f}$ of the radial coordinate:

$$\tilde{f}(R) = \frac{8\left(2868120R^4 + 461616R^8 + 25242R^{12} + 553R^{16}\right)}{41660640 + 11472480R^4 + 923232R^8 + 33656R^{12} + 553R^{16}}\,. \tag{5.5}$$

The statistical phase angle is thus,

$$\varphi(R)_{\mathrm{stat}} \equiv \int_0^{2\pi} f(R)\mathrm{d}\phi - \int_0^{\pi} \tilde{f}(R)\mathrm{d}\phi = 2\pi f(R) - \pi\tilde{f}(R)\,. \tag{5.6}$$

It is shown, as a function of $R$, in Fig. 5.3 (b). As expected, the statistical phase is zero if both quasiholes are in the same position, and it increases linearly as the distance between the quasiholes is increased. This linear behavior then saturates once the overlap between the two quasiholes, $|\langle\Psi_{\mathcal{L}\mathrm{qh}}(\xi_1)|\Psi_{\mathcal{L}\mathrm{qh}}(\xi_2)\rangle|^2$, drops below 0.1, and remains mostly constant around $\pi/2$. At larger distances $R$, the system's edge starts to play a role, and the phase angle decreases again. By increasing the number of particles $N$, the plateau of constant phase angle $\pi/2$ becomes larger, thus a definite statistical phase angle of $\pi/2$ becomes a robust property of the quasiholes.

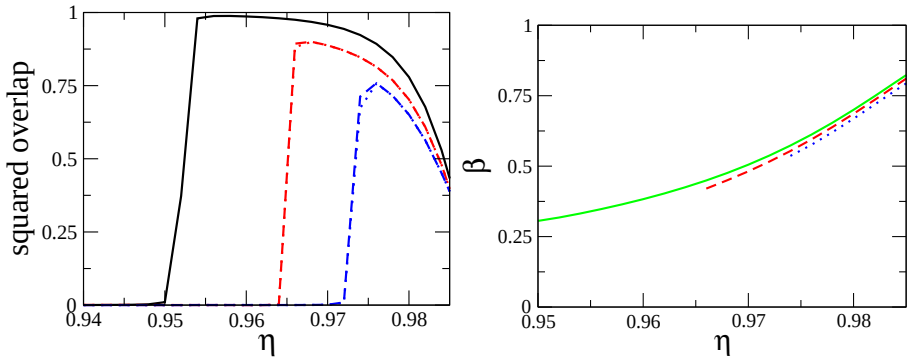


FIGURE 5.4: Left: Squared overlap of exact ground states ($N = 4$) with generalized Laughlin state (solid black), generalized Laughlin state with one quasihole (red), and generalized Laughlin state with two quasiholes (blue). The quasiholes are created by a laser with an intensity $I = 30\hbar\omega_\perp/\lambda_\perp^2$ (dotted lines) and $I = 50\hbar\omega_\perp/\lambda_\perp^2$ (dashed lines) at $\xi_1 = \lambda_\perp$ and $\xi_2 = -\lambda_\perp$. The Rabi frequency is $\hbar\Omega_0 = 100E_R$. Right: The values of the variational parameter $\beta$ for a given $\eta$ are similar for all three states.

### 5.1.2 Non-adiabatic effects on the properties of quasiholes

To study the fractionality of quasihole excitations in the non-adiabatic case we will again profit from the generalized analytical representations used to describe the ground state of the system. Following the discussion in the previous section we compute the squared overlap of the ground state obtained with no-, one-, and two-extra lasers piercing holes into the system. First, we find a significant squared overlap for the slightly perturbed case at $\hbar\Omega_0 = 100E_R$, see Fig. 5.4. As occurred in the adiabatic case, a large overlap with the analytical one- and two-quasihole states appears only at higher field strengths than the one at which the generalized Laughlin state is reached. Our study of the properties of quasiholes in the non-adiabatic case will be restricted to the parameter domain where a fair description of the states is provided by the generalized Laughlin state, see Chapter 4.

As before we test the behavior of the quasiholes by analyzing the wave function. Now we consider the generalized Laughlin wave function with one and two quasiholes, Eqs. (4.20) and (4.21). Note that, as a consequence of the anisotropy, the gradient of the state does not only depend on the radial, but also on the angular position of the quasiholes. Furthermore, there is a dependence on the parameter $\beta$, defined as a variational parameter in Eqs. (4.20) and (4.21). As shown in

Fig. 5.4, for given parameters $\eta$ and $\Omega_0$, the same value of $\beta$ optimizes simultaneously the ground state, the quasihole state, and the state with two quasiholes. This allows to interpret $\beta$ as a system parameter.

We define

$$f_\beta(R,\phi) \equiv \langle \Psi_{\mathcal{L}\mathrm{qh}}(\phi)|\partial_\phi|\Psi_{\mathcal{L}\mathrm{qh}}(\phi)\rangle\,. \tag{5.7}$$

This function $f_\beta$ is quite lengthy, so we expand it in $R$ and give only the lowest term ($\mathcal{O}(R^2)$):

$$f_\beta(R,\phi) \simeq \frac{8115904 + 2799526\beta^2 - 7102\sqrt{94958\,(1-\beta^2)}\beta\cos(2\phi)}{17142924 + 4477401\beta^2} R^2\,. \tag{5.8}$$

From the expression we see that for a fixed and small value of $R$, $f_\beta$ oscillates around $R^2/2$, such that the angular integration $\int_0^{2\pi} f_\beta(R,\phi)\mathrm{d}\phi$ again will yield a Berry phase close to the encircled area, thus half of the Berry phase accumulated by a normal particle.

Formally, we can capture this oscillating behavior by defining two effective charges $q_x$ and $q_y$, depending on the direction in which the quasihole moves. Up to linear order in the quasihole coordinates $X$ and $Y$, which is valid for small radial positions $R \lesssim 1$, the Berry connection is given by $(q_x Y, -q_y X)/\lambda_\perp^2$. The Berry phase defined in Eq. (5.2) reads:

$$\gamma_\mathrm{C} = \oint \frac{1}{\lambda_\perp^2}(q_x Y, -q_y X)\cdot \mathrm{d}\boldsymbol{R} = (q_x + q_y)\frac{A}{\lambda_\perp^2}, \tag{5.9}$$

where $A$ is the encircled area and Stokes' theorem has been applied. The effective charge, defined as $q_\mathrm{eff} = (q_x + q_y)/2$, and the gauge-dependent $q_x$ and $q_y$ are plotted as a function of $\beta$ in Fig. 5.5 for different $N$. In all cases the effective charges are close to $1/2$. For small values of $\beta$, which represent realistic states of the system, the value of the charges approaches $1/2$ as the number of atoms in the system is increased. In summary, the average charge $q_\mathrm{eff}$ has only a minor dependence on $\beta$, which decreases as $N$ increases. Though not realized in our system, we note that in the limit $\beta \to 1$, both charges $q_x$ and $q_y$ again coincide due to the recovered cylindrical symmetry of the state $\Psi_{\mathcal{L}1}$.

Finally, we introduce two quasiholes into the generalized Laughlin state. Following a procedure similar to the one for the adiabatic case presented in the previous section, we extract the statistical phase angle of the quasiholes. The result as a

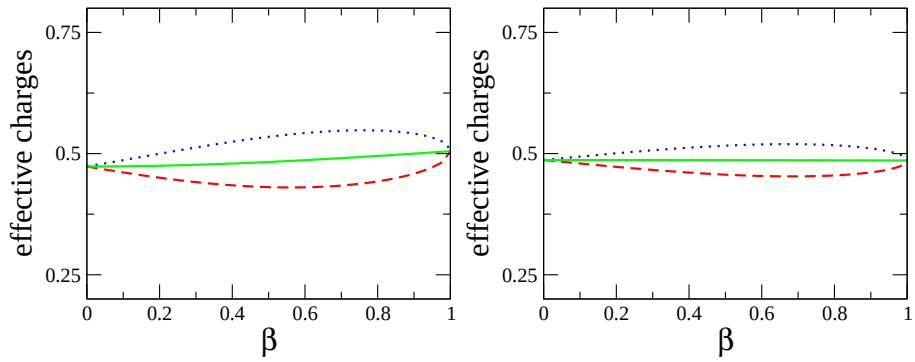


FIGURE 5.5: The effective charges $q_y$ (blue dotted) and $q_x$ (red dashed), and $q_{\text{eff}} = (q_x + q_y)/2$ (green solid) of quasiholes in the generalized Laughlin state as a function of the admixture $\beta$ of higher angular momentum to the Laughlin state, for $N = 4$ (left) and $N = 6$ (right).

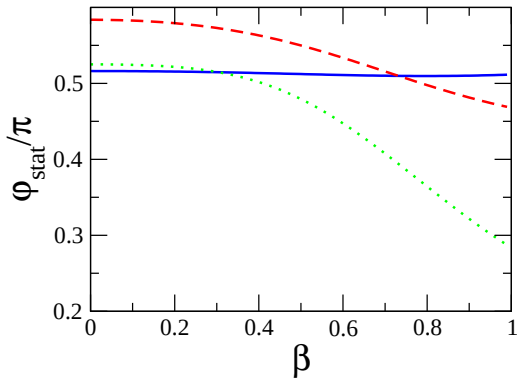


FIGURE 5.6: Statistical phase angle $\varphi_{\text{stat}}$ for two quasiholes in generalized Laughlin state as a function of the variational parameter $\beta$. The radial position of the quasiholes is at $\lambda_\perp$ (blue solid line), $1.4\lambda_\perp$ (red dashed line), and $1.8\lambda_\perp$ (green dotted line).

function of $\beta$ is shown in Fig. 5.6 for $N = 4$ and closed paths of different radii. While the quasiholes in the bulk, $R = 1$, remain with an almost constant phase angle $\varphi_{\text{stat}} \approx 0.51$, the phase angle of quasiholes closer at the edge of the system have a stronger dependence on $\beta$.

We conclude that the presence of a certain degree of non-adiabaticity ($\beta \lesssim 0.7$) does not spoil the anyonic character of quasihole excitations above the Laughlin state.

## 5.2 Dynamics of quasiholes

So far we have shown that sufficiently strong laser beams directed towards a bosonic cloud in the Laughlin state are able to create quasiholes according to Eq. (3.8) for a single quasihole, or according to Eq. (3.10) for two quasiholes. The position of the quasiholes is determined by the focus of the lasers. By adiabatically moving the lasers, the quasiholes can be moved, as they have to follow the laser. From the resulting Berry phases, we have extracted the effective charge and the quantum-statistical phase of these quasiholes.

In the present section, we will analyze the dynamics of quasiholes, if they are left on their own, i.e. if we suddenly switch off the laser which has created the holes. The subsequent time evolution of the system is then described by the time-independent Hamiltonian $H$ from Eq. (4.11). For simplicity, we now neglect the terms stemming from the non-adiabaticity of the atom-laser coupling. The dynamics of the quasihole can directly be observed in the density of the system. We will show that it yields relevant information about the ground state of the system.

We will start in Section 5.2.1 by considering a quasihole in the Laughlin state. It is the densest state with zero interaction energy in a two-body contact potential. This property reflects in the decoherence-free dynamics of a quasihole. This is in clear contrast to the case of a quasihole in ground states with $L < N(N-1)$, where an interaction-induced dephasing delocalizes the excitation. Focusing on a $L = 0$ condensate in Section 5.2.2, and on a Laughlin-type quasiparticle state in Section 5.2.3, we find a "collapse" of the quasihole which is followed by a "revival". From period and position of the revival, it will become possible to deduce information about kinetic and interaction energy in the system.

This section has been published in Ref. [108].

### 5.2.1 Quasiholes in the Laughlin state

Let us consider the situation with only one quasihole at position $\xi$. The state (3.8) can be written as

$$\Psi_{\mathrm{qh}}(\xi) = \mathcal{N}_{\mathrm{qh}} \sum_{k=0}^{N} \xi^{N-k} f_k \Psi_{\mathrm{L}}, \tag{5.10}$$

where the $f_k$ are totally symmetric polynomials of $k$th order in the coordinates $z_1, \ldots, z_N$, with the property that each of the coordinates appears at most to linear order. First of all, we note that since the Laughlin part $\Psi_\mathrm{L}$ vanishes, when two particles come together, so does every term in the sum of Eq. (5.10), i.e. its interaction energy vanishes, $V f_k \Psi_\mathrm{L} = 0$. Since every term has a well-defined total angular momentum $L_k \equiv L_\mathrm{Laughlin} + k$ (in units of $\hbar$), each term is also eigenstate of the kinetic part of the Hamiltonian, which we have chosen to be cylinder-symmetric. Recall that the single-particle energies, $E_k = \hbar\omega_\perp L_k(1-\eta)$, are proportional to the angular momentum. With this we have

$$H\xi^{N-k} f_k \Psi_\mathrm{L} = [\hbar\omega_\perp(1-\eta)k + \text{const.}]\, \xi^{N-k} f_k \Psi_\mathrm{L} \equiv (\epsilon k + \gamma)\xi^{N-k} f_k \Psi_\mathrm{L}. \quad (5.11)$$

From this, we directly obtain the time evolution of the quasihole state:

$$\Psi_\mathrm{qh}(\xi, t) \equiv \mathrm{e}^{iHt}\Psi_\mathrm{qh}(\xi) = \mathcal{N}_\mathrm{qh} \sum_{k=0}^{N} \xi^{N-k} f_k \Psi_\mathrm{L} \mathrm{e}^{i(\epsilon k+\gamma)t}. \quad (5.12)$$

By defining $\tilde{\xi}(t) \equiv \xi \mathrm{e}^{-i\epsilon t}$, we can re-write this as

$$\Psi_\mathrm{qh}(\xi, t) = \mathcal{N}_\mathrm{qh} \mathrm{e}^{i(\gamma+N\epsilon)t} \sum_{k=0}^{N} \tilde{\xi}(t)^{N-k} f_k \Psi_\mathrm{L} = \mathrm{e}^{i(\gamma+N\epsilon)t} \Psi_\mathrm{qh}(\tilde{\xi}(t)). \quad (5.13)$$

In this formula, we have split the phase evolution into an overall part, $\mathrm{e}^{i(\gamma+N\epsilon)t}$, driven by the energy $\gamma + N\epsilon$ of a quasihole state in the center, and separate terms occurring for finite $\xi$, which have been absorbed into the definition of $\tilde{\xi}$. We directly see that for $\xi = 0$ the quasihole state is a stationary state. A quasihole off the center, however, breaks the cylindrical symmetry present in the Hamiltonian $H$, and thus the quasihole encircles the origin, trying to restore the symmetry. Conservation of angular momentum does not allow any change in $|\xi|$. The angular velocity of the quasihole is given by $\omega_\perp(1-\eta)$.

Note that the above calculation can easily be repeated for more than one quasihole. It can generally be shown that the time dependence of the corresponding wave function can be absorbed into the hole position $\xi \to \xi \mathrm{e}^{-i\epsilon t}$, and an overall phase factor, as if all holes were situated in the origin. We note that the normalization factor of the wave functions, which carries the information about the anyonic statistics of the quasiholes, depends only on absolute values $|\xi|$ or $|\xi_i - \xi_j|$, thus the substitution $\xi \to \xi \mathrm{e}^{-i\epsilon t}$ poses no problem there.

### 5.2.2 Quasiholes in the $L = 0$ condensate

Next we will analyze the dynamical behavior of holes in a system in the LLL regime, but still far from the strongly correlated Laughlin regime. Namely, we will consider a system where, in the ground state, yet no vortices have been formed, i.e. $L = 0$. Such a system is a condensate described by the Fock-Darwin function $\phi^{\mathrm{FD}}_{0,0}(z) \sim \exp(-|z|^2/2)$. The many-body wave function is simply the product of $N$ such single-particle functions. We denote it by $\Phi_0 \sim \exp(-\sum_i |z_i|^2/2)$. Then, as before, we create holes by additional $\delta$-potentials according to Eq. (5.1). For the case of a single hole at position $\xi$, we get the wave function:

$$\Phi_{\mathrm{qh}}(\xi) \sim \prod_{i=1}^{N}(z_i - \xi)\Phi_0 = \sum_{k=0}^{N} f_k \xi^{N-k}\Phi_0. \tag{5.14}$$

As before in the Laughlin case, the kinetic energy associated with each term is linear in $k$. Assuming a non-interacting system, i.e. $g = 0$, we can in the same way absorb the kinetic contribution to the time evolution in the hole coordinates:

$$\Phi_{\mathrm{qh}}(\xi, t)\Big|_{g=0} = \exp\left[i(N\epsilon + \gamma')t\right] \Phi_{\mathrm{qh}}(\tilde{\xi}(t)). \tag{5.15}$$

In the overall phase factor we now have the zero-point energy $\gamma'$ of the system.

For the interacting system, however, the situation is different. The terms $\Psi_k \equiv f_k\Phi_0$ are in general no eigenstates of the interaction $V$. To describe the time evolution of this system, we thus have to decompose the $\Psi_k$'s into an eigenbasis of $V$. Since $V$ conserves angular momentum, we can restrict ourselves, for every $\Psi_k$, to the subspace with $L = k$, for which we obtain the eigenbasis via exact diagonalization. We denote the basis by $\chi^{(k)}_\alpha$ and write:

$$\Psi_k = \sum_\alpha c^{(k)}_\alpha \chi^{(k)}_\alpha. \tag{5.16}$$

The coefficients $c^{(k)}_\alpha$ can be easily obtained, since exact diagonalization yields the $\chi^{(k)}_\alpha$ in the Fock basis of occupation number states. In this basis, the state $\Psi_k$ is represented by the vector $|N-k, k, 0, \dots\rangle$, from which it differs only by a normalization factor $N_k = [(N-k+1)!\ (k+1)!]^{-1/2}$. We thus have $c^{(k)}_\alpha = N_k \left\langle \chi^{(k)}_\alpha \right| N-k, k, 0, \dots \Big\rangle$.

Obviously, the $\Psi_k$ and thus the $\chi^{(k)}_\alpha$ are within the LLL, so all $\chi^{(k)}_\alpha$ are eigenstates of the kinetic term with the same eigenvalue $k\epsilon$. The time evolution of the

quasihole state is thus described by the wave function

$$\Phi_{\rm qh}(\xi,t) = \exp\left[i(N\epsilon+\gamma')t\right]\sum_{k=0}^{N}\tilde{\xi}(t)^{N-k}\sum_{\alpha}c_{\alpha}^{(k)}\chi_{\alpha}^{(k)}\mathrm{e}^{i\epsilon_{\alpha}^{(k)}t}. \tag{5.17}$$

Here, $\epsilon_{\alpha}^{(k)}$ is the eigenvalue of $\chi_{\alpha}^{(k)}$ with respect to $V$. The presence of this term causes, in general, a dephasing of the different contributions to $\Phi_{\rm qh}(\xi)$. Therefore, we observe a radial movement of the hole stemming from the single-particle contribution, but at the same time the hole fades out due to the interactions. In clear contrast to the Laughlin case, the entire system is being deformed, as can be seen in the density plots of Fig. 5.7. One might interpret this process as the flow of excitation energy from the sharply localized hole to the edges of the system. Interestingly, this process is reversible: As visible in the right side of Fig. 5.7, the hole re-appears in the density after each integer multiple of a revival time $T$. Below we will relate this time to the interaction parameter $g$. The position of the revivals is subject to the rotation of the hole which happens even in the non-interacting case, and is thus determined by the single-particle energy scale $\eta\hbar\omega_{\perp}$.

To further establish the close relation of this dynamical behavior with collapse-and-revival effects first discussed and observed in the context of the Jaynes-Cummings model [93, 94, 97], and later for Bose-condensed matter [99–101, 104–107], we consider the eigenvalues $r$ of the density matrix

$$\rho_{ij} = \langle\Phi_{\rm qh}(\xi,t)|\,\hat{c}_i^{\dagger}\hat{c}_j\,|\Phi_{\rm qh}(\xi,t)\rangle\,,$$

i.e. the occupation of different eigenmodes. They are shown as a function of time in Fig. 5.8: Initially, $r=N$, as all particles are in a single-particle state, $(z-\xi)\exp(-|z|^2/2)$. In the course of time, interactions will occupy additional eigenmodes, causing a collapse of the condensate, clearly visible in the evolution of $r$. The nature of the corresponding eigenmodes is particularly easy to analyze, if the hole is placed in the center. Then, at any time, eigenmodes of $\rho_{ij}$ are Fock-Darwin functions, as the rotational symmetry is maintained. In that case, for all particle numbers we have studied, the most occupied mode is, at any time, $\phi_{0,1}^{\rm FD}$, while the second most occupied is always the Gaussian, i.e. $\phi_{0,0}^{\rm FD}$. While Fig. 5.8 shows that the originally condensed state collapses into a non-condensed state, Fig. 5.9 also proves the correlated nature of the system at $t=T/2$. Here, we have plotted the pair-correlation function $g(z_1,z_2)$, as defined in Eq. (3.18), after fixing the coordinate of one particle. As shown in Fig. 5.9, depending on

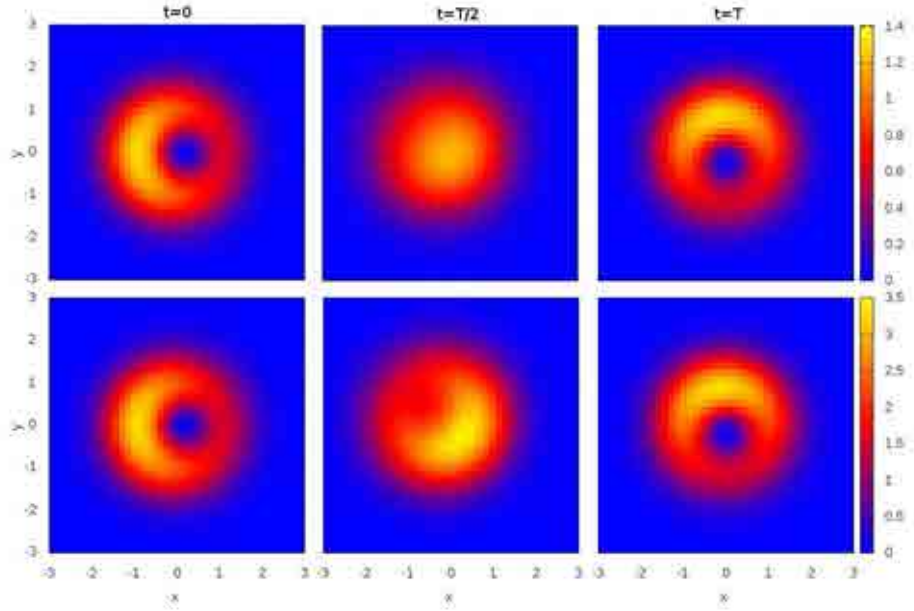


FIGURE 5.7: Density plots for $N = 8$ (upper line), and $N = 20$ (lower line). On the left, we show the initial density at $t = 0$ with one hole at $\xi = 0.2\lambda_\perp$. The pictures in the middle show the fully collapsed system, i.e. at $t = T/2$. The pictures on the right correspond to $t = T$, where we observe the revival of the hole.

where we fix one of the particles to be, the probability distribution of the other particle is heavily affected. This is a trace of entanglement and in clear contrast to the behavior at $t = 0$. Independently from where we choose one particle to be, the pair-correlation function at $t = 0$ is found to remain with the same Gaussian shape. Thus, the time evolution brings the initially fully uncorrelated system into a correlated state. The effect is most pronounced in small systems with a quasihole in the center. In this case, we find for $N = 12$ at $t = T/2$ an entangled state with almost equally populated modes, $n_0^{\mathrm{FD}} = 4.7$ and $n_1^{\mathrm{FD}} = 4.3$.

In the following, we derive expressions for $T$ and $\xi^{(n)}$. This will enable us to deduce information about different system's parameters from experimentally accessible quantities. We have to analyze the spectra $\epsilon_\alpha^{(k)}$, which define the periods $\tilde{T}_\alpha^{(k)}$ of phase oscillations of each contribution $\chi_\alpha^{(k)}$:

$$\tilde{T}_\alpha^{(k)} = \frac{2\pi\hbar}{\epsilon_\alpha^{(k)}}. \tag{5.18}$$

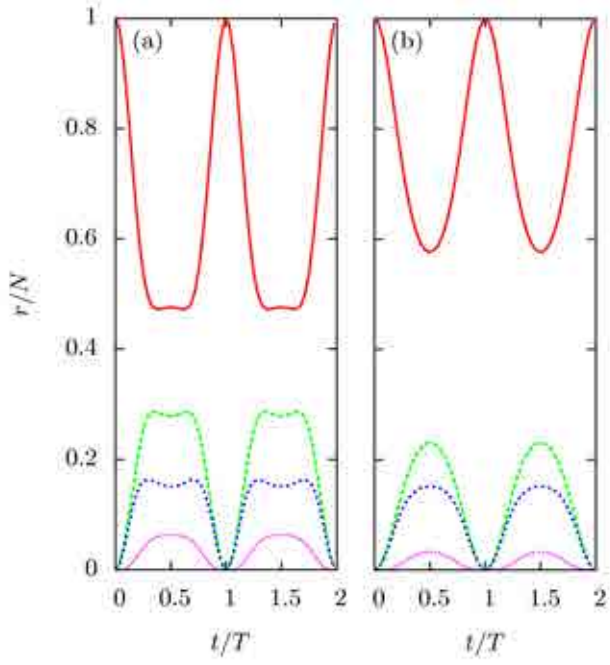


FIGURE 5.8: Eigenvalues $r$ of the density matrix $\rho$ as a function of time. **(a):** $N = 8$. **(b):** $N = 20$. Initially, one hole was pierced at $\xi = 0.2\lambda_\perp$.

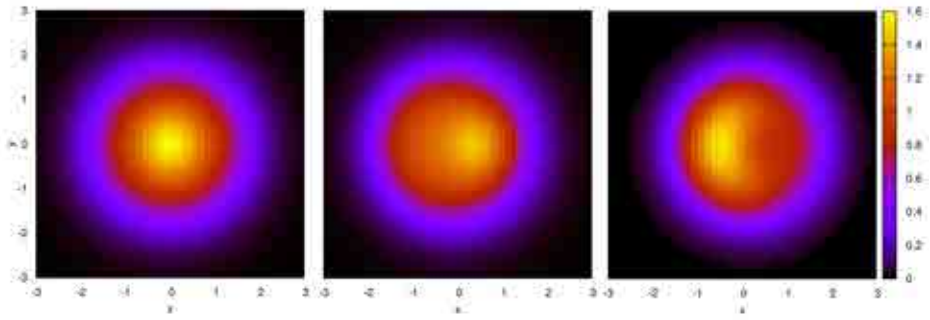

FIGURE 5.9: Contour plot of pair-correlation function $g(\boldsymbol{r}, \boldsymbol{r}')$ with one coordinate fixed at $\boldsymbol{r} = (0, 0)$ [left side], $(0.5, 0)$ [middle], or $(2, 0)$ [right side]. Since $\int g(\boldsymbol{r}, \boldsymbol{r}')\mathrm{d}\boldsymbol{r}' = \rho(\boldsymbol{r})$, we have divided each plot by the density $\rho(\boldsymbol{r})$, in order to obtain a common color scheme. The plots refer to a $L = 0$ condensate, in which initially a central hole has been pierced. They are taken after a free time evolution $t = T/2$. The system size has been set to $N = 12$. If one particle is fixed at the center (left) or close to the center (middle), the pair-correlation function signals an increased probability of the pair being close together. If one particle is found far away from the center (right), the second particle is most likely found on the opposite edge of the system. This mutual dependence proves the correlated nature of the state at $t = T/2$.

Now assume that there are some energy units $u$ and $u'$, which allow to write

$$\epsilon_\alpha^{(k)} = ku' + n_\alpha^{(k)} u, \tag{5.19}$$

with $n_\alpha^{(k)} \in \mathbb{N}$. The part linear in $k$ does not depend on $\alpha$, and thus can be absorbed into the kinetic energy contribution. The kinetic part will not affect this collapse and revival process, as it is completely absorbed in an overall phase and the time-dependent parameter $\tilde{\xi}(t)$. The phase decoherence between different $\alpha$ states is controlled by $u$, and the corresponding periods read

$$T_\alpha^{(k)} = \frac{2\pi\hbar}{n_\alpha^{(k)} u}. \tag{5.20}$$

We see that $T = 2\pi\hbar/u$ is a multiple of all $T_\alpha^{(k)}$, so at time $T$, all contributions will have the original phase relations. The positions $p_m$ at which we will find the $m$th revival of the hole is defined by the rotational movement of the hole, i.e. $p_m = \tilde{\xi}(mT)$. Note that now the time-dependence of $\tilde{\xi}$ is due to the kinetic energy $\epsilon$ plus the interaction contribution $u'$.

To determine $u$ and $u'$, we numerically analyze the spectra $\epsilon_\alpha^{(k)}$. We find that the gap above the $L = N$ subspace provides us, for any $N$, with an energy unit $u \approx 0.040 gN\hbar\omega_\perp$. All states in the spectrum are found to be given as integer multiples of $u$ plus the ground-state energy. Also in subspaces $L \leq N$, the same unit $u$ can be used to quantize most of the energies. Strikingly, the eigenstates to those energies which can not be constructed according to Eq. (5.19) have zero overlap with $\varphi_k$. Thus, they do not contribute in Eq. (5.17).

The second energy unit of Eq. (5.19) turns out to have exactly the same value, i.e. $u' = u$. As exact solutions are known for the ground state energies in subspaces with $L \leq N$ [109–111], we are able to write down an analytic expression, $u' = \frac{gN}{8\pi}\hbar\omega_\perp$. We thus obtain for the revival period

$$T = \frac{(4\pi)^2}{gN\omega_\perp}. \tag{5.21}$$

From this formula, we directly see that choosing $gN = \text{const.}$ makes the oscillation periods independent from the size of the system. This choice is convenient as it also guarantees a finite interaction energy per particle in the thermodynamic limit. Fixing $g$ rather than $gN$, the periods would decrease in larger systems. By Eq. (5.21), a measurement of the revival period $T$ directly yields information

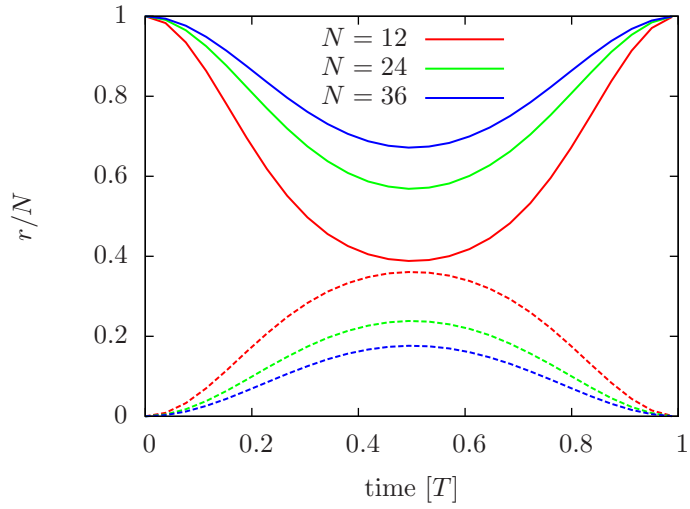


FIGURE 5.10: Eigenvalues $r$ of the density matrix $\rho$ as a function of time for different particle numbers $N$. The hole has been introduced at the origin, $\xi = 0$.

about $gN$. Measuring then the polar angle $\phi^{(n)}$ of the revival position $\xi^{(n)} = \tilde{\xi}(nT)$ will allow to extract $\eta$. We find

$$\phi^{(n)} = \frac{4n(1-\eta)}{gN} + n. \tag{5.22}$$

Comparing the densities for $N = 8$ and $N = 20$ in Fig. 5.7 we find that the density tends to maintain its hole structure, when we increase the size of the system. Accordingly, as can be seen in Fig. 5.8, the amplitudes of $r$ as a function of time become smaller. To study the role played by particle number, we have systematically increased the size up to $N = 36$ for the particularly simple situation of a hole at $\xi = 0$. The results are shown in Figs. 5.10 and 5.11. As the data in Fig. 5.10 clearly indicates, the hole state will not dephase in the thermodynamic limit. Accordingly, the density profile shown in Fig. 5.11 maintains its hole structure.

The reason for this behavior can be inferred from earlier work studying the ground state wave functions for $L \leq N$ [109–112]. There it has been shown the ground state wave functions for $L \leq N$ are closely related to the functions $f_k$, which are the wave functions where the total angular momentum $L = k \leq N$ is most equally distributed amongst $N$ particles, $f_k = \sum_{1 \leq i_1 < \cdots < i_L \leq N} z_{i_1} \cdots z_{i_L}$. From these functions, we obtain the polynomial part of the ground state wave function of $L =$

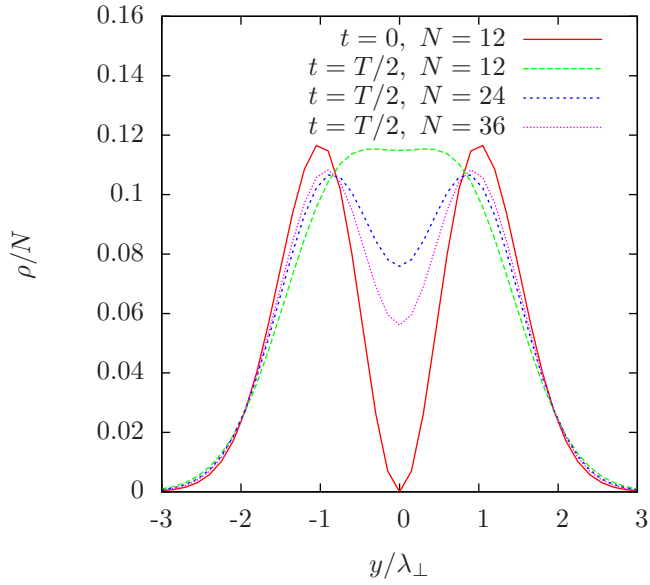


FIGURE 5.11: Density profile (along $x = 0$) for a system with initially one hole at the origin (shown in red curve) at time $t = T/2$ for different particle numbers $N$.

$k$ by replacing the coordinates $z_i$ by the relative coordinates $\tilde{z}_i \equiv z_i - Z$, where $Z$ is the center-of-mass coordinate. Note that $Z$ is not just a number, but an operator with $\langle Z \rangle = 0$. As center-of-mass fluctuations decrease with increasing particle number of the system, for large-sized systems $Z$ becomes pinned to the center, and the states $f_k \Psi_0$ become eigenstates of the Hamiltonian with eigenvalues $E_k \sim k$. Just like in the Laughlin case, we will then no more observe the collapse and revival of the hole. Of course, the rotational movement around the origin will survive the thermodynamic limit if the hole is initially placed outside the center. Still there is a quantitative difference to the Laughlin regime, as the period of rotation will be shorter due to the additional interaction energy $u'$ from Eq. (5.19) which has to be absorbed in the definition of $\tilde{\xi}(t)$. Qualitatively, however, the dynamics of a single hole does not distinguish the condensed phase from the Laughlin phase in the thermodynamic limit.

The situation becomes quite different if we pierce a second hole into the condensate. For simplicity, we choose to introduce one of them in the center. Our wave function is then a linear combinations of states $|0, 2N-k, k, 0, \cdots\rangle$ with $0 \leq k \leq N$. and we are in the angular momentum regime with $N \leq L \leq 2N$. Here, even the GS energies $E_L$ may not behave linearly with $L$ [57]. Also, much

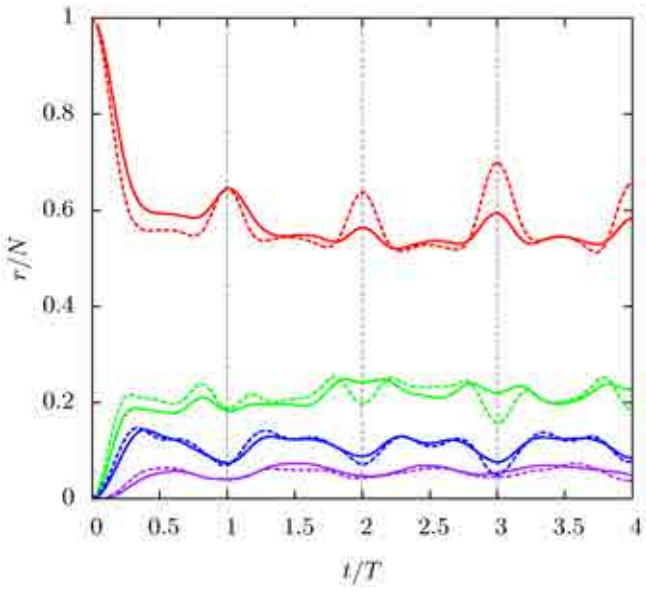


FIGURE 5.12: Occupation numbers $r/N$ of eigenmodes as a function of time in a condensate of $N = 8$ (dashed lines) and $N = 12$ (solid lines) particles, where initially one hole has been placed in the center and second hole at $|\xi| = 1$. No full revivals are observed, and the peaks at $t = nT$ are washed out in larger system.

more states are involved when expressing the states $|0, 2N - k, k, 0, \cdots\rangle$ in terms of eigenstates of the interaction, which now live in a significantly increased Hilbert space. The consequence of this is that, after a quick dephasing, the holes will never exhibit a full revival, see Fig. 5.12. Contrarily, as the comparison of the data for $N = 8$ and $N = 12$ in Fig. 5.12 suggests, the peaks at the same period as given by Eq. (5.21) must be expected to disappear quickly in the thermodynamic limit.

A $L = 0$ condensate with two quasiholes is similar to a $L = N$ condensate with one quasihole, and in the thermodynamic limit the $L = N$ condensate with one vortex in the center is the ground state of the system at this angular momentum. Fig. 5.12 therefore suggests that in regimes $L \gtrsim N$, also a single quasihole will dephase. This seems to be reasonable, as spontaneous symmetry breaking has been predicted for states with $L \gtrsim N$ [29, 87], and ground states in several $L$ subspaces become quasi-degenerate. Since within each quasi-degenerate manifold energy differences are very small, while large energy jumps occur between different manifolds, a dephasing of different contributions and thus a collapse of the

quasihole must be expected. Furthermore, the smallness of energy contributions in the quasi-degenerate manifolds make revival times unobservably long. We do not further investigate this situation of $L \gtrsim N$, as the symmetry-breaking leads to the formation of vortex lattices [29], also observed in experiments [113]. Characteristics of these lattice should allow for a clear identification of the corresponding phases.

### 5.2.3 Quasiholes in the Laughlin quasiparticle state

Upon increasing the gauge field strength, the vortex lattice has been predicted to melt when reaching filling factors $\nu \lesssim 6$ [79]. Then, a variety of strongly correlated quantum liquid phases are candidates for the ground state. Finally, for $\nu = 1/2$ or $L = N(N-1)$, the Laughlin state becomes the ground state of the system. It is certainly in this regime where observable properties to distinguish between the phases become most relevant. Let us therefore study the dynamics of a quasihole pierced in the last incompressible phase which has been predicted to occur before reaching the Laughlin state. It is characterized by $L = N(N-2)$ and by a wave function which differs from the Laughlin wave function only locally at the origin, having the form of a Laughlin quasiparticle excitation, $\Psi_{\mathrm{L,qp}} = \exp(-\sum_i |z_i|^2/2)\partial_{z_1} \dots \partial_{z_N} \prod_{i<j}(z_i - z_j)^2$, see Chapter 4.

For simplicity, we will pierce the quasihole in the origin, which makes the resulting state an eigenstate of the single-particle part of $\mathcal{H}$, and all dynamics will exclusively be driven by $\mathcal{V}$. To obtain the state $\hat{\mathrm{O}}_{\mathrm{qh}}(0)\Psi_{\mathrm{L,qp}}$ in the Fock basis, we numerically diagonalize the Hamiltonian $\mathcal{H}' = \mathcal{V} + V_I$ in the subspace $L = N(N-1)$. We then decompose this state in the corresponding eigenbasis of $\mathcal{V}$, also obtained by exact diagonalization. Several eigenstates of $\mathcal{V}$ will contribute, but the largest contribution comes from the Laughlin state with an overlap of 0.709 (0.717) for $N = 7$ ($N = 6$). Expressed in the eigenbasis of $\mathcal{V}$, we can easily perform the time evolution of $\hat{\mathrm{O}}_{\mathrm{qh}}(0)\Psi_{\mathrm{L,qp}}$.

The dynamics is clearly visible in the density shown in Fig. 5.13a: In the course of time, the hole fades out, as the center of the cloud gains a finite density. At some point, even a density maximum is developed at the origin, surrounded by a circular density valley. As the valley spreads out, the maximum becomes clearly peaked. The process is then reversed, and a hole at the center re-appears. Such oscillations between a density maximum and a density minimum in the center

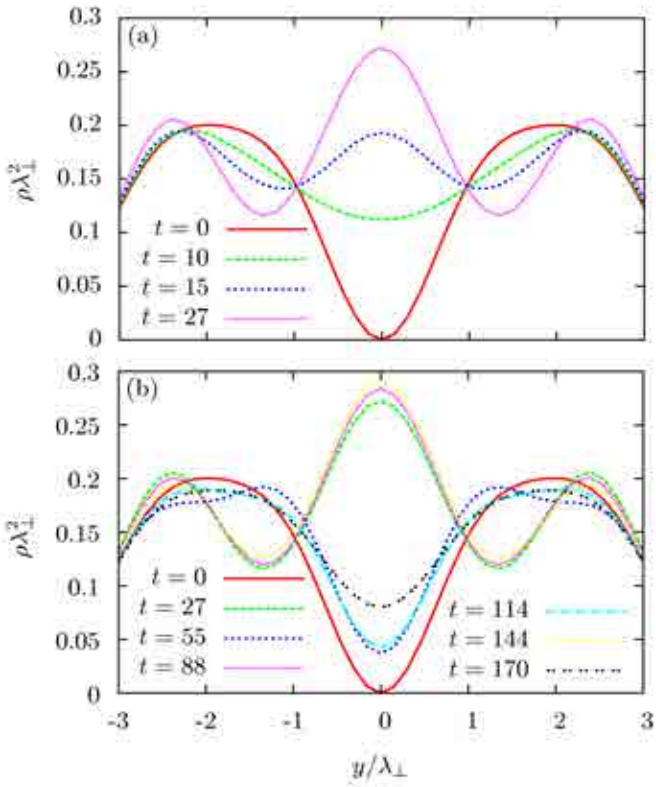


FIGURE 5.13: Radial profile of the cylindrically symmetric density for a system of $N = 6$ particles initially prepared in the state $\hat{O}_{\rm qh}(0)\Psi_{\rm L,qp}$ at different times $t$ (in units of $\omega_\perp^{-1}$) with $g = 1$. In (a) the evolution from a quasihole in the center to a density peak is shown. In (b) we plot the density for all times $t < 200$, at which it takes a temporal maximum or minimum in the center.

can be observed repeatedly. The scenario, however, differs from the collapse-and-revival process in the condensate: First, re-appearing holes are not equivalent to the original hole, as their density at the center remains finite, and their core size has decreased, see Fig. 5.13b. Second, the "revival" periods are not sharp. In Fig. 5.13b, we have chosen precisely those times at which the process is reversed. For $N = 6$, the reversal after the first re-appearance of the quasihole is found at $t = 55$, while the second revival takes place at $t = 114$.

To understand this behavior, we have to analyze the spectrum of $\mathcal{V}$ at $L = N(N-2)+N = N(N-1)$. It can be divided into a quasi-continuous excitation band and the Laughlin state. A gap $\Delta$ separates these two contributions. For

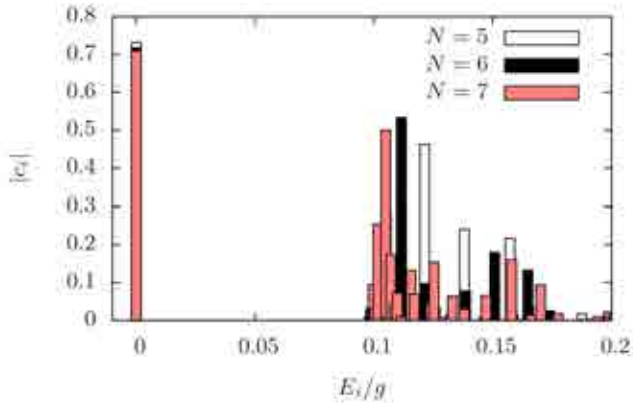


FIGURE 5.14: Overlap $c_i$ between $\hat{O}_{qh}(0)\Psi_{L,qp}$ and eigenstates of $\mathcal{V}$ with energy $E_i$ for different $N$.

$N \gtrsim 6$, the gap approaches the constant value of $\Delta \approx 0.1g$, if we choose $g$ (rather than $gN$) to be constant, cf. Section 4.3.3 or Ref. [90]. Compared to this value, the energy differences between states within the excited band are typically very small. This property of the spectrum can be seen in Fig. 5.14, where we have plotted the overlap of the eigenstates with the initial state, $c_i \equiv \langle \hat{O}_{qh}(0)\Psi_{L,qp}|\chi_i\rangle$, versus $E_i/g$. Here, $|\chi_i\rangle$ denotes the eigenstates of $\mathcal{V}$ in the $L = N(N-1)$ subspace, and $E_i$ is the corresponding eigenenergy.

Due to this structure, the relative dephasing of different contributions to $\hat{O}_{qh}(0)\Psi_{L,qp}$ from the excited band is slow compared to the dephasing of these contributions with respect to the contribution from the Laughlin state. Following this reasoning, $2\pi/\Delta \approx 63$ for $g = 1$ sets the rough time scale for a "quasi"-revival, at which the Laughlin state is again "in phase" with the low-energy contributions from the excited band. This slightly differs from the number we find by analyzing the density (cf. Fig. 5.13b), $t = 55$ for $N = 6$. But we note that the most important contribution from the excited band is a state with energy $E = 0.112g$ (cf. Fig 5.14). Thus, it is in phase with the Laughlin after a time $t = 56$. It has an overlap with $\hat{O}_{qh}(0)\Psi_{L,qp}$ of 0.533. A superposition of this state and the Laughlin state is able to reproduce the quasihole state with a fidelity of 78%. Other important states, with overlaps 0.279 and 0.110, are found at $E = 0.105g$ and $E = 0.102g$. At $t = 56$ they are still nearly in phase with the $E = 0.112g$ state. But also states with $E = 0.164g$ and $E = 0.182g$ contribute significantly with overlaps 0.180 and 0.133. These states will be clearly out of phase, making the revival imperfect. Subsequent revivals will more and more suffer from the

slow dephasing within the manifold of excited states. This explains the small irregularity in the revival periods and the loss of the quasihole character in the density profiles (see Fig. 5.13b).

Posing the question whether the described dynamics will survive in the thermodynamic, we first note that due to the similarity between the Laughlin state and $\hat{O}_{\mathrm{qh}}(0)\Psi_{\mathrm{L,qp}}$, we can always expect contributions from both the Laughlin state and the excited band. This assessment seems to agree with Fig. 5.14, where the overlap with the Laughlin state is found to be almost constant while varying particle number, $5 \leq N \leq 7$. As the Laughlin gap is known to be constant for large $N$, also the revival time has to be. The imperfection of the revival, characterized by a finite density at the center, continuously improves, as we increase the system size from $N = 4$ to $N = 7$. This seems reasonable, since energy differences in the excited band decrease with larger $N$, slowing down the dephasing in the excited band. In Fig. 5.14 this reflects in the decreased spreading of relevant states when increasing particle number. However, whether this might lead to a perfect collapse-and-revival process in the thermodynamic limit, is not clear from our calculations.

### 5.2.4 Applications

In the above section, we have shown that observing the dynamics of a quasihole might serve to classify different ground states in the LLL regime. Especially, the absence of coherence is a characteristic feature of the Laughlin regime, $L \geq N(N-1)$, due to its zero interaction energy. It is distinct to the collapse of the quasihole observed in finite systems with $L < N(N-1)$. For simplicity, we have considered an idealized system with a cylinder-symmetric Hamiltonian, but we note that even deformed Laughlin states, according to Eq. (4.19), should be characterized by a decoherence-free quasihole dynamics due to their vanishing interaction energy. In the condensed regime, the collapse of the quasihole is followed by perfect revivals, and the system oscillates between a condensed and a correlated state. System parameters like $gN$ and $\eta$, specifying the interaction and the single-particle energy, can be obtained by measuring period and positions of this revival. A collapse-and-revival is also found for a quasihole in the Laughlin-quasiparticle state, distinguishing this incompressible phase in direct vicinity of the Laughlin phase from the Laughlin regime.

# Chapter 6

# Fractional quantum Hall states of pseudospin-1/2 bosons

The strongly correlated phases we have encountered so far in this thesis described spinless or spin-polarized systems. As we have shown in Chapter 4, bosons in geometric gauge fields may be in topological phases which can well be described by the Moore-Read wave function for $\nu = 1$, Eq. (3.11), and the Laughlin wave function for $\nu = 1/2$, Eq. (3.6). These are the first two states of the so-called Read-Rezayi (RR) series of parafermionic states [59], briefly discussed in Section 3.1.2.2. Considering the case of artificial gauge fields induced by fast rotations, N. Cooper *et al.* have given numerical evidences that several RR states up to filling factor $\nu = 6$ are relevant to describe systems of spin-polarized bosons [79]. This has been a striking finding, as these states are constructed as the ground states of a $(k+1)$-body contact interaction with $k = 2\nu$.

Although also bosons with a pseudo-spin-1/2 degree of freedom have already been condensed [114, 115], and their behavior under rotation has been studied both theoretically [116–118] and experimentally [119, 120], less attention has yet been paid to the strongly correlated regime in such systems. For the electronic FQH effect, however, a variety of states has been proposed for systems with spin. Despite the strong magnetic field the electrons might be in a singlet phase due to

their small gyromagnetic ratio in many solids. Within a conformal field theory framework, a generalization of the RR series to the so-called non-Abelian spin singlet (NASS) series [67, 68, 121] has been formulated, introduced in Section 3.1.2.3. For bosons, this series of topological states occurs at fillings $\nu = 2k/3$, and includes the $(2, 2, 1)$-Halperin state [66] with Abelian excitations at $k = 1$. Like the RR states, the NASS states are constructed as the zero-energy eigenstates of a repulsive $(k + 1)$-body contact interaction.

In this chapter we show, using exact diagonalization, that also for two-component Bose gases in Abelian gauge fields two-body contact interaction leads to the formation of a series of incompressible states. They are found precisely at the NASS filling factors. For $k = 1$, this is trivially the Halperin state, but also for $k = 2$ significant overlap with the corresponding NASS state and a similar spectral structure indicate that the system can be brought into the NASS phase within this realistic setup.

This finding is in close analogy to the spin-polarized case with RR-like states at filling $\nu = k/2$. However, as it is experimentally difficult to get into the regime of low filling, the two-component system benefits from supporting analogs of the RR states at higher filling. Furthermore, the possibility of tuning independently inter-spin and intra-spin interactions provides additional control. In particular, we will show that states with zero interspin interaction energy are obtained by increasing the interspin interaction strength. The mechanism behind this are correlations which are most economically used in pairs of particles with opposite spin, favoring a singlet configuration in the case of SU(2)-symmetric interactions. Finally, effects stemming from a spin-orbit (SO) coupling can be integrated in the framework of two-component gases by generalizing to a non-Abelian gauge field. We investigate this scenario, and find the formation of Laughlin states at filling factors smaller than 1/2 [41, 122], of spin-orbit coupled analogs of Read-Rezayi states [123, 124], and the occurrence of NASS-like states at SO coupling strengths corresponding to a Landau level (LL) degeneracy.

Distinct from our work in Chapter 4, the present chapter will not focus on a concrete proposal how to achieve the artificial gauge field. Possible ways how to generate non-Abelian gauge fields have been presented in Section 2.3.2. These SU(2) gauge fields contain magnetic fields acting on two-component spinors as a limiting case. We also note that the simple proposal of rotating the gas directly generalizes to magnetic fields for multi-component gases, although it cannot be extended to SO coupling.

Considering only the effective Hamiltonian, independently from the concrete experimental setup, has the great advantage that we can try to extract the core physics. While for instance a harmonic trapping potential is certainly an important part of any real experiment, in theory we can expect it to solely adjust the total angular momentum, or, respectively, the filling factor. Explicitly, we have seen this in Chapter 4. So we now feel safe about neglecting the trap. It is then convenient to perform exact diagonalization in a geometry without edges, e.g. a sphere or a torus. We will make the latter choice, which also can be seen as a rectangle with periodic boundary conditions. Such boundary conditions have first been used for studying FQHE in Ref. [125]. Apart from eliminating edge effects from our study, they also represent a non-trivial geometry, on which topological phases can be classified by the number of degenerate ground states [126].

In the following section, we will derive the LL structure on the torus, and work out the translational symmetry [61] we can exploit for doing the exact diagonalization. The results of the numerical diagonalization in the absence of SO coupling are presented in Sections 6.3 and 6.4. The SO coupled system is described in Section 6.5: We study the fate of the Laughlin state upon tuning the SO coupling strength in Section 6.5.1. In Section 6.5.2, we focus on one special coupling strength leading to degenerate LLs and vary the filling factor.

## 6.1 Landau levels on the torus

In the absence of a trap, the single-particle Hamiltonian is just given by $H_{\mathrm{sp}} = (\boldsymbol{p}-\boldsymbol{A})^2/2M$. Considering periodic boundary conditions, i.e. working on a torus, it is convenient to choose the vector potential in the Landau gauge, $\boldsymbol{A} = B(0,x)$. This will not modify the LL spectrum, but the eigenfunctions have to be adapted to the new gauge. As before, when deriving Eq. (3.1) in the symmetric gauge, we define creation and annihilation operators (for $\hbar \equiv 1$ and $M \equiv 1/2$):

$$c \equiv \frac{1}{\sqrt{2B}}(p_x - ip_y - iBx), \tag{6.1}$$

$$c^\dagger \equiv \frac{1}{\sqrt{2B}}(p_x + ip_y + iBx), \tag{6.2}$$

with $[c, c^\dagger] = 1$ and $[c, c] = 0$. These operators bring the single-particle Hamiltonian to the harmonic oscillator form

$$H_{\mathrm{sp}} = 2B\left(c^\dagger c + \frac{1}{2}\right), \tag{6.3}$$

where, contrarily to Eq. (3.1), no trap breaks the LL degeneracy, and thus only one type of operator appears. Different degenerate states within each LL are characterized by a continuous quantum number $\kappa$, as can be seen by making a plane-wave ansatz in the $y$-direction:

$$\tilde{\Psi}_{n,\kappa}(x, y) = e^{i\kappa y}\Phi_{n,\kappa}(x). \tag{6.4}$$

This leads to a harmonic oscillator Hamiltonian $H_{\mathrm{sp}}(\kappa)$, determining $\Phi_{n,\kappa}$:

$$H_{\mathrm{sp}}(\kappa) = p_x^2 + B^2\left(x + \frac{\kappa}{B}\right)^2. \tag{6.5}$$

The unnormalized eigenfunctions of this Hamiltonian are

$$\Phi_n(\tilde{x}) = e^{-B\tilde{x}^2/2}H_n(\sqrt{B}\tilde{x}), \tag{6.6}$$

with $H_n$ the Hermite polynomials, and $\tilde{x}$ the shifted $x$ variable:

$$\tilde{x} = x + \frac{\kappa}{B}. \tag{6.7}$$

We now apply the periodic boundary conditions on the system, as done in Ref. [125]. In order to be periodic in $y$ with a period $b$, we have to restrict $\kappa$ to integer multiples of $2\pi/b$. We therefore define $X_j \equiv \kappa/B = 2\pi j/(bB)$ with $j \in \mathbb{Z}$. This quantity has dimension of a length, as $B = 1/\lambda^2$ with $\lambda$ the magnetic length. As can be seen in Eq. (6.5), it can be interpreted as a displacement of the harmonic oscillator in $x$-direction. To make the wave function also periodic in $x$, with period $a$, we can sum over all displacements $X_j + ka$ with $k$ an integer:

$$\Psi_{n,j}(x, y) \equiv \sum_{k=-\infty}^{\infty} \tilde{\Psi}_{n,B(X_j+ka)}(x, y). \tag{6.8}$$

This will not affect the $b$-periodicity in $y$, if the following condition is fulfilled:

$$ab = 2\pi\lambda^2 N_\Phi, \tag{6.9}$$

with $N_\Phi$ an integer. Thus, for a given torus size $a \times b$, only discrete values of the magnetic field are possible. We can interpret $N_\Phi$ as the number of quantized fluxes within the unit cell. Note that $N_\Phi$ is connected to the particle number $N$ through the filling factor

$$\nu = \frac{N}{N_\Phi} \equiv \frac{p}{q}, \tag{6.10}$$

where $p$ and $q$ should be taken co-prime.

The displacement in Eq. (6.8) is characterized by two parameters $j$ and $k$. We must restrict $j$ to $1 \leqslant j \leqslant N_\Phi$ to prevent double counting. In the LLL, the wave functions explicitly read

$$\Psi_{0,j}(x,y) \simeq \sum_{k=-\infty}^{\infty} \exp\left[ iy' \left( \frac{j}{N_\Phi} + k \right) \frac{a}{\lambda} - \frac{1}{2} \left( x' + \frac{a}{\lambda} \left( \frac{j}{N_\Phi} + k \right) \right)^2 \right], \tag{6.11}$$

where the unitless variables $x' = x/\lambda$ and $y' = y/\lambda$ have been introduced. After normalization and replacing the $k$-sums by elliptic theta functions, we get

$$\Psi_{0,j} = \left( 2\pi^2 N_\Phi^3 \frac{a}{b} \right)^{-1/4} e^{-\frac{y'^2}{2} - ix'y'} \theta_3 \left( \frac{j\pi}{N_\Phi} + \sqrt{\frac{\pi}{2N_\Phi a/b}}(x - iy), e^{-\frac{\pi}{N_\Phi a/b}} \right). \tag{6.12}$$

From this expression we should also note that the problem depends only on two parameters: the axis ratio $\frac{a}{b}$, and the number of fluxes $N_\Phi$. The parameter $B$ just sets an overall length scale. The excited states can easily be obtained by applying the ladder operator $c^\dagger$:

$$\sqrt{n+1}\Psi_{n+1,j} = c^\dagger \Psi_{n,j}. \tag{6.13}$$

With this, we can express the single-particle basis on the torus by the LL quantum number, and an additional quantum number $j$ which runs from 0 to $N_\Phi - 1$.

Since we will in the following consider two-component gases, each state has an additional two-fold pseudospin degeneracy. We denote the internal state by an index $s = \uparrow, \downarrow$. On the other hand, we will be able to neglect the LL index $n$ by making the convention that all particles live in the LLL, as before in Chapter 4. When we, later in this chapter, also consider a SO coupled system, the LL structure will be modified, as internal and external degrees of freedom will be mixed. For the moment, however, we will only consider particles in LLL states

$\Psi_{j,s} \equiv \Psi_j |s\rangle$. They are created (annihilated) by operators $\hat{a}^\dagger_{js}$ ($\hat{a}_{js}$). The wave function $\Psi_j$ represents the external degrees of freedom, while the spin is expressed by the ket $|s\rangle$. The second-quantized notation of the Hamiltonian reads

$$\mathcal{H} = \sum_{j,s} \epsilon\ \hat{a}^\dagger_{js}\hat{a}_{js} + \sum_{\{j,s\}} V_{\{j,s\}}\hat{a}^\dagger_{j_1 s_1}\hat{a}^\dagger_{j_2 s_2}\hat{a}_{j_3 s_3}\hat{a}_{j_4 s_4}. \tag{6.14}$$

Since $\Psi_{j,s}$ are the eigenstates of the single-particle part of the Hamiltonian Eq. (6.14), this part is already diagonal, with $\epsilon$ the energy of a particle in the LLL. Due to the LL degeneracy and neglection of higher LLs, this term is just a constant, which we will neglect in the following. The interesting part of the Hamiltonian is the second term describing a two-body interaction characterized by the matrix elements $V_{\{j,s\}}$. Here, $\{j,s\}$ denotes the set of quantum numbers $j_1,\ldots,j_4$ and $s_1,\ldots,s_4$. Assuming contact interactions we have:

$$\begin{aligned} V_{\{j,s\}} =& g_{s_1 s_2}\delta_{s_1,s_3}\delta_{s_2,s_4} \\ &\times \int_0^a \int_0^b \mathrm{d}^2 z_1 \mathrm{d}^2 z_2\ \delta(z_1 - z_2)\Psi^*_{j_1}(z_1)\Psi^*_{j_2}(z_2)\Psi_{j_3}(z_1)\Psi_{j_4}(z_2). \end{aligned} \tag{6.15}$$

with $g_{s_1 s_2}$ the spin-dependent contact interaction strength of two particles. Although this double integral, below denoted by $I$, can be evaluated by straightforward numerics, we give an analytic solution. It can be obtained by inserting the expansion of $\Psi_j$ as given by Eq. (6.11), see also [50, 127]:

$$\begin{aligned} I =& \frac{1}{2\pi N_\Phi} \sum_{s=-\infty}^{\infty}\sum_{t=-\infty}^{\infty} C_{n_1,n_4}\left(\frac{\tau}{\vartheta}s, \tau\vartheta t\right) C_{n_2,n_3}\left(-\frac{\tau}{\vartheta}s, -\tau\vartheta t\right) \\ &\times \exp\left[-\tau^2\left\{\frac{1}{2}\left(\left(\frac{s}{\vartheta}\right)^2 + (t\vartheta)^2\right) + is(j_1 - j_3)\right\}\right] \delta'_{j_1+j_2,j_3+j_4}\delta'_{j_1-j_4,t}, \end{aligned} \tag{6.16}$$

where $\delta'$ is a Kronecker delta modulo $N_\Phi$, $\tau = \sqrt{2\pi/N_\Phi}$, and $\vartheta = \sqrt{a/b}$. The coefficients $C_{n_i,n_j}$ depend on the LL. In Eq. (6.15), all particles are in the LLL, so these coefficients are just 1. Nevertheless we have included them, as for the spin-orbit coupled systems they will be needed. For interactions involving the

first excited LLs $n = 1$ and $n = 2$, they read:

$$\begin{aligned}
C_{1,0}(u,v) &\equiv -(u+iv)/\sqrt{2},\\
C_{0,1}(u,v) &\equiv (u-iv)/\sqrt{2},\\
C_{1,1}(u,v) &\equiv 1-\frac{u^2+v^2}{2},\\
C_{2,0}(u,v) &\equiv (u-iv)^2/\sqrt{2},\\
C_{0,2}(u,v) &\equiv -(u+iv)^2\sqrt{2},\\
C_{1,2}(u,v) &\equiv (u^2+v^2-4)(u+iv)/4,\\
C_{2,1}(u,v) &\equiv -(u^2+v^2-4)(u-iv)/4,\\
C_{2,2}(u,v) &\equiv (8-8(u^2+v^2)+2u^2v^2+u^4+v^4)/8.
\end{aligned}$$

The sums in Eq.(6.16) converge quickly, especially within the LLL. For LLs up to $n = 2$, taking into account only values with $|s| \leq 16$ and $|t| \leq 8$ has given very precise values.

From the expression in Eq. (6.16), one finds that the interaction conserves total momentum $J = \sum_i j_i \bmod N_\Phi$. In the next section, we will discuss symmetries on the torus in greater detail.

## 6.2 Translational symmetries on the torus

We now exploit the translational symmetry of the system, which was fully discovered by F. D. M. Haldane [61]. This will allow to work in a many-body basis where states are characterized by a "Haldane momentum" $\boldsymbol{K} = (K_x, K_y)$ which is conserved by the Hamiltonian. A comprehensive recipe for constructing this basis can also be found in Ref. [50]. The main steps are summarized in this section.

First we notice that the Hamiltonian in the Landau gauge commutes with a "pseudomomentum" $\boldsymbol{P}_i \equiv -\boldsymbol{p}_i - By_j\boldsymbol{e}_x$, which we use to define the "magnetic translation operator" $T_i(\boldsymbol{L}) \equiv \exp(-i\boldsymbol{L}\cdot\boldsymbol{P}_i)$. Further we introduce the lattice vectors $\boldsymbol{L}_{mn} \equiv ma\boldsymbol{e}_x + nb\boldsymbol{e}_y$, with $m$ and $n$ integer. Although the Fock states $|j_1, j_2, \cdots, j_N\rangle$ are eigenstates of magnetic translations $T_i(\boldsymbol{L}_{mn})$, this operator is not particularly helpful, as all its eigenvalues are simply 1. This can be seen from

writing $T_i(\boldsymbol{L}) = \exp[i(L_x y_i - L_x L_y/2)/\lambda^2] t_i(\boldsymbol{L})$, in combination with Eq. (6.9). Here, $t_i(\boldsymbol{L})$ denotes the standard translation, $\exp(-i\boldsymbol{L}\cdot\boldsymbol{p}_i)$.

Next, a "relative translation operator" is introduced, $\tilde{T}_i(\boldsymbol{L}) \equiv \prod_j T_i(\boldsymbol{L}/N) T_j(-\boldsymbol{L}/N)$, which is found to leave the Hilbert space invariant for translations along $\boldsymbol{L} = p\boldsymbol{L}_{mn}$, where $p$ is defined in Eq. (6.10) through the filling factor.

With these definitions, it is easy to see that the Fock states $|j_1, j_2, \cdots, j_N\rangle$ are eigenstates of $\tilde{T}_i(pnb\boldsymbol{e}_y)$. We have:

$$\tilde{T}_i(pnb\boldsymbol{e}_y)\,|j_1, j_2, \cdots, j_N\rangle = \exp(2\pi i q n \tilde{J}/N_\Phi)\,|j_1, j_2, \cdots, j_N\rangle\,, \tag{6.17}$$

with $\tilde{J} = \sum_i j_i$. Thus, a quantum number which characterizes the state is $\tilde{J}$ mod $(N_\Phi/q)$. However, one might also define a center-of-mass translation $T_{\mathrm{cm}}(\boldsymbol{L}) = \prod_i T_i(\boldsymbol{L})$, which leaves the single-particle states invariant for $\boldsymbol{L} = \boldsymbol{L}_{mn}/N_\Phi$. From this we find that each subspace with fixed $\tilde{J}$ mod $(N_\Phi/q)$ can further be divided in $q$ equivalent subspaces which are connected through a center-of-mass translation. We then obtain as a quantum number $J = \tilde{J}$ mod $N_\Phi$. We have already encountered this quantum number when writing down the Hamiltonian in Eq. (6.14) in second-quantized notation. For the exact diagonalization, we can thus restrict the Hilbert space to a fixed $J$, reducing significantly the dimension of the space. Of course, to fully describe the system, we have to repeat the calculation in all subspaces $J$. However, from the center-of-mass symmetry we directly know that the spectra within $J$ and $J + n\frac{N_\Phi}{q}$ must be identical. This allows to reduce the number of necessary calculations, or alternatively to crosscheck the correctness of the applied code.

So far we have only considered the relative translational symmetry in $y$-direction. This symmetry is easy to exploit, as the Fock basis is an eigenbasis of it. For translations in $x$-direction, the situation is more complicated, as the translation maps one Fock state onto another:

$$\tilde{T}_i(pma\boldsymbol{e}_x)\,|j_1, j_2, \cdots, j_N\rangle = |j_1 - qm, j_2 - qm, \cdots, j_N - qm\rangle\,. \tag{6.18}$$

To exploit this symmetry, we thus have to construct linear combinations of different Fock states which are eigenstates of $\tilde{T}_i(pma\boldsymbol{e}_x)$. From Eq. (6.18) it is clear that by repeatedly applying $\tilde{T}_i(pma\boldsymbol{e}_x)$, we will at most reach $N_\Phi/q$ different states, and then come back to the original one. This defines a class of states, labeled by $c$, and having $|c| \leq N_\Phi/q$ members. For simplicity, let us denote these Fock states by $|c, m\rangle$, with $m$ running from 0 to $|c| - 1$. In this notation, Eq.

(6.18) just reads

$$\tilde{T}_i(mka\boldsymbol{e}_x)\,|c,0\rangle = |c,m\rangle\,. \tag{6.19}$$

A sum over all the states in a class then obviously will be an eigenstate of $\tilde{T}_i(pma\boldsymbol{e}_x)$. It will also be an eigenstate of $\tilde{T}_i(pnb\boldsymbol{e}_y)$, since

$$\left(\sum_i j_i - qm\right) \bmod N_\Phi = \left(\sum_i j_i\right) \bmod N_\Phi.$$

To fully cover the Hilbert space, we will need $|c|$ linearly independent combinations of these states. This can be achieved by multiplying each state $|c,m\rangle$ with an $m$-dependent phase factor $\exp(2\pi ism/|c|)$. Varying $s$ from 0 to $|c|-1$, we will get the $|c|$ linear combinations we need:

$$|c,(s,J)\rangle \equiv \frac{1}{\sqrt{|c|}} \sum_{k=0}^{|c|-1} \exp\left(\frac{2\pi isk}{|c|}\right) |c,k\rangle\,. \tag{6.20}$$

We can easily convince ourselves that these states are eigenstates of $\tilde{T}_i(pma\boldsymbol{e}_x)$. Applying this operator, every state in the sum is mapped onto another one, $|c,k\rangle \to |c,k+m\rangle$, and by factoring out a phase $\exp\left(-\frac{2\pi ism}{|c|}\right)$, we recover the original state. This phase factor is the corresponding eigenvalue. Considering shifts from one cell into the neighboring cell, i.e. choosing $m=1$, we see that all these phases are distinct for different $s$. This allows to use $s$ as a quantum number to classify the states. Thus, the states given by Eq. (6.20) represent the most convenient basis for studying the system on the torus. Using this basis, we can divide the Hilbert space into blocks with fixed $J$ and $s$. We will therefore work in the basis of Eq. (6.20).

For deriving Eq. (6.20), we have widely followed the recipe given in Ref. [50]. However, we shall stress here that in this reference the exponential is given by $\exp\left(\frac{2\pi isqk}{N_\Phi}\right)$ with $s$ running from 0 to $\frac{N_\Phi}{q}-1$, yielding wrong results if classes $c$ with $|c| < N_\Phi/q$ exist.

Finally, let us note that the quantum numbers $J$ and $s$ can be related to a pseudomomentum $\boldsymbol{K}$:

$$\boldsymbol{K}\lambda = \sqrt{\frac{2\pi b}{N_\Phi a}}\left(s - s_0, \frac{a}{b}(J - J_0)\right). \tag{6.21}$$

The quantum numbers of zero pseudomomentum are defined as the point in the Brillouin zone with highest symmetry. In most cases, $(s_0, J_0) = (0, 0)$, but if $N$ is even and $p$ and $q$ are both odd, other values become possible [50].

## 6.3 Spin singlet states

Now we have introduced all the concepts and definitions, which allow to diagonalize in the most effective way the Hamiltonian $\mathcal{H}$, given by Eq. (6.14), in a toroidal geometry. For the rest of the chapter, if not specified differently, the torus will be chosen as a periodic square, i.e. with periodicities $a = b$. For every calculation, we fix the filling factor $\nu = N/N_\Phi$ by defining particle number $N$ and number of magnetic fluxes $N_\Phi$. Also the two quantum numbers $s$ and $J$, defining the Haldane momentum $\boldsymbol{K}$ according to Eq. (6.21) are fixed. As the interaction in Eq. (6.14) does not flip the spin of the particles, we can also fix the spin polarization $S = N_\uparrow - N_\downarrow$, where $N_\uparrow$ ($N_\downarrow$) denotes the number of spin-up (spin-down) particles.

In this section, we are interested in the spin polarization of the ground state. Most likely, this quantity will depend on the concrete choice of all interaction parameters $g_{s_1 s_2}$. Let us start with spin-independent interactions, i.e. $g_{s_1 s_2} = g$. Here, we will be able to show that the states with $S = 0$ are energetically favored, resulting in a spin singlet configuration of the ground states for most of the filling factors. Let us also note that the SU(2) symmetric interaction is a natural choice, as many experiments [114, 115] work with the $|F = 1, m_F = 0, 1\rangle$ states of $^{23}$Na, or the $|F = 1, m_F = -1\rangle$ and $|F = 2, m_F = 1\rangle$ states of $^{87}$Rb with almost equal s-wave scattering lengths within and between the components.

The mechanism which favors $S = 0$ can nicely be identified by comparing this configuration with its opposite, the fully polarized regime, $|S| = N$. There, the results from one-component gases are recovered (cf. Chapter 4, and Ref. [79]), with incompressible phases at $\nu = k/2$, forming the Read-Rezayi series. The fully polarized zero-energy state with highest filling has $\nu = 1/2$, and is the Laughlin state, Eq. (3.6). In the fully unpolarized system, however, zero-energy states occur up to $\nu = 2/3$, where the 221-Halperin state [cf. Eq. (3.15)] is the exact unique ground state of the two-body contact interaction. The analytic expression

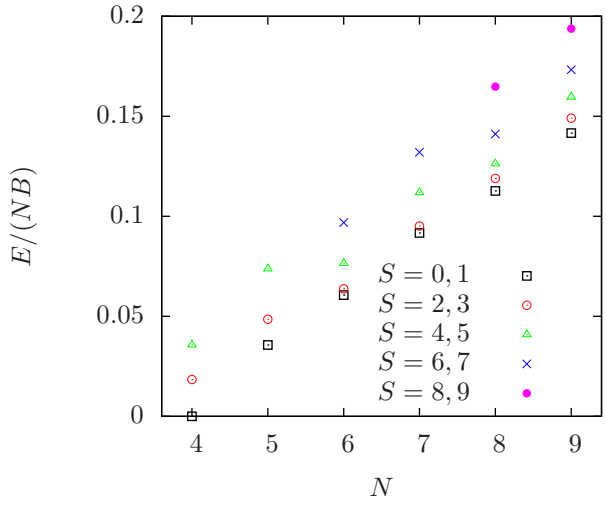


FIGURE 6.1: Ground state energies, not showing possible degeneracies, at $N_\Phi = 6$ for different $N$ and $S$ subspaces with $g_{s_1 s_2} = g$. Even (odd) values of $S$ correspond to even (odd) $N$.

of this state on a disk reads

$$\Psi_{\mathrm{H}} = \prod_{i<j}^{N_\uparrow} (z_{i\uparrow} - z_{j\uparrow})^2 \prod_{k<l}^{N_\downarrow} (z_{k\downarrow} - z_{l\downarrow})^2 \prod_{i,k} (z_{i\uparrow} - z_{k\downarrow}), \tag{6.22}$$

where we omit the irrelevant exponential term $\exp\left(-\sum |z_i|^2/4\right)$. This wave function vanishes whenever two particles are at the same position, and it is symmetric under exchange of two spin-up or two spin-down particles. However, it is antisymmetric under exchange of particles with different spin, and thus cannot be used for describing spinless bosons. For this case, also the terms in the last product had to be squared, which would result in a less dense Laughlin-like wave function. Generalizing this observation, we state that any spatial wave function which solves the fully polarized problem must also be a solution for $|S| < N$, while the opposite is not true. Thus, for a spin-independent interaction, it strictly follows for the ground state energies $E(S_i)$ with $|S_1| < |S_2|$ that $E(S_1) \leq E(S_2)$.

Our numerical data, partially shown in Fig. 6.1, supports this finding. In fact, in all cases we have investigated, the ground state of the $S = 2$ subspace occurs in the spectrum of $S = 0$ as a low-lying excitation, except for $N = 6$ and $N_\Phi = 8$, where we have a degeneracy, $E(S = 0) = E(S = 2)$. In most cases, thus, the ground state has uniquely $S = 0$, which makes it a singlet.

The mechanism behind this observation are anticorrelations of the form $z_{i\uparrow} - z_{k\downarrow}$, fully avoiding contact interactions of a $\uparrow\downarrow$-pair due to a single zero in the wave function, whereas similar anticorrelations become possible for particles with equal spin only to the power of 2 or higher, increasing the angular momentum of the system, or, respectively, the filling factor.

One of the key features of quantum gases are Feshbach resonances which allow to tune their interaction strengths at will. We can use them to tune the spin-dependency of interactions (cf. [7]). Obviously, increasing $g_{\uparrow\downarrow}$ while leaving $g_{\uparrow\uparrow} = g_{\downarrow\downarrow} = g$ should favor spin polarizations with less $\uparrow\downarrow$-pairs. However, we find that this does not necessarily drive the system into the fully polarized configuration: As shown in Fig. 6.2 for $N = 6$ at $\nu = 1$, the energy of even the fully unpolarized system saturates for large $g_{\uparrow\downarrow}$. In this limit, the real ground state has $S = 2$ and $E = 0.449$ (in units of $gB$), close to the $S = 0$ and $S = 4$ ground states with $E = 0.466$ and $E = 0.475$. All of them are well separated from the fully-polarized ground state with $E = 0.581$. In contrast to this, the energy of spin-unpolarized systems will never saturate at larger filling, as is shown in Fig. 6.2 for $\nu = 6/5$. This different behavior is understood by noting that for $\nu = 1$ the number of available zeros in the wave function is sufficient to completely suppress interactions between pairs of different spins, $\langle E_{\uparrow\downarrow}\rangle \to 0$, while it is not for larger $\nu$. Jumps in the curve of $\langle E_{\uparrow\downarrow}\rangle$ as a function of $g_{\uparrow\downarrow}$ show that the states with $\langle E_{\uparrow\downarrow}\rangle = 0$ are reached by several abrupt re-organizations of the ground states. We note that once the state with $\langle E_{\uparrow\downarrow}\rangle = 0$ is obtained, this state must be an eigenstate for arbitrary $g_{\uparrow\downarrow}$. Thus, by abruptly switching off the interspin interaction, one could produce binary mixtures of highly entangled, non-interacting systems.

## 6.4 Incompressible phases and NASS states

In this section we investigate whether, in analogy to the RR states for spin polarized systems, incompressible states can be found amongst the spin singlet ground states. Since incompressibility is connected to a discontinuity in the chemical potential, we define the particle-hole excitation gap as

$$\Delta(N) = N\left(\frac{E(N+1)}{N+1} + \frac{E(N-1)}{N-1} - 2\frac{E(N)}{N}\right). \tag{6.23}$$

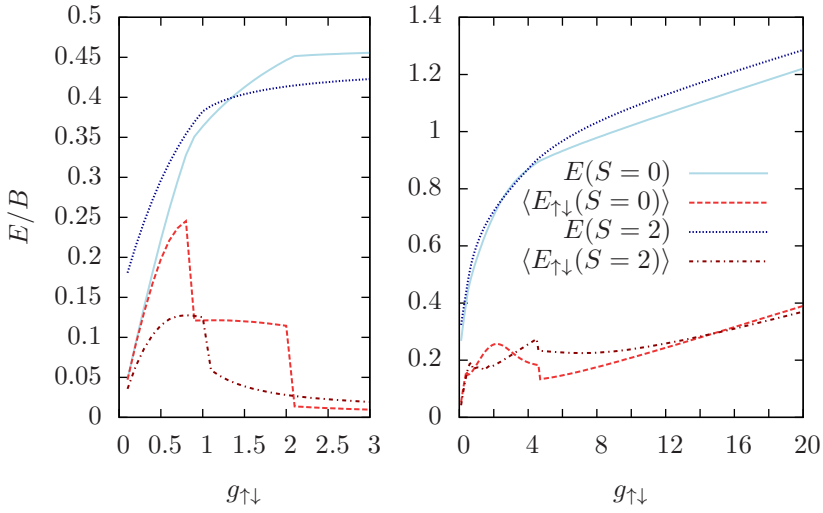


FIGURE 6.2: Interaction energy for $N = 6$ and $S = 0, 2$ as a function of $g_{\uparrow\downarrow}$. **Left:** $N_\Phi = 6$. **Right:** $N_\Phi = 5$.

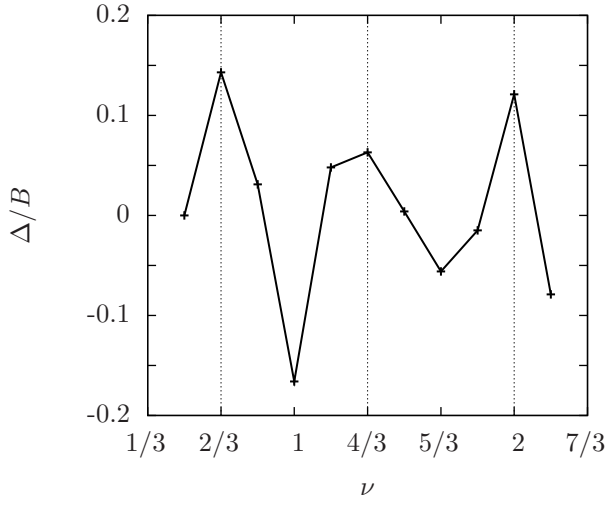


FIGURE 6.3: $\Delta$ as defined in Eq. (6.23) as a function of $\nu$, for $N_\Phi = 6$ and $g_{s_1 s_2} = g$.

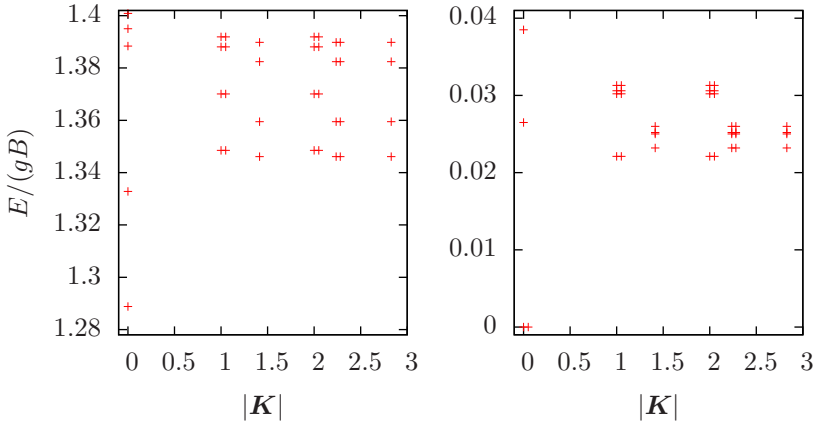


FIGURE 6.4: Energy spectra for $N = 12$ particles with total spin $S = 0$ at filling $\nu = 4/3$. **Left:** For two-body contact interaction. **Right:** For three-body contact interaction. In both cases, all interaction parameter are chosen equally, $g > 0$. We do not show the three-fold center-of-mass degeneracy, but visualize further degeneracies by slight shifts in $\boldsymbol{K}$.

This quantity is plotted for $N_\Phi = 6$ in Fig. 6.3. Upwards peaks correspond to downward cusps in the energy as a function of $\nu$, and signal incompressible phases. They occur at fillings $\nu = 2k/3$ with $k \in \mathbb{N}$. For these fillings, a series of singlet states being exact zero-energy eigenstates of a $(k+1)$-body contact interaction is known [68]. For $k = 1$, this is the 221-Halperin state, which has Abelian excitations, while the states for $k > 1$ are predicted to have non-Abelian excitations, which established the name NASS series.

We first construct these states for $k = 2$ and 3 by diagonalizing the three- and four-body contact interaction for up to $N = 12$ particles: The spectra with ground states and low-lying excitations are shown on the right side of Figs. 6.4 and 6.5. They serve as a "fingerprint" of the topological phase, where possible degeneracies of the ground state due to the torus geometry can be used to classify the phase [126]. As predicted by conformal field theory (CFT), we find the NASS states being characterized by a $(k+1)(k+2)/2$-fold topological degeneracy on the torus. A subtlety occurs at $k = 3$, where the CFT construction [68], being restricted to $N = 2kp$ with $p \in \mathbb{N}$, is not able to predict zero-energy ground states for all $N$ which are possible at $\nu = 2$. In fact, we find zero-energy states also for $N = 8$ and 10, but, in contrast to the states with $N = 6$ and 12 which have the predicted ten-fold degeneracy, they are non-degenerate, and thus belong to a different topological phase.

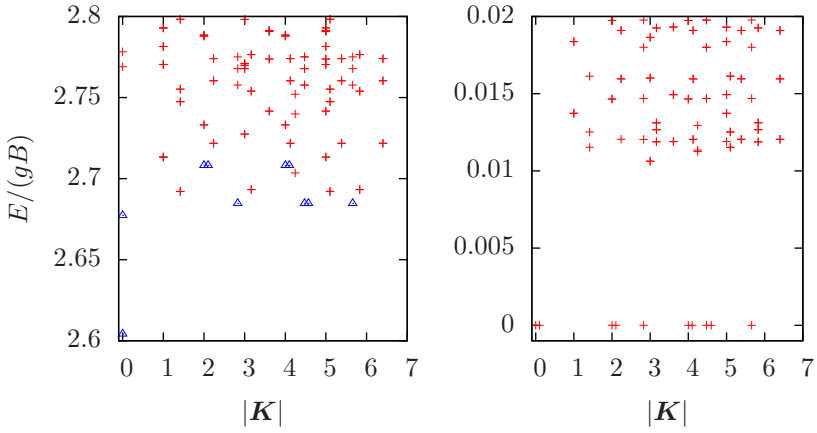


FIGURE 6.5: Energy spectra of for $N = 12$ particles with total spin $S = 0$ at filling $\nu = 2$. **Left:** For two-body contact interaction. **Right:** For four-body contact interaction. In both cases, all interaction parameter are chosen equally, $g > 0$. The eigenstates of two-body interaction which correspond to the ten ground states of four-body interaction (with respect to $\boldsymbol{K}$) are highlighted by a blue triangle. By slight shifts in $|\boldsymbol{K}|$, we visualize all of these ten states, while some of them would elsewise appear as a single point in the spectrum.

Next, we diagonalize the two-body contact interaction of our actual Hamiltonian $\mathcal{H}$, and calculate the overlaps between the ground states of $\mathcal{H}$ and the NASS states. They are given in Table 6.1, and turn out to be significant: For $k = 2$, the states are exactly equal for $N = 4$, and even for a relatively large-sized system with $N = 12$ the overlaps are still around 0.8. Such a decrease of the overlap with large $N$ also occurs in the case of the RR states in single-component systems with two-body contact interaction [29]. But one has to note that a topological *phase* is a whole class of states, which makes the overlap a weak criterion in the thermodynamic limit [126]. By the above mentioned topological degeneracies, however, one should be able to classify the topology of a state, especially as an eventual lifting of the topological degeneracy in finite systems should vanish in the thermodynamic limit.

In the case of $\nu = 4/3$ we find a strong lifting of this degeneracy (see Fig. 6.4 left), but we may consider the fact that the six lowest eigenstates of $\hat{\mathrm{H}}$ agree in their Haldane momenta $\boldsymbol{K}$ with the ones of the sixfold degenerate three-body eigenstates as a signal for belonging to the same topological phase. As can be inferred from Table 6.1, both the gap above the $\boldsymbol{K} = \boldsymbol{0}$ states and the degeneracy splitting behave non-monotonic. Additional numerical support for the two- and

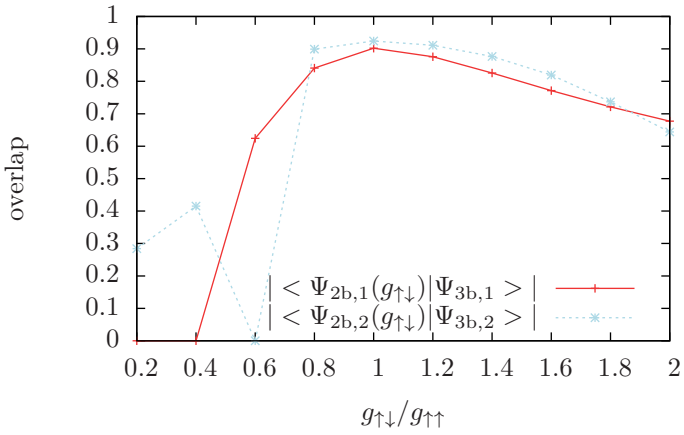


FIGURE 6.6: Overlaps between the ground-states of two-body contact interaction at filling $\nu = 4/3$ with $N = 8$ with the NASS state as a function of the interspin interaction strength $g_{\uparrow\downarrow}$.

the three-body ground state being in the same topological phase was given by S. Furukawa and M. Ueda [128]. They showed that the spectral structure becomes more robust under variation of the torus ratio for larger $N$.

While all this indicates that the $\nu = 4/3$ NASS phase can be obtained in a system with two-body contact interaction, the situation is different for $\nu = 2$. As shown in the left side of Fig. 6.5, the candidates for the degenerate ground state manifold mix up with excited states. Although most of the states have relatively high overlaps with the NASS state obtained as zero-energy state of four-body contact interaction (see Table 6.1), the discrepancies in the spectral structure suggest that the two-body interacting system is in a different phase than the four-body interacting system at $\nu = 4/3$.

For the experimental feasibility of realizing the $\nu = 4/3$ NASS to be high, it should be robust with respect to deviations from the SU(2)-symmetric interaction. In the case of a $(k+1)$-body contact interaction at $\nu = 2k/3$, the numerical values of each interaction parameter do not influence the ground states. Though this is different for two-body contact interaction at $\nu = 4/3$, the overlaps with the NASS states remain high within a wide range of $g_{\uparrow\downarrow}/g$, and have a maximum in the SU(2)-symmetric configuration. For $N = 8$, all overlaps are above 0.8 if $g_{\uparrow\downarrow}/g \in [0.8, 1.6]$. This observation is illustrated in Fig. 6.6.

| $N, N_\Phi$ | $\boldsymbol{K}$ | $\lvert\langle 2\text{b}\rvert\ 3\text{b}\rangle\rvert$ | $E_{2\text{b}}$ | $N, N_\Phi$ | $\boldsymbol{K}$ | $\lvert\langle 2\text{b}\rvert\ 4\text{b}\rangle\rvert$ | $E_{2\text{b}}$ |
|---|---|---|---|---|---|---|---|
| 4,3 | (0,0) | 1 | 0.435 | 12,6 | (0,0) | 0.334 | 2.604 |
| | | 1 | 0.520 | | | 0.828 | 2.677 |
| 8,6 | (0,0) | 0.906 | 0.901 | | (0,2) | 0.775 | 2.708 |
| | | 0.920 | 0.908 | | (0,4) | 0.775 | 2.708 |
| 12,9 | (0,0) | 0.729 | 1.289 | | (2,0) | 0.775 | 2.708 |
| | | 0.885 | 1.333 | | (2,2) | 0.646 | 2.685 |
| | | | | | (2,4) | 0.646 | 2.285 |
| | | | | | (4,0) | 0.775 | 2.708 |
| | | | | | (4,2) | 0.646 | 2.685 |
| | | | | | (4,4) | 0.646 | 2.685 |

TABLE 6.1: Overlaps between zero-energy eigenstates of $(k+1)$-body interaction with corresponding eigenstates of the two-body contact interaction at energy $E_{2\text{b}}$ (in units of $gB$) and Haldane momentum $\boldsymbol{K}$ (in units of $2\pi\hbar/a$). All states at filling $\nu = 4/3$ have an additional three-fold center-of-mass degeneracy.

## 6.5 Effects of spin-orbit coupling

Given the pseudospin degree of freedom, it is natural to ask how a coupling of this internal degree of freedom to the external motion of the particle will affect the system. In solids, this coupling represents a common scenario, as real spins interact due to their magnetic moment with the real magnetic fields induced by the motion of the electronic charge in the electromagnetic field of the nuclei.. It can be taken into account by a non-Abelian gauge potential. Choosing a coupling which is equivalent to the Rashba coupling [75], the total gauge potential, consisting of the magnetic vector potential from the previous section and the spin-orbit (SO) coupling, is given by

$$\boldsymbol{A} = B(0, x, 0)\mathbb{1} + q(\sigma_x, \sigma_y). \tag{6.24}$$

Here, the strength of the SO coupling is controlled by the parameter $q$, and $\sigma_i$ are Pauli matrices.

The gauge potential of Eq. (6.24) has the same form as the more general gauge potential of Eq. (3.31) which we have already discussed in Section 3.2.2.1. There we had distinguished between isotropic and anisotropic potentials, where the latter had been treated via a squeezing transformation in Section 3.2.2.2, using the fact that there is one uncoupled LL, which in the fermionic system can be chosen to be the lowest not completely filled LL. Since the energetically lowest

LL turns out to be a coupled one, the procedure of Section 3.2.2.2 would not work for bosons. With the isotropic choice of Eq. (6.24), however, this poses no problem. As shown by M. Burrello and A. Trombettoni [41, 122], the single-particle Hamiltonian can in this case be solved analytically in closed form. The solution yields new LLs which are superpositions of solely two levels of the Abelian problem.

To see this explicitly, we can proceed in the same way as in Section 3.2.2.1, but taking as annihilation and creation operators the ones defined in Eq. (6.1). We then obtain the single-particle Hamiltonian

$$H_{\mathrm{sp}} = \begin{pmatrix} 2B(c^\dagger c + \frac{1}{2}) + 2q^2 & 2\sqrt{2B}qc \\ 2\sqrt{2B}qc^\dagger & 2B(c^\dagger c + \frac{1}{2}) + 2q^2 \end{pmatrix}. \tag{6.25}$$

The diagonal part imposes the LL structure with the functions $\Psi_{n,j}$ from Eq. (6.8) being eigenfunctions in both components. Since the off-diagonal terms raise or lower the LL quantum number $n$, the eigenspinors must be of the form

$$\mathbf{\Psi}^{\pm}_{n,j} \equiv (\alpha^{\pm}_n \Psi_{n,j}, \beta^{\pm}_n \Psi_{n+1,j})^T, \tag{6.26}$$

where $\alpha^{\pm}_n$ and $\beta^{\pm}_n$ are functions of $q$ [41]. With this, we directly find the spectrum of the system:

$$E^{\pm}_n = 2B(n+1) + 2q^2 \pm \sqrt{B^2 + 8Bq^2(n+1)}. \tag{6.27}$$

For all finite $q$ and $B$, the ground state solution is given by either a single $E^-_n$, so the former spin degeneracy is lifted, or by two degenerate $E^-_n$ and $E^-_{n+1}$, cf. Fig. 6.7. The latter happens at $q^2/B = 2n+3$, around which it becomes necessary to include two LLs in the many-body problem, as the gap between the LLs becomes very small or even vanishes. The solutions corresponding to $E^+_n$, however, are always at higher energies, so they never play a role. The coefficients $\alpha^-_n$ and $\beta^-_n$ are given by

$$\alpha^-_n = N\left(B + 2q\sqrt{2B(n+1)} + \sqrt{B^2 + 8Bq^2(n+1)}\right), \tag{6.28}$$

$$\beta^-_n = N\left(B - 2q\sqrt{2B(n+1)} - \sqrt{B^2 + 8Bq^2(n+1)}\right), \tag{6.29}$$

$$N = \left(2\sqrt{B^2 + 8Bq^2(n+1) + 2q\sqrt{2B(n+1)}\sqrt{B^2 + 8Bq^2(n+1)}}\right)^{-1}. \tag{6.30}$$

The multiplication with $N$ normalizes the spinors to 1.

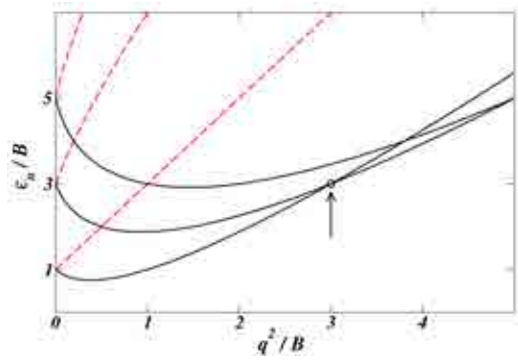


FIGURE 6.7: LL energies as a function of the SO coupling strength: The solid lines refer to the solutions with $E_n^-$, the red dashed lines to the solutions $E_n^+$, cf. Eq. (6.27). While within a wide range, only one "minus" solutions forms the LLL, at a certain SO coupling strength (marked by the arrow), two such solutions become degenerate. Reprinted from: [41].

We then have to calculate the interaction matrix $V_{\mu\nu\sigma\tau}$ with respect to the eigenspinors $\mathbf{\Psi}^-_{n,j}$:

$$V_{\mu\nu\sigma\tau} = \frac{1}{2}\int \mathrm{d}^2 z_1\ \mathrm{d}^2 z_2 \mathbf{\Psi}^{-\dagger}_{n_\mu,j_\mu}(z_1)\mathbf{\Psi}^{-\dagger}_{n_\nu,j_\nu}(z_2)V(z_1,z_2)\mathbf{\Psi}^-_{n_\sigma,j_\sigma}(z_1)\mathbf{\Psi}^-_{n_\tau,j_\tau}(z_2). \tag{6.31}$$

Again we take two-body contact interactions, so we have to evaluate

$$\begin{aligned} V_{\mu\nu\sigma\tau} = \Big\{ & g_{\uparrow\uparrow}\alpha_{n_\mu}\alpha_{n_\nu}\alpha_{n_\sigma}\alpha_{n_\tau}\int \mathrm{d}^2 z\ \bar{\Psi}_{n_\mu,j_\mu}(z)\bar{\Psi}_{n_\nu,j_\nu}(z)\Psi_{n_\sigma,j_\sigma}(z)\Psi_{n_\tau,j_\tau}(z) \\ & + g_{\downarrow\downarrow}\beta_{n_\mu}\beta_{n_\nu}\beta_{n_\sigma}\beta_{n_\tau}\int \mathrm{d}^2 z\ \bar{\Psi}_{n_\mu+1,j_\mu}(z)\bar{\Psi}_{n_\nu+1,j_\nu}(z)\Psi_{n_\sigma+1,j_\sigma}(z)\Psi_{n_\tau+1,j_\tau}(z) \\ & + g_{\uparrow\downarrow}\alpha_{n_\mu}\beta_{n_\nu}\alpha_{n_\sigma}\beta_{n_\tau}\int \mathrm{d}^2 z\ \bar{\Psi}_{n_\mu,j_\mu}(z)\bar{\Psi}_{n_\nu+1,j_\nu}(z)\Psi_{n_\sigma,j_\sigma}(z)\Psi_{n_\tau+1,j_\tau}(z) \\ & + g_{\downarrow\uparrow}\beta_{n_\mu}\alpha_{n_\nu}\beta_{n_\sigma}\alpha_{n_\tau}\int \mathrm{d}^2 z\ \bar{\Psi}_{n_\mu+1,j_\mu}(z)\bar{\Psi}_{n_\nu,j_\nu}(z)\Psi_{n_\sigma+1,j_\sigma}(z)\Psi_{n_\tau,j_\tau}(z)\Big\}/2. \end{aligned} \tag{6.32}$$

In Eq. (6.16), we have already provided formulas how to evaluate each of these integrals above for $n_\mu \leq 2$.

In the following, we will restrict ourselves to a SO coupling strength around the degeneracy point at $q^2/B = 3$, thus we will have to take into account the LLs $\mathbf{\Psi}^-_{0,j}$ and $\mathbf{\Psi}^-_{1,j}$. The Hamiltonian from Eq. (6.14) can then be mapped onto

the new problem just by identifying the spin quantum number of the previous case with the $n$ quantum number. Similarly, we can map between the old basis, constructed from the states $\Psi_{0,j}\,|\uparrow\rangle$ and $\Psi_{0,j}\,|\downarrow\rangle$, and the new basis, which has to be constructed from the single-particle states $\mathbf{\Psi}^{-}_{0,j}$ and $\mathbf{\Psi}^{-}_{1,j}$. We will describe this mapping in more detail in the next subsection.

In principle, the Hamiltonian can now be diagonalized as before, but some important differences should be stressed. First we note that now also single-particle energies given by Eq. (6.27) have to be taken into account, as long as we are not precisely on the degeneracy point. However, this poses no problem, as these energies are known analytically from Eq. (6.27), and thus can be directly evaluated for each many-body state just by considering the population numbers $N_0$ of particles in $\mathbf{\Psi}^{-}_{0,j}$ and $N_1$ of particles in $\mathbf{\Psi}^{-}_{1,j}$.

More important is the fact that now the analog of spin polarization, $S = N_\uparrow - N_\downarrow$, is the population imbalance, $P \equiv N_0 - N_1$. But while the interaction of Eq. (6.15) conserves the spin polarization $S$, the interaction matrix given by Eq. (6.32) does not conserve $P$. This makes the SO coupled problem numerically much more costly, as all subspaces from $-N \leq P \leq N$ need to be taken into account.

The situation becomes simpler, however, if we are sufficiently far away from the degeneracy point. As we have confirmed by explicit calculation, for a wide range of $q^2/B$ the LL gap is large enough, to make a LLL assumption, i.e. completely neglect the state $\mathbf{\Psi}^{-}_{1,j}$ for $q^2/B \lesssim 3$, or the state $\mathbf{\Psi}^{-}_{0,j}$ for $q^2/B \gtrsim 3$. Then we have $P = N$ (or $P = -N$), and we expect states which are similar to the fully polarized states, i.e. the Laughlin state or other states of the Read-Rezayi series discussed in Section 3.1.2.2. Based on general arguments, the occurrence of Laughlin-like or Moore-Read-like states in the SO coupled system has been predicted in Refs. [41, 122]. Numerical evidence herefore has also been provided in Refs. [123, 124]. The latter works, however, do not go beyond the LLL approximation, and thus are valid only in those regions where the LL gap is sufficiently large. In the following, we will be interested in what happens when we approach the first degeneracy point $q^2/B = 3$.

### 6.5.1 Laughlin-like states

#### 6.5.1.1 At filling $\nu = 1/2$.

In this section, we investigate the occurrence of Laughlin-like in the SO coupled system. We therefore first fix the filling factor to the value $\nu = 1/2$. For the one-component system, as discussed in Chapter 4, the Laughlin state at this filling is an exact solution with zero energy in the case of contact interactions. As argued before, also the two-component system behaves similarly, if the SO coupling lifts the degeneracy between two LLs. In order to compare the ground state of the SO coupled system with the original Laughlin state, we shall map between the distinct LL structures.

Performing such a mapping is trivial in the many-body Fock basis: Without SO coupling, we encountered single-particle states which are fully described by the quantum numbers $n_i$, $j_i$, and $s_i$. Due to the LL gap, a restriction to the LLL, i.e. $n_i = 0$ was justified. The spin quantum number takes two values, say 0 for $\uparrow$ and 1 for $\downarrow$. The Fock states are given by a ket $|j_1, s_1; j_2, s_2; \ldots; j_N, s_N\rangle$. The single-particle states in the SO coupled system are characterized by the quantum numbers $n_i$ and $j_i$. Furthermore, in Eq. (6.27) we found two kinds of solutions which we distinguished by the index $\pm$ as a third quantum number. The structure of the energy spectrum around $q^2/B \approx 3$ allowed to restrict ourselves on the minus solutions, and consider only $n_i = 0$ or 1. The resulting Fock states $|n_1, j_1; n_2, j_2; \ldots; n_N, j_N\rangle$ then simply map one-to-one onto $|j_1, s_1; j_2, s_2; \ldots; j_N, s_N\rangle$ just by identifying $s_i$ with $n_i$.

Since the upper component of $\mathbf{\Psi}^-_{n,j}$ reads $\alpha^-_n \Psi_{n,j}$ according to Eq. (6.26), this mapping is equivalent to filtering out the lower spin component and renormalizing to one. We denote this mapping by a projection operator $\mathcal{P}$ acting as

$$|n_1, j_1; n_2, j_2; \ldots; n_N, j_N\rangle = \mathcal{P}\,|j_1, s_1; j_2, s_2; \ldots; j_N, s_N\rangle \quad \text{with} \quad n_i = s_i. \tag{6.33}$$

With this, applying the operator $\mathcal{P}$ to the Laughlin state, which is given in terms of $|j_1, s_1; j_2, s_2; \ldots; j_N, s_N\rangle$, yields a new state in the SO coupled basis. We may choose for the Laughlin state all $s_i = 0$, so we obtain a state with all $n_i = 0$, but as well we might take $s_i = 1$, which yields a state with $n_i = 1$. While the first choice amounts for comparing the upper component of the SO-coupled ground state with the original Laughlin state, the latter choice can be seen as a

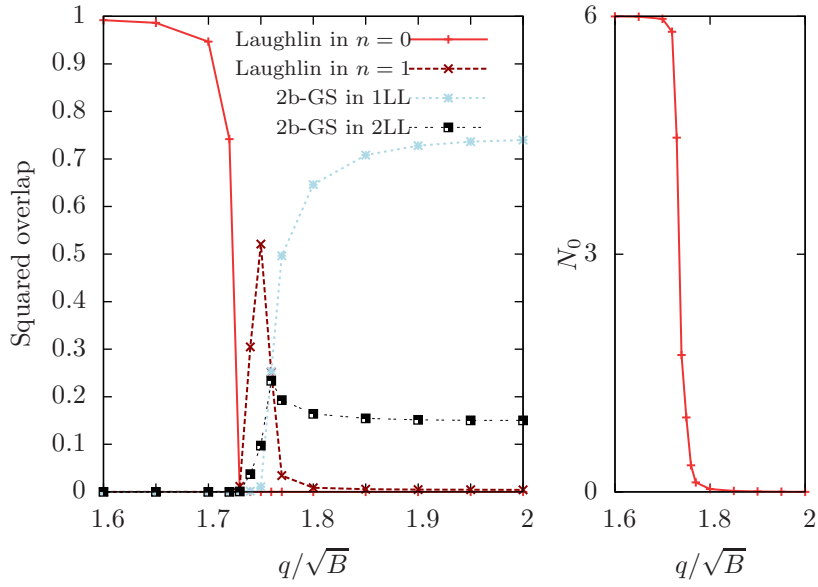


FIGURE 6.8: **Left:** Overlap of ground state with different test states as further explained in the text: Laughlin projections, and ground states of two-body contact interaction in the first and second excited LL. The system size is $N = 6$ at half filling, with spin-independent interactions $g_{s_1 s_2} = 0.2$. **Right:** Occupation of $n = 0$ level.

comparison between the upper component of the SO-coupled ground state with a state which is obtained from the Laughlin state by shifting it into the first excited LL, i.e. just by raising all LL quantum numbers by one.

We note that this "raised" Laughlin state poorly represents the ground state of two-body contact interaction of a one-component system restricted to the first-excited LL. We have calculated the true first LL ground state, denoted by $\Psi_{1\mathrm{LL}}$, for a comparison with the ground state of the SO coupled system. Since also the second-excited LL is involved in the lower component of $\mathbf{\Psi}^{-}_{1,j}$, we have also calculated the ground state of two-body contact interaction restricted to the second-excited LL, $\Psi_{2\mathrm{LL}}$. For the comparison in Fig. 6.8, these states, $\Psi_{1\mathrm{LL}}$ and $\Psi_{2\mathrm{LL}}$, are projected onto the LL structure of the SO coupled problem via Eq. (6.33), making the choice $s_i = 1$, as these states should become relevant only after the LL crossing, i.e. when the single-particle ground states are the states $\mathbf{\Psi}^{-}_{n_i,j_i}$ with $n_i = 1$.

The overlaps between the projected test states and the ground state of the SO coupled are shown in Fig. 6.8 as a function of $q/\sqrt{B}$. On the right side of this figure, we also show how the occupation number $N_0$ decreases when passing through the degeneracy point. In the plots, we have chosen an SU(2) symmetric choice for the interaction parameters. For $q/\sqrt{B} \lesssim \sqrt{3}$, our study agrees with the results from [123], as the LL state projected onto $n_i = 0$ is up to a high fidelity the ground state of the SO coupled system. None of the test states, however, is able to describe the system precisely at the degeneracy point. For a small range above the degeneracy point, the projection of the Laughlin state onto $n_i = 1$ turns out to have high overlap with the exact ground state. The system organizes in a non-Laughlin-like way for larger coupling strengths. It is the ground state of two-body contact interaction within the first excited LL which then becomes a good trial state. Interestingly, this state has no significant overlap with the Laughlin state shifted to the first excited LL. Similar curves are obtained when setting the intercomponent interactions to zero, i.e. choosing $g_{\uparrow\downarrow} = 0$.

The SO coupling therefore allows to study the behavior of bosons in higher LLs. This is particularly relevant with respect to fermionic systems, where higher LLs can be reached solely by filling the lower levels. In the field of strongly correlated electrons, very much attention has been paid to the Hall plateau at $\nu = 5/2$. For a spin-polarized system, this represents the situation of a half-filled first excited Landau level, which might be described by a Moore-Read-like wave function. It could thus be interesting to explore this regime also within bosonic systems.

More information about the different phases can be obtained from the excitation spectra. In the right side of Fig. 6.9, we show the low-lying excitation energies as a function of $q/\sqrt{B}$. On both sides of the degeneracy point, the system is gapped, while it is not at the degeneracy point. These gapped phases correspond to the configuration where good overlaps with the projected Laughlin states are obtained. Also the fact that the unique ground state (apart from the center-of-mass degeneracy) has Haldane momentum $\boldsymbol{K} = \boldsymbol{0}$, indicates the Laughlin-like behavior of the system. For larger $q/\sqrt{B}$, states at different Haldane momenta have almost the same energy. For $N = 6$ and SU(2) symmetric interactions, these are states with $\boldsymbol{K} = (0,0)$, $(2,0)$, $0,2)$, $(4,0)$, and $(0,4)$ (in units of $2\pi\hbar/a$ with $a$ the side of the square torus), while for $N = 5$ we find $\boldsymbol{K} = (0,0)$, $(1,0)$, $0,1)$, $(4,0)$, and $(0,4)$. Restricting ourselves to only one LL, which is justified in this regime by the reappearance of a gap, we have been able to extend our calculations to $N = 8$, where four states with $\boldsymbol{K} = (0,0)$, $(4,0)$, $0,4)$, and $(4,4)$

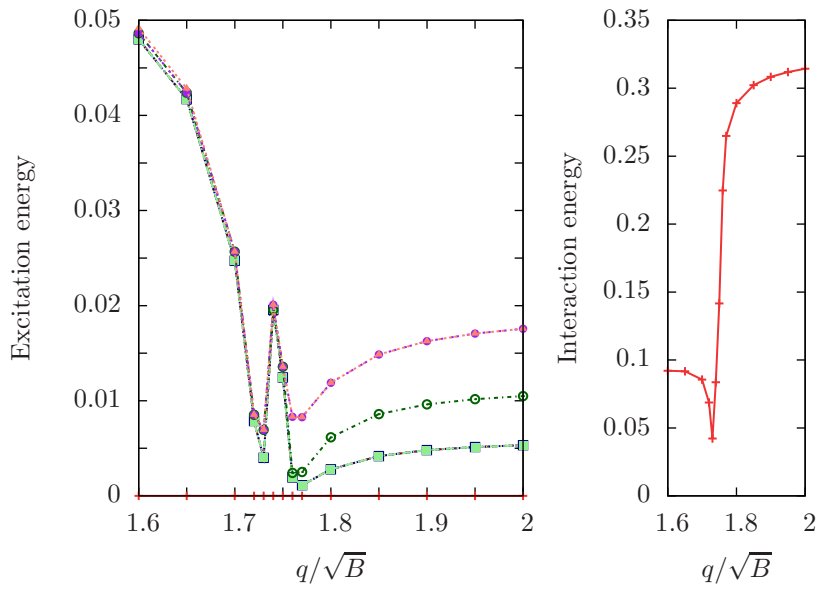


FIGURE 6.9: **Left:** Low-lying excitation energies. **Right:** Interaction energy of the ground state. System parameters are chosen as in Fig. 6.8. Energies are in units of $gB$.

form a degenerate ground state manifold. These observations suggest that in this regime phases with a broken translational symmetry occur, like crystalline phases or bubble phases [129–131]. Such phases have been discussed in the context of fermions as possible candidates for substituting the Laughlin state in higher Landau level. Due to the limited system sizes we can treat, this regime does not seem to be appropriately explored by means of exact diagonalization.

#### 6.5.1.2 At filling $\nu < 1/2$.

In spin-polarized systems, the Laughlin state at $\nu = 1/2$ is easily seen to be the ground state of two-body contact interactions, as the wave function vanishes when two particles are at the same position. In the SO coupled system, this is not the case. Mapping the $\nu = 1/2$ Laughlin state according to Eq. (6.33) to higher Landau levels induces effectively long range interaction [124]. The $\nu = 1/2$ Laughlin state acquires in general a positive interaction energy, as seen in the right side of Fig. 6.8. This is due to the fact that in the spin-orbit coupled Landau level the corresponding wave function does not vanish when $z_i \to z_j$.

However, as has been pointed out in Refs. [41, 122], Laughlin states with $\nu < 1/2$ remain states with zero interaction energy even after a mapping into the Landau level structure of the spin-orbit coupled system according to Eq. (6.33) with the choice $s_i = 0$. The resulting wave function describes a system with all atoms exclusively in the $|n = 0\rangle$ level. It thus represents the ground state for spin-orbit coupling strengths $q^2 \leq 3B$ at filling factor $\nu$.

We have explicitly checked for $\nu = 1/4$ (and $N = 3,\ 4$) that such a zero interaction energy state exists for $q^2 \leq 3B$. Also, no zero interaction energy states are found for $q^2 \leq 3B$ at filling factors larger than $\nu = 1/4$. In agreement with its Laughlin-like character, it is located at Haldane momentum $\boldsymbol{K} = (0, 0)$, and it is the unique ground-state for $q^2 < 3B$. Precisely at the degeneracy point, $q^2 = 3B$, additional states with zero interaction energy occur within a ground state manifold which then contains 7 (4) states for $N = 4$ ($N = 3$) at $\boldsymbol{K} = (0, 0)$, and additional states at different pseudomomenta.

The origin of one of the additional ground states at the degeneracy point can be traced back to the $\nu = 1/4$ Laughlin state. Therefore one has to note that every pair of coordinates appears with a $(1/\nu)$th order zero of the form $z_i - z_j$ in the wave function of Eq. (3.6). The mapping of Eq. (6.33) brings a state which lives in the LLL of the Abelian problem to state which, in terms of these Abelian LLs, occupies partly the first or even the second excited LL. This mapping is thus associated with a multiplication of the wave function with complex conjugate variables $z_i^*$, and with taking the derivatives $\partial_{z_i}$. The latter operation may affect the property of being a zero interaction energy state. But since in every term $(z_i - z_j)^{1/\nu}$ at most the second derivative $\partial_{z_i}\partial_{z_j}$ is taken, the mapping of Eq. (6.33) applied to the Laughlin wave function at filling $\nu$ yields a wave function where every pair of particles still has a zero of at least $(\frac{1}{\nu} - 2)$th order. For $\nu = 1/4$, this gives a second order zero, and thus still allows to raise the Landau level index of one particle from $n = 0$ to $n = 1$. This yields a second zero-energy state. This state is also present in the spectrum for $q^2 < 3B$, but there it appears as an excited state due to the occupation of an excited LL. The symmetry of this state is characterized by $\boldsymbol{K} = (0, 0)$. By lowering the quantum number of the particle in $n = 1$ to $n = 0$, we have been able to explicitly check that this state is the partially raised Laughlin state.

The other zero interaction energy states occuring at the degeneracy point do not exist in the spectrum for $q^2 < 3B$. They are not polarized with respect to the Landau level quantum number, that is, not all contributing Fock states contain

the same number of particles in each Landau level. Only at the degeneracy point such levels can be combined arbitrarily. This property allows for a larger number of ground states at the degeneracy point.

For larger spin-orbit coupling strengths, $q^2 > 3B$, the $\nu = 1/4$ Laughlin state and its partially raised counterpart remain zero interaction energy eigenstates of the system. However, their single-particle energy now is higher than the lowest possible one given by $NE_1^-$ with $E_1^-$ from Eq. 6.27. This will quickly give rise to a ground state with higher occupation of the $n = 1$ level. This state has finite interaction energy, as predicted by Ref. [122]. The precise localization of the transition into the new ground state depends on the interaction strength. For the SU(2) symmetric choice with $g = 1$, we get a ground state with finite interaction energy already for $q^2 = 3.03\sqrt{B}$.

A state of zero interaction energy which is fully polarized in the $n = 1$ level is a Laughlin state with $\nu = 1/6$ projected into $n = 1$. At such a low filling, our numerics is restricted to $N = 3$ particles. Of course, a lot of states with zero interaction energy exist at this filling, but only one has the property of being completely within the $n = 1$ level. Such a state is not found at higher filling, that is for $N = 3$ and $N < N_\Phi = 18$. Obviously, this state is the true ground state between the first and the second degeneracy point. If we consider, instead of the SU(2) symmetric choice, an interaction only between different pseudospins, that is $g_{\uparrow\uparrow} = g_{\downarrow\downarrow} = 0$ and $g_{\uparrow\downarrow} > 0$, zero interaction energy states within the $n = 1$ level have been predicted for fillings up to $\nu = 1/4$ [122]. We have checked this prediction for $N = 4$. For spin-orbit coupling strengths $q$ which are sufficiently far above the degeneracy point, the unique ground state, with Haldane symmetry $\boldsymbol{K} = (0, 0)$, is given by this fully polarized state of zero interaction energy.

### 6.5.2 Incompressible phases at the degeneracy point

We have seen in the previous section that the SO coupled system behaves as an incompressible liquid at $\nu = 1/2$ for a range extending from $0 \lesssim q/\sqrt{B} \lesssim \sqrt{3}$, and $\sqrt{3} \lesssim q/\sqrt{B} \lesssim 1.77$. Precisely at the degeneracy point, $q/\sqrt{B} = \sqrt{3}$, the incompressibility is lost. In this section we focus on that particular choice for the SO coupling strength, and look for filling factors which might support gapped phases.

$\nu = 1$.

As has been pointed out in several works [41, 123, 124], off the degeneracy points, incompressible phases are supported not only at $\nu = 1/2$, but also at other fillings corresponding to the RR series. Let us therefore have a look at the Moore-Read filling, $\nu = 1$. We find a gapped phase, which according to its three ground states at $\boldsymbol{K} = (N_\Phi/2, 0)$, $(0, N_\Phi/2)$, and $(N_\Phi/2, N_\Phi/2)$ can be identified with the Moore-Read phase for $q^2 < 3B$. It disappears at the degeneracy point, where we find ground states at different pseudomomenta, which also depend on the size of system: $(3,3)$, $(3,5)$, $(5,3)$, $(5,5)$, $(4,0)$, and $(0,4)$ for $N = 5$, and $(3,0)$, $(0,3)$, $(2,2)$, $(2,4)$, $(4,2)$, and $(4,4)$ for $N = 6$. Since the gap between these states, compared to other energy differences in the spectrum, is not extraordinarily big, the system is expected to be compressible.

$\nu = 3/2$.

The situation is a bit different at the next Read-Rezayi filling, $\nu = 3/2$, where, at $N = 6$, a ground-state at $\boldsymbol{K} = \boldsymbol{0}$ is separated by a sizable gap of about twice the typical energy difference from a second state at $\boldsymbol{K} = \boldsymbol{0}$. Since a two-fold degenerate ground state at $\boldsymbol{K} = \boldsymbol{0}$ characterizes the $\nu = 3/2$ Read-Rezayi state on the torus, one might expect that at this filling a Read-Rezayi phase exists on the degeneracy point. We have thus calculated the ground-states of a spin-polarized system with four-body contact interaction. Projecting the two zero-energy states into the LL structure of the SO coupled system, we obtain an overlap of 0.70 with the real ground state. This number is close to the total weight of the state within the polarized subspace $P = 6$, being 0.72. For the second state, an overlap of 0.32 is found. Increasing the particle number to $N = 9$, we still find overlaps of 0.39 and 0.42, but the spectral structure is not robust. While one state at $\boldsymbol{K} = \boldsymbol{0}$ remains the ground state, the second state at this pseudomomentum lies above other states in the spectrum.

$\nu = 2$.

A clearly gapped phase shows up at filling $\nu = 2$, where a unique ground state at $\boldsymbol{K} = \boldsymbol{0}$ is found for $N = 8$ and $N = 10$. This fact makes this phase distinct from the Read-Rezayi states and the NASS states which are both possible candidates due to the filling factor. Apart from the large gap, the robustness of the spectrum against deformations of the torus ratio, shown in Fig. 6.10, signals the incompressibility of this phase.

*NASS fillings.*

Let us also pay attention to the NASS filling factors, $\nu = 2/3$ and $\nu = 4/3$,

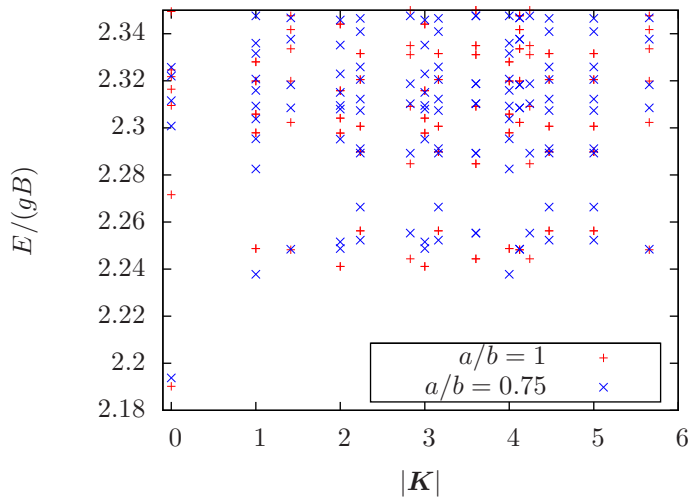


FIGURE 6.10: Spectrum at $\nu = 2$ for SU(2) symmetric interactions. Axis ratios $a/b = 1$ and 0.75 are plotted. Note that the degeneracy between 90° rotations in $\boldsymbol{K}$-space is lifted for ratios different from 1, and therefore, more states seem to be present at ratio 0.75.

which support incompressible phases in the system without SO coupling. Also in the SO coupled system, we find a clear gap in the spectrum at $\nu = 2/3$ with $N = 6$, and a small gap at $\nu = 4/3$ with $N = 8$. Projecting the 221-Halperin state, Eq. (3.15), onto the LL structure of the SO coupled system according to Eq. (6.33), we calculate its overlap with the $\nu = 2/3$ ground state. We find the value of 0.19, but it should be noted that, as mentioned above, interactions now can induce flips within the two-fold degenerate manifold, and therefore the analog of spin polarization, namely population imbalance $P$, is not conserved. In fact, the projected 221-Halperin state describes well the $P = 0$ fraction of the $\nu = 2/3$ ground state, but for a complete description of this state, we have to use generalizations of the Halperin state, obtained by diagonalizing the two-body contact interaction at $\nu = 2/3$ in an Abelian field ($q = 0$) within different spin subspaces. Then, after projection according to Eq. (6.33), the highest overlap of 0.60 is obtained with the state having $S = -6$. This corresponds to all particles being in $\Psi^{-}_{0,j}$, which is the most populated LL. Thus, population of $n = 0$ is still favored, despite the degeneracy with $n = 1$ on the single-particle level. This shows that interactions favor the LL with lower $n$. The total fidelity for $-6 \leq S \leq 6$ is 0.82.

For $\nu = 4/3$ with $N = 8$, the overlap with the projected NASS state is vanishing small. However, if we again consider generalizations to arbitrary spin polarizations, obtained by diagonalizing a three-body contact interaction at $q = 0$ for different $S$, we find a total fidelity of 0.52, after the usual projection of Eq. (6.33), and summing from $-8 \leq S \leq 8$.

*Low filling.*
Finally we note that an incompressible phase can be expected at a critical $\nu_0$, defined as the largest filling supporting states with zero interaction energy. For any $\nu < \nu_0$, the interaction energy should remain zero, while for $\nu > \nu_0$ it is by definition larger than zero. Thus, at $\nu_0$ a kink in the energy as a function of $\nu$ can be expected, resulting in an incompressibility of the system.

For spinless systems and two-body contact interactions, this critical filling is $\nu_0 = 1/2$. With spin-orbit coupling of a strength $q < \sqrt{3B}$, we have seen that $\nu_0$ is shifted down to $1/4$. At the degeneracy point, a zero interaction energy state of the form of a (464) Halperin state has been predicted in Ref. [122]. With half of the particles in the $n = 0$ level, and half of the particles in the $n = 1$ level, this state has been constructed as an unpolarized state with $P = 0$. However, such a state is ill-defined on a torus: The filling factor of the $n = 0$ level is given as $\nu_{n=0} = 1/(4+4) = 1/8$, while for $n = 1$ it reads $\nu_{n=1} = 1/(4+6) = 1/10$. Thus, the state cannot have $P = 0$, if both levels are assumed to fill the same area.

However, for arbitrary polarization $P$, we find states of zero interaction energy at even larger filling factors: The Laughlin state with $\nu = 1/4$ remains a ground state at the first degeneracy point. Apart from the Laughlin state ($P = N$), a second Laughlin-like state with one particle shifted into the first excited Landau level ($P = N - 2$) shows up in the ground state manifold. Additional states with zero interaction energy, not present in the spectrum of the system at any $q$, appear at the degeneracy point. For $N = 4$ ($N = 3$), there are 5 (2) additional zero interaction energy states with $K = (0, 0)$. Further states with zero interaction energy appear at finite pseudomomenta. For $N = 3$, there are two such states for each pseudomomenta, while for $N = 4$ this number varies between 4 and 5. This huge degeneracy of zero interaction energy eigenstates at $\nu = 1/4$ suggests that this is not yet the critical filling $\nu_0$ at the degeneracy point.

In fact, we find a unique zero interaction energy state at $\boldsymbol{K} = (0, 0)$ for $\nu = 2/7$ and $N = 4$. This state has no well defined polarization $P$, but the large weight $w_4 = 0.9298$ indicates that the atoms are mostly in the lowest Landau level, $n = 0$.

However, this makes the state to be an eigenstate only at the degeneracy point, leaving the Laughlin filling $\nu = 1/4$ to be the critical filling off the degeneracy point. We do not find states with zero interaction energy are for $\nu = 1/3$ (for $N = 4$ and $N = 5$) or $\nu = 4/13$ (for $N = 4$). Here, we therefore expect $\nu = 2/7$ to be the critical filling of the system.

This would shift the incompressible phase from $\nu = 1/4$ for $q^2 < 3B$ to $\nu = 2/7$ for $q^2 = 3B$. However, we should also note that the excitation gap above the ground state at $\nu = 2/7$ state takes the tiny value of $2 \cdot 10^{-4} gB$. The energy as a function of $\nu$ is a concave function, and in the thermodynamic limit it might happen that $\frac{\mathrm{d}E}{\mathrm{d}\nu} \to 0$, when $\nu \searrow \nu_0$. This would render a compressible phase even at $\nu_0$. We therefore conclude that, at the degeneracy point, robust incompressible phases are rather located in the denser regime. This should facilitate the experimental observation.

# Part II

# Condensed Systems

# Chapter 7

# Bose-Einstein condensates with spin-orbit coupling

Gauge fields couple the internal and the external evolution of a particle. In the case of spinless particles, the internal degree of freedom is just the phase of the particle's wave function. However, as we have already seen in Chapters 3 and 6, for two-component bosons the internal state is given by a spinor, and gauge fields having a matrix structure can connect them with the external evolution of the particle. Such a coupling is quite a fundamental effect. Consider for instance a single atom: Since an electron's movement within the electric field of the nucleus generates a magnetic field which may interact with the electron spin, naturally a *spin-orbit coupling*, i.e. a connection between the spin state of the electron and its external state, occurs. The effect is directly visible in the fine structure of the atom's spectral lines.

Spin-orbit (SO) coupling can also be encountered within condensed matter systems. In two dimensions, this coupling is well described by

$$H_{\mathrm{SO}} = \frac{\hbar^2 \mathbf{k}^2}{2m}\hat{1} + \alpha(k_x\sigma_y - k_y\sigma_x) + \beta(-k_x\sigma_y - k_y\sigma_x) + \mathrm{const.} \tag{7.1}$$

The term proportional to $\alpha$ represents a SO coupling of the Rashba type [75], whereas the term proportional to $\beta$ is of the Dresselhaus type (cf. [132]). The values of these coefficients depend on the crystal structure. It is directly seen

that a non-Abelian gauge potential of the form $\boldsymbol{A} = [(\alpha - \beta)\sigma_y, -(\alpha + \beta)\sigma_x, 0]$ describes this coupling.

SO coupling in solids is responsible for a variety of interesting effects. For instance, it allows materials to be topological insulators [19], which have conductance properties similar to quantum Hall systems, where the bulk is an insulator, while a topologically protected conductivity is provided through the edge states (cf. Chapter 3). But while in quantum Hall systems, this property is due to an external magnetic field breaking time-reversal symmetry, topological insulators show this behavior as an inherent property of the material.

SO coupling also plays the crucial role in the emerging field of spintronics. An old idea proposed by S. Datta and B. Das is the spin field-effect transistor (or Datta-Das transistor) [133]. Different from conventional transistors, this recently realized device [134] uses the electron's spin rather than its charge to operate information.

In 2011, the coupling from Eq. (7.1) with $\alpha = \beta$ has been synthesized experimentally in a Bose-Einstein condensed gas of $^{87}$Rb atoms [42]. Note that for this choice, only the $\sigma_x$ component of the spin couples to the orbital motion, and the gauge field describing the coupling reads $\boldsymbol{A} \simeq (0, \sigma_x, 0)$. Since all but one components vanish, the gauge potential is not non-Abelian in the strict sense, but as the authors of Ref. [42] point out, with additional lasers more general couplings can be synthesized. In this chapter, we will consider cold bosons with a purely non-Abelian gauge potential of the form $\boldsymbol{A} \simeq (\sigma_x, \sigma_y, 0)$. A 90° spin rotation yields the equivalence of this gauge potential with a Rashba coupling. Differing from our study of the fractional quantum Hall regime in the first part of the thesis, now there is no external magnetic field. We will find rich physics purely originating from the SO term. Now we will also allow the system to extend into the $z$-direction.

Most of the work presented in the remainder of this chapter has been published in Ref. [135].

## 7.1 Mean-Field Solution

We consider the single-particle Hamiltonian given by

$$\mathcal{H}_0 = \int \mathrm{d}\boldsymbol{r}\ \hat{\boldsymbol{\Psi}}^\dagger(\boldsymbol{r}) \left( \frac{p^2}{2M} - \frac{Q}{M}\sigma_\perp \cdot \mathbf{p} \right) \hat{\boldsymbol{\Psi}}(\boldsymbol{r}), \tag{7.2}$$

where $\hat{\boldsymbol{\Psi}}(\boldsymbol{r}) = (\Psi_\uparrow(\boldsymbol{r}), \Psi_\downarrow(\boldsymbol{r}))^T$ is a two-component bosonic field operator, $\mathbf{p}$ is the momentum operator, $Q$ is the magnitude of the SO coupling, and $\sigma_\perp$ is a vector composed of Pauli matrices as $\sigma_\perp = (\sigma_x, \sigma_y, 0)$ (we set $\hbar = 1$). To solve this Hamiltonian, we transform into Fourier space, and find the eigenspinors to be given by

$$\varphi_{\boldsymbol{k}}^{(\alpha)} = \frac{\mathrm{e}^{i\boldsymbol{k}\cdot\boldsymbol{r}}}{2V} \begin{pmatrix} \mathrm{e}^{-i\phi_{\boldsymbol{k}}/2} \\ \mathrm{e}^{i\phi_{\boldsymbol{k}}/2} \end{pmatrix} \quad \text{and} \quad \varphi_{\boldsymbol{k}}^{(\beta)} = \frac{\mathrm{e}^{i\boldsymbol{k}\cdot\boldsymbol{r}}}{2V} \begin{pmatrix} -\mathrm{e}^{-i\phi_{\boldsymbol{k}}/2} \\ \mathrm{e}^{i\phi_{\boldsymbol{k}}/2} \end{pmatrix}. \tag{7.3}$$

Here, $\phi_{\boldsymbol{k}} = \tan^{-1}\frac{k_y}{k_x}$ is the polar angle of $\boldsymbol{k}$. The single-particle eigenstates of Eq. (7.2) thus have spins pointing either parallel or antiparallel to their momenta in the $xy$ plane.

With this, we can write the field operator as

$$\hat{\boldsymbol{\Psi}}(\boldsymbol{r}) = \sum_{\boldsymbol{k}} \hat{\alpha}_{\boldsymbol{k}} \varphi_{\boldsymbol{k}}^{(\alpha)} + \hat{\beta}_{\boldsymbol{k}} \varphi_{\boldsymbol{k}}^{(\beta)}, \tag{7.4}$$

where $\hat{\alpha}_{\boldsymbol{k}}$ and $\hat{\beta}_{\boldsymbol{k}}$ are annihilation operators. Accordingly, we expand the conjugate field operator $\hat{\boldsymbol{\Psi}}^\dagger(\boldsymbol{r})$. The Hamiltonian (7.2) then reads

$$\mathcal{H}_0 = \sum_{\boldsymbol{k}} \left( E_{\boldsymbol{k}}^{(+)} \hat{\alpha}_{\boldsymbol{k}}^\dagger \hat{\alpha}_{\boldsymbol{k}} + E_{\boldsymbol{k}}^{(-)} \hat{\beta}_{\boldsymbol{k}}^\dagger \hat{\beta}_{\boldsymbol{k}} \right), \tag{7.5}$$

where the eigenenergies are, up to a constant, given by

$$E_{\boldsymbol{k}}^{(\pm)} = \frac{1}{2M} \left[ (k_\perp \pm Q)^2 + k_z^2 \right], \tag{7.6}$$

where $\mathbf{k}_\perp = (k_x, k_y, 0)$. The ground state to which the system may condense is given by the $\alpha$-mode, which has a minimum on a ring with $k_z = 0$ and $|\mathbf{k}_\perp| = Q$ in momentum space (Fig. 7.1). Correspondingly, there is a macroscopic number of ways in which $N$ non-interacting bosons can occupy this manifold of states.

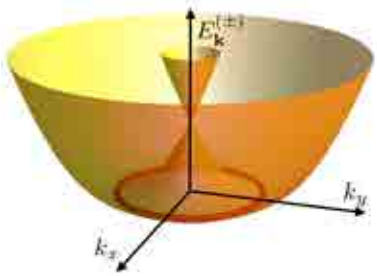


FIGURE 7.1: The non-interacting (Rashba) energy spectrum of the Hamiltonian Eq. (7.2) with $k_z = 0$. The red circle indicates the degenerate lowest-energy single-particle states. From: [135]

Next, we take the simplest SU(2) invariant form for two-body contact interactions

$$\mathcal{H}_{\rm int} = \int \mathrm{d}\boldsymbol{r} \ \left( \frac{g}{2} \left[ \hat{\rho}(\boldsymbol{r}) \right]^2 - \mu \hat{\rho}(\boldsymbol{r}) \right), \tag{7.7}$$

where $\hat{\rho}(\boldsymbol{r}) = \hat{\boldsymbol{\Psi}}^\dagger(\boldsymbol{r})\hat{\boldsymbol{\Psi}}(\boldsymbol{r})$, $\mu$ is the chemical potential, and $g = \frac{4\pi a}{M}$ where $a$ is an effective scattering length. At the mean-field level one replaces the operators by c-numbers $\hat{\boldsymbol{\Psi}}(\boldsymbol{r}) \to \boldsymbol{\Psi}(\boldsymbol{r})$. The states that minimize the kinetic energy, Eq. (7.2), are in general given by

$$\boldsymbol{\Psi}(\boldsymbol{r}) = \sum_{|\boldsymbol{k}_\perp|=Q, k_z=0} A_{\boldsymbol{k}} \frac{e^{i\boldsymbol{k}\cdot\boldsymbol{r}}}{\sqrt{2}} \begin{pmatrix} 1 \\ \mathrm{e}^{i\phi_{\boldsymbol{k}}} \end{pmatrix} \tag{7.8}$$

where $A_{\boldsymbol{k}}$ are arbitrary coefficients.

Minimizing the interaction energy restricts the mean-field states of Eq. (7.8) to having a constant density, $\rho(\boldsymbol{r}) = \boldsymbol{\Psi}^\dagger(\boldsymbol{r})\boldsymbol{\Psi}(\boldsymbol{r}) \equiv \rho_0$. The large degeneracy on the single-particle level allows to fulfill this constraint within the manifold of states given by Eq. (7.8). One finds that $\boldsymbol{\Psi}(\boldsymbol{r})$ can have at most two nonzero coefficients $A_{\boldsymbol{k}}$ occurring at opposite momenta. To see this, we notice that the spatial dependence of $\boldsymbol{\Psi}^\dagger(\boldsymbol{r})\boldsymbol{\Psi}(\boldsymbol{r})$ cancels, if all contributions to $\boldsymbol{\Psi}(\boldsymbol{r})$ are orthogonal to all contributions of $\boldsymbol{\Psi}^\dagger(\boldsymbol{r})$ except for those having opposite phases. Since the spinor space is two-dimensional, only pairs of orthogonal configurations can exist. These are found at opposite momenta.

Without loss of generality, we take the momenta to point along the $x$-axis and thereby obtain the state

$$\boldsymbol{\Psi}(\boldsymbol{r}) = \sqrt{\frac{\rho_0}{2}} \left( a\mathrm{e}^{iQx} \begin{pmatrix} 1 \\ 1 \end{pmatrix} + b\mathrm{e}^{-iQx} \begin{pmatrix} -1 \\ 1 \end{pmatrix} \right), \tag{7.9}$$

where $|a|^2 + |b|^2 = 1$. We can take $a$ and $b$ to be real and parametrized as $a = \cos\left(\frac{\theta}{2}\right)$ and $b = \sin\left(\frac{\theta}{2}\right)$ since changing the phases of $a$ and $b$ amounts to position displacements and overall phase shifts of $\boldsymbol{\Psi}(\boldsymbol{r})$ in Eq. (7.9).

The selection of $(a, b)$ as a result of spin-symmetry breaking interactions (which is resolved at the mean-field level) was worked out in [136]. In contrast, for the SU(2) symmetric interactions there remains a two-fold degeneracy at the mean-field level. We note that SU(2) symmetry is a realistic choice due to the relatively small spin-dependent interaction in $^{87}$Rb. More importantly, however, SO coupling in atoms relies on dressed states [32, 42], which may induce anisotropic interactions [137]. Whether this might lift the degeneracy on the mean-field level is left to future work when it becomes clear which of the proposed schemes is most promising to realize a 3D Rashba coupling.

Another experimental entity which could lift this mean-field degeneracy is the trapping potential. We have neglected this term, which we assume to be weak. Then the conditions for the local density approximation (LDA) are satisfied [138]. Recent studies of SO coupled systems in harmonic traps can be found in Refs. [139, 140]. Let us briefly sketch the analysis of Ref. [139] to clarify the conditions under which the trapped system behaves similarly to the infinite system considered in our approach. To the Hamiltonian as given by Eq. (7.2), we add a harmonic potential which in Fourier space is given by $V = -\nabla_k^2/2$. We restrict ourselves to two dimensions.

In polar coordinates, the ansatz $\Psi_m(k, \Phi_k) = e^{i\Phi_k m}\Big(f_m(k), -e^{i\Phi_k} g_m(k)\Big)^T$ removes the $\Phi_k$ dependence from the Schrödinger equation. The quantum number $m$ can be identified with angular momentum. We obtain the coupled differential

equations

$$E_m f_m(k) = \frac{1}{2}\left[k^2 + \frac{m^2}{k^2} - \frac{1}{k}\frac{\mathrm{d}}{\mathrm{d}k} - \frac{\mathrm{d}^2}{\mathrm{d}k^2} + \left(\frac{Q}{M}\right)^2\right] f_m(k) + \frac{Q}{M} k g_m(k), \quad (7.10)$$

$$E_m g_m(k) = \frac{1}{2}\left[k^2 + \frac{(m+1)^2}{k^2} - \frac{1}{k}\frac{\mathrm{d}}{\mathrm{d}k} - \frac{\mathrm{d}^2}{\mathrm{d}k^2} + \left(\frac{Q}{M}\right)^2\right] g_m(k) + \frac{Q}{M} k f_m(k). \quad (7.11)$$

Taking the difference between Eqs. (7.10) and (7.11), we arrive at

$$\left[k^2 + \left(\frac{Q}{M}\right)^2 + \frac{m^2+m+1/2}{k^2} - 2\frac{Q}{M}k - 2E_m\right](f_m - g_m) - \frac{1}{k}\frac{\mathrm{d}}{\mathrm{d}k}(f_m - g_m) - \frac{\mathrm{d}^2}{\mathrm{d}k^2}(f_m - g_m) - \frac{2m+1}{2k^2}(f_m + g_m) = 0. \quad (7.12)$$

From the solutions of the system without trap, given in Eq. (7.3), we know that for the low-energy mode $\varphi^{(\alpha)}$ the spinors are oriented along $(1, \mathrm{e}^{i\phi_k})$, i.e. $f_m = -g_m$. We thus solve Eq. (7.12) by setting $f_m + g_m = 0$ and making the ansatz $f_m - g_m = k^{-1/2}\Phi_m$. This yields

$$\left[\frac{(m+1/2)^2}{k^2} + (k - \frac{Q}{M})^2 - 2E_m\right]\Phi_m - \Phi_m'' = 0. \quad (7.13)$$

Expanding around the minimum of the free dispersion at $\tilde{k} \equiv k - \frac{Q}{M}$, it reads

$$\left[\frac{(m+1/2)^2}{(Q/M)^2} - \tilde{k}^2 - 2E_m\right]\Phi_m - \Phi_m'' = 0, \quad (7.14)$$

with solutions in terms of parabolic cylinder functions $D_\nu(\sqrt{2}k)$ where [139]

$$\nu = \frac{(m+1/2)^2}{(Q/M)^2} - \frac{1}{2} - E_{\nu,m}. \quad (7.15)$$

This equation defines the energy levels $E_{\nu,m}$, which are given by the quantum number $\nu$. From this equation we find that due to the trap the different angular momentum states within each level, characterized by $m$, are split. For the mean-field result from Eq. (7.9) not to be affected by this splitting, we have to demand that it is small compared to the interaction energy. As can directly been seen from Eq. (7.15), this energy splitting becomes small for strong SO coupling and/or a weak trapping. As a result, a large quasi-degenerate manifold of single-particle states will allow for the same mean-field construction as in Eq. (7.9). Conversely,

in the weakly interacting limit (where LDA is inapplicable) the ground states of the RBEC system in a trap can form vortex lattices [139, 140].

## 7.2 Quantum Fluctuations

### 7.2.1 Order-by-disorder mechanism

The degeneracy of the mean-field solution from the previous section is accidental, i.e. it does not correspond to any symmetry of the Hamiltonian $\mathcal{H} = \mathcal{H}_0 + \mathcal{H}_{\rm int}$. We thus expect quantum fluctuations about the mean-field state, Eq. (7.9), to remove this degeneracy and to select a unique ground state. Such a mechanism, where a degeneracy on the classical level is removed through fluctuations, of either quantum or thermal nature, is called order-by-disorder. It has first been discussed in the context of frustrated spin models [141], and later also in the context of quantum magnetism [142] and magnetic ordering of ultracold atoms [143], but clear experimental demonstrations are missing. The effect is reminiscent of the Casimir effect, where two parallel metallic plates in the vacuum attract each other due to the boundary conditions which they impose to electromagnetic fluctuations of the vacuum. While in between the plates, the fluctuations are restricted to eigenmodes of the cavity, outside of them fluctuations at any wavelengths may occur, resulting in a higher vacuum pressure from outside, and thus an effective attractive force on the plates

To analyze the effect of fluctuations in our system, we will have to determine the excitation spectrum of the system. Therefore we numerically solve the coupled Bogoliubov-de Gennes equations. Integrating over the resulting modes then yields the free energy as a function of the relative condensate weights and temperature. On this level, fluctuations should have lifted the degeneracy, and we will directly see which state is selected as the ground state.

### 7.2.2 Collective Excitations

We start writing $\hat{\mathbf{\Psi}}(\boldsymbol{r}) = \mathbf{\Psi}(\boldsymbol{r}) + \hat{\boldsymbol{\psi}}(\boldsymbol{r})$ and perform a Bogoliubov expansion of $\mathcal{H}$ to quadratic order in the fluctuations $\hat{\psi}(\boldsymbol{r})$. Up to a constant the interaction Hamiltonian becomes $\mathcal{H}_{\rm int} = \frac{g}{2}\int d\boldsymbol{r}\,[\delta\hat{\rho}(\boldsymbol{r})]^2$ where $\delta\hat{\rho}(\boldsymbol{r}) = \mathbf{\Psi}^\dagger(\boldsymbol{r})\hat{\boldsymbol{\psi}}(\boldsymbol{r}) + \hat{\boldsymbol{\psi}}^\dagger(\boldsymbol{r})\mathbf{\Psi}(\boldsymbol{r})$. We will now perform several exact manipulations on this Hamiltonian, to arrive

at a form from which we can read off the Bogoliubov-de Gennes equations. We will follow the pedagogical derivation from [144]. In the basis which diagonalizes $\mathcal{H}_0$, cf. Eq. (7.4), the first term of this expression reads

$$\boldsymbol{\Psi}^\dagger(\boldsymbol{r})\hat{\boldsymbol{\psi}}(\boldsymbol{r}) = \sqrt{\frac{\rho_0}{V}}\sum_{\boldsymbol{k}}\left[\mathrm{e}^{i(\boldsymbol{k}-\boldsymbol{Q})\cdot\boldsymbol{r}}a^*\left(\cos\left(\frac{\phi_{\boldsymbol{k}}}{2}\right)\hat{\alpha}_{\boldsymbol{k}} + i\sin\left(\frac{\phi_{\boldsymbol{k}}}{2}\right)\hat{\beta}_{\boldsymbol{k}}\right) + \right.$$
$$\left. \mathrm{e}^{i(\boldsymbol{k}+\boldsymbol{Q})\cdot\boldsymbol{r}}b^*\left(i\sin\left(\frac{\phi_{\boldsymbol{k}}}{2}\right)\hat{\alpha}_{\boldsymbol{k}} + i\cos\left(\frac{\phi_{\boldsymbol{k}}}{2}\right)\hat{\beta}_{\boldsymbol{k}}\right)\right]. \quad (7.16)$$

We thus define

$$\hat{\gamma}_{\boldsymbol{k}} \equiv \cos\left(\frac{\phi_{\boldsymbol{k}}}{2}\right)\hat{\alpha}_{\boldsymbol{k}} + i\sin\left(\frac{\phi_{\boldsymbol{k}}}{2}\right)\hat{\beta}_{\boldsymbol{k}}, \quad (7.17)$$

$$\hat{\eta}_{\boldsymbol{k}} \equiv i\sin\left(\frac{\phi_{\boldsymbol{k}}}{2}\right)\hat{\alpha}_{\boldsymbol{k}} + i\cos\left(\frac{\phi_{\boldsymbol{k}}}{2}\right)\hat{\beta}_{\boldsymbol{k}}, \quad (7.18)$$

and next

$$\hat{\mu}_{\boldsymbol{k}} \equiv a^*\hat{\gamma}_{\boldsymbol{k}+\boldsymbol{Q}} + b^*\hat{\eta}_{\boldsymbol{k}-\boldsymbol{Q}}. \quad (7.19)$$

With this, the term (7.16) reduces to

$$\boldsymbol{\Psi}^\dagger(\boldsymbol{r})\hat{\boldsymbol{\psi}}(\boldsymbol{r}) = \sqrt{\frac{\rho_0}{V}}\sum_{\boldsymbol{k}}\mathrm{e}^{i\boldsymbol{k}\cdot\boldsymbol{r}}\hat{\mu}_{\boldsymbol{k}}, \quad (7.20)$$

and therefore

$$\mathcal{H}_{\mathrm{int}} = \sum_{\boldsymbol{k}}\frac{1}{2}g\rho_0\left(\hat{\mu}^\dagger_{\boldsymbol{k}}\hat{\mu}_{\boldsymbol{k}} + \hat{\mu}_{\boldsymbol{k}}\hat{\mu}_{-\boldsymbol{k}} + \mathrm{h.c.}\right). \quad (7.21)$$

In order to re-write $\mathcal{H}_0$, we will have to define another operator, which is given by the transformation orthogonal to Eq. (7.19):

$$\hat{\nu}_{\boldsymbol{k}} \equiv -b\hat{\gamma}_{\boldsymbol{k}+\boldsymbol{Q}} + a\hat{\eta}_{\boldsymbol{k}-\boldsymbol{Q}}. \quad (7.22)$$

After some algebra, we find the total Hamiltonian $\mathcal{H}$ to be given by

$$\mathcal{H} = \sum_{\boldsymbol{k}}\left[\hat{\boldsymbol{\chi}}^\dagger_{\boldsymbol{k}}\left(\frac{k^2}{2M} + gX\right)\hat{\boldsymbol{\chi}}_{\boldsymbol{k}} + \left(-i\frac{k_yQ}{M}\hat{\boldsymbol{\chi}}^\dagger_{\boldsymbol{k}+2\boldsymbol{Q}}\Gamma\hat{\boldsymbol{\chi}}_{\boldsymbol{k}} + \mathrm{h.c.}\right)\right.$$
$$\left. + \frac{g\rho_0}{2}\left(\hat{\boldsymbol{\chi}}^T_{\boldsymbol{k}}X\hat{\boldsymbol{\chi}}_{-\boldsymbol{k}} + \mathrm{h.c.}\right)\right], \quad (7.23)$$

where for convenience, the matrices

$$X = \begin{pmatrix} 1 & 0 \\ 0 & 0 \end{pmatrix} \quad \text{and} \quad \Gamma = \begin{pmatrix} b^* a & -b^{*2} \\ a^2 & -ab^* \end{pmatrix} \tag{7.24}$$

have been defined. With our parametrization of $a$ and $b$, $\Gamma$ can also be written as $\Gamma = \frac{-i}{2}\left[\sigma_y + i(\sin\theta\sigma_z + \cos\theta\sigma_x)\right]$. The operators $\hat{\mu}_{\boldsymbol{k}}$ and $\hat{\nu}_{\boldsymbol{k}}$ have been combined in the vector operator $\hat{\boldsymbol{\chi}}_{\boldsymbol{k}} = (\hat{\mu}_{\boldsymbol{k}}, \hat{\nu}_{\boldsymbol{k}})^T$.

The Hamiltonian (7.23) is quadratic in $\hat{\boldsymbol{\chi}}_{\boldsymbol{k}}$, however, modes at momentum $\boldsymbol{k}$ are not only coupled to modes at $-\boldsymbol{k}$, as is the case for bosons without SO coupling, but also to modes with $\boldsymbol{k} + 2\boldsymbol{Q}$. The Hamiltonian thus cannot be represented by a finite matrix. However, we can bring Eq. (7.23) to the form

$$\mathcal{H} = \sum_{\boldsymbol{k}\in \mathrm{BZ}'} \hat{\boldsymbol{\Phi}}_{\boldsymbol{k}}^{\dagger} M_{\boldsymbol{k}} \hat{\boldsymbol{\Phi}}_{\boldsymbol{k}}, \tag{7.25}$$

if we consider a matrix $M_{\boldsymbol{k}}$ and vector operators $\hat{\boldsymbol{\Phi}}_{\boldsymbol{k}}$ of infinite dimensions. The first Brillouin zone (BZ) extends over $-Q \leq k_x < Q$, while $k_y$ and $k_z$ run from $-\infty$ to $\infty$. In the reduced Brillouin zone (BZ'), $k_x$ is restricted to positive values. The modes at different $k_x$ are accounted for by higher bands, included in the following definition of the vector operator $\hat{\boldsymbol{\Phi}}_{\boldsymbol{k}}$:

$$\hat{\boldsymbol{\Phi}}_{\boldsymbol{k}} \equiv \begin{pmatrix} \vdots \\ \hat{\boldsymbol{\chi}}_{\boldsymbol{k}+2\boldsymbol{Q}} \\ \hat{\boldsymbol{\chi}}_{\boldsymbol{k}} \\ \hat{\boldsymbol{\chi}}_{\boldsymbol{k}-2\boldsymbol{Q}} \\ \vdots \\ (\hat{\boldsymbol{\chi}}^{\dagger}_{-\boldsymbol{k}-2\boldsymbol{Q}})^T \\ (\hat{\boldsymbol{\chi}}^{\dagger}_{-\boldsymbol{k}})^T \\ (\hat{\boldsymbol{\chi}}^{\dagger}_{-\boldsymbol{k}+2\boldsymbol{Q}})^T \\ \vdots \end{pmatrix}. \tag{7.26}$$

The corresponding matrix $M_{\boldsymbol{k}}$ can be obtained by comparison with Eq. (7.23). It can conveniently be written as a Kronecker product of three matrices if we

define a matrix $D_{\boldsymbol{k}}$ of (in principle) infinite dimension

$$D_{\boldsymbol{k}} = \mathrm{Diag}\left(\ldots, \frac{(\boldsymbol{k}+4\boldsymbol{Q})^2}{2M}, \frac{(\boldsymbol{k}+2\boldsymbol{Q})^2}{2M}, \frac{\boldsymbol{k}^2}{2M}, \frac{(\boldsymbol{k}-2\boldsymbol{Q})^2}{2M}, \frac{(\boldsymbol{k}-4\boldsymbol{Q})^2}{2M}, \ldots\right), \tag{7.27}$$

and a matrix $n_+$ of the same size which is non-zero only on the first diagonal, where it has ones. With this we obtain

$$\begin{aligned} M_{\boldsymbol{k}} =& \mathbf{1}\otimes D_{\boldsymbol{k}}\otimes\mathbf{1} + \mathbf{1}\otimes\mathbf{1}\otimes Xg\rho_0 + \sigma_x\otimes\mathbf{1}\otimes Xg\rho_0 - \\ & \left[\mathbf{1}\otimes n_+\otimes\sigma_y + i\sigma_z\otimes n_+\otimes(\sin\theta\sigma_z+\cos\theta\sigma_x) + \mathrm{h.c.}\right]\frac{k_y Q}{2M}. \end{aligned} \tag{7.28}$$

The left and the right matrices in the Kronecker products are $2\times 2$ matrices. The left matrix is due to the inclusion of operators $\hat{\boldsymbol{\chi}}$ and their conjugates $\hat{\boldsymbol{\chi}}^\dagger$ in a single vector, Eq. (7.26). The block form stemming from the right matrix is due to the fact that the $\hat{\boldsymbol{\chi}}$'s are two-component operators. The infinite matrix in the middle takes into account the coupling of $\boldsymbol{k}$-modes to $(\boldsymbol{k}+2\boldsymbol{Q})$-modes, and vanishes for $\boldsymbol{Q}=0$. Then, $M_{\boldsymbol{k}}$ reduces to a $4\times 4$ matrix, as it should be for the Bogoliubov description of a normal two-component Bose gas.

With the definition from Eq. (7.28), we can write down the Bogoliubov-de Gennes equations as the eigenvalue problem [145]:

$$\eta M_{\boldsymbol{k}}\boldsymbol{v}_{\boldsymbol{k}n} = \mathcal{E}_{\boldsymbol{k}n}\boldsymbol{v}_{\boldsymbol{k}n}, \tag{7.29}$$

where $\eta = \sigma_z\otimes\mathbf{1}\otimes\mathbf{1}$, i.e. a diagonal matrices with entries $+1$ in the upper, and entries $-1$ in the lower half. Eigenenergies are the positive eigenvalues, and the eigenstates are given by the corresponding eigenvectors, normalized according to $\boldsymbol{v}^\dagger_{\boldsymbol{k}n}\boldsymbol{\eta}\boldsymbol{v}_{\boldsymbol{k}'n'} = \delta_{\boldsymbol{k}\boldsymbol{k}'}\delta_{nn'}\mathrm{sgn}(\mathcal{E}_{\boldsymbol{k}n})$. We have labeled eigenvectors and eigenvalues with a momentum index $\boldsymbol{k}$ and a band index $n$.

Since large momenta should not contribute to low-energy excitations, we can truncate the matrix $M_{\boldsymbol{k}}$ at some point, which is necessary to solve Eq. (7.29) numerically. Truncating the inner matrix in Eq. (7.28) to $n_{\max}$ dimensions will restrict Eq. (7.29) to having $2n_{\max}$ positive eigenvalues. Certainly, the higher eigenvalues will suffer from the truncation, so $n_{\max}$ must be chosen large enough to make the modes of interest independent from the cutoff.

Eq. (7.28) is convenient to numerically solve the problem, which now reduces to the diagonalization of finite matrices. Alternatively, a closed notation of the

Hamiltonian as a 4×4 matrix is possible in real space [135]. We therefore note that in real space the manipulations Eqs. (7.19) and (7.22) correspond to transforming the field operator $\hat{\psi}(\boldsymbol{r})$ according to

$$\hat{\boldsymbol{\chi}}(\boldsymbol{r}) = e^{i\boldsymbol{\sigma}_y \frac{\theta}{2}} e^{-i\boldsymbol{\sigma}_z Q x} e^{i\boldsymbol{\sigma}_y \frac{\pi}{4}} \hat{\boldsymbol{\psi}}(\boldsymbol{r}). \tag{7.30}$$

If we define the four-component vector

$$\hat{\boldsymbol{\Phi}}(\boldsymbol{r}) = \left(\hat{\boldsymbol{\chi}}^T(\boldsymbol{r}), \hat{\boldsymbol{\chi}}^\dagger(\boldsymbol{r})\right)^T, \tag{7.31}$$

then, up to a constant independent of $\theta$, we find that

$$\mathcal{H} = \frac{1}{2}\int d\boldsymbol{r}\ \hat{\boldsymbol{\Phi}}^\dagger(\boldsymbol{r}) M(\boldsymbol{r},\boldsymbol{p}) \hat{\boldsymbol{\Phi}}(\boldsymbol{r}),$$

with

$$\begin{aligned} M(\boldsymbol{r},\boldsymbol{p}) =& \mathbf{1}\otimes\mathbf{1}\,\frac{p^2}{2m} + \frac{g\rho_0}{2}(\mathbf{1}+\boldsymbol{\sigma}_x)\otimes(\mathbf{1}+\boldsymbol{\sigma}_z) - \frac{Qp_y}{m} \\ &\times\left\{\mathbf{1}\otimes\boldsymbol{\sigma}_y\cos(2Qx) - \boldsymbol{\sigma}_z\otimes[\cos(\theta)\boldsymbol{\sigma}_x + \sin(\theta)\boldsymbol{\sigma}_z]\sin(2Qx)\right\}. \end{aligned} \tag{7.32}$$

Differently to the infinite matrix $M_{\boldsymbol{k}}$ in Eq. (7.28), the corresponding real space matrix $M(\boldsymbol{r},\boldsymbol{p})$ is just the Kronecker product of two $2\times 2$ matrices. We will need this representation later for a large-$T$ expansion.

We now proceed by analyzing the spectrum of the system which is found by diagonalizing $\eta M_{\boldsymbol{k}}$. As shown in Fig. 7.2 for different $\theta$, there exist two gapless (Goldstone) modes. Following the experimental parameters of Ref. [42], we have chosen $\frac{Q^2}{2m} = g\rho_0$. The dispersion is plotted along $k_y$. As can be seen from Eq. (7.29), the spectrum $\mathcal{E}_{\boldsymbol{k}n}$ has no $\theta$-dependence when $k_y = 0$. We refer to the dispersions as 'density' and 'spin' modes since they reduce to the known expressions $\mathcal{E}_{\boldsymbol{k}d} = \sqrt{\varepsilon_{\boldsymbol{k}}(\varepsilon_{\boldsymbol{k}} + 2g\rho_0)}$ and $\mathcal{E}_{\boldsymbol{k}s} = \varepsilon_{\boldsymbol{k}}$ in the limiting case of $Q = 0$, where $\varepsilon_{\boldsymbol{k}} = \frac{k^2}{2m}$ is the free particle dispersion. One sees that upon increasing $\theta$ from zero to $\pi/2$, the spin mode decreases in energy while the density mode increases. Thus, there is a competition which $(a, b)$ configuration is selected by the fluctuations. In the right panel we have therefore plotted the average of the spin and density modes for each value of $\theta$. The average is always lowest in energy for $\theta = 0$. This indicates that the zero-point fluctuations from the Goldstone modes will select $\theta = 0$ state. This state, as can be seen from Eq. (7.9), corresponds to all bosons condensing into a single momentum state of the Rashba coupled

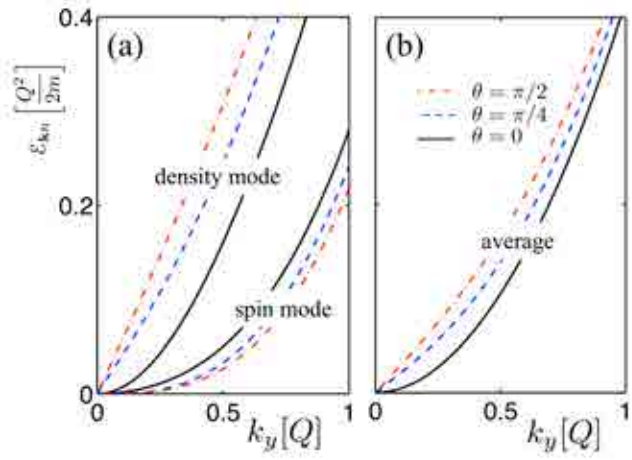


FIGURE 7.2: (a) The dispersions for the density and spin Goldstone modes for three values of $\theta$ for $k_x = k_z = 0$. (b) The average (arithmetic mean) of the density and spin modes. In both plots we have fixed $g\rho_0 = \frac{Q^2}{2m}$. From: [135]

system. This order-by-disorder mechanism, also including thermal fluctuations, will be considered more quantitatively in the next section.

Analytical expressions for the dispersion relations and the eigenvectors of Eq. (7.29) can be found in the low-energy limit where $\boldsymbol{\kappa} = \boldsymbol{k} - Q\hat{\boldsymbol{e}}_x$ is small. One therefore expands the eigenvalue problem from Eq. (7.29) in powers of $\boldsymbol{\kappa}$ [146], i.e.

$$M_{\boldsymbol{\kappa}+Q\hat{\boldsymbol{e}}_x} \equiv M_0 + M_1 + M_2, \tag{7.33}$$

$$\boldsymbol{v}_{(\boldsymbol{\kappa}+Q\hat{\boldsymbol{e}}_x)n} \equiv \boldsymbol{v}_{0n} + \boldsymbol{v}_{1n} + \boldsymbol{v}_{2n} + \ldots, \tag{7.34}$$

$$\mathcal{E}_{(\boldsymbol{\kappa}+Q\hat{\boldsymbol{e}}_x)n} \equiv \mathcal{E}_{0n} + \mathcal{E}_{1n} + \mathcal{E}_{2n} + \ldots\ . \tag{7.35}$$

We are interested in the modes with $\mathcal{E}_{0n} = 0$, so we obtain one equation to first power in $\boldsymbol{\kappa}$, and another equation to second power in $\boldsymbol{\kappa}$:

$$\eta M_0 \boldsymbol{v}_{1n} + \eta M_1 \boldsymbol{v}_{0n} = \mathcal{E}_{1n}\boldsymbol{v}_{0n}. \tag{7.36}$$

$$\eta M_0 \boldsymbol{v}_{2n} + \eta M_1 \boldsymbol{v}_{1n} + \eta M_2 \boldsymbol{v}_{0n} = \mathcal{E}_{1n}\boldsymbol{v}_{1n} + \epsilon_{2n}\boldsymbol{v}_{0n}. \tag{7.37}$$

By projecting the first of these equations into the null vector space of $M_0$ and multiplying with $\eta$, $\boldsymbol{v}_{0n}$ is found. Multiplying with this vector, one obtains $\mathcal{E}_{1n}$ and $\boldsymbol{v}_{1n}$. Finally, one obtains an eigenvalue problem for $\mathcal{E}_{2n}$ [146].

The analytic expressions read [135]

$$\mathcal{E}_{\boldsymbol{k}d} = \sqrt{2g\rho_0\left(\varepsilon_{k_{xz}} + \lambda\varepsilon_{k_y}\sin^2(\theta)\right)}, \tag{7.38}$$

and

$$\mathcal{E}_{\boldsymbol{k}s} = \sqrt{\frac{\varepsilon_{k_{xz}}(\varepsilon_{k_{xz}} + \lambda\varepsilon_{k_y})^2}{\varepsilon_{k_{xz}} + \lambda\varepsilon_{k_y}\sin^2(\theta)}}, \tag{7.39}$$

for the density and spin modes respectively, where $\lambda = g\rho_0/(4\varepsilon_Q + 2g\rho_0)$ and $k_{xz} = \sqrt{k_x^2 + k_z^2}$. These agree well with the numerical results shown in Fig. 7.2 for small $\kappa$ except for two special cases which require a more careful analysis. In particular, for $\theta = 0$, the density mode disperses quadratically along $k_y$ while for $0 < \theta \leq \pi/2$ the spin mode disperses as $k_y^3$ along $k_y$. Otherwise the density and spin mode have, respectively, linear and quadratic dispersions about their minima. It is interesting to compare these to the non-interacting energies shown in Fig. 7.1, which have quadratic and quartic dispersions about their minima.

### 7.2.3 Free energy

We will now quantify the order-by-disorder effect by calculating the free energy of the system. Due to the $\theta$-dependence of the collective excitations, also the free energy will depend on the configuration of the system. To calculate it, we start writing the partition function:

$$\mathcal{Z} = \sum_{\{m_{n,\boldsymbol{k}}\}} \exp\left[-\beta \sum_{n,\boldsymbol{k}} \mathcal{E}_{\boldsymbol{k}n}(m_{\boldsymbol{k}n} + 1/2)\right], \tag{7.40}$$

where $m_{\boldsymbol{k}n}$ is the occupation number of the mode characterized by $\boldsymbol{k}$ and $n$, and $\beta = 1/k_{\mathrm{B}}T$ the inverse temperature. The zero-point term can be taken out of the sum over the basis states, and then the free energy, defined as $\mathcal{F} = -\frac{1}{\beta}\ln\mathcal{Z}$, reads:

$$\mathcal{F} = -\frac{1}{\beta}\left\{-\beta\sum_{\boldsymbol{k}n}\frac{\mathcal{E}_{\boldsymbol{k}n}}{2} + \ln\left[\sum_{\{m_{\boldsymbol{k}n}\}}\exp\left(-\beta\sum_{\boldsymbol{k}n}E_{\boldsymbol{k}n}m_{\boldsymbol{k}n}\right)\right]\right\}. \tag{7.41}$$

The sum over $\{m_{\boldsymbol{k}n}\}$ can be factorized into a product of sums:

$$\mathcal{F} = \sum_{\boldsymbol{k}n} \frac{\mathcal{E}_{\boldsymbol{k}n}}{2} - \frac{1}{\beta} \ln \left[ \prod_{\boldsymbol{k}n} \sum_{m=0}^{\infty} \mathrm{e}^{-\beta \mathcal{E}_{\boldsymbol{k}n} m} \right]. \tag{7.42}$$

The sum over $m$ is a geometric sum, such that the free energy finally reads

$$\mathcal{F} = \sum_{\boldsymbol{k}n} \frac{\mathcal{E}_{\boldsymbol{k}n}}{2} + \frac{1}{\beta} \ln \left[ \prod_{\boldsymbol{k}n} 1 - \mathrm{e}^{-\beta \mathcal{E}_{\boldsymbol{k}n}} \right]. \tag{7.43}$$

It is useful to separate out the contribution from zero-point fluctuations and write $\mathcal{F}(\theta) = F_q(\theta) + F_t(\theta)$ where

$$F_q(\theta) = \frac{1}{2} \sum_{\boldsymbol{k} \in \mathrm{BZ}, n} \mathcal{E}_{\boldsymbol{k}n}(\theta), \tag{7.44}$$

$$F_t(\theta) = k_B T \sum_{\boldsymbol{k} \in \mathrm{BZ}, n} \ln \left( 1 - e^{-\beta \mathcal{E}_{\boldsymbol{k}n}(\theta)} \right). \tag{7.45}$$

The purely quantum contribution $F_q(\theta)$ diverges, but this divergence can be regularized by subtracting the free energy for a particular mean-field configuration, e.g. $\theta = 0$: $\Delta F_q(\theta) \equiv F_q(\theta) - F_q(0)$. This regularized expression converges, and no renormalization of the effective range of interactions is needed. The zero-point contribution to the free energy, numerically computed as a function of $\theta$, is shown in Fig. 7.3(a) where the summation is performed over 26 bands. We emphasize that in order to obtain quantitatively correct results, including only the gapless modes is insufficient. One sees, indeed, that the $\theta = 0$ state has the lowest energy and at $T = 0$ such a state is unambiguously selected.

We now turn to the finite-temperature contribution to the free energy. Interestingly, one finds that the sign of the thermal contribution $\Delta F_t(\theta) = F_t(\theta) - F_t(0)$ is negative and opposite to that of $\Delta F_q(\theta)$. Furthermore, the magnitude of the thermal contribution is always smaller than the contribution from zero-point fluctuations, in contrast to typical situations where thermal fluctuations enhance the degeneracy lifting and are larger in magnitude for modest temperatures (see, e.g. [143]). The sign of $\Delta F_t$ at low $T$ can be understood by noting that the spin mode has the lowest energy for $\theta = \pi/2$ (Fig. 7.2).

As seen in Fig. 7.3(b), the magnitude of $\Delta F_t(\theta)$ approaches $\Delta F_q(\theta)$ at high $T$, so that $\Delta F(\theta) = \Delta F_q(\theta) + \Delta F_t(\theta) = \mathcal{O}\left(T^{-1}\right) \to 0$ in this limit. This behavior

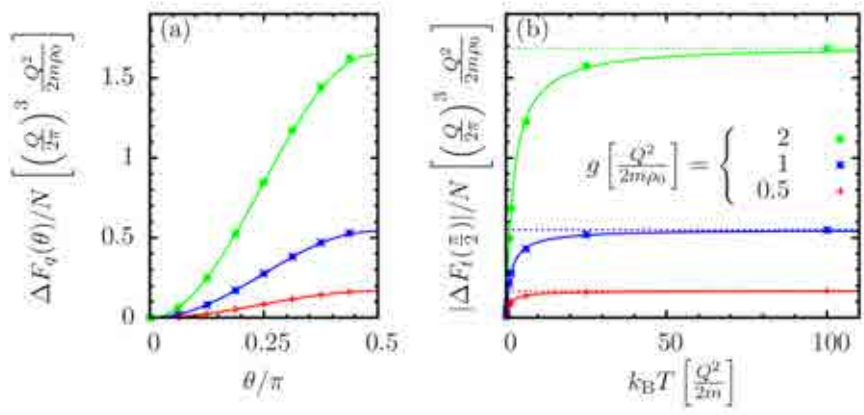


FIGURE 7.3: (a) The zero-point contribution to the free energy $\Delta F_q$ as a function of $\theta$ for three different values of $g$. (b) The absolute value of the (negative) thermal free energy splitting between the $\theta = 0$ and $\theta = \pi/2$ configurations $|\Delta F_t(\pi/2)|$ as a function of temperature (solid line). This is seen to approach the quantum zero-point splitting $\Delta F_q(\pi/2)$ at high temperatures (dashed line). In both panels the solid lines are fits to the numerically computed data points. From: [135]

can be understood through a high $T$ expansion of the free energy [135]:

$$F_t(\theta) \approx k_B T \sum_{\boldsymbol{k}\in \mathrm{BZ},n} \ln\left[\beta \mathcal{E}_{\boldsymbol{k}n}(\theta)\right] - \frac{1}{2}\sum_{\boldsymbol{k}\in \mathrm{BZ},n} \mathcal{E}_{\boldsymbol{k}n}(\theta). \tag{7.46}$$

As the second term cancels the quantum contribution, we focus on the larger first term which can be written as

$$\begin{aligned} k_B T \sum_{\boldsymbol{k}\in \mathrm{BZ},n} \ln\left[\beta \mathcal{E}_{\boldsymbol{k}n}(\theta)\right] &= \frac{1}{2} k_B T \ln\left|\det(\beta \boldsymbol{\eta} M_{\boldsymbol{k}})\right| \\ &= k_B T \sum_{\boldsymbol{k}\in \mathrm{BZ}',n} \ln\left|\beta \lambda_{\boldsymbol{k}n}\right| \end{aligned}$$

where $\lambda_{\boldsymbol{k}n}$ are the eigenvalues of $M_{\boldsymbol{k}}$, and we have used $|\det(\boldsymbol{\eta})| = 1$. The eigenvalues $\lambda_{\boldsymbol{k}n}$ are independent of the condensate configuration given by $\theta$. This can be seen in real space by noting that the $\theta$-dependence of $M(\boldsymbol{r},\boldsymbol{p})$ from Eq. (7.32) can be removed through the unitary transformation $M(\boldsymbol{r},\boldsymbol{p}) \to \mathbf{U}^\dagger M(\boldsymbol{r},\boldsymbol{p})\mathbf{U}$ where $\mathbf{U} = \frac{1}{2}(\mathbf{1}+\boldsymbol{\sigma}_x)\otimes \mathbf{1} + \frac{1}{2}(\mathbf{1}-\boldsymbol{\sigma}_x)\otimes e^{i\theta\boldsymbol{\sigma}_y}$. The same transformation introduces a $\theta$-dependence into $\boldsymbol{\eta}$ and so the eigenvalues of $\boldsymbol{\eta} M(\boldsymbol{r},\boldsymbol{p})$ generally depend on $\theta$, which determine the Bogliubov spectrum. Thus, to this order we find that $\Delta F_t(\theta) = -\Delta F_q(\theta)$. The next-order term in the high-temperature expansion has

$1/T$ dependence, as can be seen from the numerical results shown in Fig. 7.3(b).

We now quantify the magnitude of the degeneracy lifting considering realistic experimental values. As in Ref. [42], we consider $^{87}$Rb in the $F = 1$ hyperfine state. The spin-independent interaction constant $g/h$ is given by $7.6{\cdot}10^{-12}$ J cm$^3$. Note that the spin-dependent interaction term is two orders of magnitude smaller. As a typical density we choose $\rho_0 = 2 \times 10^{14}\text{cm}^{-3}$, and we set the SO coupling strength such that $g\rho_0 = \frac{Q^2}{2m}$. We then find that at zero temperature the free energy splitting per particle due to fluctuations is $\Delta F(\pi/2)/k_B N = 110\,\text{pK}$. One should note that this number should not be directly compared with the condensate temperature since the *total* energy determines the ground state. It is this energy which will determine experimental timescales for the relaxation to the ground state, which in sufficiently large systems should be short enough to occur within the duration of the experiment.

### 7.2.4 Condensate Depletion

Finally, we have to check the self-consistency of our approach. This is determined by the depletion or the number of particles excited out of the condensate $N_{\text{ex}}$ considered as a fraction of the total particle number $N$. Consistency of course requires that this be finite, as neglecting terms beyond quadratic order in $\mathcal{H}$ from Eq. (7.23) is quantitatively reliable only if $N_{\text{ex}} \ll N$. The quantum and thermal contributions to $N_{\text{ex}} = N_q + N_t$ are [3]

$$N_q = \frac{1}{2} \sum_{\boldsymbol{k}\in\text{BZ},n} \langle v_{\boldsymbol{k}n}| \left(\mathbf{1} - \boldsymbol{\eta}\right) |v_{\boldsymbol{k}n}\rangle \tag{7.47}$$

$$N_t = \sum_{\boldsymbol{k}\in\text{BZ},n} \langle v_{\boldsymbol{k}n}|\, v_{\boldsymbol{k}n}\rangle\, f(\mathcal{E}_{\boldsymbol{k}n}), \tag{7.48}$$

where $f(x) = (e^{\beta x} - 1)^{-1}$ is the Bose-Einstein distribution function.

To check whether these expressions converge, we numerically evaluate them for $k_c \leq k \leq K_c$, where $k_c$ is a small-momentum cutoff, and $K_c$ is a large-momentum cutoff. By varying $K_c$ we find that none of them has an ultraviolet divergence. The situation is more complicated in the infrared, as for an infinite system, the sums become integrals over an integrand which diverges at $k = 0$. Decreasing $k_c$ therefore also requires to increase the numerical resolution, in order to not overestimate the value of the integral. As shown in Figs. 7.4 and 7.5 for $\theta = 0$, this introduces large numerical errors for small $k_c$, which may make the integral

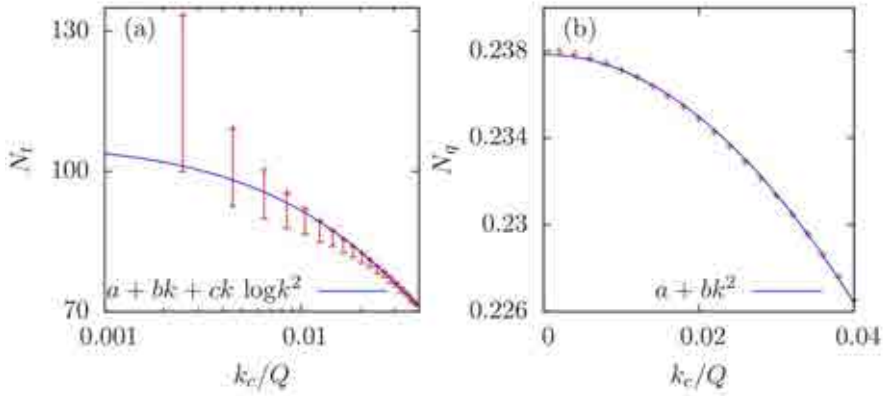


FIGURE 7.4: (a) Thermal depletion (at $\beta = 0.1$) in 3D as a function of the small cutoff momentum $k_c$, for $\theta = 0$. The sum is performed over a small grid ($\Delta k = 0.001$, $\Delta\phi = \Delta\theta = 2\pi/128$). The errorbars are defined as the numerical difference to the sum over a grid with step sizes increased by 30%. They point downwards, as increasing the resolution is found to decrease the value of the sum. For fitting the data, we take into account values with relative errors less than 5 %, which amounts for excluding the first 5 values. These poorly converged values make the depletion look divergent, though the fit according to the expectation from the small-momentum expansion [146] shows that it converges. We find the density mode (which is linear in $k_x$) as the mode which predominantly contributes to the thermal depletion. (b) Quantum depletion in 3D for $\theta = 0$. The grid resolution is $\Delta k = 0.002$, $\Delta\phi = \Delta\theta = 2\pi/64$. The quantum depletion clearly converges with a quadratic $k_c$-dependence.

look divergent though it is not. An exception is the quantum depletion $N_q$ in 3D, where the integrand does not diverge for $k = 0$, and the sum clearly converges [see Fig. 7.4(b)].

In all other cases, the numerical results seem to be less reliable, but luckily in the infrared limit we can also resort to analytical results from the small-$k$ expansion sketched before. At $\theta = 0$, the density mode dominates the depletion integrals, which read [146]:

$$N_q \sim \int \mathrm{d}^d\boldsymbol{\kappa}\ \frac{1}{\sqrt{\kappa^2 \sin^2\Phi + \kappa^4 \cos^4\Phi}}, \tag{7.49}$$

$$N_t \sim \int \mathrm{d}^d\boldsymbol{\kappa}\ \frac{1}{\kappa^2 \sin^2\Phi + \kappa^4 \cos^4\Phi}, \tag{7.50}$$

where $\boldsymbol{\kappa} = \boldsymbol{k} - \boldsymbol{Q}$, and $\Phi$ is the polar angle (in 2D), or the azimuthal angle (in 3D). Note that for the 3D-integral $\mathrm{d}^3\boldsymbol{\kappa} \sim \kappa^2 \sin\Phi\ \mathrm{d}\kappa\ \mathrm{d}\theta\ \mathrm{d}\Phi$, while the 2D-integral

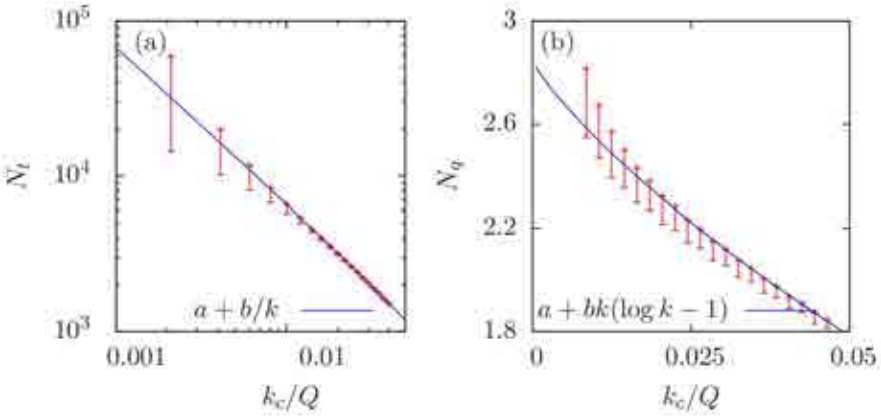


FIGURE 7.5: (a) Thermal depletion (at $\beta = 0.1$) in 2D as a function of the small cutoff momentum $k_c$, for $\theta = 0$. The grid resolution is$\Delta k = 0.0002$, $\Delta\phi = 2\pi/640$). The errorbars are defined as the numerical difference to the sum over a grid with doubled step sizes. For fitting the data, we take into account values with relative errors less than 5 % (which amounts for excluding the first 6 values). The thermal depletion in 2D has a $1/k$ divergence. (b) Quantum depletion in 2D for $\theta = 0$. The grid resolution is$\Delta k = 0.001$, $\Delta\phi = 2\pi/96$). The errorbars are defined as the numerical difference to the sum over a grid with step sizes increased by 33%. These first seven values are not taken into account for the fit, as they are poorly converged. They make the 2D quantum depletion look divergent, though the fit according to the expectation from the small-momentum expansion [146] shows that it converges.

reads $\mathrm{d}^2\boldsymbol{\kappa} \sim \kappa\, \mathrm{d}\kappa\, \mathrm{d}\Phi$. To evaluate Eq. (7.49) in 2D, we note that for small $\boldsymbol{\kappa}$ the integral is dominated around $\Phi = 0$, so we expand the trigonometric functions around this point. Then performing the $\Phi$-part of the integral, we end up with $N_q \sim \int \mathrm{d}\kappa\ \log\kappa$, which depends as $k_c(1 - \log k_c)$ on the small-momentum cutoff. Our numerical result shown in Fig. 7.5(b) perfectly agrees with this functional behavior taking into account the numerical errors. Thus, at $T = 0$, the depletion is finite in both two and three dimensions.

For $T > 0$, we again expand the trigonometric functions around $\Phi = 0$, where the integrand diverges, and perform the integral in $\Phi$. In 3D, this yields $N_t \sim \int \mathrm{d}\kappa\ \log\left(1 + \frac{c}{\kappa}\right) \sim a + bk_c + ck_c \log k_c^2$. In 2D, we obtain $N_t \sim \int \mathrm{d}\kappa\ \kappa^{-2} \sim \frac{1}{\kappa}$. The numerical results shown in Figs. 7.4(a) and 7.4(a) agree with these functional dependencies. Thus, while finite temperature leads to a divergence of the thermal depletion in 2D, the 3D system remains stable also for $T > 0$ [147, 148]. Qualitatively the same results are obtained for $\theta > 0$, though in this case the spin mode dominates the depletion integrals.

To conclude this chapter, we summarize our results. As shown, for sufficiently weak trapping potentials, Rashba SO-coupled bosons have a large ground state degeneracy, which on the mean-field level is not fully lifted by isotropic interactions. Within a Bogoliubov approximation, we have calculated the collective excitations of the system. Thereby we have established that fluctuations select a single mode into which the bosons are expected to condense. Such an ordering due to fluctuations is called order-by-disorder, and we have discussed the feasibility to observe this effect in an experiment with Rashba coupled bosons. Especially we have argued that such a configuration is stable in 3D even for finite temperature, while the 2D system requires $T = 0$. We expect bosons with Rashba SO coupling to be realized in the near future for which the predicted configuration should be observable in Stern-Gerlach experiments.

# Chapter 8

# Mott transition in synthetic gauge fields

So far we have considered continuous systems. But as we already have sketched in the introduction of this thesis, spectacular progress in the field has been achieved by subjecting cold atoms to optical lattices [6]. These are trapping potentials built by counter-propagating lasers which lead to a potential with a periodic modulation. Optical lattices therefore allow to realize lattice models as they might for instance be relevant in solid-state or high-energy physics. One of the simplest of such models, realized with cold atoms in a pioneering experiment [6], is the Bose-Hubbard (BH) model [5, 8]. The appeal of this model stems from the competition between a hopping strength $J$, due to which the bosons may build up long-range correlations, and a repulsive on-site interaction of strength $U$. For integer filling, $U$ penalizes hopping processes, as a local increase of particle number costs more energy than the corresponding decrease of particle number on the neighboring site saves. Correlations between atoms in different sites are therefore hindered by the interaction part. At a certain ratio $J/U$, the bosons undergo a phase transition from such an uncorrelated phase, the so-called Mott insulating (MI) phase, to a correlated phase, the superfluid (SF) phase. This phase transition is not triggered by thermal fluctuations, that is, it can also occur at zero temperature. Instead it depends critically on the Hamiltonian parameters $J$ and $U$, and is therefore a paradigm of a quantum phase transition (QPT) [9]. The experiment of Ref. [6] has pushed QPTs from a theoretical concept to an experimental reality.

One has then been able to go even deeper: When the system becomes superfluid, the phase correlations between particles must spontaneously break the phase-rotational symmetry of the Hamiltonian. From the theoretical point of view, it is well known that this has to result in massless collective excitations, the so-called Nambu-Goldstone bosons [149, 150]. In 2009, experimentalists from Hamburg have been able to detect this mode in a BH system [151]. While the Nambu-Goldstone mode is considered to be an excitation of the phase of the SF order parameter, it should also be possible to excite its amplitude, which has theoretically been predicted to result in a gapped and massive mode [152–155]. Very recently, these excitations have been seen in an experiment in Munich [156]. When quenching from the phase-correlated phase into the Mott phase, the BH system has also been used to study interesting quantum dynamics, giving rise to collapse-and-revival effects similar to the ones we have discussed in Chapter 5 [106].

In this chapter, we wish to further enrich the BH model by providing it with an artificial gauge field. As we pointed out in Chapter 2, it is possible to achieve artificial gauge fields for particles in optical lattices via a laser-assisted hopping term [43, 44]. Other techniques which recently have been proven experimentally are Rashba induced Peierls phases [47], or a shaking of the lattice [48]. Thus, artificial magnetic fields in optical lattices already exist, and even artificial spin-orbit (SO) coupling for cold atoms on optical lattices are in reach.

The motivation for implementing gauge fields in lattice systems are manifold. The periodic structure relates such system to solids, and in the context of spin-orbit coupling to the physics of topological insulators. But it is also very appealing from a theoretical point of view. For decades, the intriguing energy spectrum of non-interacting electrons in a two-dimensional periodic potential with a perpendicular magnetic field is known to be a fascinating fractal figure, the so-called *Hofstadter butterfly* [157]. Depending on the precise value of the magnetic flux per plaquette, the energy bands are split and shifted within the Brillouin zone. Detecting this structure of the spectrum experimentally is still a challenge, which might be achieved by realizing the Hofstadter model in a cold atomic setup. The presence of an additional non-Abelian gauge field has been shown to further enrich the spectrum to a figure which has been named the *Hofstadter moth* [44].

The scenario we investigate in this chapter combines the two aspects of an MI-SF transition driven by local interactions, and a modification of the single-particle dispersion due to an artificial gauge field. The interplay between single-particle

and many-body physics can very conveniently be studied within a resummed hopping expansion, since the many-body problem becomes exactly solvable in the limit of no hopping. Thus, a formula based on the exactly known Green's functions of the system without hopping can be derived which, just by plugging in the free dispersion subjected to the gauge field, yields a good approximation to the full Green's function up to hopping strengths where the system enters the SF phase. For the case of a BH system without gauge fields, this method has allowed to precisely localize the MI-SF phase boundary [11], and to describe the different excitations of the system [154, 155].

In the setup considered here we study bosons on a square lattice with a pseudospin-$\frac{1}{2}$ degree of freedom. This allows to go beyond the effects due to a magnetic field [158–160], and consider also SU(2) gauge fields, mimicking an SO coupling. Even in the absence of any gauge fields, the extension of the BH model to systems of multi-species and higher spin bosons has been shown to provide rich phase diagrams [161–163]. In this chapter, we will show that for the simplest non-Abelian gauge field, described by a constant SU(2) gauge potential, the interplay of inter- and intra-species interactions and the presence of the external gauge field leads to qualitative changes in several aspects of the MI-SF transition. Computing the momentum distribution of the bosons in the MI phase near the MI-SF transition, we show that the precursor peaks occur at finite, rather than zero, momenta due to the presence of the gauge field. We find a sudden change of the peak positions when the strength of the gauge field is varied in certain parameter regimes. This indicates that a slight change in the gauge field strength has strong impact on the dynamical behavior of the system and might be especially relevant for its non-equilibrium dynamics. This behavior is somewhat reminiscent of the QPT of excited states discussed in Ref. [164] and of the abrupt sign change of the Hall conductivity which has recently been found for a system of hardcore bosons [165]. We demonstrate that the phase boundary displays a non-monotonic dependence on the strength of the gauge field leading to re-entrant MI-SF transitions with the variation of the strength of the gauge field at a fixed hopping strength. Finally, we construct an effective Landau-Ginzburg theory and use it to chart out the nature of the SF phase into which the transition takes place. We show that for a constant non-Abelian gauge field, the SF density near the transition does not exhibit any spatial ordering. This feature is to be contrasted with the case where an Abelian flux (with half flux quanta per lattice plaquette) is added over the existing SU(2) potential leading to a spatial pattern in the SF density.

The work presented in this chapter has been published in Ref. [166].

## 8.1 The Model

As explained in chapter 2, an SU(2) gauge field can be generated for a system of two-species ultracold bosons by distinguishing between the atoms in two different Zeeman levels representing the two 'flavors' of the non-Abelian theory [44]. In doing so, one substitutes the standard hopping process by a laser-assisted tunneling, which may depend on the position and the state of the atom. One of the crucial features of such a tunneling is its ability to flip the state of the atom. Taking into account local interactions between the atoms, the effective Hamiltonian describing the system can be seen to be the same as that of a two-species BH model [161, 162, 167], with an additional non-Abelian vector potential in the hopping term providing the additional inter-species coupling. Defining the number operators $\hat{\mathrm{n}}_i^{\mathrm{a}} = \hat{\mathrm{a}}_i^\dagger \hat{\mathrm{a}}_i$ and $\hat{\mathrm{n}}_i^{\mathrm{b}} = \hat{\mathrm{b}}_i^\dagger \hat{\mathrm{b}}_i$, where $\hat{\mathrm{a}}_i$ and $\hat{\mathrm{b}}_i$ denote the boson annihilation operators of the two species, the local part of the Hamiltonian reads

$$\hat{\mathrm{H}}_0 = \sum_i \left[ \frac{U^{\mathrm{aa}}}{2} \hat{\mathrm{n}}_i^{\mathrm{a}} (\hat{\mathrm{n}}_i^{\mathrm{a}} - 1) + \frac{U^{\mathrm{bb}}}{2} \hat{\mathrm{n}}_i^{\mathrm{b}} (\hat{\mathrm{n}}_i^{\mathrm{b}} - 1) + U^{\mathrm{ab}} \hat{\mathrm{n}}_i^{\mathrm{a}} \hat{\mathrm{n}}_i^{\mathrm{b}} - \mu^{\mathrm{a}} \hat{\mathrm{n}}_i^{\mathrm{a}} - \mu^{\mathrm{b}} \hat{\mathrm{n}}_i^{\mathrm{b}} \right], \quad (8.1)$$

where $U^{\mathrm{xy}}$ is the strength of the interaction between a pair of particles with flavors x and y and $\mu^{\mathrm{x}}$ denotes the chemical potential of species x. The Hamiltonian $\hat{\mathrm{H}}_0$ is easily diagonalized using the Fock state basis: $\hat{\mathrm{H}}_0 \left| n^{\mathrm{a}}, n^{\mathrm{b}} \right\rangle = E_{n^{\mathrm{a}}, n^{\mathrm{b}}} \left| n^{\mathrm{a}}, n^{\mathrm{b}} \right\rangle$. It is easy to see that $\hat{\mathrm{H}}_0$ allows for ground-state degeneracies which are lifted in the presence of a hopping term leading to different types of "magnetic" orderings in the Mott state[161].

As we wish to focus on the influence of gauge fields on the MI-SF transition, we shall first consider the parameter regime for which $\hat{\mathrm{H}}_0$ has a unique ground-state in the local limit. The simplest choice in this regard is to assume two independent, identical systems, i.e. $U^{\mathrm{aa}} = U^{\mathrm{bb}} \equiv U$, $\mu^{\mathrm{a}} = \mu^{\mathrm{b}} \equiv \mu$, and $U^{\mathrm{ab}} = 0$. With this, $\hat{\mathrm{H}}_0$ describes a system which in its ground-state is in both flavors occupied by an equal number $n$ of particles, with $\mu/U < n < \mu/U + 1$ as in the one-component BH model. This setup will be further investigated in Sections 8.2.2 and 8.3, for the MI and SF phase, respectively.

In another scenario, investigated in Sections 8.2.3 and 8.3, we take into account repulsive interactions between the components ($U^{\mathrm{ab}} > 0$). In this case, a subspace

spanned by all states $\left|n^{\mathrm{a}}, n^{\mathrm{b}}\right\rangle$ with $n^{\mathrm{a}}+n^{\mathrm{b}}=\tilde{n}$ forms the degenerate ground state manifold, where $\tilde{n}$ is the particle number per site. For $0<\mu/U<U^{\mathrm{ab}}/U$, one single atom occupies each site, such that any linear combination $c_1\left|1,0\right\rangle+c_2\left|0,1\right\rangle$ at every site is a ground state of the unperturbed Hamiltonian $\hat{\mathrm{H}}_0$. The hopping lifts this degeneracy. As shown in Ref. [162], for small $\lambda\equiv U^{\mathrm{ab}}/U$, an antiferromagnetic ordering is preferred, while for $\lambda\sim 1$, the system chooses a translational-invariant ferromagnetic phase. Between these two limits an XY ordering with $c_1=c_2=1/\sqrt{2}$ occurs. In the rest of this work, we shall focus on the ferromagnetic and the XY phases, where the ground state preserves translational symmetry.

The kinetic part of the Hamiltonian is given by

$$\hat{\mathrm{H}}_1=-\sum_{i,j}(\hat{\mathrm{a}}_i^{\dagger},\hat{\mathrm{b}}_i^{\dagger})J_{ij}\begin{pmatrix}\hat{\mathrm{a}}_j\\ \hat{\mathrm{b}}_j\end{pmatrix}, \tag{8.2}$$

where $J_{ij}=\delta_{<ij>}J\mathrm{e}^{-i(\boldsymbol{A}_j\cdot\boldsymbol{r}_j-\boldsymbol{A}_i\cdot\boldsymbol{r}_i)}$ is a nearest-neighbor hopping with a constant strength $J$, and we have chosen $\hbar=1$. The phase factor associated with the hopping is defined by the gauge potential $\boldsymbol{A}_i$, which we choose to be of the following form

$$\boldsymbol{A}_i=(\alpha\sigma_y,\ \beta\sigma_x+2\pi\boldsymbol{r}_i\cdot\hat{e}_x\Phi,\ 0), \tag{8.3}$$

where $\sigma_{x,y}$ are the Pauli matrices, $\Phi$ is an Abelian flux, $\hat{e}_x$ denotes the unit vector along $x$, $\boldsymbol{r}_i$ is the spatial coordinate of site $i$, and $\alpha,\beta$ are parameters characterizing the non-Abelian vector potential. Although interesting anisotropy effects can be expected from choosing $\alpha\neq\beta$ (see Refs. [73, 77] and Section 3.2.2.2), here we shall consider $\alpha=\beta$ for simplicity. With this choice, the intra-species hopping terms ($\hat{\mathrm{a}}_i^{\dagger}\hat{\mathrm{a}}_j$ and $\hat{\mathrm{b}}_i^{\dagger}\hat{\mathrm{b}}_j$) become proportional to $\cos\alpha$, while the inter-species hopping terms due to the non-Abelian vector potential ($\hat{\mathrm{a}}_i^{\dagger}\hat{\mathrm{b}}_j$ and $\hat{\mathrm{b}}_i^{\dagger}\hat{\mathrm{a}}_j$) become proportional to $\sin\alpha$. For $\alpha=0$ and $\Phi\neq 0$, we thus recover the Hofstadter problem of a constant magnetic field perpendicular to the two-dimensional (2D) system in the Landau gauge [157]. Note that also in the opposite limit, $\Phi=0$ and $\alpha\neq 0$, where the vector potential becomes constant, the non-Abelian character of the gauge potential, i.e. $[A_i,A_j]\neq 0$, yields a constant but finite gauge field. For the Abelian flux, we shall focus on $\Phi=p/q$, where $p$ and $q$ are co-prime integers. Most of our work has been done for $\Phi=0$ or $1/2$; however, the method developed here can be straightforwardly extended to other values of $\Phi$ as shown in Ref. [159].

## 8.2 Mott insulating phase

### 8.2.1 Hopping expansion

Our approach to study the full Hamiltonian $\hat{\mathrm{H}} = \hat{\mathrm{H}}_0 + \hat{\mathrm{H}}_1$ is based on a resummed hopping expansion as developed in Refs. [11, 154, 155, 168] for the single species BH model. In this formalism, one considers the hopping term as a perturbation and focuses on the time evolution of the operators. For a description of the equilibrium physics at zero or finite temperature, it is convenient to work in imaginary time. In the Dirac picture, where $\hat{\mathrm{H}}_0$ is assumed to drive the time evolution of the operators, we have: $\hat{\mathrm{a}}(\tau) = \mathrm{e}^{\hat{\mathrm{H}}_0\tau}\ \hat{\mathrm{a}}\ \mathrm{e}^{-\hat{\mathrm{H}}_0\tau}$. We introduce artificial sources $j_i^{\mathrm{a}}(\tau)$, $j_i^{\mathrm{b}}(\tau)$ and define $\hat{\mathrm{H}}_1[\{j\}](\tau) \equiv \hat{\mathrm{H}}_1(\tau) + \sum_i \Big(\bar{j}_i^{\mathrm{a}}(\tau)\hat{\mathrm{a}}_i(\tau) + \bar{j}_i^{\mathrm{b}}(\tau)\hat{\mathrm{b}}_i(\tau) + \mathrm{h.c.}\Big)$ with $\beta$ the inverse temperature, and $\{j\}$ denoting the set of all four currents. The free energy of the system can then be written as a functional of the sources:

$$\mathcal{F}[\{j\}] = -\frac{1}{\beta}\ln\mathrm{Tr}\Big(\mathrm{e}^{-\beta\hat{\mathrm{H}}_0}\hat{\mathrm{T}}_\tau \mathrm{e}^{-\int_0^\beta \mathrm{d}\tau\ \hat{\mathrm{H}}_1[\{j\}](\tau)}\Big), \tag{8.4}$$

where $\hat{\mathrm{T}}_\tau$ indicates imaginary-time ordering. From this it can directly be seen that the derivatives $\beta\delta\mathcal{F}/\delta\bar{j}_i^{\mathrm{a(b)}}(\tau) = \langle\hat{\mathrm{a}}_i(\hat{\mathrm{b}}_i)(\tau)\rangle = \Psi_i^{\mathrm{a(b)}}(\tau)$ yield the order parameter fields $\Psi_i^{\mathrm{a(b)}}(\tau)$ which vanish within the MI phase. For a description of the Mott physics, it is thus sufficient to expand $\mathcal{F}[\{j\}]$ up to second order in the currents. Furthermore, as quantum fluctuations of the hopping term scale down with dimension [169], in a two-dimensional system an expansion of $\mathcal{F}[\{j\}]$ up to first order in the hopping strength $J$ and a subsequent resummation is expected to yield qualitatively correct results. The resummation is automatically achieved by performing a Legendre transformation iteratively in the hopping, which substitutes the source fields $\{j\}$ by the physical order-parameter field. Carrying out these steps, as detailed in Refs. [11, 168], we finally obtain the effective action of the system up to second order in $J/U$:

$$S[\{\Psi\}]^{\mathrm{MI}} = \frac{1}{\beta}\sum_{i,j}\left(\bar{\Psi}_i^{\mathrm{a}}, \bar{\Psi}_i^{\mathrm{b}}\right)\left[\left(\hat{G}_{ij}^0\right)^{-1} - J_{ij}\right]\begin{pmatrix}\Psi_j^{\mathrm{a}}\\ \Psi_j^{\mathrm{b}}\end{pmatrix} \tag{8.5}$$

where $\hat{G}_{ij}^0 = \langle\hat{\mathrm{T}}_\tau\hat{\mathrm{O}}_i^\dagger(\tau)\hat{\mathrm{O}}_j(\tau')\rangle_0$ is the unperturbed two-point function. Here the operators $\hat{\mathrm{O}}_i^\dagger$ and $\hat{\mathrm{O}}_j$ may be of type $a$ or $b$, and the thermal average, $\langle\cdot\rangle_0$, is with respect to $\hat{\mathrm{H}}_0$ at the inverse temperature $\beta$. Note that $\hat{G}^0$ is a function of $\tau - \tau'$; thus $(\hat{G}^0)^{-1}$ is most easily found in frequency space. We point out that an

alternative way to derive the same effective action within a random phase approximation is described in Ref. [170] for the BH model, and can straightforwardly be generalized to systems with an Abelian gauge field [159]. From Eq. (8.5), we find that $\hat{G} = [(\hat{G}^0)^{-1} - J_{ij}]^{-1}$ is the resummed two-point function which can be used, for example, to find the boson momentum distribution [159, 170]

$$n_{\boldsymbol{k}} = -\lim_{T\to 0} \frac{1}{\beta} \sum_{\omega_{\mathrm{M}}} \mathrm{Tr}[\hat{G}(\boldsymbol{k}, i\omega_{\mathrm{M}})]. \tag{8.6}$$

These momentum distributions can be observed in time-of-flight (TOF) measurements, as we shall discuss later.

The excitation spectra of the bosons can be obtained from the poles of $\hat{G}$ or equivalently by setting up the equation of motion: $\delta S[\{\Psi\}]^{\mathrm{MI}}/\delta\bar{\Psi}^{\mathrm{a,b}} = 0$. In Fourier space, this reads

$$\sum_{\boldsymbol{k}} \left[ \delta_{\boldsymbol{k},\boldsymbol{k}'} \hat{G}^0(\omega_{\mathrm{M}})^{-1} - J_{\boldsymbol{k},\boldsymbol{k}'} \right] \begin{pmatrix} \Psi^{\mathrm{a}}_{\boldsymbol{k}'}(\omega_{\mathrm{M}}) \\ \Psi^{\mathrm{b}}_{\boldsymbol{k}'}(\omega_{\mathrm{M}}) \end{pmatrix} = 0, \tag{8.7}$$

where $J_{\boldsymbol{k},\boldsymbol{k}'}$ is the Fourier transform of $J_{ij}$. After an analytic continuation to real frequencies $i\omega_{\mathrm{M}} \to \omega + i\epsilon$, the solutions of Eq. (8.7) yield the dispersion relations. In the following subsections, we apply this general procedure to specific choices of gauge potentials and parameters $\lambda$ and $\mu$.

### 8.2.2 Independent species

The simplest non-trivial parameter choice which we shall treat in this section corresponds to $\lambda = 0$ and $0 \le \mu/U \le 1$. In this case, $\hat{\mathrm{H}}_0$ describes two independent standard BH systems with unique non-degenerate ground state having one boson of each species per site. The coupling between them is provided by the inter-species hopping terms arising from the non-Abelian gauge potential. For this case, it is clear that the unperturbed Green function has vanishing off-diagonal terms, i.e. $G^0_{12} \sim \langle \hat{\mathrm{a}}^\dagger(0)\hat{\mathrm{b}}(\tau)\rangle_0 = 0$ and $\hat{G}^0_{21} \sim \langle \hat{\mathrm{b}}^\dagger(0)\hat{\mathrm{a}}(\tau)\rangle_0 = 0$. From our symmetric choice of parameters, it also follows that $G^0_{11} = G^0_{22}$ rendering $\hat{G}^0 \sim \mathbf{1}_{2\mathrm{x}2}$. Further, the site-factorizable nature of $\hat{H}_0$ guarantees that the diagonal elements of $\hat{G}^0$ are given by $\delta_{\boldsymbol{k},\boldsymbol{k}'}$ times a function $G^0(\omega_{\mathrm{M}})$ of a single Matsubara frequency

$$G^0(\omega_{\mathrm{M}}) = \sum_{n,m=0}^{\infty} \frac{\mathrm{e}^{\beta E_{n,m}}}{\mathcal{Z}^0} \left( \frac{n+1}{\Delta_{n+1} - i\omega_{\mathrm{M}}} - \frac{n}{\Delta_n - i\omega_{\mathrm{M}}} \right), \tag{8.8}$$

where $\mathcal{Z}^0 = \sum_{n,m=0}^{\infty} \mathrm{e}^{\beta E_{n,m}}$, and $\Delta_n = E_{n,m} - E_{n-1,m}$. In the zero-temperature limit, the Boltzmann sums in Eq. (8.8) reduce to a single term corresponding to the ground-state occupation numbers, $n = m = 1$. In the following two subsections, we shall compute $\hat{G}$ for the two simplest choices of gauge potentials corresponding to a constant non-Abelian gauge field: the one without Abelian flux, $\Phi = 0$, and that with an Abelian flux $\Phi = 1/2$.

#### 8.2.2.1 Constant gauge potential without magnetic flux ($\Phi = 0$)

For a constant gauge potential without Abelian flux, $\Phi = 0$, the hopping matrix is diagonal with respect to momentum $\boldsymbol{k}$, i.e.

$$J_{\boldsymbol{k},\boldsymbol{k}'} = 2J\Big\{ \cos\alpha[\cos(k_x) + \cos(k_y)]\mathbf{1} - \sin\alpha[\sin(k_x)\sigma_y + \sin(k_y)\sigma_x]\Big\}\delta_{\boldsymbol{k},\boldsymbol{k}'}, \quad (8.9)$$

where here and in the rest of the paper, we have set the lattice spacing $a \equiv 1$. As the unperturbed Green function $\hat{G}^0$ is already diagonal with respect to the internal degree of freedom, we need to diagonalize only the hopping matrix. Its eigenvalues are

$$E^{\pm}_{\boldsymbol{k}} = 2J\Big\{ \cos\alpha\,[\cos(k_x) + \cos(k_y)] \pm \sin\alpha\sqrt{\sin^2(k_x) + \sin^2(k_y)}\Big\}. \quad (8.10)$$

The energy bands of the system at zero temperature are thus given by $[G^0(\omega + i\eta)]^{-1}|_{T=0} - E^{\pm}_{\boldsymbol{k}} = 0$, where we have Wick rotated back to real frequency. This yields two quadratic equations

$$\begin{aligned} \omega^2 + \omega(2\mu - U + E^+_{\boldsymbol{k}}) + \mu^2 - \mu U + (\mu + U)E^+_{\boldsymbol{k}} &= 0, \\ \omega^2 + \omega(2\mu - U + E^-_{\boldsymbol{k}}) + \mu^2 - \mu U + (\mu + U)E^-_{\boldsymbol{k}} &= 0, \end{aligned} \quad (8.11)$$

leading to four energy bands shown in Fig. 8.1. Two of these bands occur at $\omega > 0$ and the other two at $\omega < 0$, so that they may be interpreted as particle/hole excitation spectra of the system. We note that as $\alpha \to 0$, the particle and the hole spectra become increasingly similar and ultimately indistinguishable for $\alpha = 0$ yielding the standard dispersion of MI bosons with no gauge potential [170]. Furthermore, the particle and hole excitations have a gap in the Mott phase which closes as one approaches the superfluid-insulator transition by increasing $J/U$. Beyond the transition point, which occurs at $J = J_c$, the solutions of Eq. (8.11) are complex, indicating instability of the Mott phase.

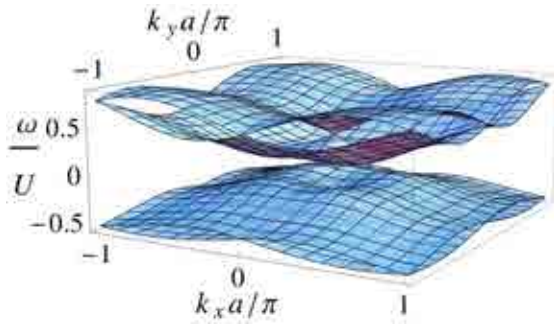


FIGURE 8.1: Boson energy dispersion for $\Phi = 0$, $\alpha = 1$, $\mu/U = 0.41$, and $J/U = 0.05$. See text for details. From: [166].

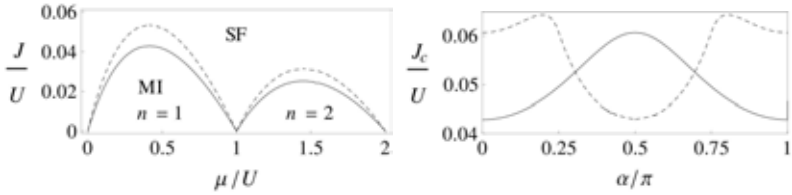


FIGURE 8.2: **Left:** The Mott lobes with $\alpha$ dependent heights. The solid (dashed) lines indicate the lobes for $\alpha = 0(1)$. **Right:** Value of $J_c$ at the tip of the $n = 1$ Mott lobe as a function of $\alpha$. The solid (dashed) lines correspond to $\Phi = 0(1/2)$. From: [166].

The MI-SF phase boundary, as obtained by the procedure described above, is shown in Fig. 8.2. We find that the phase boundary has the usual lobe structure. However, the value of $J_c$ at the tip of the Mott lobe is strongly influenced by $\alpha$ and can thus be tuned by varying the strength of the gauge field. This leads to re-entrant superfluid-insulator transitions in the system by variation of $\alpha$, provided that $J$ is appropriately fixed at (say) $J = J_c(\alpha = 0.2\pi)$ as can be seen from Fig. 8.2. We also note that the universality class of the superfluid-insulator transition has the same properties as in the standard BH case [8]. At the lobe tip, the additional particle-hole symmetry renders the dynamical critical exponent $z$ of the transition to be unity; at other points, $z = 2$.

One of the key difference of the superfluid-insulator transition in the present system from the normal BH model is that the position of the minima of the low-energy excitations at and near the critical point in the first Brillouin zone are at finite momenta and strongly depend on $\alpha$ (see Fig. 8.3). Since the position of these minima correspond to precursor peaks of the bosons near the critical point

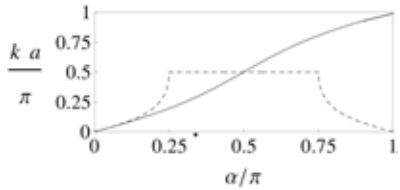


FIGURE 8.3: The position of the boson energy minima at finite wavevector parametrized by $k$ (see text) in systems without flux (solid line) and with 1/2 flux (dashed line). In the latter, a QPT of the excited band occurs at $\alpha = \pi/4$.From: [166].

[170], this feature is reflected in the momentum distribution of the bosons in the Mott phase near the transition. From the Green function $G$, we compute the momentum distribution using Eq. (8.6). The results of this calculation are shown in the top panel of Fig. 8.4. We find that at finite $\alpha$, the precursor peaks of the momentum distribution at $J \approx 0.97 J_c(\alpha)$ are at finite momenta, reflecting the fact that the subsequent condensation of the bosons at $J = J_c(\alpha)$ will occur at non-zero momenta. We note that such a pattern in the momentum distribution should be easily picked up in TOF experiments. Since standard TOF experiments will measure the distribution of both species simultaneously, the presence of the non-condensing mode will slightly reduce the visibility of the pattern. However, we expect that one should be able to easily subtract this background in order to observe the sharp peaks of the condensing mode. The most significant feature distinguishing the non-Abelian scenario from the known standard one, is the number of peaks which in general is quadrupled by the non-Abelian gauge field. We predict this feature to be clearly observable in TOF experiments.

#### 8.2.2.2 Gauge potential with magnetic flux ($\Phi = 1/2$)

Turning to the case with an Abelian flux $\Phi$ in the gauge potential of Eq. (8.3), the hopping matrix becomes space-dependent:

$$J_{ij} = J \exp\Big\{ -i\big[\alpha\sigma_y x_{ij} + (\alpha\sigma_x + 2\pi\Phi x_i \mathbf{1}) y_{ij}\big]\Big\}, \tag{8.12}$$

for nearest neighbors, so either the distances $x_{ij} \equiv x_j - x_i = 0$ and $y_{ij} \equiv y_j - y_i = \pm 1$, or vice versa. In Fourier space the general structure of the hopping matrix now reads:

$$J_{\boldsymbol{k},\boldsymbol{k}'} = A\delta_{\boldsymbol{k},\boldsymbol{k}'} + B\delta_{k_y,k'_y}\delta_{k_x,k'_x+2\pi\Phi} + B^*\delta_{k_y,k'_y}\delta_{k_x,k'_x-2\pi\Phi}, \tag{8.13}$$

where $A$ and $B$ are functions of momentum which will be specified later. Since the hopping matrix now connects momenta in the magnetic Brillouin zone which differ by $\pm 2\pi\Phi$, the $\boldsymbol{k}$-sum in Eq. (8.7) won't reduce to a single term as before without flux, but we can get rid of the sum by taking into account the periodic boundary conditions. For a generic $\Phi = p/q$, the periodicity of the lattice, $\Psi_{\boldsymbol{k}} = \Psi_{\boldsymbol{k}+2\pi n \boldsymbol{e}_x}$, ensures that Eq. (8.7) leads to a set of $q$ closed equations. To write them down, we introduce the notation

$$\boldsymbol{\Psi}_{\boldsymbol{k},n} \equiv \boldsymbol{\Psi}_{\boldsymbol{k}+n\times 2\pi\Phi \boldsymbol{e}_x} \tag{8.14}$$

with $n = 0, \cdots, q-1$. In this notation, the hopping matrix takes the form

$$J_{\boldsymbol{k}n,\boldsymbol{k}'n'} = \delta_{\boldsymbol{k},\boldsymbol{k}'} \left( A\delta_{n,n'} + B\delta_{n-1,n'} + B^*\delta_{n+1,n'} \right), \tag{8.15}$$

with

$$A \equiv A_{k_x,n} \equiv 2J \times \begin{pmatrix} \cos(k_x + 2\pi\Phi n)\cos\alpha & i\sin(k_x + 2\pi\Phi n)\sin\alpha \\ -i\sin(k_x + 2\pi\Phi n)\sin\alpha & \cos(k_x + 2\pi\Phi n)\cos\alpha \end{pmatrix}, \tag{8.16}$$

and

$$B \equiv B_{k_y} \equiv J\mathrm{e}^{ik_y} \begin{pmatrix} \cos\alpha & i\sin\alpha \\ i\sin\alpha & \cos\alpha \end{pmatrix}. \tag{8.17}$$

Since the interaction part is diagonal in $\boldsymbol{k}$ and $n$, it enters the equation of motion only in the diagonal elements, which according to Eq. (8.7) are given by

$$M_{k_x,n}(\omega_{\mathrm{M}}) \equiv [G^0(\omega_{\mathrm{M}})]^{-1}\mathbf{1}_{2\mathrm{x}2} - A_{k_x,n}. \tag{8.18}$$

With this, the equation of motion can be written in the Harper-like form:

$$M_{k_x,n}\boldsymbol{\Psi}_{\boldsymbol{k},n} - B_{k_y}\boldsymbol{\Psi}_{\boldsymbol{k},n-1} - B^*_{k_y}\boldsymbol{\Psi}_{\boldsymbol{k},n+1} = 0. \tag{8.19}$$

For each $n = 0, \cdots, q-1$ this yields a two-component equation, so we totally have $2q$ equations. Here we shall focus on $\Phi = 1/2$, i.e. $q = 2$, which allows us to find the solutions of these equations analytically via diagonalization of a $4 \times 4$

matrix $M_{\boldsymbol{k}}$, which is explicitly given by

$$M_{\boldsymbol{k}} = \begin{pmatrix} M_{k_x,0} & -2\mathrm{Re}(B_{k_y}) \\ -2\mathrm{Re}(B_{k_y}) & M_{k_x,1} \end{pmatrix}. \tag{8.20}$$

From this we now get four particle and four hole excitations, i.e. twice as in the $\Phi = 0$ case as discussed before. Accordingly, the presence of the magnetic flux $\Phi = 1/2$ can be seen to split each band. Again the most relevant bands are the particle (hole) excitation at lowest (highest) frequency. The gap between these excitations closes at $J = J_c$ leading to a second-order QPT separating the MI and the SF phases. The lobe structure of the phase boundary (and also the universality class of the transition) remain unchanged by the flux, as can be seen from Fig. 8.2. We note however that the plot of $J_c(\alpha)$ as a function of $\alpha$, shown in the bottom panel of Fig. 8.2, has a qualitatively different behavior compared to the case without Abelian flux discussed previously; nonetheless, the system will show similar re-entrant superfluid-insulator transitions as $\alpha$ is varied for a fixed $J$.

The most interesting difference between $\Phi = 0$ and $\Phi = 1/2$ concerns the number and positions of the extrema of the particle and hole excitations. We find that within the first magnetic Brillouin zone ($k_x \in [-\pi/q, \pi/q]$, $k_y \in [-\pi, \pi]$) and in the absence of a non-Abelian field ($\alpha = 0$), there are two extrema at $\boldsymbol{k} = (0,0), (0, \pm\pi)$, in agreement with Ref. [159]. Denoting these three points in the Brillouin zone as $\boldsymbol{k}_0$, $\boldsymbol{k}_+$, and $\boldsymbol{k}_-$, the extrema for non-zero $\alpha$ can be shown to occur at $\boldsymbol{k}_0 + (\pm k, \pm k)$, $\boldsymbol{k}_+ + (\pm k, -k)$, and $\boldsymbol{k}_- - (\pm k, +k)$, where $k$ as a function of $\alpha$ is plotted in Fig. 8.3. From this plot, we find eight extrema as long as $\alpha < \pi/4$. When $\alpha = \pi/4$, we get $k = \pi/2$ and the extrema are completely shifted to the zone edges, i.e. again we have only two extrema per Brillouin zone. For $\pi/4 < \alpha < 3\pi/4$, a plateau with a single fixed extremum is found. The derivative $\mathrm{d}k/\mathrm{d}\alpha$ diverges at $\alpha \to \pi/4$ which means that at this critical value of the non-Abelian field the global minima of the excited bands abruptly change their position. Thus a slight change in the gauge field strength is expected to completely modify the dynamical behavior of the system. This remarkable behavior can be directly observed in the momentum distribution shown in the bottom panel of Fig. 8.4. In particular, the abrupt change in the pattern of the momentum distribution when the flux is varied across $\pi/4$ reflects the sudden change in the position of the band minima with small change in $\alpha$. This behavior is reminiscent of the QPT of excited states discussed in Ref. [164]. Also the

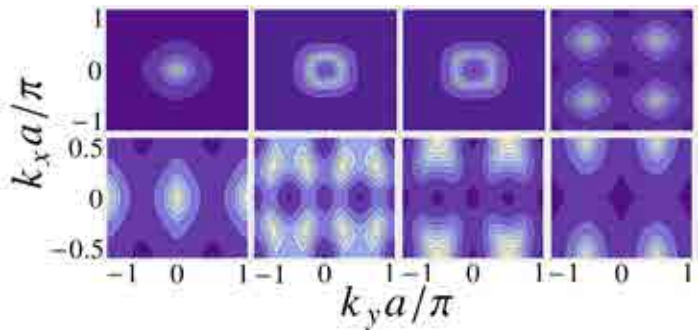


FIGURE 8.4: Momentum distributions of the bosons at $J \approx 0.97 J_c$. Bright regions correspond to high densities. The upper (lower) rows correspond to $\Phi = 0(1/2)$. The non-Abelian field strengths $\alpha$ are, from left to right in each panel, 0, 0.7, 0.8, and $\pi/2$. From: [166].

abrupt sign reversal of the Hall conductivity at half filling in a system of hard-core bosons subjected to a gauge field as studied in Ref. [165] falls into this category of phenomena where some control parameter modifies the system's dynamics in a discontinuous way.

### 8.2.3 XY configuration

In this section, we consider the case where $\lambda > 0$ such that the ground state of the two-species model without the gauge field correspond to the XY phase discussed in Ref.[162] where the bosons are in a superposition of both the states. Consequently, $\hat{G}^0$ will have non-zero off-diagonal components and one needs to diagonalize the full matrix $(\hat{G}^0)^{-1} - J_{\boldsymbol{k}}$ in the presence of the non-Abelian flux.

We begin by computing the elements of $\hat{G}^0$ at $T = 0$ which are given by

$$\hat{G}^0 = \begin{pmatrix} \langle \hat{\mathrm{T}}_\tau \hat{\mathrm{a}}_i^\dagger(\tau) \hat{\mathrm{a}}_i(\tau') \rangle_{\mathrm{GS}S} & \langle \hat{\mathrm{T}}_\tau \hat{\mathrm{a}}_i^\dagger(\tau) \hat{\mathrm{b}}_i(\tau') \rangle_{\mathrm{GS}} \\ \langle \hat{\mathrm{T}}_\tau \hat{\mathrm{b}}_i^\dagger(\tau) \hat{\mathrm{a}}_i(\tau') \rangle_{\mathrm{GS}} & \langle \hat{\mathrm{T}}_\tau \hat{\mathrm{b}}_i^\dagger(\tau) \hat{\mathrm{b}}_i(\tau') \rangle_{\mathrm{GS}} \end{pmatrix} . \tag{8.21}$$

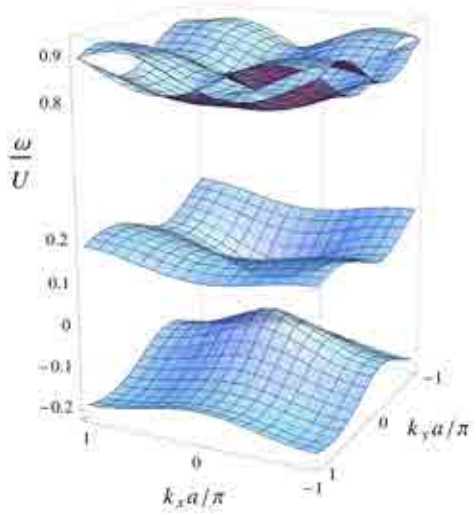


FIGURE 8.5: The excitation spectrum of the bosons in the XY phase system for $\alpha = 1$, $\Phi = 0$, $\mu/U = 0.15$, $\lambda = 0.3$, and $J/U = 0.021$.

For the XY ground state $|\mathrm{GS}\rangle = \frac{1}{\sqrt{2}}(|10\rangle + |01\rangle)$, discussed in Ref.[162], this matrix reads

$$\hat{G}^0(i\omega) = \left[\frac{1}{2U\lambda - 2(\mu + i\omega)} + \frac{1}{U - \mu - i\omega} + \frac{1}{2\mu + 2i\omega}\right]\mathbf{1} + \left[-\frac{U\lambda}{2(\mu + i\omega)(-U\lambda + \mu + i\omega)}\right]\sigma_x. \tag{8.22}$$

Inserting Eq. (8.22) into Eq. (8.7), and considering the case $\Phi = 0$, we find that the presence of the off-diagonal elements in $\hat{G}^0$ leads to two independent equations for the band dispersions given by

$$\begin{aligned} M_1 + A_k + \sqrt{M_2^2 + |B_k|^2 + M_2(B_k + B_k^*)} &= 0 \\ M_1 + A_k - \sqrt{M_2^2 + |B_k|^2 + M_2(B_k + B_k^*)} &= 0 \end{aligned} \tag{8.23}$$

where

$$\begin{aligned} M_1 &= \frac{(\omega + \mu - U)(U^2\lambda + U\lambda(\omega + \mu) - 2(\mu + \omega)^2)}{2U^2\lambda - 2(\mu + \omega)^2} \\ M_2 &= \frac{U\lambda(\mu + \omega - U)^2}{2U^2\lambda - 2(\mu + \omega)^2} \\ A_k &= 2J\cos\alpha(\cos k_x + \cos k_y) \\ B_k &= 2J\sin\alpha(\sin k_y + i\sin k_x) \end{aligned} \tag{8.24}$$

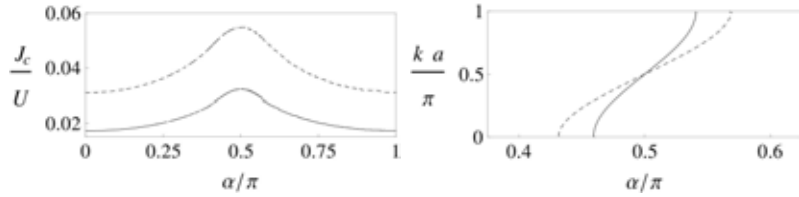


FIGURE 8.6: **Left:** The critical hopping $J_c$ marking the tip of the lobe for $\lambda = 0.3$ (solid line) and $\lambda = 0.6$ (dashed line) as a function of $\alpha$. **Right:** The minima (maxima) of the lowest (highest) particle (hole) excitation are found at $k_y a = -\alpha$ and $k = \pm k_x$ as shown in the plot (the solid line corresponds to $\lambda = 0.3$, the dashed line to $\lambda = 0.6$). It is different from 0 or $\pm\pi$ only within a small region around $\alpha = \pi/2$, in which the single extremum suddenly splits into two. From: [166].

Solving the first of these equations, we find two positive ($E > 0$) and one negative ($E < 0$) solutions, while the second equation has solely one positive solution which is the second highest band. The resulting bandstructure is shown in Fig. 8.5. Note that here the presence of the off-diagonal component of the Green function which originates from the XY ground state leads to more particle-like than hole-like excitations. This feature is a consequence of particle-hole asymmetry originating from $U^{\mathrm{ab}} \neq U$. Also, the splitting of the two highest particle-like excitations is a consequence of the non-Abelian nature of the hopping. This splitting vanishes in the limit $\alpha \to 0$.

For the QPT into the SF state these higher modes again do not play a role. The Mott lobe, on which at least one mode becomes gapless, now extends from $0 < \mu < \lambda U$. The value of $J_c$ marking the height of the lobe depends on both $\alpha$ and $\lambda$, as illustrated on the left panel of Fig. 8.6. Furthermore, as in the cases studied before, we find that the minima of the dispersion occur at finite wavevectors. However, in contrast to the cases studied before, the band spectrum in the XY phase is not symmetric under $k_y \to -k_y$. This property of the dispersion can be traced back to $G$ since $B_k$ in Eq. (8.24) is not invariant under such a transformation.

The above-mentioned properties of the dispersion of the particle- and hole-like excitations are reflected in the nature of the momentum distribution of the bosons in the Mott phase near the quantum critical point. We find that for any given $\alpha$, the condensing modes are located at $k_y = -\alpha$. As shown in Fig. 8.7, there are no analogous peaks at $k_y = \alpha$ which clearly reflects the breaking of the parity symmetry discussed above. Also we note that for the range $0 \leq \alpha \lesssim 1.5$

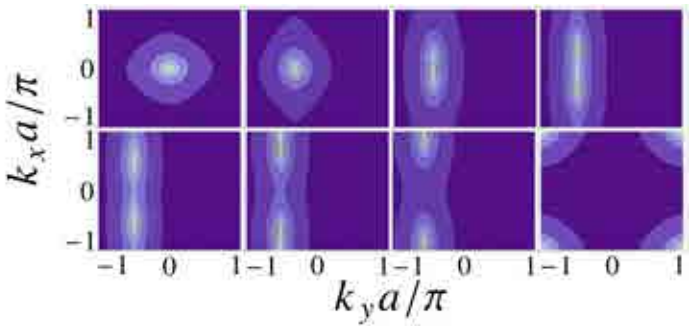


FIGURE 8.7: Momentum distributions at $J \approx 0.97 J_c$ in XY system for $\lambda = 0.3$. The bright regions correspond to high densities. The field strengths $\alpha$ are, from left to right, 0, 1, 1.4, 1.5, $\pi/2$, 1.65, 1.75, and $\pi$. From: [166].

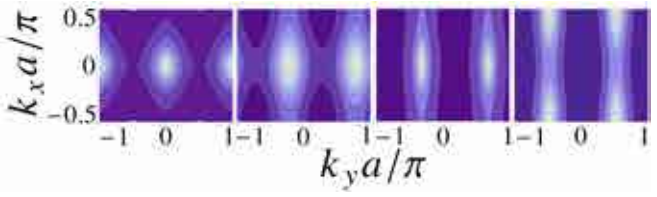


FIGURE 8.8: The momentum distributions of the bosons at $J \approx 0.97 J_c$ in the XY system with $\Phi = 1/2$ for $\lambda = 0.3$ and field strengths $\alpha$, from left to right, 0, 0.7, 1, and 1.5. From: [166].

$(1.65 \lesssim \alpha \leq \pi)$, there is a single condensing mode at $k_x = 0$ $(k_x = \pm\pi)$. Around $\alpha = \pi/2$, however, the condensing mode splits into two at momenta $\boldsymbol{k} = (\pm k, -\alpha)$, where $k$ is plotted on the right panel of Fig. 8.6 as a function of $\alpha$. We note that such a splitting can modify the dynamical behavior of the system.

Finally, we study the influence of a magnetic flux on the XY system, as done before for $\lambda = 0$. As expected we find the Abelian flux $\Phi = 1/2$ to split each band into two, such that the system exhibits two hole and six particle excitations. As before, for $\alpha = 0$, the presence of this flux provides the band structure with two extrema at $\boldsymbol{k} = (0, 0)$ and $(0, \pm\pi)$. The resulting momentum distribution near condensation is shown in Fig. 8.8. As $\alpha$ is increased, the position of the peaks of the momentum distribution initially shifts along $k_y$. However, close to $\alpha = \pi/2$, the peaks split along $k_x$ leading to four peaks which finally reach the zone edge $\boldsymbol{k} = (\pm\pi/2, \pm\pi/2)$ at $\alpha = \pi/2$. These features, as in the case of $\Phi = 0$, should be experimentally observable via standard TOF experiments.

## 8.3 Superfluid phase

In this section, we investigate the nature of the SF phase into which the transition takes place. We note that, as pointed out in Ref. [159, 170], the quadratic action (Eq. (8.5)) does not capture the physics of the ordered phase but needs to be supplemented by the quartic term at the mean-field level. These terms can be directly computed using the methods of Ref. [159, 170] within a strong coupling expansion; however, it is often enough to guess their forms from the symmetry of the underlying Hamiltonian. In this section, we are going to take the latter route and chart out the characteristics of the resulting SF phase.

For determining the order parameters in the SF phase we need to construct the quartic part of the effective action in terms of the order parameter fields and minimize it. To this end, we first rewrite the quadratic action by diagonalizing its kernel as shown in Section 8.2. Let us denote the eigenvalues and eigenmodes of the quadratic action as $m_{n,\boldsymbol{k}}(\omega)$ and $\Psi_{n,\boldsymbol{k}}(\omega)$, respectively. In the case when the Abelian flux is $\Phi = p/q$, $n$ varies from 0 to $2q-1$. Note that here we have adopted the convention that for $\Phi = 0$, the system remains with only two eigenmodes, so that we have $n = 0, 1$. In the zero-temperature limit we may then write,

$$S^{\mathrm{MI}} = \sum_{n=0}^{2q-1} \sum_{\boldsymbol{k}} \int \mathrm{d}\omega \; m_{n,\boldsymbol{k}}(\omega) |\Psi_{n,\boldsymbol{k}}(\omega)|^2. \tag{8.25}$$

Here, the sum over $\boldsymbol{k}$ is restricted to the first magnetic Brillouin zone. The fourth-order term can be written in this basis as

$$S^{(4)} = g/2 \sum_{n=0}^{2q-1} \sum_{i} \int_0^\beta \mathrm{d}\tau \; |\bar{\Psi}_n(\boldsymbol{r}_i, \tau) \cdot \Psi_n(\boldsymbol{r}_i, \tau)|^2, \tag{8.26}$$

where we have transformed the $\Psi_n$ and $\bar{\Psi}_n$ fields to real space. Here, $g > 0$ is the exact two-particle vertex function of the bosons in the local limit, which has been computed in Refs. [168, 170] and $i$ denotes lattice sites.

With this the SF action may be written as

$$S^{\mathrm{SF}} = S^{\mathrm{MI}} + S^{(4)}. \tag{8.27}$$

Now we note that at the onset of superfluidity only one of the eigenmodes condenses; therefore, it is possible to analyze the SF phase within a mean-field approximation by ignoring the other modes. This observation allows us to get rid of the $n$-sum over all bands in Eq. (8.26):

$$S^{(4)} = g/2 \sum_i \int_0^\beta \mathrm{d}\tau \; |\bar{\Psi}(\boldsymbol{r}_i, \tau) \cdot \Psi(\boldsymbol{r}_i, \tau)|^2. \tag{8.28}$$

In the presence of a non-Abelian gauge field with magnetic flux $\Phi = 0$, or flux $\Phi = p/q = 1/2$, we have one or more than one minima of the boson energy spectrum depending upon the non-Abelian field strength $\alpha$. If the particle/hole modes consist of $s$ degenerate minima, then the corresponding Ginzburg-Landau theory can be expressed by $s$ low-energy fluctuating two-component fields (order parameters) $\phi_n(r,t)$ around these minima [159, 160]:

$$\Psi(\boldsymbol{r}_i, t) = \sum_{n=1}^{s} \chi_n(\boldsymbol{r}_i), \phi_n(\boldsymbol{r}_i, t), \tag{8.29}$$

where we have Wick rotated to real time. The coefficients $\chi(\boldsymbol{r}_i)$ are the real space eigenfunctions corresponding to the minimum energy band at $\boldsymbol{k} = (k_x^{\min}, k_y^{\min})$ which can be expressed as:

$$\chi_n(\boldsymbol{r}_i) = \sum_{l=0}^{q-1} c_l \mathrm{e}^{(ik_x^{\min} + 2\pi l/q)x_i} \mathrm{e}^{ik_y^{\min} y_i}, \tag{8.30}$$

Note that the sum in the above expression is restricted to $q$ terms, since the functions $\chi_n(\boldsymbol{r}_i)$ describe only the part of the spatial dependence of $\Psi(\boldsymbol{r}_i, t)$ that can be factored out for each term in the sum in Eq. (8.29). Here $c_l$ denotes the components of eigenvectors corresponding to the minimum energy band at $\boldsymbol{k} = (k_x^{\min}, k_y^{\min})$.

In general, the quartic part of the Landau-Ginzburg action is difficult to obtain, since it is restricted only by the invariance under projective symmetry group (PSG) of the underlying square lattice [171]. The elements of PSG include in this case translations along the $x$ and $y$ axes, rotation by $\pi/2$ around the $z$ axis, and reflections about $x$ and $y$ axes. In our case, the situation is, however, much simpler, since we know the microscopic form of the quartic action, Eq. (8.26). We may therefore substitute Eq. (8.29) into Eq. (8.26), and obtain the explicit form of the quartic action in terms of the order parameters $\phi_n(\boldsymbol{r}_i, t)$. We can then find

the saddle point of the total action with respect to $\phi_n(\boldsymbol{r}_i, t)$, and thus directly calculate the order parameters in the SF phase.

Let us first consider the case where the number of both flavors at each site is equal, as discussed in Sec. 8.2.2. If the boson spectrum has one minimum in the magnetic Brillouin zone, then the corresponding low-energy field can be written as

$$\psi(\boldsymbol{r}_i, t) = \chi_1(\boldsymbol{r}_i)\phi_1(\boldsymbol{r}_i, t), \tag{8.31}$$

and thus the SF density reads

$$\rho_s = |\langle\psi\rangle|^2 = \left|\sum_{l=0}^{q-1} c_l \mathrm{e}^{(ik_x^{\min}+2\pi l/q)x_i}\mathrm{e}^{ik_y^{\min}y_i}\right|^2 |\phi_1|^2. \tag{8.32}$$

For $\Phi = 0$, we can get rid of the sum in Eq. (8.30) and $\rho_s$ is simply equal to $|\phi_1|^2$, which has no modulation along $x$. In contrast, for $\Phi = p/q = 1/2$, we find that $\rho_s$ displays a spatial pattern.

Next, we consider the case where there are two minima at $\boldsymbol{k}_1^{\min} = (\pi/2, \pi/2)$ and $\boldsymbol{k}_2^{\min} = (\pi/2, -\pi/2)$ within the magnetic Brillouin zone for $\alpha = \pi/4$ and $\Phi = 1/2$. Note that these are on the zone edge, such that the minima at the opposite edge are equivalent. In this case, $\psi(\boldsymbol{r}_i, t) = \chi_1(\boldsymbol{r}_i)\phi_1(\boldsymbol{r}_i, t) + \chi_2(\boldsymbol{r}_i)\phi_2(\boldsymbol{r}_i, t)$. Following the coarse-graining procedure charted out in Ref. [159], we find that the SF ground state corresponds to the condensation of any one of the low-energy fluctuating fields $\langle\phi_1\rangle \neq 0, \langle\phi_2\rangle = 0$ or $\langle\phi_1\rangle = 0, \langle\phi_2\rangle \neq 0$. The corresponding plot for $\alpha = \pi/4$ and $\Phi = 1/2$ in Fig. 8.9a, shows a similar periodic pattern as found for a single minimum for $\Phi = 1/2$. Similar analysis can be done for four minima at $(\pm\pi/2, \pm\pi/2)$ for $\alpha = \pi/2$ and $\Phi = 0$; in this case we find that only one out the four field condenses; consequently there is no modulation of SF density. Note that we have restricted ourselves so far to the minima occurring at the wavevectors $(\pi/s_1, \pi/s_2)$, where $s_{1,2} = \pm 1$. In principle the analysis can be extended to the situations when the minima occur at $(\gamma\pi/2, \delta\pi/2)$ with rational and small $\gamma$ and $\delta$; however, the analysis becomes technically involved and we have not attempted that in this work. We do not have general understanding of implementing the above-mentioned coarse-graining procedure for irrational $\gamma$, $\delta$.

Finally, we briefly comment on the SF density in the XY phase. Following the procedure discussed before, we again find a constant SF density for any non-Abelian gauge field with $\Phi = 0$. For $\alpha = \pi/2$ and $\Phi = 1/2$, there are two

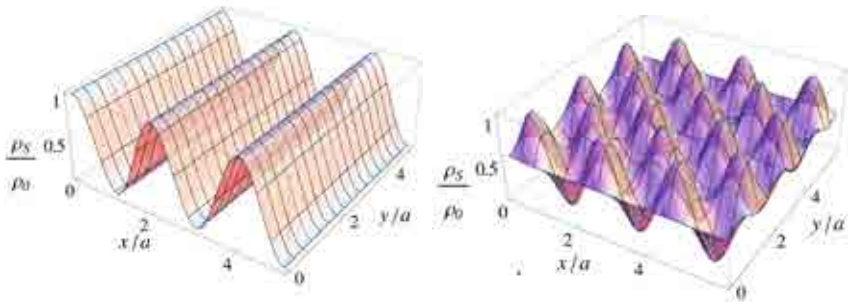


FIGURE 8.9: **Left:** Plot of SF density $\rho_s/\rho_0$ for $\Phi = 1/2$ and $\alpha = \pi/4$ at $\boldsymbol{k}^{\min} \equiv (\pi/2, \pm\pi/2)$ for even filling. **Right:** Same plot for $\Phi = 1/2$ and $\alpha = \pi/2$ at $\boldsymbol{k}^{\min} \equiv (\pi/2, \pm\pi/2)$ for XY phase. From: [166].

minima of the spectrum, and we find that the SF ground state corresponds to the condensation of both fields around these minima. The corresponding plot for $\alpha = \pi/2$ is shown in Fig. 8.9b.

Thus we generically find that in the presence of a non-Abelian gauge field, the SF density displays a spatial periodic pattern if there is a finite flux ($\Phi = 1/2$); however, there is no such modulation without flux, $\Phi = 0$. The method that has been discussed here can be used for any filling fraction $\Phi = p/q$. We expect different spatial patterns of the SF density for other $\Phi$, and leave the detailed analysis of it for future study.

# Chapter 9

# Gauge fields for cold atoms - Where, when, and why?

This thesis has studied a variety of cold atomic systems where the atoms are exposed to a synthetic gauge field. As we have argued in the beginning, the interest in quantum gases is triggered by their immense controllability. This makes them particularly useful for realizing exotic phases or doing quantum simulations. In Chapter 2 of this thesis, we have presented different proposals to engineer Hamiltonians with static gauge potentials acting on cold atoms. These proposals widely extend the range of systems which are accessible with cold atoms, covering also quantum Hall systems, which we have studied in Part I of this thesis, or Bose-Einstein condensates with spin-orbit coupling, which we have studied in Part II.

Thus, by summarizing these two parts of this thesis in Sections 9.1 and 9.2, we shall be able to answer the first of the three questions posed in the title of this final chapter: Where, or in which contexts, may we futurely find cold atoms with artificial gauge fields? Also the third question, why?, should be addressed by this summary.

We note that the systems we have investigated are realizable with techniques not far from those which are already available. By pointing out the recent experimental development in Section 9.3, we shall also answer the second question: When? - Now! However it is tempting to think of longer timescales, decades

maybe. Then, the answers to the last question, why?, become particularly alluring. Giving a brief outlook on technological applications of topological quantum states, we shall answer it in Section 9.3.

## 9.1 Summary of Part I

In the first part of the thesis, we have focused on fractional quantum Hall systems, that is, repulsively interacting, two-dimensional systems exposed to a sufficiently strong artificial magnetic field perpendicular to the atomic cloud. We have studied fractional quantum Hall effect in various contexts, illustrating the versatility of the cold atoms: In Chapter 3 fermionic gases with dipolar interactions have been considered, while in Chapters 4–6 bosons with contact interactions have been studied. While the particles in Chapters 4 and 5 have no internal degree of freedom, a pseudospin-$\frac{1}{2}$ degree of freedom has been assumed in Chapter 6. The pseudospin can also be coupled to the external motion via a non-Abelian gauge field, a scenario which we have discussed for fermions in Chapter 3, and for bosons in Section 6.5.

The proposal for realizing a synthetic magnetic field by rotating the system has been known for a long time (cf. [79]). However, it has so far not been possible to reach experimentally the parameter region in which fractional quantum Hall states are expected to occur. This failure has been due to the weak effective trapping in this region, which requires a configuration where the rotation frequency falls into a tiny window just below the instability limit. In this thesis we have therefore discussed in detail an alternative proposal, where the gauge field is obtained by a laser-dressing of the atoms. In this scheme, the analog of the rotation frequency is given in terms of the wavenumber of the laser. This should allow for a more precise tuning. A drawback of any proposal based on dressed atomic states is the inclusion of more internal states than the simulated system is supposed to have. Thus, the desired Hamiltonian is only obtained after an adiabatic approximation, neglecting those additional degrees of freedom. By means of exact diagonalization we have studied the validity of this approximation in Chapter 4. We show which consequences waiving this assumption has on the fractional quantum Hall states. As shown in Fig. 4.9 focusing on the Laughlin state regime, significant changes in the wave function occur when the Rabi frequency of the atom-laser coupling is decreased. The physical behavior of

the system, however, seems to change less (see Fig. 4.4), and can, up to a certain degree, be understood by generalizing the Laughlin wave function according to Eq. (4.19). This makes the proposal a promising scheme to mimic fractional quantum Hall physics. In Section 4.3.3, we have also discussed its experimental feasibility with respect to larger system sizes. Possible difficulties which might arise in the thermodynamic limit could be answered by increasing the interaction strength by means of Feshbach resonances.

The most fascinating property of fractional quantum Hall states are certainly their anyonic excitations. As exotic theoretical predictions, they strongly motivate the realization of fractional quantum Hall effects in an environment like cold atoms, where detecting their intriguing properties, including the fractional quantum-statistical behavior, might become possible [92]. In Section 5.1 we have investigated the properties of quasihole excitations above the generalized Laughlin state obtained in Chapter 4. Although an anisotropy due to the non-adiabatic term in the Hamiltonian will also show up in the Berry connections of the corresponding quasiholes, this will not affect their effective "charge" and statistical phase, as these quantities must be defined by moving the quasiholes along closed contours, see Fig. 5.5. Furthermore, we have shown that systems of sizes as small as $N = 6$ have a bulk which is large enough to pierce two Laughlin-type quasiholes, see Fig. 5.3. This is important in view of the conclusions drawn from Chapter 4, favoring experiments on finite systems rather than in the thermodynamic limit. We also note that very small systems have already been claimed to be brought into the Laughlin regime [172].

Apart from their anyonic properties, quasiholes can also be interesting as a tool for detecting the Laughlin state. As we have discussed in Section 5.2, due to the zero interaction energy of the Laughlin state for particles interacting via a two-body contact potential, no decoherence of the quasiholes takes place in the Laughlin regime, see Eq. (5.13). This is in contrast to less correlated systems, where a collapse and revival of the holes can be observed, see Fig. 5.8 for a condensed system and Fig. 5.13 for a system almost as correlated as the Laughlin state. We have derived a relation for the revival period, which could prove useful for doing spectroscopy, Eq. (5.21).

While the one-component systems considered in Chapters 4 and 5 should allow for realizing the Laughlin state, or other states from the Read-Rezayi series (cf. Chapter 4 and Ref. [79]), systems of particles with an internal degree of freedom, considered in Chapter 6, are shown to support a new class of fractional quantum

Hall states, the non-Abelian spin singlet (NASS) states, see Table 6.1. Like the Read-Rezayi states, these quantum states are interesting due to their topological excitations, which apart from being anyonic, also might behave in a non-Abelian way upon braiding. One might see the additional spin degree of freedom as an experimental obstacle, but considerable advantages arise:

- The NASS states appear at higher filling factors than their spin-polarized counterparts, i.e. in a regime of lower angular momentum. This might favor the experimental realization.
- The spin-degree of freedom allows for additional control. Interaction parameters within every spin component and between the components can be tuned independently. As we have shown in Fig. 6.2, tuning the intercomponent interaction strength while leaving the others constant, the system undergoes several abrupt re-organizations. The observed behavior upon tuning these quantities might turn out helpful for detecting the state.
- In the spinful system, the coupling of internal and external degrees of freedom via a non-Abelian gauge field can be studied. In the context of fractional quantum Hall states, this scenario has been considered in Section 6.5, where both Read-Rezayi and NASS states turn out to be relevant, depending on the coupling strength. New states, like the apparently very robust gapped state at filling $\nu = 2$, see Fig. 6.10, appear when the spin-orbit coupling causes a degeneracy between different Landau levels.

## 9.2 Summary of Part II

In the second part of this thesis, we have considered Bose condensed systems in the continuum (Chapter 7) and on a lattice (Chapter 8) subjected to some artificial gauge potential. In Chapter 7, we have considered a purely non-Abelian, constant gauge potential, which effectively describes a Rashba spin-orbit coupling. Calculating the dispersion relation of such a spin-orbit coupled Bose-Einstein condensate, we obtained a two-fold degeneracy on the mean-field level which is lifted by quantum fluctuations considered in a Bogoliubov approximation. Quantifying this degeneracy lifting, see Fig. 7.3, we have argued that this effect might be observable in experiments. The feasibility of the setup has been proven by calculating the quantum and the thermal depletion of the condensate, which

remain finite in three spatial dimensions, see Fig. 7.4. For decades, the possibility of such an *order-by-disorder*, i.e. fluctuation-induced degeneracy lifting, has been discussed in various contexts, but an experimental observation of this phenomenon is still missing. Cold atoms might close this gap between theory and experiment.

One of the milestone achievements in cold atomic physics has been the observation of a quantum phase transition of bosons on an optical lattice. In Chapter 8, we have considered bosonic atoms in a square lattice, enriched by synthetic gauge fields, for which we have chosen: 1) a purely non-Abelian form as in Chapter 7, 2) a non-Abelian gauge potential combined with a magnetic flux as in Chapter 6. Even in the simplest case without magnetic flux and no interactions between different species, we have found an intriguing energy dispersion where the bands touch each other in Dirac cones, see Fig. 8.1. As shown in Figs. 8.2 and 8.3, the strength of the non-Abelian coupling modifies the position of the Mott-superfluid phase boundary, and the wavenumber of the mode into which the system condenses at the phase transition. Thus, the gauge field allows for generating condensates of finite momenta, and of re-entrant superfluids, where the quantum phase transition can be reached not only by tuning the hopping strength, but also by varying the non-Abelian gauge potential. Taking into account an additional magnetic flux, or interactions between the species, the behavior at the phase boundary becomes even more interesting. Upon tuning the non-Abelian field strength, the wavenumber of the superfluid abruptly jumps within the Brillouin zone, which is observable in the momentum distribution (Figs. 8.4 and 8.7), or, on the experimental level, in time-of-flight absorptions pictures. The existence of a magnetic flux might also give rise to spatial modulation of the SF density, as shown in Fig. 8.9.

## 9.3 A brief perspective

With the fractional quantum Hall systems studied in Part I, a goal of fundamental relevance is addressed: Realizing fractional quantum Hall states can, in some sense, be considered the discovery of a new world, the flat world. In the past decade, the discovery of graphene has already been a Nobel awarded step into this two-dimensional world, but still there is a lot to explore. Within a many-body system, quasiparticle excitations have the status of elementary particles. In a flat many-body system, thus, anyonic excitations represent elementary particles

which are quite different from the bosonic or fermionic ones we used to know in our three-dimensional world. Although we already know theoretically such exotic properties of the flat world, proving them experimentally would significantly advance physics. As we have shown in this thesis, cold atoms with artificial gauge fields could do this job.

Apart from physicists, however, many people might not care too much about discovering the flat world. When a new generation of smartphones is launched, however, this uses to attract a great deal of attention. So what about an anyonic smartphone? In fact, from the hardware perspective, progress in information technologies will be exhausted at some point in the future, if no quantum leap in transistor technology is accomplished. Proposals for quantum gates are known for a long time [173], but a problem with them is the handling of errors. It was therefore proposed to use topological quantum states for quantum information processing, as these states are robust against perturbations [27]. In this context, quantum gates operating with (non-Abelian) anyons have been discussed. From this point of view, realizing and controlling fractional quantum Hall states could indeed be the first step towards a quantum smartphone.

What can be expected to turn out a problem still, is that such a quantum smartphone based on cold atoms might not fit into our pocket. It can be argued against this point that also the first classical computers were of the size of a whole laboratory. But in view of the sophisticated cooling techniques which are needed for cold atoms, scaling down the setups to handy sizes indeed seems to be unrealistic. Luckily, there might be alternatives. During the last years, spin-orbit coupling in solids has turned out to be a very important ingredient of several materials, which are called topological superfluids or topological insulators (TIs) [19]. Importantly, these materials allow for a new kind of transistors [133] which achieve spin-dependent information processing. As in the case of quantum Hall states, also the properties of TIs are topologically protected. For non-interacting systems, TIs are well understood and classified, but the role of interactions remains an important and widely open question. Systems of cold atoms in an optical lattice with a non-Abelian gauge field, as discussed in Chapter 8, may be used to simulate TIs [174]. The simulated TIs themselves might not be useful for practical purposes, especially if a desired property is offered as an intrinsic property of some solid material. But for finding this material and understanding its intrinsic mechanisms, cold atoms could turn out extremely helpful.

Let us also note that fractional quantum Hall states or topologically insulating states are by far not the only effects which can be implemented in cold atomic systems by means of artificial gauge fields. Especially, we should keep in mind that implementing static gauge fields would also be the first step towards much more general applications with dynamical gauge fields. Once this is achieved, it might also become possible to study any physical model in cold atomic systems.

These perspectives may sound unrealistic, prospecting quite sophisticated applications in a field which can be considered still in its infancy. But artificial gauge fields for cold atoms are developing rapidly: Not counting the limited schemes of rotation, only the group of I. Spielman had achieved an artificial magnetic field when the work on this thesis was started in April 2010 [38]. In the meantime, Spielman's group has not only pushed forward their techniques now also covering gauge fields in optical lattices [47] and synthetic spin-orbit coupling [42], but also several other groups have successfully implemented artificial gauge fields [48, 175]. In view of this worldwidely growing number of experimentalists in the field, an optimistic perspective as sketched here seems to be justified.

# Appendix A

# Strongdeco: Expansion of analytical, strongly correlated quantum states into a many-body basis

In this appendix, we present a Mathematica code, published in Ref. [81], which translates analytic trial wave functions in the lowest Landau level (LLL) on a disk from a first-quantized representation into a Fock basis as defined in Eq. (4.9). We have used this code extensively for obtaining many of the results presented in Chapters 4 and 5: Since trial wave functions like the Laughlin wave function in Eq. (3.6) are given in first quantization, while the output of a numerical diagonalization is in terms of second quantized states, overlaps can only be calculated by switching from one to the other representation. Going from the second-quantized expression to the first-quantized expression is straightforward, but in first quantization the overlap is given as an integral over all coordinates. We have thus pursued the opposite way: Translating the first-quantized expression into the Fock basis, overlaps are simply given as scalar products of the state vectors. This translation is achieved by the code which we present here. Note that there are also many other calculations which are facilitated by translating from a first-quantized to a second-quantized notation. In Chapter 5 we have used the many-body representation of the Laughlin quasihole state to explicitly find

the normalization factor as a function of the quasihole position. From this we have calculated the Berry connection of the quasiholes. A third application will be given at the end of this appendix.

The Fock basis is constructed from the Fock-Darwin (FD) states, as given in Eq. (3.5). Let us remind, however, that we will follow our convention for the length scales given in chapter 4, according to which the exponential reads $\exp(-|z|^2/2)$. This is relevant for the normalization factors of the states, and thus for a correct translation from one basis into another. We will restrict ourselves on the LLL. Noting that the FD functions are orthonormal, we can generate the many-body basis by considering products of the FD functions, which in the case of bosons have to be combined in a symmetric way, while antisymmetric combinations must be constructed in the case of fermions. Here, we will concentrate on the bosonic case, but with only slight modifications which are explicitly shown in the code file, fermionic systems can be treated in the same way. For the bosonic system we write the many-body state as,

$$\{\ell_1, \ell_2, \ldots, \ell_N\} \equiv \mathcal{S}\ \left[\phi^{\mathrm{FD}}_{0,\ell_1}(z_1)\phi^{\mathrm{FD}}_{0,\ell_2}(z_2)\ldots\phi^{\mathrm{FD}}_{0,\ell_N}(z_N)\right] \tag{A.1}$$

where $\mathcal{S}$ symmetrizes over the $N$ particles. These states are called permanents, which are the bosonic analog of the Slater determinants, with the difference that all terms have a positive sign. Without loss of generality we may assume that $\ell_1 \leq \ell_2 \leq \cdots \leq \ell_N$. The orthonormality of the permanents then reads

$$\{\ell_1, \ell_2, \ldots, \ell_N\} \cdot \{\ell'_1, \ell'_2, \ldots, \ell'_N\} = \delta_{\ell_1,\ell'_1}\delta_{\ell_2,\ell'_2}\cdots\delta_{\ell_N,\ell'_N}\,. \tag{A.2}$$

For simplicity we will from now on suppress the exponential term which is common to all $N$-body states, and, as an overall Gaussian, fixes the center of mass to the origin. We can then simplify the problem to dealing with permanents of the form,

$$\mathcal{S}\left[z_1^{\ell_1} z_2^{\ell_2}\ldots z_N^{\ell_N}\right]\,. \tag{A.3}$$

From Eq. (A.2) follows that, for a given $N$, all states of a fixed total angular momentum $L = \sum_{i=1}^{N}\ell_i$ form a subspace which is orthogonal to the subspace with total angular momentum $L' \neq L$. We can therefore perform the decomposition independently in each subspace, and thus restrict ourselves to a subspace with fixed $L$. Its basis (up to normalization factors and the overall exponential term) can be constructed through the command,

```
ConjS[na_, L_] := Module[{poty, dimy},
  poty = Pots[na, L];
  dimy = Dimensions[poty][[1]];
  Table[Perm[na, poty[[i]]], {i, 1, dimy}]]
```

which makes use of the function **Perm** [176], that builds the appropriate permanent, and of **Pots[N,L]**, which constructs the set of indexes $\ell_1, \ldots \ell_N$ for a given $N$ and $L$, represented by **na** and **L** in the code,

```
cc[0] = 0;
tab[n_, l_] :=
Table[{cc[i], cc[i - 1],
If[i == 1, l, (l - Sum[cc[j], {j, 0, i - 1}])/2]},
{i, 1, n - 1}];
Pots[na_, L_] := If[na == 2, Table[{i, L - i}, {i, 0, L/2}],
Module[{pat},
Clear[pat];
pat[na] = Join[Table[
cc[i], {i, 1, na - 1}], {L - Sum[cc[i], {i, 1, na - 1}]}];
pat[a_] := Table[pat[a + 1], Evaluate[tab[na, L][[a]]]];
Flatten[pat[1], na - 2]]]
```

For instance, for $N = 4$ and $L = 2$ we have [1],

```
Pots[4,2]={{0,0,0,2},{0,0,1,1}}
```

and correspondingly,

```
ConjS[4, 2]=
{6 z[1]^2+6 z[2]^2+6 z[3]^2+6 z[4]^2,
4 z[1] z[2]+4 z[1] z[3]+4 z[2] z[3]
+4 z[1] z[4]+4 z[2] z[4]+4 z[3] z[4]}
```

As can be seen in this example, due to multiple occupation of the same single-particle state, some of the permutations contributing to the symmetrized wavefunction are described by the same monomials which thus have prefactors given

[1] Note that the state $\{1, 1, 0, 0\}$ is equivalent to $\{0, 0, 1, 1\}$ due to the symmetrization of the states.

by the factorial of the number of permutations. These factors need to be taken into account to correctly normalize the many-body states, and can be obtained through, **nami[N, L]**, which gives a table with the same ordering as **Pots** or **ConjS**, for our previous example, **nami[4,2]={6,4}**, as could be inferred from the obtained expressions.

```
nami[na_, L_] := Module[{potty, pp, inde, ta},
  potty = Pots[na, L];
  pp = Dimensions[potty][[1]];
  inde = Table[Complement[potty[[i]]], {i, 1, pp}];
  ta = Table[Table[Count[potty[[i]], inde[[i, j]]],
{j, 1, Dimensions[inde[[i]]][[1]]}], {i, 1, pp}];
  Table[ Product[ta[[i, j]]!,
{j, 1, Dimensions[ta[[i]]][[1]]}]   , {i, 1, pp}]]
```

Once these factors are known it is easy to build the normalization coefficient. Therefore we first have to normalize the FD functions, yielding a factor $1/\sqrt{\pi\ell!}$. Then, the function **tip[N, L]** gives the normalization coefficients for the many-body states. Their explicit coding is,

```
tip[na_, L_] := Module[{potty, nimy},
potty = Pots[na, L];
nimy = nami[na, L];
Table[Sqrt[nimy[[i]]]Sqrt[Product[Pi Gamma[potty[[i, jj]]+1],
{jj, 1, na}]  ], {i, 1, Dimensions[nimy][[1]]}]]
```

The trial states described in Chapter 3, are, up to the common exponential factor, polynomials in the $z$ variables. To write down the states in terms of the many-body ones, we can suppress the exponential and work out the decomposition of the polynomial in terms of the permanents. While the Laughlin and the Pfaffian state have a definite total angular momentum, for the quasi-hole and quasi-particle states this is only true if we fix the position of the quasi-particle to the origin $\xi = 0$. Otherwise, we must first sort the polynomial by the different contributions with a definite order in $z$, and can then proceed, for each contribution separately, in the way described here, where we assume an analytical state, $\Psi(z_1, z_2, \ldots, z_N)$

with fixed $N$ and $L$. We are looking for an expansion of the form,

$$\Psi(z_1, z_2, \ldots, z_N) = \sum_{j=1}^{n_D} C_j \{\ell_{1,j}, \ell_{2,j}, \ldots, \ell_{N,j}\} \tag{A.4}$$

where $n_D$ is the total size of the many-body basis, which can be computed as

$$n_D = \text{Dimensions}[\text{PotsN}[N, L]][[1]]. \tag{A.5}$$

To get a feeling of how this grows with $N$ and $L$ the dimension of these spaces for the $L$ corresponding to the Laughlin wave functions are, $n_D = 7, 34, 192, 1206, 8033, 55974$ for $N = 3, 4, 5, 6, 7$ and $8$, respectively.

To decompose a polynomial into these states, we have to find the monomials which correspond to a given Fock state and read out their coefficients. Since we know that the polynomial is symmetric (antisymmetric) under exchange of two coordinates, it is sufficient to find only one monomial contributing to a given Fock state, as all the others must have the same coefficient (up to a sign in the antisymmetric case). This can be achieved by taking derivatives:

$$\partial_{z_1}^{\ell_{1,j}} \cdots \partial_{z_N}^{\ell_{N,j}} \Psi(z_1, z_2, \ldots, z_N)|_{z_1=0,\cdots,z_N=0} = c_j, \tag{A.6}$$

where $c_j$ is not yet the coefficient $C_j$ in Eq. (A.4), but is directly related to it through the normalization procedure described in the previous section. Hereby, we have to take into account that an additional factor $\prod_{i=1}^{N} \ell_{i,j}!$ occurs through the derivatives. Thus we obtain

$$C_j = c_j \left( P \prod_{i=1}^{N} \ell_{i,j}! \; \pi \right)^{-1/2} \equiv \alpha_j c_j, \tag{A.7}$$

where the $P$ is the factorial of permutations leading to the same expression, obtained by **nami[N,L]**. We thus see that $\alpha_j$ equals the inverse of the $j$th component of **tip**$[\mathbf{N}, \mathbf{L}]$. The decomposition of, for instance, the Laughlin wavefunction can therefore be obtained by the following piece of code:

```
DDecoLaug[na_,nu_] :=
 Module[{Lmin, Lmax, state, base, dim, fac, d, prf, outp},
  Lmin = na (na - 1);
  Lmax = na (na - 1);
  state = Laughlin[na,nu];
  base = Flatten[Table[Pots[na, i], {i, Lmin, Lmax}], 1];
  dim = Dimensions[base][[1]];
  fac = Flatten[Table[tip[na, i], {i, Lmin, Lmax}], 1];
  d[0] = state;
  prf = Table[
    For[i = 1, i < na + 1, i++,
     d[na] = 0;
     d[i] = D[d[i - 1], {z[i], base[[j, i]]}];
     d[i] = d[i] /. z[i] -> 0;
     If[d[i] == 0, Break[]]
     ];
    d[na]/fac[[j]],
    {j, 1, dim}];
  outp = prf/Sqrt[prf.prf]]
```

Here, **Laughlin[N,nu]** describes the Laughlin wavefunction for $N$ particles at filling $\nu$. For even $1/\nu$, this is a symmetric function describing bosons, while odd values yield an antisymmetric function for fermionic systems. In principle, we can use the code for both the symmetric and the antisymmetric case. In the latter, however, it is convenient to exclude states with multiple occupied single-particle levels from the basis, as they obviously make no contribution. This can be done by replacing **Pots[N,L]** by its fermionic analogue **PotsF[N,L]** defined in the code file. Consequently, we will also have to replace **tip[N,L]** by **tipF[N,L]**.

An alternative way to achieve the decomposition is by means of a particular, built-in Mathematica function, **PolynomialReduce**. This function provides the decomposition of a given multivariate polynomial in terms of a set of polynomials. The code for decomposing the bosonic Laughlin state then reads

```
LaugDeco[na_,nu_] :=
Module[{state, base, symb, laur, prf, outp},
  state = Laughlin[na,nu];
  base = ConjS[na, na (na - 1)];
  symb = Table[z[i], {i, 1, na}];
  laur = PolynomialReduce[state, base, symb];
  If[laur[[2]] != 0, Print["Problem in reduction"]];
  prf = laur[[1]] tip[na, na (na - 1)];
  outp = prf/Sqrt[prf.prf];
  outp]
```

For most states that we have considered, the decomposition by means of derivatives is faster. However, making use of **PolynomialReduce** turns out to be quicker for the fermionic Laughlin state as well as for quasiparticle excitations.

In figure A.1, a snapshot of the code for the decomposition of the Laughlin state is provided for $N = 3$, $N = 4$ and $N = 5$. The code has been tested for $N \leq 7$ on a laptop running on linux with 1Gb of RAM memory. The full notebook file with some examples is provided on the journal webpage [81].

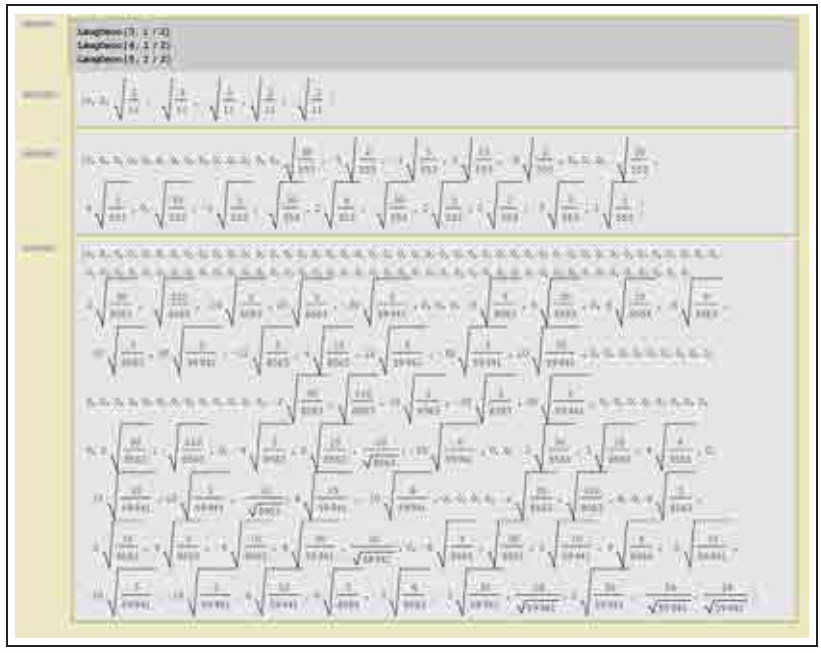

FIGURE A.1: Snapshot of the code where the decomposition of the Laughlin state with $\nu = 1/2$ is obtained for $N = 3$, $N = 4$ and $N = 5$.

| $\ell =$ | 0 | 1 | 2 | 3 | 4 | 5 | 6 | 7 | 8 | 9 |
|---|---|---|---|---|---|---|---|---|---|---|
| $m = 2$ | $\frac{257}{553}$ | $\frac{264}{553}$ | $\frac{303}{553}$ | $\frac{446}{553}$ | $\frac{447}{553}$ | $\frac{330}{553}$ | $\frac{165}{553}$ | 0 | 0 | 0 |
| $m = 3$ | $\frac{185}{706}$ | $\frac{185}{706}$ | $\frac{209}{706}$ | $\frac{321}{706}$ | $\frac{417}{706}$ | $\frac{465}{706}$ | $\frac{455}{706}$ | $\frac{339}{706}$ | $\frac{186}{706}$ | $\frac{62}{706}$ |

TABLE A.1: Angular-momentum distribution for Laughlin states of $N = 4$ particles for bosons ($m = 2$) and fermions ($m = 3$).

**Applications** Within this thesis, we have used the presented code in chapter 4 in order to calculate the overlap between states obtained by exact diagonalization and first-quantized trial wave functions like the Laughlin or Moore-Read state. Furthermore, this representation is often convenient to analyze properties of these states. In chapter 5 we have translated quasihole states into the Fock basis in order to study the effective charge and statistics of the excitations.

Here we briefly present a third application of the code: Our code can also be used to calculate the angular momentum distribution of a test state in the LLL. From this, one also gains insight into its one-body density matrix and other correlation functions. For the fermionic Laughlin state this problem has been considered in Ref. [177], where exact results are obtained by calculating the density and then extracting the angular momentum distribution. This method, however, fails for systems larger than $N = 3$, for which Monte Carlo methods have been applied. By means of our code, we are able to reproduce these results by decomposing the Laughlin state into a basis from which the angular momentum of each particle can be directly read off. It is straightforward to go beyond the analytical results of Ref. [177]. As an example, we give in Table A.1 the angular momentum distributions for the fermionic Laughlin state at $m = 3$ and the bosonic Laughlin state at $m = 2$ of a system with $N = 4$ particles.

# Bibliography


[1] K. B. Davis, M.-O. Mewes, M. R. Andrews, N. J. van Druten, D. S. Durfee, D. M. Krun, and W. Ketterle, Phys. Rev. Lett. **75**, 3969 (1995).

[2] M. H. Anderson, J. R. Ensher, M. R. Matthews, C. E. Wieman, and E. A. Cornell, Science **269**, 198 (1995).

[3] C. J. Pethick and H. Smith, *Bose–Einstein Condensation in Dilute Gases* (Cambridge University Press, 2001).

[4] L. P. Pitaevskii and S. Stringari, *Bose–Einstein Condensation* (Clarendon Press, 2003).

[5] D. Jaksch, C. Bruder, J. I. Cirac, C. W. Gardiner, and P. Zoller, Phys. Rev. Lett. **81**, 3108 (1998).

[6] M. Greiner, O. Mandel, T. Esslinger, T. W. Hänsch, and I. Bloch, Nature **415**, 39 (2002).

[7] M. Lewenstein, A. Sanpera, and V. Ahufinger, *Ultracold Atoms in Optical Lattices - Simulating quantum many-body systems* (Oxford University Press, 2012).

[8] M. P. A. Fisher, P. B. Weichman, G. Grinstein, and D. S. Fisher, Phys. Rev. B **40**, 546 (1989).

[9] S. Sachdev, *Quantum Phase Transitions* (Cambridge University Press, 1999).

[10] J. K. Freericks and H. Monien, Phys. Rev. B **53**, 2691 (1996).

[11] F. E. A. dos Santos and A. Pelster, Phys. Rev. A **79**, 013614 (2009).

[12] N. Teichmann, D. Hinrichs, M. Holthaus, and A. Eckardt, Phys. Rev. B **79**, 100503 (2009).

[13] N. Teichmann, D. Hinrichs, M. Holthaus, and A. Eckardt, Phys. Rev. B **79**, 224515 (2009).

[14] B. Capogrosso-Sansone, N. V. Prokof'ev, and B. V. Svistunov, Phys. Rev. B **75**, 134302 (2007).

[15] K. Günter, T. Stöferle, H. Moritz, M. Köhl, and T. Esslinger, Phys. Rev. Lett. **96**, 180402 (2006).

[16] R. Jördens, N. Strohmaier, Günter K., H. Moritz, and T. Esslinger, Nature **455**, 204 (2008).

[17] Y. Aharonov and D. Bohm, Phys. Rev. **115**, 485 (1959).

[18] D. Yoshioka, *The Quantum Hall Effect* (Springer, 1998).

[19] M. Z. Hasan and C. L. Kane, Rev. Mod. Phys. **82**, 3045 (2010).

[20] D. C. Tsui, H. L. Stormer, and A. C. Gossard, Phys. Rev. Lett. **48**, 1559 (1982).

[21] R. Willett, J. P. Eisenstein, H. L. Störmer, D. C. Tsui, A. C. Gossard, and J. H. English, Phys. Rev. Lett. **59**, 1776 (1987).

[22] R. B. Laughlin, Phys. Rev. Lett. **50**, 1395 (1983).

[23] F. Wilczek and A. Zee, Phys. Rev. Lett. **52**, 2111 (1984).

[24] G. Moore and N. Read, Nucl. Phys. B **360**, 362 (1991).

[25] D. Arovas, J. R. Schrieffer, and F. Wilczek, Phys. Rev. Lett. **53**, 722 (1984).

[26] R. Laughlin, Nobel Lecture (1998).

[27] C. Nayak, S. H. Simon, A. Stern, M. Freedman, and S. Das Sarma, Rev. Mod. Phys. **80**, 1083 (2008).

[28] I. Carusotto and C. Ciuti, arXiv:1205.6500, to appear in Rev. Mod. Phys. .

[29] N. Cooper, Adv. Phys. **57**, 539 (2008).

[30] I. Coddington, P. C. Haljan, P. Engels, V. Schweikhard, S. Tung, and E. A. Cornell, Phys. Rev. A **70**, 063607 (2004).

[31] I. Bloch, J. Dalibard, and W. Zwerger, Rev. Mod. Phys. **80**, 885 (2008).

[32] J. Dalibard, F. Gerbier, G. Juzeliūnas, and P. Öhberg, Rev. Mod. Phys. **83**, 1523 (2011).

[33] B. Juliá-Díaz, T. Graß, N. Barberán, and M. Lewenstein, New J. Phys. **14**, 055003 (2012).

[34] B. Juliá-Díaz, D. Dagnino, K. J. Günter, T. Graß, N. Barberán, M. Lewenstein, and J. Dalibard, Phys. Rev. A **84**, 053605 (2011).

[35] M. V. Berry, Proceedings of the Royal Society of London. A. Mathematical and Physical Sciences **392**, 45 (1984).

[36] J. L. Basdevant and J. Dalibard, *The Quantum Mechanics Solver* (Springer, 2006).

[37] C. Cohen-Tannoudji, J. Dupont-Roc, and G. Grynberg, *Atom-Photon Interactions: Basic Processes and Applications* (Wiley-Interscience, 1992).

[38] Y.-J. Lin, R. L. Compton, K. Jiménez-García, J. V. Porto, and I. B. Spielman, Nature **462**, 628 (2009).

[39] Y.-J. Lin, R. L. Compton, A. R. Perry, W. D. Phillips, J. V. Porto, and I. B. Spielman, Phys. Rev. Lett. **102**, 130401 (2009).

[40] J. Ruseckas, G. Juzeliūnas, P. Öhberg, and M. Fleischhauer, Phys. Rev. Lett. **95**, 010404 (2005).

[41] M. Burrello and A. Trombettoni, Phys. Rev. Lett. **105**, 125304 (2010).

[42] Y. J. Lin, K. Jiménez-García, and I. B. Spielman, Nature **471**, 83 (2011).

[43] D. Jaksch and P. Zoller, New J. Phys. **5**, 56 (2003).

[44] K. Osterloh, M. Baig, L. Santos, P. Zoller, and M. Lewenstein, Phys. Rev. Lett. **95**, 010403 (2005).

[45] N. R. Cooper, Phys. Rev. Lett. **106**, 175301 (2011).

[46] N. R. Cooper and J. Dalibard, EPL (Europhysics Letters) **95**, 66004 (2011).

[47] K. Jiménez-García, L. J. LeBlanc, R. A. Williams, M. C. Beeler, A. R. Perry, and I. B. Spielman, Phys. Rev. Lett. **108**, 225303 (2012).

[48] J. Struck, C. Ölschläger, M. Weinberg, P. Hauke, J. Simonet, A. Eckardt, M. Lewenstein, K. Sengstock, and P. Windpassinger, Phys. Rev. Lett. **108**, 225304 (2012).

[49] K. v. Klitzing, G. Dorda, and M. Pepper, Phys. Rev. Lett. **45**, 494 (1980).

[50] T. Chakraborty and P. Pietilainen, *The Quantum Hall Effects* (Springer, 1995).

[51] M. A. Paalanen, D. C. Tsui, and A. C. Gossard, Phys. Rev. B **25**, 5566 (1982).

[52] P. Hawrylak and D. Pfannkuche, Phys. Rev. Lett. **70**, 485 (1993).

[53] C. L. Kane and E. Mele, Phys. Rev. Lett. **95**, 146802 (2005).

[54] B. Bernevig, T. L. Hughes, and S.-C. Zhang, Science **314**, 1757 (2006).

[55] J. Moore and L. Balents, Phys. Rev. B **75**, 121306 (2007).

[56] J. K. Jain, Phys. Rev. Lett. **63**, 199 (1989).

[57] N. R. Cooper and N. K. Wilkin, Phys. Rev. B **60**, R16279 (1999).

[58] A. Lopez and E. Fradkin, Phys. Rev. B **44**, 5246 (1991).

[59] N. Read and E. Rezayi, Phys. Rev. B **59**, 8084 (1999).

[60] A. H. MacDonald and S. M. Girvin, Phys. Rev. B **34**, 5639 (1986).

[61] F. D. M. Haldane, Phys. Rev. Lett. **55**, 2095 (1985).

[62] X.-G. Wen, *Quantum Field Theory of Many-Body Systems* (Oxford University Press, 2004).

[63] N. Read and E. Rezayi, Phys. Rev. B **54**, 16864 (1996).

[64] E. Fradkin, C. Nayak, A. Tsvelik, and F. Wilczek, Nucl. Phys. B **516**, 704 (1998).

[65] S. Girvin and A. H. MacDonald, *Perspectives in Quantum Hall Effects*, edited by S. Das Sarma and A. Pinczuk (John Wiley & Sons, 1997) Chap. 5.

[66] B. I. Halperin, Helv. Phys. Acta **56**, 75 (1983).

[67] E. Ardonne and K. Schoutens, Phys. Rev. Lett. **82**, 5096 (1999).

[68] E. Ardonne, N. Read, E. Rezayi, and K. Schoutens, Nucl. Phys. B **607**, 549 (2001).

[69] N. Metropolis, A. W. Rosenbluth, M. N. Rosenbluth, A. H. Teller, and E. Teller, J. Chem. Phys. **21**, 1087 (1953).

[70] R. Morf and B. I. Halperin, Phys. Rev. B **33**, 2221 (1986).

[71] S. M. Girvin, Phys. Rev. B **30**, 558 (1984).

[72] M. A. Baranov, K. Osterloh, and M. Lewenstein, Phys. Rev. Lett. **94**, 070404 (2005).

[73] T. Graß, M. A. Baranov, and M. Lewenstein, Phys. Rev. A **84**, 043605 (2011).

[74] K. Osterloh, N. Barberán, and M. Lewenstein, Phys. Rev. Lett. **99**, 160403 (2007).

[75] Y. A. Bychkov and E. I. Rashba, J. Phys. C **17**, 6039 (1984).

[76] G. Dresselhaus, Phys. Rev. **100**, 580 (1955).

[77] N. Goldman, A. Kubasiak, A. Bermudez, P. Gaspard, M. Lewenstein, and M. A. Martin-Delgado, Phys. Rev. Lett. **103**, 035301 (2009).

[78] A. G. Morris and D. L. Feder, Phys. Rev. A **74**, 033605 (2006).

[79] N. R. Cooper, N. K. Wilkin, and J. M. F. Gunn, Phys. Rev. Lett. **87**, 120405 (2001).

[80] G. H. Golub and C. F. van Loan, *Matrix Computations* (The John Hopkins University Press, 1996).

[81] B. Juliá-Díaz and T. Graß, Comput. Phys. Comm. **183**, 737 (2012).

[82] N. K. Wilkin and J. M. F. Gunn, Phys. Rev. Lett. **84**, 6 (2000).

[83] M. Popp, B. Paredes, and J. I. Cirac, Phys. Rev. A **70**, 053612 (2004).

[84] D. Dagnino, N. Barberán, M. Lewenstein, and J. Dalibard, Nature Phys. **5**, 431 (2009).

[85] N. K. Wilkin, J. M. F. Gunn, and R. A. Smith, Phys. Rev. Lett. **80**, 2265 (1998).

[86] R. A. Smith and N. K. Wilkin, Phys. Rev. A **62**, 061602 (2000).

[87] D. Dagnino, N. Barberán, and M. Lewenstein, Phys. Rev. A **80**, 053611 (2009).

[88] L. Jacak, P. Hawrylak, and A. Wojs, *Quantum Dots* (Springer, 1998).

[89] M. A. Cazalilla, Phys. Rev. A **67**, 063613 (2003).

[90] N. Regnault and T. Jolicoeur, Phys. Rev. Lett. **91**, 030402 (2003).

[91] M. Roncaglia, M. Rizzi, and J. Dalibard, Sci. Rep. **1**, 43 (2011).

[92] B. Paredes, P. Fedichev, J. I. Cirac, and P. Zoller, Phys. Rev. Lett. **87**, 010402 (2001).

[93] J. H. Eberly, N. B. Narozhny, and J. J. Sanchez-Mondragon, Phys. Rev. Lett. **44**, 1323 (1980).

[94] I. S. Averbukh, Phys. Rev. A **46**, R2205 (1992).

[95] G. Rempe, H. Walther, and N. Klein, Phys. Rev. Lett. **58**, 353 (1987).

[96] J. A. Yeazell, M. Mallalieu, and C. R. Stroud, Phys. Rev. Lett. **64**, 2007 (1990).

[97] M. Brune, F. Schmidt-Kaler, A. Maali, J. Dreyer, E. Hagley, J. M. Raimond, and S. Haroche, Phys. Rev. Lett. **76**, 1800 (1996).

[98] D. M. Meekhof, C. Monroe, B. E. King, W. M. Itano, and D. J. Wineland, Phys. Rev. Lett. **76**, 1796 (1996).

[99] M. Lewenstein and L. You, Phys. Rev. Lett. **77**, 3489 (1996).

[100] E. M. Wright, D. F. Walls, and J. C. Garrison, Phys. Rev. Lett. **77**, 2158 (1996).

[101] A. Imamoḡlu, M. Lewenstein, and L. You, Phys. Rev. Lett. **78**, 2511 (1997).

[102] A. Sørensen, L. M. Duan, J. I. Cirac, and P. Zoller, Nature **409**, 63 (2001).

[103] B. Juliá-Díaz, T. Zibold, M. K. Oberthaler, M. Melé-Messeguer, J. Martorell, and A. Polls, Phys. Rev. A **86**, 023615 (2012).

[104] Y. Castin and J. Dalibard, Phys. Rev. A **55**, 4330 (1997).

[105] E. M. Wright, T. Wong, M. J. Collett, S. M. Tan, and D. F. Walls, Phys. Rev. A **56**, 591 (1997).

[106] M. Greiner, O. Mandel, T. Hänsch, and I. Bloch, Nature **419**, 51 (2002).

[107] S. Will, T. Best, U. Schneider, L. Hackermüller, D.-S. Lühmann, and I. Bloch, Nature **465**, 197 (2010).

[108] T. Graß, B. Juliá-Díaz, and M. Lewenstein, Phys. Rev. A **86**, 053629 (2012).

[109] G. F. Bertsch and T. Papenbrock, Phys. Rev. Lett. **83**, 5412 (1999).

[110] A. D. Jackson and G. M. Kavoulakis, Phys. Rev. Lett. **85**, 2854 (2000).

[111] R. A. Smith and N. K. Wilkin, Phys. Rev. A **62**, 061602 (2000).

[112] M. Ueda and T. Nakajima, Phys. Rev. A **73**, 043603 (2006).

[113] V. Schweikhard, I. Coddington, P. Engels, V. P. Mogendorff, and E. A. Cornell, Phys. Rev. Lett. **92**, 040404 (2004).

[114] H.-J. Miesner, D. M. Stamper-Kurn, J. Stenger, S. Inouye, A. P. Chikkatur, and W. Ketterle, Phys. Rev. Lett. **82**, 2228 (1999).

[115] C. J. Myatt, E. A. Burt, R. W. Ghrist, E. A. Cornell, and C. E. Wieman, Phys. Rev. Lett. **78**, 586 (1997).

[116] E. J. Mueller and T.-L. Ho, Phys. Rev. Lett. **88**, 180403 (2002).

[117] S. Bargi, J. Christensson, G. M. Kavoulakis, and S. M. Reimann, Phys. Rev. Lett. **98**, 130403 (2007).

[118] K. Kasamatsu, M. Tsubota, and M. Ueda, Phys. Rev. Lett. **91**, 150406 (2003).

[119] M. R. Matthews, B. P. Anderson, P. C. Haljan, D. S. Hall, C. E. Wieman, and E. A. Cornell, Phys. Rev. Lett. **83**, 2498 (1999).

[120] V. Schweikhard, I. Coddington, P. Engels, S. Tung, and E. A. Cornell, Phys. Rev. Lett. **93**, 210403 (2004).

[121] B. Estienne and B. A. Bernevig, Nucl. Phys. B **857**, 185 (2012).

[122] M. Burrello and A. Trombettoni, Phys. Rev. A **84**, 043625 (2011).

[123] R. N. Palmer and J. K. Pachos, New J. Phys. **13**, 065002 (2011).

[124] S. Komineas and N. R. Cooper, Phys. Rev. A **85**, 053623 (2012).

[125] D. Yoshioka, B. I. Halperin, and P. A. Lee, Phys. Rev. Lett. **50**, 1219 (1983).

[126] X. G. Wen and Q. Niu, Phys. Rev. B **41**, 9377 (1990).

[127] K. Výborný, *Spin in fractional quantum Hall systems*, Ph.D. thesis, University of Hamburg (2005).

[128] S. Furukawa and M. Ueda, Phys. Rev. A **86**, 031604 (2012).

[129] M. M. Fogler and A. A. Koulakov, Phys. Rev. B **55**, 9326 (1997).

[130] F. D. M. Haldane, E. H. Rezayi, and K. Yang, Phys. Rev. Lett. **85**, 5396 (2000).

[131] F. Grusdt and M. Fleischhauer, arXiv:1207.3716 (2012).

[132] J. Schliemann, D. Loss, and R. M. Westervelt, Phys. Rev. B **73**, 085323 (2006).

[133] S. Datta and B. Das, Appl. Phys. Lett. **56**, 665 (1990).

[134] H. C. Koo, J. H. Kwon, J. Eom, J. Chang, S. H. Han, and M. Johnson, Science **325**, 1515 (2009).

[135] R. Barnett, S. Powell, T. Graß, M. Lewenstein, and S. Das Sarma, Phys. Rev. A **85**, 023615 (2012).

[136] C. Wang, C. Gao, C.-M. Jian, and H. Zhai, Phys. Rev. Lett. **105**, 160403 (2010).

[137] R. A. Williams, L. J. LeBlanc, K. Jiménez-García, M. C. Beeler, A. R. Perry, W. D. Phillips, and I. B. Spielman, Science **335**, 314 (2012).

[138] F. Dalfovo, S. Giorgini, L. P. Pitaevskii, and S. Stringari, Rev. Mod. Phys. **71**, 463 (1999).

[139] S. Sinha, R. Nath, and L. Santos, Phys. Rev. Lett. **107**, 270401 (2011).

[140] H. Hu, B. Ramachandhran, H. Pu, and X.-J. Liu, Phys. Rev. Lett. **108**, 010402 (2012).

[141] J. Villain, R. Bidaux, J. Carton, and C. R., J. Phys. (France) **41**, 1263 (1980).

[142] C. L. Henley, Phys. Rev. Lett. **62**, 2056 (1989).

[143] A. M. Turner, R. Barnett, E. Demler, and A. Vishwanath, Phys. Rev. Lett. **98**, 190404 (2007).

[144] R. Barnett, Internal notes .

[145] J.-P. Blaizot and G. Ripka, *Quantum Theory of Finite Systems* (MIT Press, 1986).

[146] S. Powell, Internal notes .

[147] R. Barnett, S. Powell, T. Graß, M. Lewenstein, and S. Das Sarma, Phys. Rev. A **85**, 049905 (2012).

[148] T. Ozawa and G. Baym, Phys. Rev. Lett. **109**, 025301 (2012).

[149] Y. Nambu, Phys. Rev. **117**, 648 (1960).

[150] J. Goldstone, A. Salam, and S. Weinberg, Phys. Rev. **127**, 965 (1962).

[151] P. T. Ernst, S. Götze, J. S. Krauser, K. Pyka, D.-S. Lühmann, D. Pfannkuche, and K. Sengstock, Nat. Phys. **6**, 56 (2009).

[152] S. D. Huber, E. Altman, H. P. Buchler, and G. Blatter, Phys. Rev. B **75**, 085106 (2007).

[153] S. D. Huber, B. Theiler, E. Altman, and G. Blatter, Phys. Rev. Lett. **100**, 050404 (2008).

[154] T. Grass, F. dos Santos, and A. Pelster, Laser Physics **21**, 1459 (2011).

[155] T. D. Graß, F. E. A. dos Santos, and A. Pelster, Phys. Rev. A **84**, 013613 (2011).

[156] M. Endres, T. Fukuhara, D. Pekker, M. Cheneau, P. Schauß, C. Gross, E. Demler, S. Kuhr, and I. Bloch, Nature **487**, 454 (2012).

[157] D. R. Hofstadter, Phys. Rev. B **14**, 2239 (1976).

[158] S. Powell, R. Barnett, R. Sensarma, and S. Das Sarma, Phys. Rev. Lett. **104**, 255303 (2010).

[159] S. Sinha and K. Sengupta, Europhys. Lett. **93**, 30005 (2011).

[160] K. Saha, K. Sengupta, and K. Ray, Phys. Rev. B **82**, 205126 (2010).

[161] E. Altman, W. Hofstetter, E. Demler, and M. D. Lukin, New J. Phys. **5**, 113 (2003).

[162] A. Isacsson, M.-C. Cha, K. Sengupta, and S. M. Girvin, Phys. Rev. B **72**, 184507 (2005).

[163] E. Altman, E. Demler, and M. D. Lukin, Phys. Rev. A **70**, 013603 (2004).

[164] P. Pérez-Fernández, P. Cejnar, J. M. Arias, J. Dukelsky, J. E. García-Ramos, and A. Relaño, Phys. Rev. A **83**, 033802 (2011).

[165] N. Lindner, A. Auerbach, and D. P. Arovas, Phys. Rev. B **82**, 134510 (2010).

[166] T. Graß, K. Saha, K. Sengupta, and M. Lewenstein, Phys. Rev. A **84**, 053632 (2011).

[167] K. V. Krutitsky and R. Graham, Phys. Rev. A **70**, 063610 (2004).

[168] B. Bradlyn, F. E. A. dos Santos, and A. Pelster, Phys. Rev. A **79**, 013615 (2009).

[169] K. Byczuk and D. Vollhardt, Phys. Rev. B **77**, 235106 (2008).

[170] K. Sengupta and N. Dupuis, Phys. Rev. A **71**, 033629 (2005).

[171] L. Balents, L. Bartosch, A. Burkov, S. Sachdev, and K. Sengupta, Phys. Rev. B **71**, 144508 (2005).

[172] N. Gemelke, E. Sarajilic, and S. Chu, arXiv:1007.2677 (2010).

[173] A. Barenco, C. H. Bennett, R. Cleve, D. P. DiVincenzo, N. Margolus, P. Shor, T. Sleator, J. A. Smolin, and H. Weinfurter, Phys. Rev. A **52**, 3457 (1995).

[174] N. Goldman, I. Satija, P. Nikolic, A. Bermudez, M. A. Martin-Delgado, M. Lewenstein, and I. B. Spielman, Phys. Rev. Lett. **105**, 255302 (2010).

[175] M. Aidelsburger, M. Atala, S. Nascimbène, S. Trotzky, Y.-A. Chen, and I. Bloch, Phys. Rev. Lett. **107**, 255301 (2011).

[176] E. W. Weisstein, *"Permanent." From MathWorld–A Wolfram Web Resource.* (http://mathworld.wolfram.com/Permanent.html).

[177] S. Mitra and A. H. MacDonald, Phys. Rev. B **48**, 2005 (1993).

# List of Figures


2.1 Vortex lattice . . . 13
2.2 Scheme for geometric phases . . . 14
2.3 Closed loop along a square contour . . . 20

3.1 Hall resistance . . . 28
3.2 Gap above squeezed Laughlin . . . 48

4.1 System behavior as function of $\eta$ . . . 61
4.2 Gap as function of $\eta$ . . . 62
4.3 Yrast line . . . 62
4.4 System behavior as function of $\eta$ and $\Omega_0$ . . . 64
4.5 Density and pair correlations in Laughlin-like regime . . . 65
4.6 Overlap with generalized states . . . 68
4.7 Overlap with generalized Pfaffian state . . . 68
4.8 Overlap with generalized Laughlin quasi-particle state . . . 69
4.9 Overlap with (generalized) Laughlin state . . . 70
4.10 Gap as function of $N$ . . . 71

5.1 Overlaps as function of $\eta$ . . . 76
5.2 Moving quasiholes . . . 77
5.3 Quasihole overlaps . . . 79
5.4 Overlaps with quasiholes in generalized Laughlin . . . 80
5.5 Effective charges . . . 82
5.6 Statistical phase . . . 82
5.7 Condensate with a hole: time evolution of density . . . 87
5.8 Condensate with hole: Eigenvalues of density matrix . . . 88
5.9 Pair-correlation function at different times . . . 88
5.10 Condensate with hole: Eigenvalues of density matrix for different $N$ 90
5.11 Condensate with hole: Density profile for different $N$ . . . 91
5.12 Condensate with two holes: Occupations of natural orbits . . . 92
5.13 Density profile at different times of the initial the state $\hat{\mathrm{O}}_{\mathrm{qh}}(0)\Psi_{\mathrm{L,qp}}$ 94
5.14 Overlap $c_i$ between $\hat{\mathrm{O}}_{\mathrm{qh}}(0)\Psi_{\mathrm{L,qp}}$ and eigenstates of $\mathcal{V}$ with energy $E_i$ for different $N$. . . . 95

6.1 GS energies for different $N$ and $S$ . . . 107
6.2 Interaction energy as a function of $g_{\uparrow\downarrow}$ . . . 109
6.3 Gap vs. filling . . . 109
6.4 Spectra at $\nu = 4/3$ . . . 110
6.5 Spectra at $\nu = 2$ . . . 111
6.6 Overlap with NASS states for different interaction configurations . 112
6.7 LL spectrum with SO coupling . . . 115
6.8 Overlap with Laughlin projections as a function of SO coupling strength . . . 118
6.9 Spectrum as a function of SO coupling strength . . . 120
6.10 Spectrum of SO coupled system at $\nu = 2$ . . . 124

7.1 Non-interacting dispersion . . . 132
7.2 Dispersion of collective excitations . . . 140
7.3 Free energy . . . 143
7.4 Depletion 3D . . . 145
7.5 Depletion 2D . . . 146

8.1 BH energy dispersion with SO coupling I . . . 157
8.2 MI-SF boundary with SO coupling . . . 157
8.3 Wavevector of energy minima I . . . 158
8.4 Momentum distribution I . . . 161
8.5 BH energy dispersion with SO coupling I . . . 162
8.6 Wavevector of energy minima I . . . 163
8.7 Momentum distribution II . . . 164
8.8 Momentum distribution III . . . 164
8.9 SF density . . . 168

A.1 Snapshot of the code . . . 183

# *Acknowledgements*

This thesis has become possible through the help and support of many people and institutions. To me it is a great pleasure to express my gratitude to them.

First, I wish to acknowledge the financial support by ERC Advanced Grant QUAGATUA, MINCIN Toqata, the ESF Programme EUROCORES entitled 'Cold Quantum Matter', AAII-Hubbard, and the EU projects AQUTE and NAMEQUAM.

I am indebted to Maciej Lewenstein for his constant guidance during the past years, and especially for obliging me to have an optimistic view. Certainly, if a calculus goes wrong but you are well, there is enough reason to be happy. But from time to time it happened to be quite relieving to be reminded of such simple rules by the boss.

Motivation and feedback on an almost daily basis I received when Bruno Juliá Díaz came to ICFO. This was very good, and I thank Bruno for his help.

I could also learn a lot from Nuria Barberán. To do so, I usually had to travel from Castelldefels to Barcelona. But sometimes Nuria sent me notes with instructions to ICFO by telefax. I am very grateful to her for the care she took of my progress.

Also the collaborations on quite longer distances have been very stimulating. For the support I received via e-mail or skype, I wish to thank Ryan Barnett, Michele Burrello, Daniel Dagnino, Jean Dalibard, Sankar Das Sarma, Kenneth Günter, Stephen Powell, Kush Saha, and Krishnendu Sengupta. For the hospitality at IQOQI in Innsbruck and the collaboration which started there, I am grateful to Mikhail Baranov.

Work at ICFO has always been pleasant due to the people who make ICFO a lively place. Representative for all of them, I here wish to express my gratitude to the present and past members of the quantum optics theory group, Remigiusz Augusiak, Sybille Braungardt, Alessio Celi, Marcelo Ciappina, Fernando Cucchietti, Omjyoti Dutta, Ulrich Ebling, André Eckart, Philipp Hauke, Stephan Humeniuk, Jaroslaw Korbicz, Anna Kubasiak, Michal Maik, Lluis Masanes, Pietro Massignan, Piotr Migdal, Simon Moulieras, Christine Muschik, Armand Niederberger, Javier Rodriguez-Laguna, Tahir Shaaran, Gergely Szirmai, Edina Szirmai, Luca Tagliacozzo, Olivier Tieleman, Christian Trefzger, Jordi Tura, Alejandro Zamora. I am especially grateful to my room-mate John Lapeyre. The support I received

from him was not only due to the short distance from my desk to his one, but also due to his immense willingness to help.

My stay at ICFO was enormously facilitated by its impressive administration, who took care of basically everything even before I arrived in Barcelona. I am also very grateful to ICFO's IT unit. It is already some time ago that I contacted them for the last time.

Finally, I wish to thank my friends, my family, and my wife. Without them, I would not even have started to write this thesis, and now I am finished.